ENGINEERED BIOMATERIALS AS EXTRACELLULAR MICROENVIRONMENTS FOR GUIDING CELL PROGRAMMING AND REPROGRAMMING

BY

JUNMIN LEE

DISSERTATION

Submitted in partial fulfillment of the requirements
for the degree of Doctor of Philosophy in Materials Science and Engineering
in the Graduate College of the
University of Illinois at Urbana-Champaign, 2017

Urbana, Illinois

Doctoral Committee

Associate Professor Kristopher A. Kilian, Chair
Professor Jianjun Cheng
Associate Professor Timothy M. Fan
Assistant Professor Cecilia Leal

ABSTRACT

The interface between cells and materials is a dynamic and complex environment where cells in contact with materials can sense their properties such as stiffness, matrix protein, and geometry and respond to these cues in multiple ways including through mechanical forces exerted on the matrix by the cells. Cells incorporate these cues via signal propagation through integrins, and translate this information through intracellular signal transduction cascades to regulate gene expression and cell fate decisions. Advances in biomaterials to direct stem cell lineage decisions have focused on designing biomimetic materials that realize the "in vivo" microenvironments' ability to interact with cells. However, not only is designing tailored biomaterials that present multiple signals challenging, but the precise roles of physical and biochemical cues in coordinating cellular processes such as migration, proliferation, and differentiation remains difficult to dissect.

After a short introduction we explore using model polyacrylamide hydrogel systems in Chapter 2-5 to study the effects of biophysical (elasticity and geometry) and chemical (matrix protein) cues on mesenchymal stem cell (MSC) fate decisions, showing these cues can play a large role in differentiation. In Chapter 6 we explore how switching the biophysical microenvironment (matrix stiffness and cell shape) can be used to understand the plasticity of MSC lineage specification. Finally, in Chapter 7-9, we demonstrate how geometric cues at the interface of tissue, where interfacial energy and curvature can be modulated in vitro, will dictate cancer cell tumorigenicity, metastatic potential, and the regulation of tumorangiogenesis. Moreover, we reveal a mechanism where perimeter features initiate $\alpha 5\beta 1$ adhesion and epithelial-to-mesenchymal transition, Mitogen Activated Protein Kinase (MAPK) and Signal Transducer and Activator of Transcription (STAT) pathways, and regulation of distinct histone marks, to guide gene expression underlying the phenotypic alterations of malignant melanoma.

Overall, we believe the work presented here demonstrates the importance and utility of extracellular properties in modulating cell programming and reprogramming, and should aid in the development of biomaterials for more efficiently directing distinct cellular states for the development of synthetic model systems that more accurately recapitulate the in vivo microenvironment.

ACKNOWLEDGEMENTS

First, I would like to thank Prof. Kristopher Kilian for his excellent support and expert guidance during my PhD studies. If not for the suggestions and help given by him, these works could have never been done. In addition, I especially appreciate his consideration for me when I started my PhD. I did not have any deep knowledge about biomaterials but only have a great enthusiasm about research. He recognized my passion immediately and gave me an opportunity to conduct my PhD in his group. I do not want to imagine my PhD without him. Again, I appreciate your dedication and investment in me as one of your graduate students.

I would also like to thank my committee members: Professors Jianjun Cheng, Timothy Fan, and Cecilia Leal. They have helped shape the work with their insightful direction and have helped me develop as a scientist during my PhD, even from before serving on my committee. In addition, I really appreciate their great support and for providing letters of recommendation for awards and postdoctoral applications. Specifically, I thank Professors Jianjun Cheng for his valuable and constructive comments for my future, Professors Timothy Fan for giving me the opportunity to work with him, and learn more about the clinical aspects of this work, and Professors Cecilia Leal for her consideration and valuable time she spent guiding me during the course of my doctoral work.

I would like to show my grateful appreciation to Professor Wooyoung Lee, who taught me and was my supervisor when I was a Master degree student. Professor

Lee is a warm-hearted and discipline-keeping person. Without him, I may not be able to start my PhD study in the US.

I am further thankful to the Kilian group members. I would like to especially thank Amr Abdeen from whom I have learned a lot about work ethic, genius and humility and who contributed to significant aspects of the work presented here. Further thanks to Doug Zhang (one of great friends for me), Yanfen Li (like a mother teresa in the Lab), Yi Pei (complains but do her best always), Phuong Le (Vietnam monster), Sarith Bandara, Sam Mo, Claire Tang, and Alex Kim as they taught me a lot and made my research journey more fruitful, enjoyable and interesting.

I also wish to heartily thank our collaborators including Kathryn Wycislo, Christopher Serward, Huimin Zhang, Jamila Hedhli, and Xin Tang and Professors Timothy Fan, Lisa Stubbs, Wawrzyniec Dobrucki, and Taher Saif. Without them, everything would not have gone as smoothly.

I also appreciate the encouragement and support of all of my friends in the US and Korea who helped me during my PhD studies.

Finally, I'd like to thank my family. Especially my parents (Seung-Gil Lee and Kwang-Hee Kim), parent-in-law (Kwan-Dong Kim and Keum-Sook Seok), my wife (Ji-hyun Kim), and my two sons, Nathan Sungbin Lee and Caleb Woobin Lee, without whom none of this would be possible, and who have supported my passions and so often put my aspirations above all other considerations. I would like to say I love you so much.

TABLE OF CONTENTS

CHAPTER 1

INTRODUCTION

1.1 Biomaterials for the Study/Control of Cell-ECM Interactions

Hydrogels based biomaterials are an appealing scaffold material for tissue engineering distinguished by high water content and diverse physical properties (1–7). They can be engineered to mimic the ECM of many tissues in ways that allows being used as scaffold materials for drug-delivery systems, engineering tissue replacements and various other applications (8–12). It is well known that cells in vivo can sense their mechanical microenvironments such as the inherent matrix elasticity or external mechanical force through the process of mechanotransduction by an interplay between actomyosin based cellular contractions and integrin mediated focal adhesions, resulting in modulations of cell functions (13–20). Synthetic hydrogel biomaterials can be designed to emulate the properties of natural biomaterials, where mechanical and biochemical properties are "built-in" to the materials to convey mechanochemical signals to adherent/encapsulated cells. This mechanotransduction plays a key role in guiding cellular activities and lineage choices across a range of physiological and pathological contexts.

1.2 Microenvironments for Directing Mesenchymal Stem Cell Fate Decisions[1]

Cells adhering to the extracellular matrix (ECM) can sense the mechanical properties through specific interactions of cell surface integrins with adhesion ligands (21–26). Traction forces exerted by the cell through these interactions influence cytoskeletal tension and lead to changes in cell shape and associated signaling cascades that ultimately regulate gene expression (27–32). This process of mechanotransduction has emerged as an important aspect of stem cell differentiation and is dependent on both the mechanics and the composition of the microenvironment. For example, Datta et al. revealed the importance of the mechanical and biochemical microenvironment by culturing osteoprogenitor cells on a decellularized osteoblast matrix leading to increased expression of osteogenic markers (33). Work in the Schaffer and Healey groups has demonstrated that mechanical properties can guide neurogenesis in neural stem cells where softer matrices promote dendritic process extension (7). A study by Engler, Discher and colleagues demonstrated the importance of matrix mechanics in guiding MSC fate by studying cells adherent to collagen coated polyacrylamide hydrogels of variable stiffness (28). MSCs were found to commit to lineages based on the similarity to the committed cells' native matrix; soft polyacrylamide gels (<1 kPa) promote

[1] Parts of this chapter have been adapted from the following publications:
Junmin Lee, Amr A. Abdeen, Douglas Zhang, and Kristopher A. Kilian, Directing stem cell fate on hydrogel substrates by controlling cell
geometry, matrix mechanics and adhesion ligand composition, Biomaterials, 2013, 34, 8140-8148

neurogenesis, intermediate stiffness gels (~10 kPa) promote myogenesis and stiff gels (>30 kPa) promote osteogenesis.

In addition to stiffness, the composition and presentation of adhesion ligands on a substrate has been shown to influence MSC differentiation (34–36). Cooper-White and co-workers demonstrated that different matrix proteins—collagen, fibronectin and laminin—grafted to hydrogel substrates of different stiffness will significantly influence the expression of myogenic and osteogenic markers (22). This work suggests that the identity of adhesion ligand and its presentation to the cell can play an important role in promoting competing differentiation outcomes. Kilian and Mrksich recently showed how the density and affinity of surface bound adhesion peptides could modulate the expression of markers associated with neurogenesis, myogenesis and osteogenesis, further confirming the importance of the type and presentation of ligand in guiding stem cell differentiation (23).

Another important physical parameter that has emerged as an important cue in guiding the differentiation of stem cells, and is influenced by stiffness and the presentation of adhesion ligands, is cell shape (6, 37–39). For instance, Chen and colleagues demonstrated that MSCs captured on small islands tended to prefer adipocyte differentiation when exposed to a mixture of osteogenic and adipogenic soluble cues while cells captured on large islands developed a higher degree of cytoskeletal tension and preferred to adopt an osteoblast outcome (37). In a related study, Mrksich and colleagues demonstrated that MSCs patterned in geometries with subcellular concave regions and moderate aspect ratios increase the actomyosin contractility of the cell and promote osteogenesis (38). In both of

these studies, keeping cell shape the same across a population of MSCs was shown to normalize the differentiation outcome when compared to unpatterned cells that take on a host of different geometries.

1.3 Microenvironments for Directing Cancer Cell Fate Decisions

Emerging evidence suggests that tumor cells may show `plasticity' in response to microenvironmental cues. For example, melanoma cells have been shown to adopt a tumorigenic, CSC like state and form new tumors after transplantation (40). An exciting recent report showed how soft fibrin gels can promote selected growth of tumorigenic melanoma cells (41), and further investigation demonstrated how the mechanical properties of the matrix can regulate Sox2 expression (42). However, the canonical self-renewal transcription factors Oct4 and Nanog were not activated in these cells. The influence of matrix mechanics on cancer cell tumorigenicity has been demonstrated in several other cancers (43). Taken together, these reports show that, in addition to the classical models underlying tumour heterogeneity, tumour cells may exhibit more plasticity than originally anticipated, and may be influenced through biophysical cues in the tumour microenvironment. Substrate stiness is known to modulate cell behavior (44) and gene expression (45). Furthermore, the geometric organization of cells in tissue places them into variable regions of mechanical stress (46), which can influence proliferation (47), migration (48), branching (49), stem cell characteristics (50), and cancer cell survival and invasiveness (51, 52). For example, Nelson and colleagues demonstrated how geometry can guide epithelial to mesenchymal transitions (EMT) through mechanical stress in micropatterned mammary epithelial cells (51).

1.4 Cell plasticity: cell programming and reprogramming

Differentiation of stem cells is not a binary event but involve several phases, where a less specialized cell becomes more specialized through several transitory states (53–56). For instance, mesenchymal stem cells (MSCs) under specific contexts are coaxed to specify osteoprogenitor markers and then mature to pre-osteoblasts before finally committing to osteoblast and osteocyte phenotypes (57). This gradual lineage progression may serve as an amplifying function to regulate the spatiotemporal distribution of cells that are required for a specific regeneration or homeostasis process (53). Alternatively, subtle changes in cell state may foster transitions where a progenitor is more prone to reprogramming back to the stem cell state compared to a committed cell (39). Emerging evidence suggests the latter scenario occurs more readily than anticipated and that cellular plasticity enables dynamic shifting of cell state through regulation of distinct epigenetic marks (58–60). In addition to plasticity within a defined lineage program, numerous reports now indicate that MSCs may harbor the potential to trans-differentiate across germ layers (28, 61–63).

Phenotypes of cells such as epithelial or mesenchymal are not always permanent (64, 65). For instance, EMT or mesenchymal to epithelial transition (MET) leads to reversible reprogramming of cancer cells under appropriate conditions (66). Recent evidences support that EMT program which has emerged as a central driver of tumor malignancy is associated with epigenetic modifications (51, 67–69). The fact that cells under the EMT could acquire stem-like properties like expressing stem cell markers indicates that activation of EMT programs function as a major mechanism

for generating cancer stem cells (CSC) (70). These CSC phenotypes possessing mesenchymal characteristics could locally invade, which is a necessary first step in metastatic dissemination and eventually contributes to tumor progression (71, 72). In addition, epigenetic modifications are known to be reversible, and thus metastasized cells (mesenchymal states) to switch back to the epithelial states on colonization could be allowed at a secondary site (40).

Understanding the plasticity and mechanisms underlying cell programming and reprogramming in response to the microenvironments is important for fundamental biology as well as for establishing appropriate in vitro culture conditions to direct a desired outcome or therapeutic development.

1.5 Hypothesis and Thesis Structure

With the knowledge of the essential role the ECM plays in regulating cellular behavior, we hypothesize that properties of the extracellular matrix such as elasticity, composition, and geometric presentation affect, and can be used to guide, cell fate decisions. We propose using microengineered biomaterials to deconstruct and study the effects of these parameters on guiding cellular processes, in particular the programming of MSCs and the reprogramming of cancer cells, and to explore if combinations of biophysical properties will influence the cell state in order to gain a fundamental understanding of the role of the microenvironment during these cellular processes.

This hypothesis is tested throughout this thesis. In chapter 2-5, we use a polyacrylamide model system with microcontact printing to investigate the influence

of matrix elasticity and composition on the programming of MSCs, especially differentiation. In chapter 6, to answer the question on whether changing the biophysical aspects of the substrate could modulate the degree of MSC lineage specification, we chose to explore two diverse differentiation outcomes: MSC osteogenesis and trans-differentiation to neuron-like cells, and study the effect of switching the biophysical microenvironment on rewiring MSC lineage specification. Finally, in chapter 7-9, we use soft hydrogel microengineering to pattern populations of tumor cells on two-dimensional (2D) and within three-dimensional (3D) hydrogels of variable stiffness, with combinations of perimeter geometric cues, to explore how biophysical parameters influence CSC characteristics, metastasis, tumorigenicity, histone modifications, and even angiogenic potential.

CHAPTER 2

THE INFLUENCE OF BIOPHYSICAL PARAMETERS ON MAINTAINING THE MESENCHYMAL STEM CELL PHENOTYPE[2]

2.1 Introduction

When proliferating in culture, MSCs are devoid of hematopoietic and endothelial markers (e.g., CD34, CD45) and express distinct level of CD90, CD105 (Endoglin), and Stro-1 (73). These MSC-positive markers serve to classify the degree of "stemness" for in vitro culture with a significant decrease during differentiation (74). The biophysical and biochemical properties of the extracellular matrix (ECM) play a significant role in regulating stem cell migration, proliferation and differentiation (22, 28, 75–79). A major research effort has gone into devising in vitro engineered ECMs to unravel the complex interplay of factors that control stem cell differentiation (24, 25, 50, 80, 81). However, the role that ECM properties play in guiding the multipotent phenotype and self-renewal has received significantly less attention. Gilbert et al. demonstrated skeletal muscle stem cell self-renewal was heavily influenced by the stiffness of the surrounding material (82), and Winer et al. showed how soft substrates promote MSC quiescence; MSCs on very soft substrates (~0.25 kPa) that mimic the stiffness of bone marrow are quiescent but retain the ability to differentiate when exposed to induction media (78). Recently, Skardal et al. reported how soft substrates promote the expression of MSC surface markers in

[2]This chapter is adapted from the following publication:
Junmin Lee, Amr A. Abdeen, Alex S. Kim, and Kristopher A. Kilian, The influence of biophysical parameters on maintaining the mesenchymal stem cell phenotype, ACS Biomaterials Science & Engineering, 2015, 1, 218-226

amniotic fluid-derived stem cells (83). These reports suggest that the mechanical properties of the cell culture substrate may influence MSC multipotency.

In the present chapter 2, we explore the role of substrate stiffness alone and when combined with geometric cues in modulating the MSC multipotent phenotype. Polyacrylamide hydrogels are fabricated across a range of mechanical properties and microcontact printed with matrix proteins in shapes that accommodate single cells to several hundreds of cells. Immunofluorescence characterization of MSC markers, coupled with computer simulations and pharmacological inhibitors of actomyosin contractility, reveals spatial control of multipotency directed by the stiffness of the underlying substrate and cellular organization.

2.2 Materials and Methods

General materials and methods are given in Appendix A.

Materials:

Mouse anti-Stro-1 antibody was purchased from R&D Systems (MAB1038), rabbit anti-Endoglin was purchased from Sigma (E7534), and rabbit anti-BrdU was purchased from Sigma (B2531).

Immunocytochemistry:

Cells on surfaces were fixed with 4% paraformaldehyde (Alfa Aesar) for 20 min, permeablized in 0.1% Triton X-100 in PBS for 30 min and blocked with 1% bovine serum albumin (BSA) for 15 min. Primary antibody labeling was performed in 1% BSA in PBS for 2 h at room temperature (20 °C) with mouse anti-Stro-1 and rabbit

anti-Endoglin and anti-BrdU (1:200 dilution). Secondary antibody labeling was performed using the same procedure with Tetramethylrhodamine-conjugated antirabbit IgG antibody, Alexa Fluor 488-phalloidin (1:200 dilution), Alexa647-conjugated antimouse IgG antibody, and 4,6-diamidino-2-phenylindole (DAPI, 1:5000 dilution) for 20 min in a humid chamber (37 °C). Immunofluorescence microscopy was conducted using a Zeiss Axiovert 200 M inverted research-grade microscope (Carl Zeiss, Inc.) or an LSM 700 (Carl Zeiss, Inc.) which is a four laser point scanning confocal with a single pinhole. Immunofluorescent images from the immunofluorescence microscopy or the LSM 700 were analyzed using ImageJ; the fluorescence intensity of single cells (over 20 cells) and multiple cells (over 20 patterns) for each condition were measured to compare stemness marker expression. All results were confirmed at least three times. The relative intensity of the fluorescence was determined by comparing each intensity value to the average intensity of one condition. The intensity value for single cells was obtained from cytoplasmic staining intensity minus backgrounds and for multiple cells total cell intensities (minus background) were obtained for each condition.

BrdU Staining:

BrdU staining was conducted to check MSC proliferation as reported previously (39). Briefly, 1 h postseeding, nonadherent cells were aspirated and BrdU labeling reagent was added (1:100 (v/v)), and incubated for 24 h. Cultures were fixed in 70% ethanol for 30 min and then denatured with 2 M HCl for 30 min. Cultures were permeabilized with 0.1% Triton X-100 in PBS for 30 min and blocked with 1% BSA in PBS for 15 min and then incubated with mouse anti-BrdU primary antibody

(1:200 dilution, 3 h at room temperature) followed by Alexa Fluor 647-conjugated antimouse IgG antibody (1:200 dilution, 20 min in a humid chamber (37 °C)). Cell nuclei were stained with DAPI (1:5000 dilutions). Percent incorporation of BrdU was counted manually.

Modeling of Cell Monolayer:

A finite-element model of contractile cell monolayers was constructed using ABAQUS FEA software as described before (47). Briefly, a model with the desired geometry was constructed consisting of 2 layers: an active 20 μm thickness top layer and a passive 5 μm bottom layer fixed at the bottom surface. The physical parameters used were those described previously (47). Contractility was introduced to the active layer by applying a 5K temperature drop to induce isotropic thermal strain. The von Mises stress at the bottom surface was reported. Convergence of results was confirmed by testing multiple mesh sizes and layer properties.

Inhibition Assays:

Inhibitors were added to cell culture media at the following concentrations before and after cell seeding and with each media change: Blebbistatin (1 μM) and Y-27632 (2 μM) (Calbiochem).

Statistical Analysis:

Error bars represent standard deviation and N value is the number of experimental replicates. For statistical analysis, we used one-way ANOVA for comparing multiple

groups and two-tailed p-values from unpaired t test for comparing two groups, and values of $P < 0.05$ were considered statistically significant.

2.3 Results

Hydrogel Fabrication and Patterning

In order to study the combined influence of substrate stiffness and cell shape on MSC phenotype, we used protein conjugated polyacrylamide hydrogels. The procedure is schematically presented in Fig. 2.1a. Soft (0.5 kPa) and stiff (30 kPa) hydrogels were prepared according to established methods (84). Microcontact printing was employed to transfer oxidized fibronectin from polydimethylsiloxane (PDMS) stamps—patterned using photolithography to present geometric features in relief—to the hydrazine treated gels (13). We employed fluorescently labeled protein to demonstrate uniform protein coating with no sign of enhanced border deposition, for both soft and stiff substrates (Fig. 2.2). After seeding cells on these surfaces, we confirmed that single cells can be confined in small patterns ranging from 1000 - 20,000 μm^2 and multiple cells can exist in larger sized patterns ranging from 5000 - 400,000 μm^2 area. Laser scanning confocal microscopy of patterned cells shows that cell height is higher in soft gels than stiff gels, decreases with increasing area and is higher for multi-cellular patterns than patterns with single cells (Fig. 2.3 and 2.4). Morphological analysis reveals the average area of cells on stiff substrates is comparable to the pattern size (See Fig. 2.4). Patterned cells remained viable and restricted to the islands adhesive area for approximately 10 days in culture.

The influence of single cell area and geometry on MSC phenotype

To examine the phenotype of patterned MSCs in response to hydrogel stiffness (0.5 and 30 kPa) and shape (different sizes and geometries), we studied the expression of the canonical MSC multipotency surface markers Endoglin and Stro-1 (Fig. 2.1b, c, and d) (39, 85). Constraining single cells to small islands leads to quiescence. Cells cultured on soft substrates show higher expression of multipotency markers compared to stiff substrates (~3-fold higher for Endoglin and ~2-fold higher for Stro-1). In addition, cells cultured in smaller islands (1000 μm^2) tend to express elevated MSC markers compared to cells cultured in large islands (20,000 μm^2) (~16.9-fold (soft) and ~4.4-fold (stiff) higher for Endoglin and ~5.9-fold (soft) and ~3.8-fold (stiff) higher for Stro-1). MSCs cultured on soft matrices showed higher expression of multipotency markers compared to those cultured on stiff substrates throughout the experiments (Fig. 2.5). Since subcellular geometric cues have been shown to influence lineage specification (86, 87), we tested various shapes of the same area (3000 μm^2) (Fig. 2.6a and b). We cultured MSCs in these patterns for 10 days, and found that cells on circular patterns showed higher levels of MSC markers relative to other shapes. Interestingly, regardless of stiffness, cells cultured in ovals (8:1 aspect ratio) showed the lowest levels of Endoglin expression compared to circular shapes (9.4-fold (soft) and 5.3-fold (stiff)) while Stro-1 marker expression was the lowest for cells in star shapes compared to circle shapes (11.6-fold (soft) and 21.7-fold (stiff) lower for Stro-1) (Fig. 2.4c and d). The distributions of single cells that express MSC markers was also analyzed and demonstrate that both substrate stiffness and size dependence (for single cells) influence the retention of the MSC phenotype (Fig. 2.7). In addition, flow cytometry for endoglin and Stro-1

expression in MSCs cultured on TCP and on patterned and non-patterned hydrogels of 0.5 kPa and 30 kPa were performed (Fig. 2.8). While the differences in Endoglin expression were not significant across conditions as determined by flow, soft hydrogels promoted maintenance of Stro-1 expression for 10 days at levels comparable to cells freshly seeded from cryopreservation.

The influence of cell density on MSC phenotype

Although cells in vivo integrate and respond to various biophysical cues present in their microenvironments such as matrix stiffness and cell shape, cells are also often in contact with neighboring cells. This contact may change how cells respond to these cues. Thus, we next investigated the effects of patterning multiple cells in large patterns on MSC phenotype. We employed circular patterns of 100,000 μm^2 and cultured cells for 10 days. Analogous to our single cell results, multiple cells cultured on soft substrates had higher expression of MSC markers compared to those cultured on stiff substrates. Islands with higher cell density showed increased expression of MSC markers (Fig. 2.9a). Cells on soft substrates showed higher expression of MSC markers as cell number increased compared to those on stiff substrates (Fig. 2.9b). The average number of cells per pattern was ~40 cells with a range from 1 to ~120 cells in the 100,000 μm^2 area of each pattern. Since seeding density was fixed, variations are likely due to irregular cell deposition after seeding. We also confirmed the effect of cell density on the maintenance of MSC multipotency marker expression by using square shapes (Fig. 2.10), and we saw good correspondence with the results from the circular shapes. From confocal microscopy analysis, we confirmed that the results are not artifacts of cell density

or debris (Fig. 2.9c and 2.11). We also examined the proliferation of MSCs in large circular patterns (100,000 μm^2) by culturing MSCs in 5-bromo-2'-deoxyuridine (BrdU) labeling reagent-containing media for 24 h at similar densities. At that time point, ~22% (soft) and ~26% (stiff) of cells cultured in patterns stained positive for BrdU (Fig. 2.12). We found that the number of cells confined within a pattern—which influences the degree to which they can spread—was correlated to the expression of MSC markers. For patterns on soft substrates (0.5 kPa), as the number of cells increase within a pattern, the spread area decreases (Fig. 2.13) with an associated increase in the expression of MSC markers (Fig. 2.14b). This observation is consistent with our studies of constraining single cell area (Fig. 2.1). Furthermore, we compared large patterned cells to non-patterned cells with similar density. Cells residing in central locations of very large patterns (400,000 μm^2) showed similar intensities to non-patterned cells of similar density (Fig. 2.14b and c). However, as pattern size decreases to ~100,000 μm^2, cell organization and packing are more homogenous compared to the elongated spread cells observed on non-patterned substrates. To demonstrate this, MSCs were cultured for 10 days on 100,000 μm^2 circles or non-patterned surfaces where cell density was the same. The results show that MSC marker expression is higher in patterned regions than non-patterned regions (Fig. 2.15).

We next investigated whether position within the pattern affected MSC state. To compare the MSC phenotype in different regions of circular patterns (5000; 20,000; 100,000; and 400,000 μm^2; with an average of ~5, 12, 48, and 175 cells per pattern, respectively), we superimposed a circle of half radius to divide the patterns

into two regions (Fig. 2.14a). Cells in region 1 (central region) show ~2-fold increase in Endoglin and Stro-1 expression compared to those in region 2 (outer region) (Fig. 2.14b and c). In addition, cells in smaller sized patterns display higher levels of MSC marker expression. The average cell area when cultured in 5000 μm^2 was ~2-fold smaller than larger sized patterns (20,000, 100,000, and 400,000 μm^2) (Fig. 2.14d). MSCs cultured on soft substrates showed a less pronounced intensity difference between the two regions compared to stiff substrates (Fig 2.16). In order to further verify the influence of pattern region, we generated immunofluorescence heatmaps from both stains (Endoglin and Stro-1) via averaging the intensity of multiple overlaid immunofluorescence images using ImageJ (Fig 2.14e). Heatmaps showed cells on soft substrates maintain higher levels of multipotency compared to those on stiff substrates and that highest expression is localized to the central regions. We used finite element modelling of mechanical stress distributions in circular patterns and found that, for a connected layer, mechanical stress decreases closer to the center regions, which corresponds with the results of the experiments (Fig. 2.14f). The division rates for MSCs cultured on soft or stiff substrates do not show statistically significant differences (Fig. 2.12). Taken together, our results demonstrate a clear influence of substrate stiffness, cell shape and position in multicellular architectures on maintaining the expression of multipotency markers. However, we acknowledge that some variability in cell division (self-renewal or differentiation) across the substrates may affect the multipotent outcome.

The role of cytoskeletal tension in maintaining MSC phenotype

From the results of multicellular studies in circular patterns, mechanical stress at the will influence the expression of MSC markers. To explore whether the stress from the patterns influence the MSC phenotype through cytoskeletal tension, we treated cells with Y-27632 (an inhibitor of rho-associated kinases) and blebbistatin (an inhibitor of myosin II). MSCs were cultured in 100,000 μm^2 circular geometries with or without 2 mM Y-27632 or 1 mM blebbistatin for 10 days. Cells cultured with Y-27632 show increased expression of both Endoglin and Stro-1 which reveals that restriction of cytoskeletal tension plays a significant role. However, treatment with blebbistatin did not influence expression levels (Fig. 2.17). In terms of cell spreading, untreated and blebbistatin treated cells were similar but Y-27632 treated cells displayed lower spreading. The degree of cell spreading with Y-27632 treatment was less than untreated cells, resulting in higher levels of multipotency markers. Since the seeding density of cells was fixed, we could indirectly compare the proliferation rates between untreated and drug treated cells. Average cell densities were similar suggesting that drug treatment at the tested concentration makes little difference in proliferation rates. In addition, cells on stiff substrates express lower levels of multipotency markers compared to those on soft substrates (Fig 2.18).

2.4 Discussion

Within the stem cell niche, cells are exposed to various combinations of biochemical and biophysical factors. MSC fate decisions are influenced by the properties of the niche which provide a highly specialized microenvironment for maintenance of the multipotent phenotype and for lineage specification. Recently Yang et al. (88) and

Lee et al. (79) demonstrated how MSCs cultured on stiff materials can "remember" their environment which may limit their potential to differentiate to softer lineages. Understanding how biophysical cues influence the MSC phenotype, and controlling these aspects ex vivo will be critical for leveraging the broad therapeutic potential of MSCs.

Previously we had shown that restricting cell spreading using micropatterned islands on rigid materials leads to maintenance of the multipotent phenotype and prevention of inappropriate lineage specification (39). Since the degree of cell spreading—by micro-confinement or through control of substrate stiffness—has been shown to modulate cytoskeletal tension and MSC fate decisions (2, 37, 89, 90), we fixed the adhesion area of the cells while tuning the stiffness of the substrate. Single MSCs captured in circular shapes show elevated expression of multipotency markers compared to those cultured on non-patterned gels. This expression decreases as the cell adhesive area is increased. This trend in MSC marker expression holds for both soft and stiff substrates; however, in all cases, MSCs adherent to soft hydrogels display higher MSC marker expression levels. This finding is consistent with our work with micro-confined MSCs on rigid materials (39) and suggests that soft materials—previously demonstrated to influence MSC quiescence (78)—may also serve to retain multipotency. Interestingly, the expression of multipotency markers for cells cultured in 1000 μm^2 features on stiff substrates is similar to the level of that for cells cultured in 5000 μm^2 patterns on soft substrates. This result demonstrates how MSC multipotency may be influenced by combinations of the interrelated biophysical parameters stiffness and cell size

(the degree of spreading). This led us to ask whether controlling subtle geometric features in cells of the same total adhesive area may have an influence on the MSC phenotype. We micropatterned single cells in various geometries with a constant adhesive area (3000 μm^2). Shapes that foster high degrees of cytoskeletal stress such as stars and ovals of different aspect ratios (76) showed lower expression levels of MSC markers over time compared to circular shapes. This result suggests that, in addition to spreading, discreet geometric cues at the perimeter of single cells will promote the loss of the multipotent phenotype. Certain shapes appeared to differentially modulate different markers. For instance, MSCs in the elongated oval shape led to the largest decrease in Endoglin expression, while star shaped cells showed the largest decrease in Stro-1. Both of these shapes have been shown previously to enhance osteogenesis in single MSCs (76). Exploring differences between these shapes in regulating multipotency (and differentiation) is outside of the scope of this study. Nevertheless, it demonstrates how micropatterning platforms may be used in future work to explore subtle mechanobiology phenomena.

In addition to single cells, geometric features at the multicellular level have been demonstrated to modulate cell behavior ranging from growth control to differentiation (47, 91). For example, Ruiz et al. demonstrated how MSC aggregates grown on outer regions, which show high local strains, tend to differentiate into the osteogenic lineage while those cultured at inner regions, which display low cytoskeletal tension, prefer to differentiate into the adipocyte lineage when cultured with mixed induction media (91). Inspired by this study, and our observations that

significant numbers of MSCs in culture on these materials remain multipotent, we hypothesized that MSCs cultured in multicellular arrangements would show patterns of multipotency marker expression. Patterns with a higher density of cells (which restricts spreading) led to higher expression of multipotency markers compared to patterns with a lower density of cells (which promotes spreading). To investigate how mechanical stress fostered by multicellular geometries may influence MSC multipotency, we explored circular patterns of various areas (5000 to 400,000 μm^2) and examined two different regions within each pattern (perimeter and interior). MSC marker expression decreased in cells that were cultured near the perimeter region while cells in the pattern interior showed the highest levels of expression. This trend in regional expression of MSC markers is observed on both soft and stiff substrates enhanced expression seen, but with on the softer materials. Using a finite element model of cellular sheet contraction, we see that the perimeter region promotes the highest degree of stress. This model is based on interconnected nodes and its results would only apply where there is force transmission between cells in multicellular aggregates, through cell-cell interaction. Cadherin junctions have been implicated in 3D MSC aggregation (92) and, although this is a 2D system, there may be an aggregating effect due to patterning the cells. Further investigation is needed to determine whether such interactions are present or are promoted in this system. Note that patterning influences the degree in which cells can spread initially and leads to the development of two types of cells within the geometric confinement: 1) cells experiencing a high degree of stress at the perimeter, and 2) tightly packed cells in the interior. Therefore the large patterns

separated the cells into two distinct regions with different patterns of marker expression.

To further verify the importance of low cytoskeletal tension in maintaining MSC phenotype, we used inhibitors of actomyosin contractility on our patterned cultures. Cells were treated with the Rho-associated protein kinase inhibitor (ROCK) Y-27632 and the non-muscle myosin inhibitor blebbistatin. Inhibiting cytoskeletal tension after cell adhesion using pharmacological inhibitors promotes higher expression of MSC markers, particularly when targeting ROCK. This suggests that signaling through Rho-kinase may play a role in regulating the multipotent phenotype, which is consistent with the role of ROCK during MSC differentiation (37, 38).

2.5 Conclusion

In this chapter 2, we explored the combined influence of matrix elasticity and cell/tissue geometry on regulating the MSC phenotype. Conditions that foster a low state of cytoskeletal tension—either through control of substrate stiffness, restricting spreading via high cell density, or through micropatterning single cells or constraining populations of cells in defined multicellular islands—will maintain the expression of MSC multipotency markers compared to cells grown on tissue culture plastic ware. From finite element models and the results of our immunofluorescence experiments, we see that interior regions of large populations of cells foster a low degree of tension which promotes maintenance of the MSC phenotype. This work shows how multiple biophysical parameters on cell culture materials can be tuned alone and in parallel to maintain the MSC phenotype, to guide our understanding of

the MSC microenvironment, and assist the selection of appropriate cell culture materials for regenerative therapies.

2.6 Figures

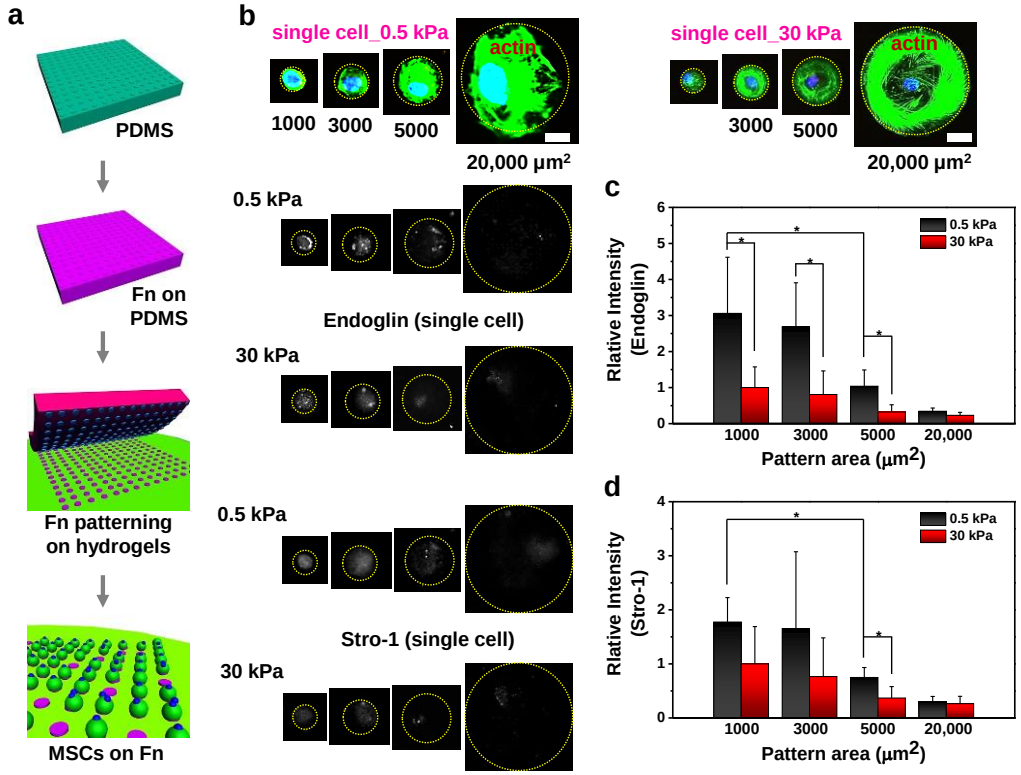

Figure 2.1 Combinations of stiffness and cell size differentially modulate MSC marker expression. *(a) Schematic showing the process used to pattern cells on polyacrylamide (PA) (b) Representative immunofluorescence microscope images of MSCs stained for Endoglin and Stro-1 cultured on soft (0.5 kPa) and stiff (30 kPa) PA hydrogels for 10 days (1000 ~ 20,000 μm2). Scale bar: 40 μm. Quantitation of (c) Endoglin and (d) Stro-1 markers for patterned cells cultured on soft and stiff substrates for 10 days. (N = 4). (*P<0.05, one-way ANOVA)*

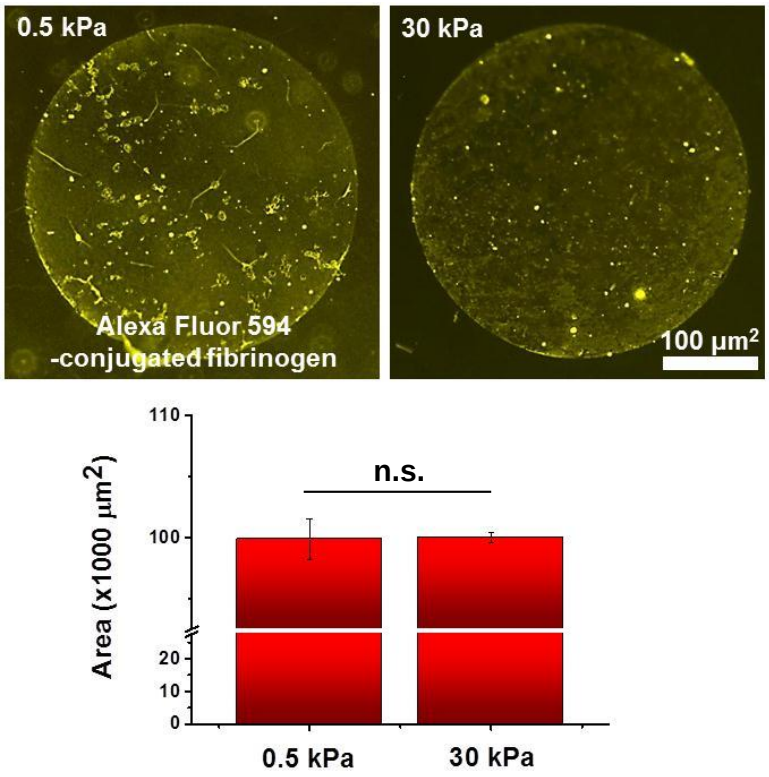

Figure 2.2 *Representative fluorescence images of patterned adhesion ligands on PA gels (0.5 and 30 kPa) with fluorescent fibrinogen (100,000 μm²).*

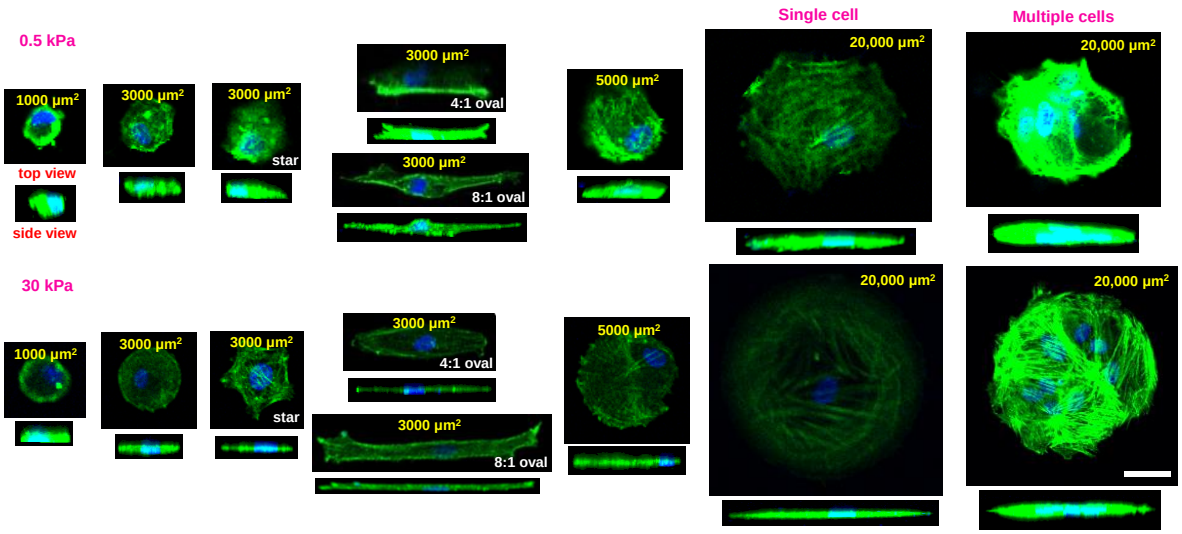

Figure 2.3 Top and side view of cells in soft and stiff substrates. *Representative laser scanning confocal microscope images of MSCs on soft (0.5 kPa) and stiff (30 kPa) substrates: MSC nuclei (blue), actin (cyan-green) (Scale bar: 40 μm).*

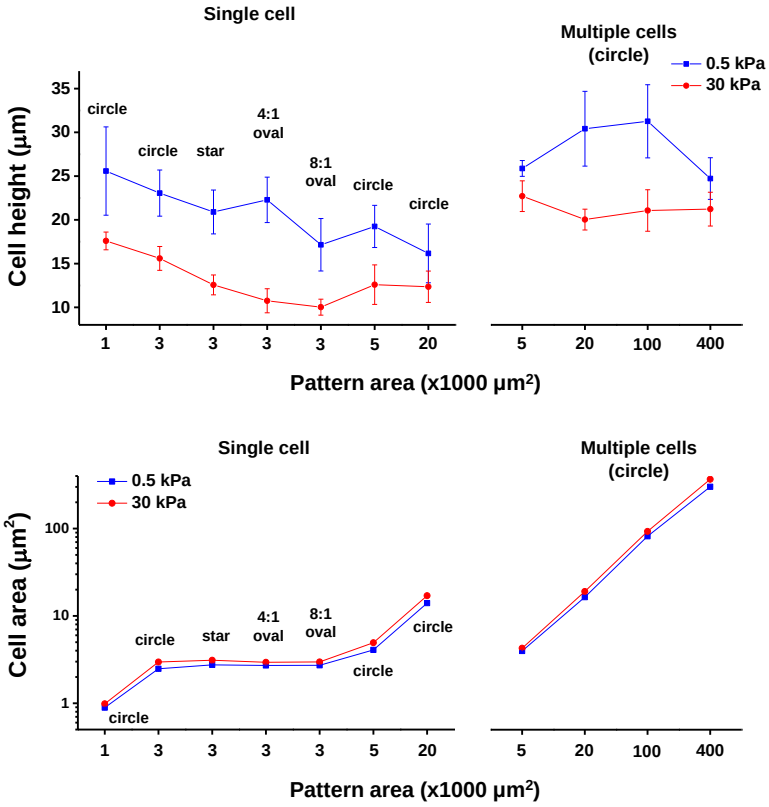

Figure 2.4 The height and area of cells in soft and stiff substrates. *MSC height and spread area on fibronectin-coated PA gels with circular patterns (1000 to 400,000 μm2) at single cell and multicellular levels.*

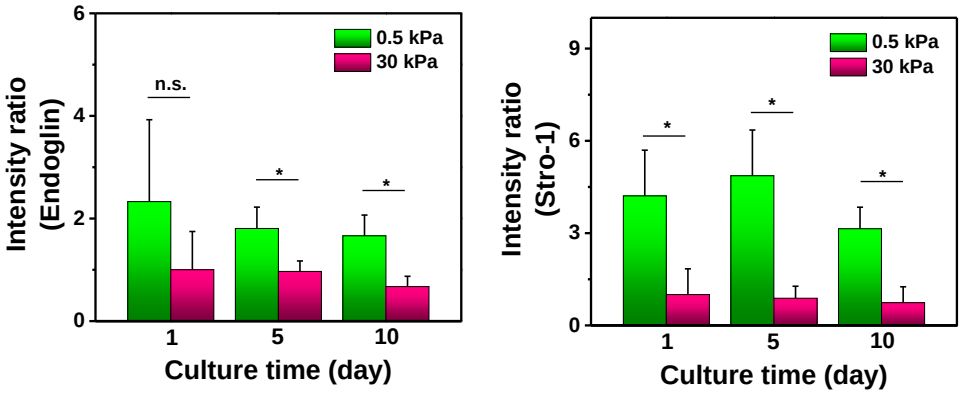

Figure 2.5 MSC multipotency marker expressions according to cultural time. *Expression of Endoglin and Stro-1 markers for cells cultured on soft and stiff substrates for 10 days. (N = 3). (*P<0.05, one-way ANOVA).*

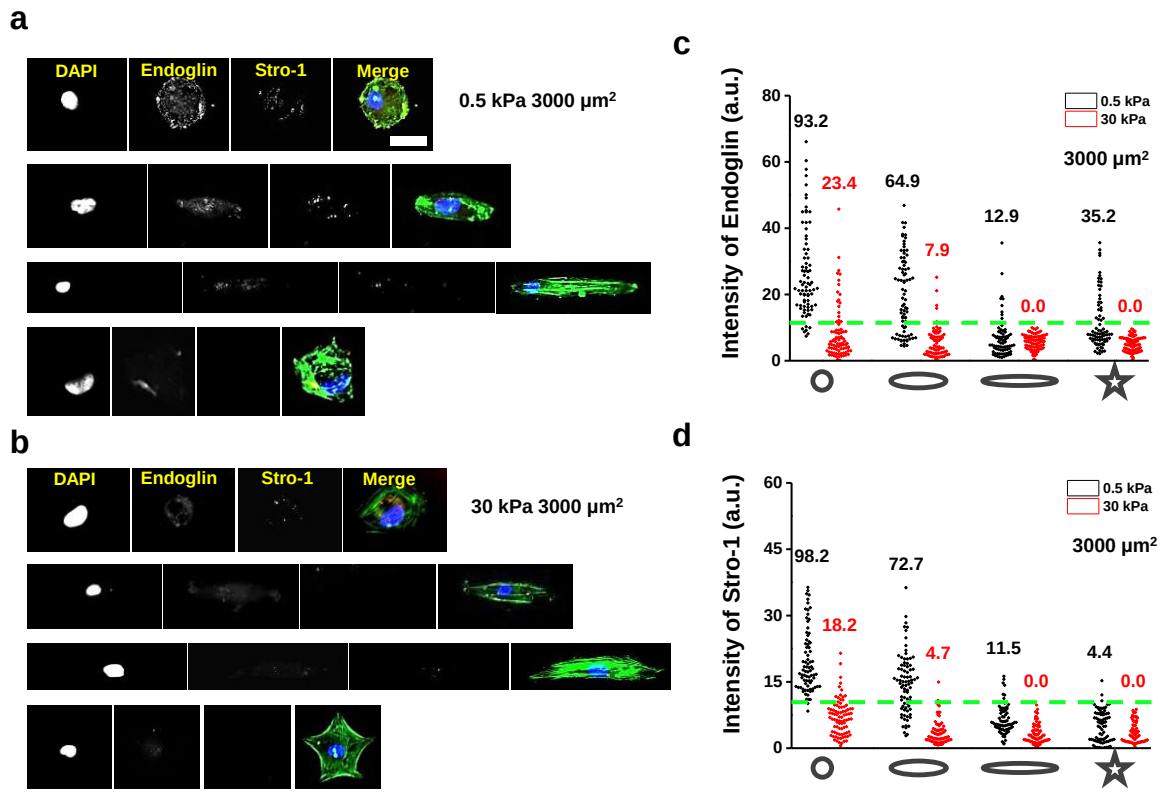

Figure 2.6 Combining geometric cues and matrix stiffness to study the maintenance of MSC multipotency. *(a) Representative immunofluorescence microscope images of MSCs stained for Endoglin and Stro-1 cultured in various geometries (circle, ovals (4:1 and 8:1), and star) on (a) soft (0.5 kPa) and (b) stiff (30 kPa) substrates (Scale bar: 40 μm). Quantitation (%) of (c) Endoglin and (d) Stro-1 markers for patterned cells cultured on soft and stiff substrates for 10 days. The threshold (dashed line) was selected by comparing the highest and lowest marker intensities.*

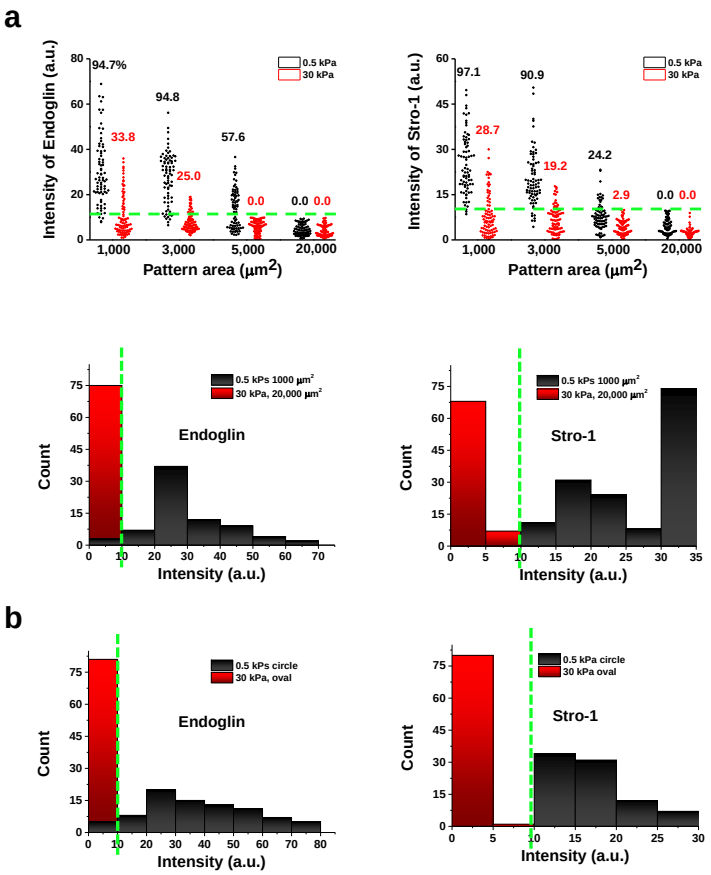

Figure 2.7 Single cell data with the % of total cells in each condition. *Expression of Endoglin and Stro-1 markers for patterned cells cultured on soft and stiff substrates for 10 days. The threshold (green dashed line) was selected by comparing the highest and lowest marker intensities.*

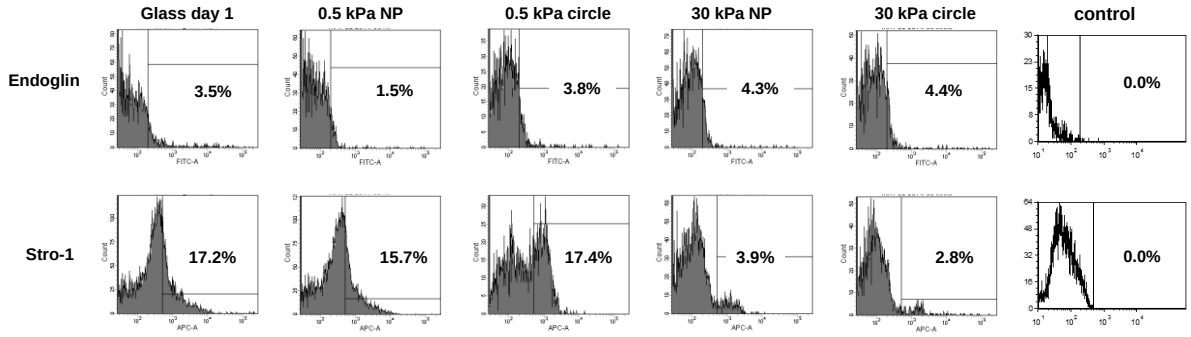

Figure 2.8 *Flow cytometry for endoglin and Stro-1 expression in MSCs cultured on TCP and on patterned and non-patterned hydrogels of 0.5 kPa and 30 kPa.*

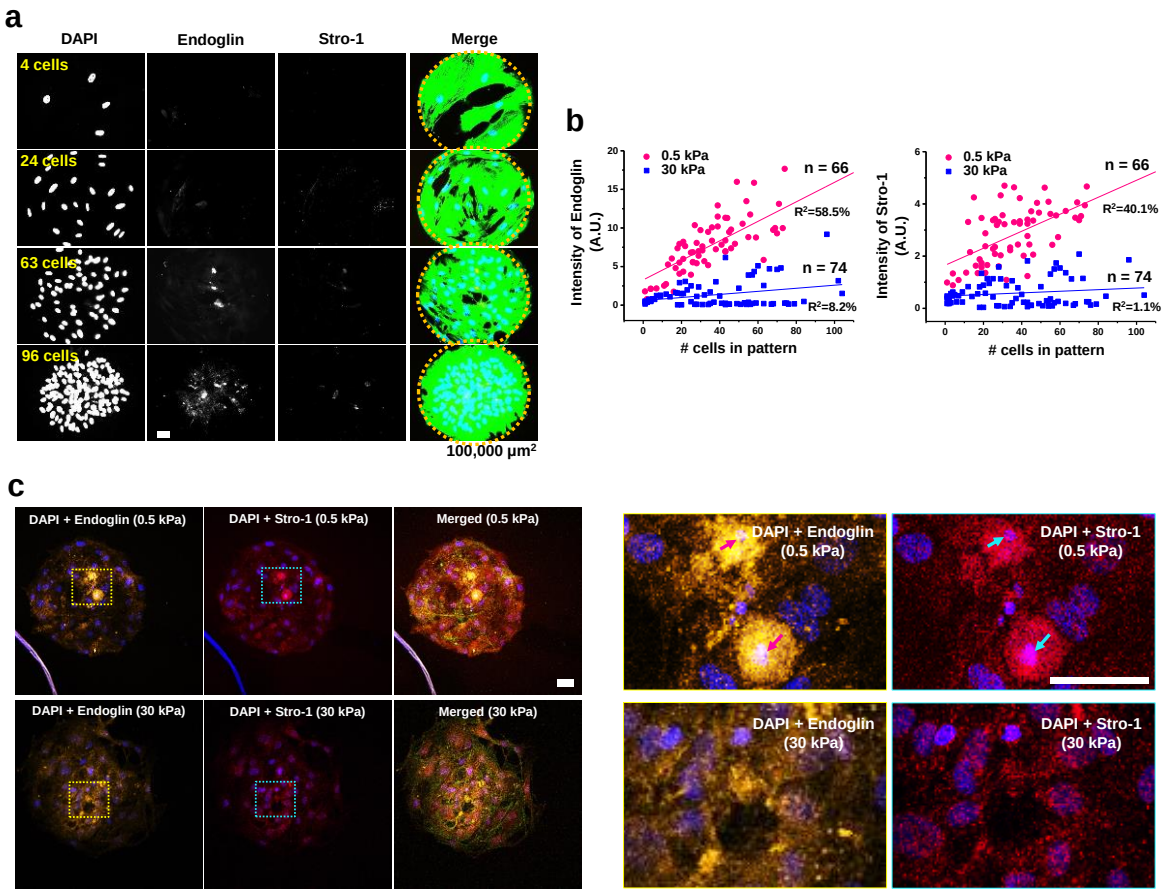

Figure 2.9 Cell density in multicellular patterns leads to different degrees of MSC marker expression. *(a) Representative immunofluorescence microscope images of MSCs with different density in the same size patterns (100,000 μm2). Plot of all measured immunofluorescence intensity data (Endoglin and Stro-1) versus a number of (b) MSCs (stem cells from bone marrow). (c) Representative laser scanning confocal microscope images of MSCs on soft (0.5 kPa) or stiff (30 kPa) substrates: MSC nuclei (blue), actin (cyan-green), Endoglin (yellow-orange), Stro-1 (red). Scale bar: 40 μm.*

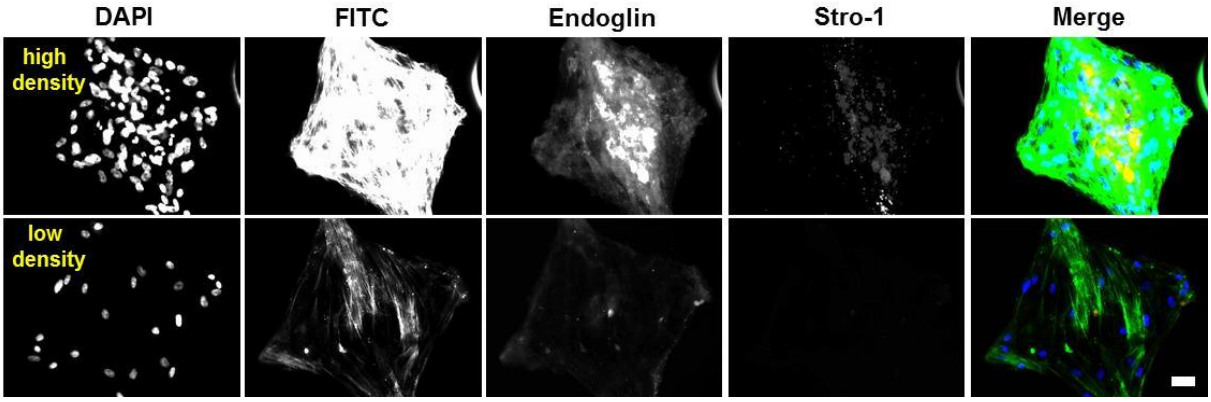

Figure 2.10 Cell density effect on the maintenance of MSC multipotency marker expression. *Representative immunofluorescence microscope images of MSCs (30 kPa) stained for Endoglin and Stro-1 cultured for 10 days (Scale bar: 40 μm).*

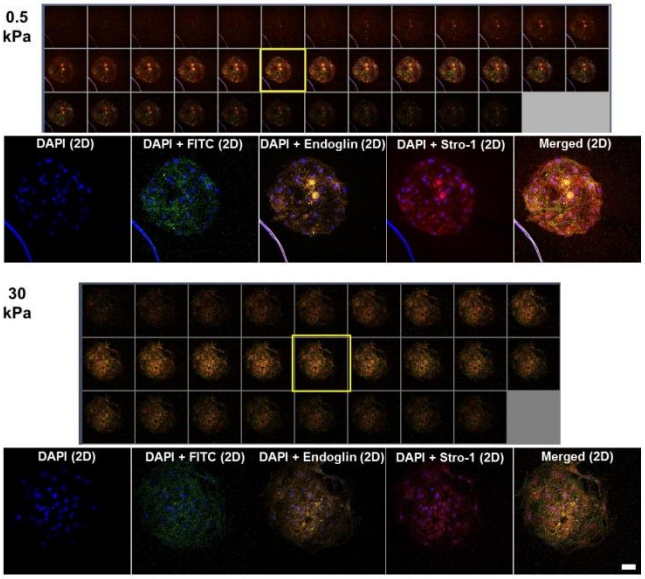

Figure 2.11 Multipotency marker expression depending on matrix stiffness and different regions. *Representative laser scanning confocal microscope images of MSCs on soft (0.5 kPa) and stiff (30 kPa) substrates stained with Endoglin and Stro-1: MSC nuclei (blue), actin (cyan-green), Endoglin (yellow-orange), Stro-1 (red). Scale bar: 40 μm.*

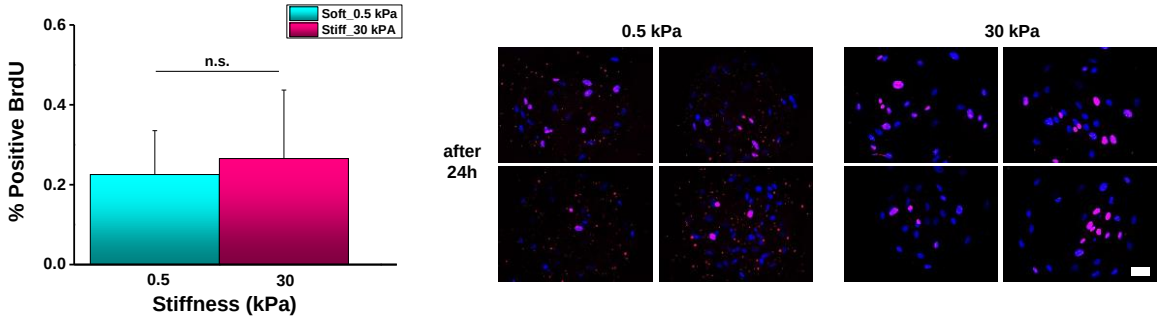

Figure 2.12 BrdU marker expressions of MSCs on soft and stiff substrates with circular patterns (100,000 μm^2). *After 24 h, MSCs seeded on soft substrates showed little BrdU incorporation compared to those on stiff substrates. Representative immunofluorescence microscope images of MSCs soft and stiff substrates stained with BrdU marker: MSC nuclei (blue), BrdU (red). Scale bar: 40 μm.*

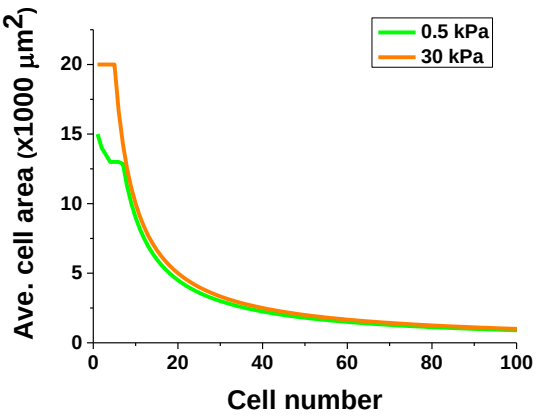

Figure 2.13 Average area filled by a cell depending on cell numbers on soft and stiff patterned substrates (100,000 μm^2). *Cells on soft substrates showed less average cell area compared to those on stiff substrates.*

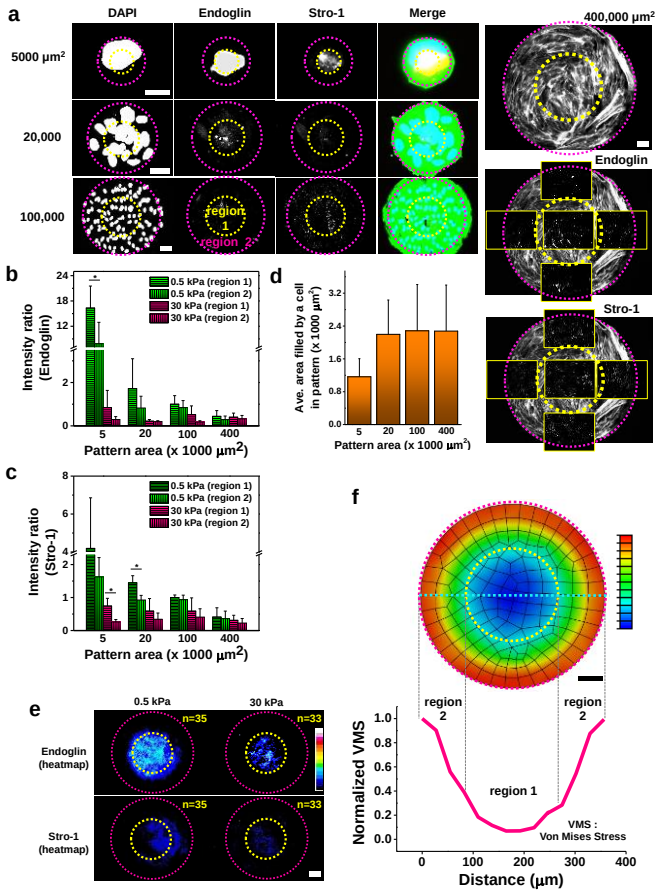

Figure 2.14 Geometry guides the spatial distribution of multipotency in multicellular patterns. *(a) Representative immunofluorescence microscope images of multiple cells cultured in various sized circle patterns (5000, 20,000, 100,000, and 400,000 µm2); dashed lines represent region 1 (interior) and region 2 (exterior). Quantitation of (b) Endoglin and (c) Stro-1 markers for patterned multiple cells divided by two different regions (cultured on soft (0.5 kPa) and stiff (30 kPa) substrates). (d) Average area filled by a cell cultured for 10 days in each sized pattern. (e) Representative immunofluorescence heatmaps of >30 patterns of multiple cells stained for Endoglin and Stro-1 cultured in 100,000 µm2 size patterns for 10 days. (f) Representative modelled mechanical stress distribution of multicellular sheet of cells contracting on a 100,000 µm2 sized pattern and normalized von mises stress (VMS) across the patterns. Scale bar: 40 µm. (N = 4). (*P<0.05, one-way ANOVA).*

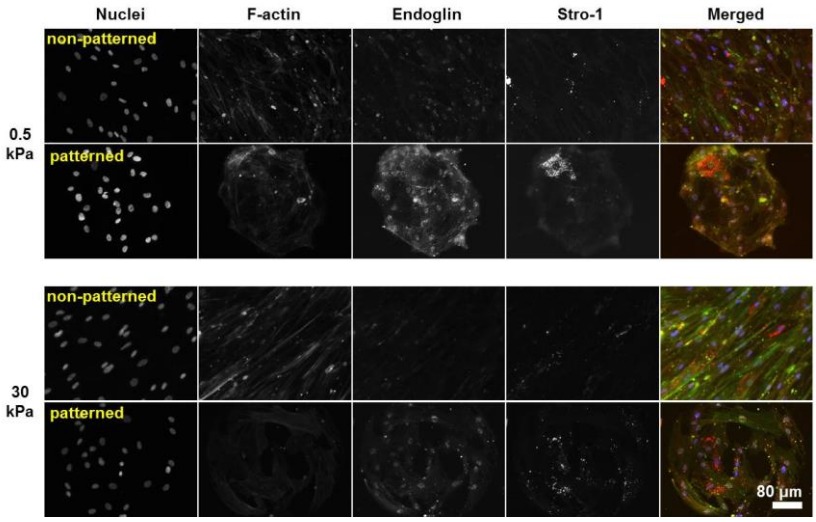

Figure 2.15 Cell patterning effect on the maintenance of MSC multipotency marker expression. *Representative immunofluorescence microscope images of patterned and non-patterned MSCs (0.5 and 30 kPa) stained for Endoglin and Stro-1 cultured for 10 days.*

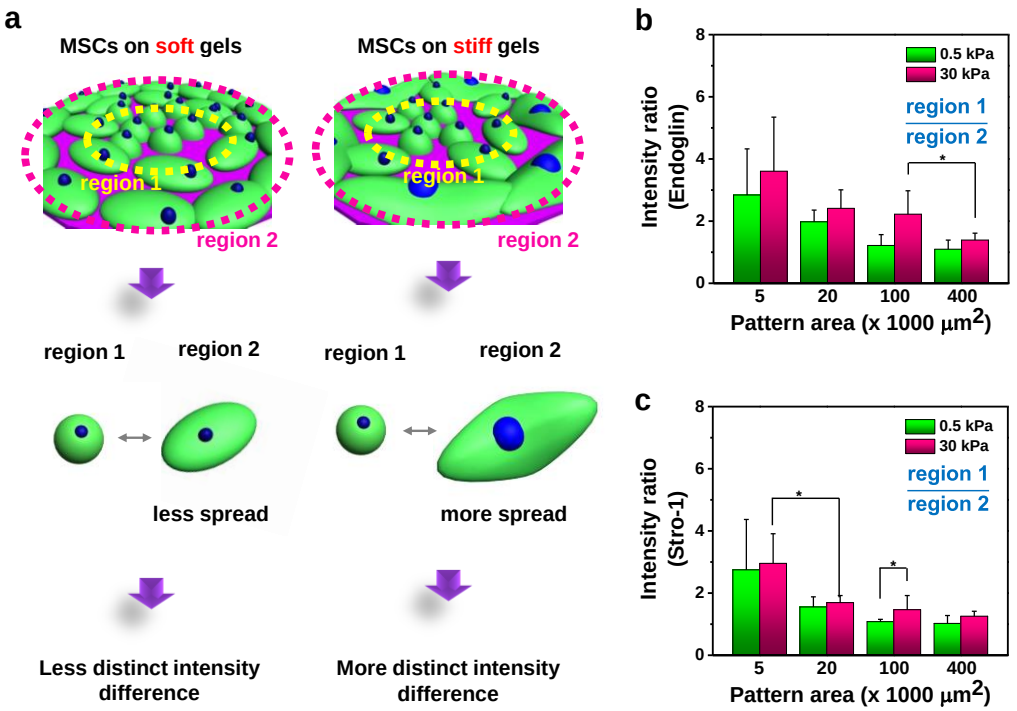

Figure 2.16 Multipotency marker expression depending on different regions, outer and inner regions. *(a) Schematic of MSC density on fibronectin patterned soft and stiff PA hydrogels. Expression ratio of Endoglin and Stro-1 markers for cells cultured on (c) soft and (d) stiff substrates; intensities of region 1 were divided by those of region 2. Since more distinct intensity difference existed for cells on stiff substrates, intensity ratio of cells on stiff substrates is higher than those on soft substrates. (N=3) (*P<0.05, one-way ANOVA).*

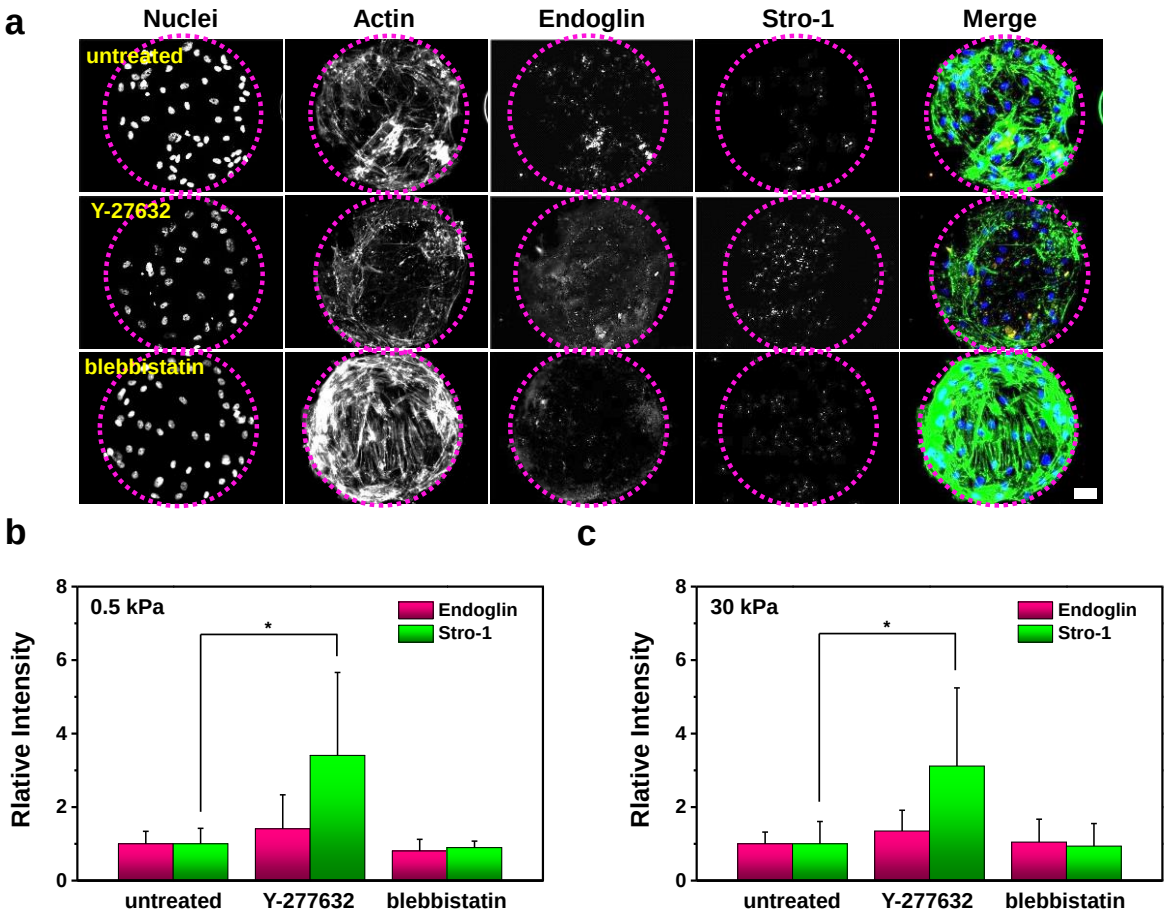

Figure 2.17 MSCs treated with actomyosin contractility inhibitors show elevated levels of multipotency markers. *(a) Representative immunofluorescence microscope images of MSCs (0.5 kPa) stained for Endoglin and Stro-1 cultured with or without drug treatment (Scale bar: 40 μm). Expression of Endoglin and Stro-1 markers for cells cultured on (c) soft and (d) stiff substrates with and without drug treatment. (N = 3). (*P<0.05, one-way ANOVA).*

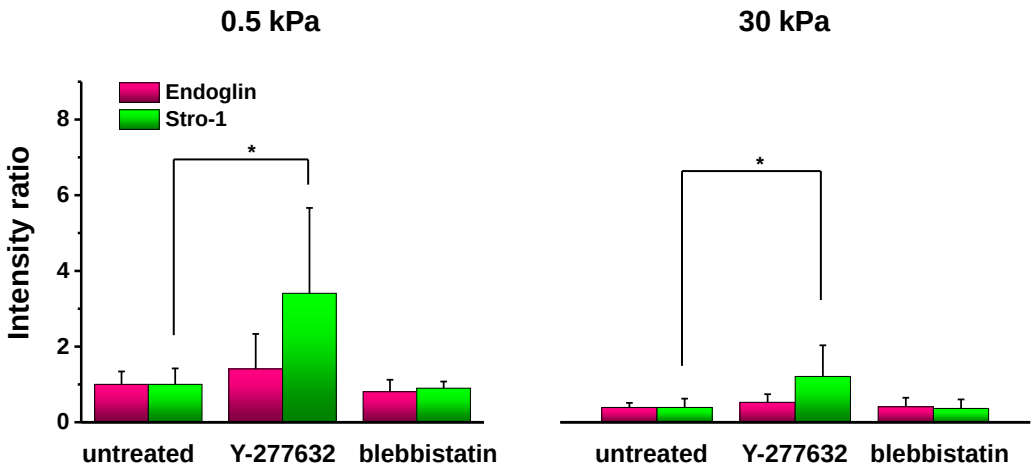

Figure 2.18 *Expression of Endoglin and Stro-1 markers for cells cultured on soft and stiff substrates with and without drug treatment in the same scale. (N = 3). (*P<0.05, one-way ANOVA).*

CHAPTER 3

DIRECTING STEM CELL FATE ON HYDROGEL SUBSTRATES BY CONTROLLING CELL GEOMETRY, MATRIX MECHANICS AND ADHESION LIGAND COMPOSITION[3]

3.1 Introduction

There is a dynamic relationship between physical and biochemical signals presented in the stem cell microenvironment to guide cell fate determination. Model systems that modulate cell geometry, substrate stiffness or matrix composition have proved useful in exploring how these signals influence stem cell fate. An important lesson that has emerged from the studies regarding physical and biochemical regulations for MSC fate decision is that there is clearly interplay between matrix mechanics, adhesion ligand presentation and cell geometry during differentiation (8, 24, 25). The majority of research efforts have focused on varying one physical cue while exploring the influence on biological activity. However, in vivo cell fate is likely influenced by a combination of geometry, mechanics and ECM composition (17, 93). Thus we reasoned that combining these cues would prove useful in designing materials that more closely emulate the in vivo microenvironment and "fine-tune" a desired differentiation outcome.

In this chapter 3, we use soft lithography to micropattern multiple matrix proteins—alone and in combinations—on hydrogel substrates with the mechanical properties

---

[3]This chapter is adapted from the following publication:
Junmin Lee, Amr A. Abdeen, Douglas Zhang, and Kristopher A. Kilian, Directing stem cell fate on hydrogel substrates by controlling cell
geometry, matrix mechanics and adhesion ligand composition, Biomaterials, 2013, 34, 8140-8148

of soft tissue to explore the physical and biochemical cues that guide MSCs towards adipogenesis and neurogenesis outcomes. Immunofluorescence staining and real-time PCR are employed to assess the expression of key markers during differentiation. We explore the translation of our findings to a pseudo-3D hydrogel format that more closely represents the in vivo environment.

3.2 Materials and Methods

General materials and methods are given in Appendix A.

Materials:

Mouse anti-ß3 tubulin was purchased from Sigma (T8660), rabbit anti-PPARγ was purchased from Cell Signaling (C26H12), and chicken anti-MAP2 was purchased from abcam (ab5392) Technologies.

Pseudo-3D microwells:

Pseudo-3D microwells were fabricated by templating the polyacrylamide gels on a SU-8 photolithography master displaying the inverse features used in fabricating the PDMS stamps. After subjecting the microwells to hydrazine treatment and oxidized protein, adhesive tape was applied to the gel and removed quickly to shear off the top layer of protein-conjugated gel.

RNA isolation and RT-PCR:

Adherent cells were lysed directly in TRIZOL reagent (Invitrogen) and total RNA was isolated by chloroform extraction and ethanol precipitation. Total RNA in DEPC

water was amplified using TargetAmp™ 1-Round aRNA Amplification Kit 103 (Epicentre) according to vendor protocols. Total RNA was reverse transcribed using Superscript III® First Strand Synthesis System for RT-PCR (Invitrogen). RT-PCR was performed linearly by cycle number for each primer set using SYBR® Green Real-Time PCR Master Mix (Invitrogen) on an Eppendorf Realplex 4S Real-time PCR system. Primer sequences were as follows: C/EBPα—GCAAACTCACCGCTCCAATG and TTAGGTTCCAAGCCCCAAGT, PPARG2—AGAGCCTTCCAACTCCCTCA and CAAGGCATTTCTGAAACCGA, LPL—CATCCCATTCACTCTGCCT and AGTTCTCCAATATCTACCTCTGTG, β3Tubulin—CCATTTCTCGACTTTCCAAACTG and CTGCGAACTTGCCTGTGGA, MAP2—GGAGACAGAGATGAGAATTCCT and GAATTGGCTCTGACCTGGT, GAPDH—CTCTGCTCCTCCTGTTCGAC and GTTTCTCTCCGCCCGTCTTC. All reactions were performed linearly by cycle number for each set of primers.

3.3 Results

Hydrogel fabrication and single cell patterning

Previous reports of patterning on hydrogels used substrates of relatively high modulus (>2.5 kPa) (17). In order to study the combinatorial effects of cell shape, substrate stiffness and matrix composition in directing neurogenesis and adipogenesis on soft hydrogels (<1 kPa), we developed a protocol based on soft lithography and chemically modified polyacrylamide (PAAm). Patterning ECM proteins on soft hydrogels via direct contact with an elastomeric stamp is challenging due to the substrate compliance and the presence of surface water, and

few studies of microcontact printing on hydrogels have been reported (5). We systematically varied curing, drying and contact times to identify an operating regime in which precise patterning of complex features on PAAm was possible (Fig. 3.1a). Polydimethylsiloxane (PDMS) stamps were prepared using photolithography to present geometric features in relief or flat surfaces without structure (unpatterned). Polyacrylamide (PAAm) hydrogels were prepared according to established literature methods (84), and we confirmed their stiffness (~0.6 kPa) via atomic force microscopy (AFM) (Fig. 3.2). The PAAm gels were treated with hydrazine hydrate and the stamps were inked with an oxidized glycoprotein solution to promote covalent immobilization after microcontact printing (13). After seeding cells on these surfaces, we confirmed that a substantial number of cells adhered to patterned regions (Fig. 3.1 and Fig. 3.3). Laser scanning confocal microscopy of patterned and unpatterned cells confirms that the average cell height is around 70 μm and 15 μm respectively (Fig. 3.4a). Morphological analysis reveals the average cell area is comparable to the desired pattern size (1000 μm^2) while the unpatterned cells show a variable spread area (1500 μm^2 - 9500 μm^2, Fig. 3.4b). Patterned cells remained viable and restricted to the islands for 13 days in culture, after which they escaped geometric confinement and proliferated (Fig. 3.5a).

MSC differentiation on micropatterned soft hydrogels

Our initial analysis of MSCs on unpatterned soft gels showed a mixture of cells expressing markers associated with adipogenesis (p-par γ) and neurogenesis (beta3 tubulin) (Fig. 3.5c and Fig. 3.6). Cells that adopt a rounded, compact morphology express higher levels of adipogenesis markers while cells that spread

and extend dendrite-like processes show elevated neurogenesis markers. We hypothesized that small isotropic geometries which restrict cell spreading may promote higher expression of adipogenesis markers compared to cells that are allowed to spread (Fig. 3.7a). To evaluate the temporal regulation of adipogenic and neurogenic marker expression, we cultured MSCs on fibronectin coated islands and on unpatterned fibronectin coated substrates for several weeks (Fig. 3.5b and c); protein expression was analyzed with histograms of intensities for patterned and unpatterned cells to assign thresholds for designating lineage (Fig. 3.8). MSCs on small islands always showed higher level of adipogenic marker expression relative to unpatterned cells regardless of time in cell culture while beta3 tubulin expression decreased dramatically after 10 days (Fig. 3.5b). Since MSCs cultured for 10 days showed clear distinction between the expressions of the two different markers, all further analysis was performed at 10 days in culture. The 1000 μm^2 patterned cells display high expression of p-par γ while the spread cells tend to express elevated beta3 tubulin (Fig. 3.5b and c). These results suggest that geometric confinement may prevent process extension—a hallmark characteristic of neuronal cells—and thus limit this differentiation potential. Restricting spreading may also enhance signaling associated with adipogenesis as has been observed previously (37).

MSC differentiation on micropatterned hydrogels with different matrix proteins

Since the early reports of MSCs undergoing neurogenesis on soft matrices used collagen as the adhesion protein (28), we next investigated whether different matrix proteins would influence the degree of adipogenesis and neurogenesis. Adipose tissue is comprised of a complex matrix containing collagen, laminin and

fibronectin while brain tissue is predominantly composed of hyaluronan enmeshed with collagen and some laminin (94). Therefore we investigated the degree of lineage specification for both programs when cells were adherent to combinations of these proteins. Fig. 3b shows representative fluorescent images of MSCs cultured on small islands conjugated with fibronectin, laminin, and collagen. Across these different matrices, MSCs cultured on fibronectin display the highest expression of p-par γ while cells on collagen show the highest beta3 tubulin expression (Fig. 3.7c). MSCs cultured on laminin display intermediate expression of both markers. Quantitative analysis reveals that cells undergoing differentiation on the small fibronectin islands display nearly 80% adipogenic fate compared to 60% on laminin and 40% on collagen. In contrast, < 20% of cells adherent to fibronectin islands are expressing beta3 tubulin compared to >40% on laminin and >60% on collagen. For all of the adhesion ligands, approximately 80% of the spread cells choose a neurogenic fate. Figure 3.7d shows all data points we measured from five separate experiments with over 700 cells on small circular islands with the three different matrix proteins. We obtained intensity ratio via the comparisons with thresholds used to define lineage specification (Fig. 3.9) and describe populations of cells that display the adipocytes or neuronal stains or neither (Fig. 3.7d). Fitting lines of patterned cells on each matrix protein were produced using all data points; the trendline from fibronectin experiments corresponds to adipogenic specification while the trendline from collagen corresponds to the neurogenic specification. These results are comparable to that observed in percentages of round cells differentiating to adipocytes or neurons, which provides evidence that different matrix proteins have a strong influence on directing the differentiation of MSCs on these soft

hydrogel matrices. Taken together, these results show that restricting cell spreading promotes adipogenesis regardless of ligand composition; however, matrix composition in conjunction with cell geometry can further tailor the differentiation outcome.

To further verify the observed trends in differentiation, we performed immunofluorescence staining of the neurogenesis marker microtubule-associated protein 2 (MAP2) (Fig. 3.10), and histochemical analysis of accumulated lipid vacuoles using Oil Red O staining (Fig. 3.11). The lowest expression of MAP2 was observed with cells on small fibronectin islands while the highest expression was shown for spread cells on collagen. For Oil Red O staining, over 60% of cells in patterns expressed lipid droplets regardless of ligands compared to less than 40% in un-patterned cells. We also performed gene expression analysis using real-time polymerase chain reaction (PCR) of a panel of markers associated with adipogenesis (CEBPa and LPL) and neurogenesis (beta3 tubulin and MAP2).

After 10 days in culture we see a higher degree of adipogenic transcript expression for micropatterned cells and higher expression of neurogenic transcripts in spread cells, consistent with the protein analysis using immunofluorescence and histology (Fig. 3.12). Patterned cells on fibronectin matrix showed ~10-fold enhanced expression of the adipogenic master regulator CEBPa compared to spread cells on fibronectin or laminin and ~20-fold higher expression than spread cells on collagen. The same trend was also observed in expression of lipoprotein lipase (LPL); patterned cells cultured on fibronectin, laminin and collagen displayed ~8-fold, ~6-fold, and ~40-fold enhancement in LPL expression respectively compared to

unpatterned cells. In contrast, spread cells on collagen and laminin coated gels showed a ~10-fold increase in beta3 tubulin expression compared to ~2-fold increase on fibronectin. Similar trends were observed for MAP2 expression: ~3-fold for collagen and laminin and ~2-fold for fibronectin. These results reveal marked differences in gene expression associated with both cell geometry and matrix composition that corroborate the immunofluorescence results.

The combined influence of geometric cues and matrix proteins

We have shown that cell spreading and the composition of adhesion ligand (fibronectin, laminin, and collagen) will influence MSC differentiation on soft hydrogels. To explore the role that cell spreading plays in guiding neurogenesis, we used microcontact printing of geometries that modulate cell area, aspect ratio and dendritic process extension. Figure 3.13a and b show representative immunofluorescence images of cells on circular features with different areas and anisotropic features after 10 days in culture. We observed that not only could smaller circular feature promote higher expression of adipogenesis markers (1000 μm^2 (~75%) > 3000 μm^2 (~63%) > 5000 μm^2 (~51%)), but also cells in anisotropic features such as 4-branched star and ovals (4:1 and 8:1 ratio) favored a neurogenic outcome (Fig. 3.13c). These anisotropic features allowed MSCs on soft hydrogels to spread and extend processes, resulting in enhanced expression of neurogenic markers (about 85% for 8:1 oval) compared to round cells of the same area (3000 μm^2, less than 40%). These trends were also shown for different adhesion ligands (laminin and collagen, Fig. 3.14), and we revealed a similar relation that cells confined to the same geometries but on different ligands showed

a higher level of adipogenic (or neurogenic) expression on fibronectin (or collagen). An important outcome of these results is the demonstration that cell spreading promotes neuronal lineage specification irrespective of protein on the soft hydrogels. This suggests that spreading is necessary for the extension of dendritic processes and a requirement for initiation of neurogenic gene expression.

Since the composition of adhesion ligands can differentially regulate adipogenesis and neurogenesis, we compared differentiation of MSCs on various combinations of protein ligands at the same total concentration (Fig. 3.13d and 3.15). Patterned cells cultured on fibronectin or laminin matrices and a combination of both proteins tended to undergo adipogenesis. In sharp contrast, MSCs cultured on any combination of proteins containing collagen preferred to adopt a neurogenic outcome even on small circular islands (Fig. 3.13d). Unpatterned MSCs show a similar trend corresponding to matrix protein composition albeit with the majority of MSCs undergoing neurogenesis on account of spreading (Fig. 3.15).

MSC differentiation in pseudo-3D microenvironments

To explore whether our findings in the 2D screens could translate to a more physiologically relevant 3D system, we developed a templating approach to fabricate pseudo-3D microwells that vary geometry, stiffness and protein composition (Fig. 3.16a). Polyacrylamide gels were cast on the silicon master containing SU-8 photoresist using the same formulations chemistry described above. After polymerization the PAAm gel was subjected to hydrazine treatment and oxidized glycoprotein. To restrict the protein to the microwells, we removed surface protein with the use of adhesive tape to shear off the top layer of protein-

conjugated gel. After seeding, cells only adhered within the microwell demonstrating the validity of this approach (Fig. 3.16b). After 10 days in culture MSCs encapsulated in the small circular fibronectin-coated microwells show equal expression of adipogenic and neurogenic markers. In contrast, cells encapsulated in high aspect ratio microwells show significantly higher expression of neurogenic markers. The decreased expression of adipogenic markers in the small pseudo-3D microwells is likely on account of the increased area the cell comes in contact with. Using the 1000 μm^2 template, the microwell depth will be ~15-20 μm, and the final adhesive area the encapsulated cell is exposed to will be ~2000 μm^2. This result is consistent with the experiments that varied area (Fig. 3.13). The fraction of cells undergoing differentiation in either case is comparable to the 2D assays using the same geometric pattern, demonstrating the validity of this approach.

3.4 Discussion

The fate of mesenchymal stem cells cultured in soft hydrogel materials is controversial with literature demonstrating quiescence (78), neurogenesis (9, 28), and adipogenesis (when cultured in the presence of differentiation media) (34, 93, 95). The different outcomes in these studies are likely on account of differences in polymerization strategies, bioconjugation schemes and culture conditions. One commonality across these works is a variability in cell shape, where some cells extend dendrite-like processes while others fail to spread. To explore this further, we immunostained MSCs adherent to soft fibronectin-coated gels for markers associated with adipogenesis and neurogenesis and found a correlation between cell morphology and lineage marker expression. Round cells tend to express higher

levels of adipogenesis markers while spread cells express higher levels of neurogenesis markers. This finding is significant because previous studies have only demonstrated adipogenesis on hydrogel materials in the presence of media supplements (33, 93, 95). To discern whether cell shape may influence these different outcomes, we developed a microengineering platform to control single cell geometry on our hydrogel substrates. MSCs captured to small circular microislands express high levels of adipogenesis markers. MSCs that are induced to spread in anisotropic geometries—either directly on unpatterned gels or when patterned in shapes that vary cell area, aspect ratio and branching—display elevated expression of neurogenic markers. It is tempting to speculate that these geometric features relate to the in vivo morphological characteristics of these lineages –adipocytes show a characteristic isotropic morphology while neurons exhibit a branched dendritic phenotype. Nevertheless, it is clear that cell spreading is important for the extension of dendrite-like processes and initiation of neurogenic gene expression in adherent MSCs. In contrast, cells that are restricted from spreading prefer to initiate the adipogenesis program.

Another notable difference across previous studies is the composition of matrix protein grafted to the hydrogel. To explore the role of adhesion protein in guiding adipogenesis and neurogenesis, we covalently immobilized fibronectin, laminin and collagen to the PAAm hydrogels. MSCs cultured on fibronectin tend to express elevated adipogenic markers while MSCs on collagen tend to express elevated neurogenic markers. Gene expression analysis of key transcripts involved in regulating these differentiation potentials confirm the immunofluorescence results.

This finding supports the early work that demonstrates primary neurogenesis of MSCs cultured on collagen coated PAAm (28). In general, the extracellular matrix of neural tissue is enriched in hyaluronic acid (HA), collagen, and laminin. Schmidt et al showed that schwann cells prefer to differentiate into a neuronal phenotype when cultured in a 3D polymer matrix containing collagen (94). In contrast, fibronectin is a significant component of adipose extracellular matrix (96) which suggests a specific role for this matrix protein in regulating adipogenesis in vivo.

Towards the identification of an optimal combination of cues for directing these different outcomes, we arrayed MSCs across geometries that vary area, aspect ratio and dendritic branch cues, with combinations of fibronectin, laminin and collagen grafted to the surface. Cells in fibronectin or laminin patterns preferred an adipogenesis fate while cells cultured on collagen matrices tended to show a high neurogenesis outcome regardless of geometry. This finding suggests that neurogenesis is the preferred lineage on collagen matrices, irrespective of cell shape, while restricting cell spreading promotes adipogenesis, particularly on matrices containing fibronectin. Thus, we hypothesize that the shape of stem and progenitor cells fostered by their microenvironment—and the composition of their surrounding adhesion proteins—are intimately connected to functional biological activity to direct or maintain cellular identity in vivo.

Previous studies have demonstrated that adhesion and associated signaling can be very different in 2D versus 3D environments (27). To test the validity of our results in a more physiologically relevant 3D environment, we seeded MSCs within protein conjugated microwells that were engineered to present the optimal geometry,

stiffness and protein ligand discovered in our 2D assays. Cells that are encapsulated in large anisotropic microwells show enhanced neurogenesis compared to cells that are cultured within small isotropic microwells. This result is in-line with our 2D experiments and demonstrates the feasibility of translating these design criteria into pseudo-3D arrangements.

3.5 Conclusion

This chapter 3 demonstrates that cell shape, matrix mechanics and the composition of adhesion protein all influence the lineage specification in MSCs, individually and when presented together. Moreover, combining these cues can be used to maximize a desired differentiation outcome without the use of small molecule media supplements. Using this platform to combine physical and biochemical cues for directing other differentiation outcomes, and across other stem and progenitor cell types, may prove similarly revealing. Advances in controlling multiple cues reproducibly at the biomaterials interface and within 3D architectures will enable next generation assays that more closely recapitulate the structure of the in vivo environment. This work will prove useful in the design of tailored hydrogel biomaterials that more efficiently direct distinct differentiation outcomes.

3.6 Figures

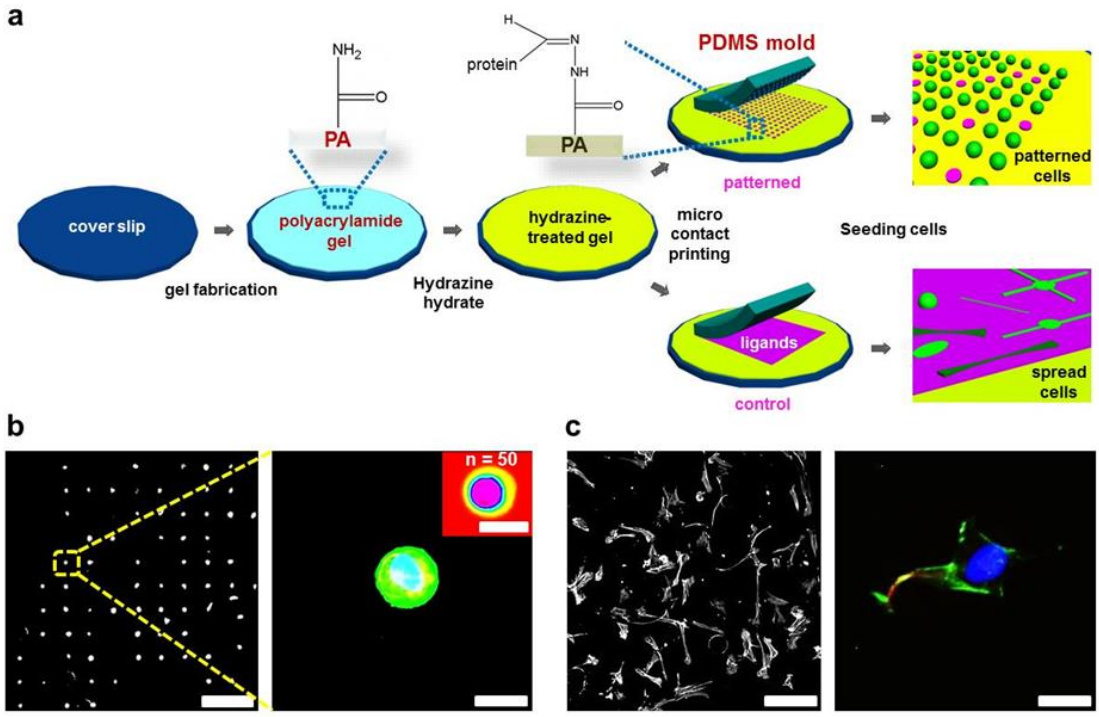

Figure 3.1 Hydrazine treated polyacrylamide enables protein immobilization and single cell patterning on soft hydrogels. *(a) Schematic of the process used to pattern cells on polyacrylamide hydrogels. (b)-(c) Representative immunofluorescence microscopy images of MSCs cultured for 10 days: Inset shows a heat map of 50 different cells on small circular islands. Staining for MSC nuclei (blue), actin (cyan-green), p-par γ (yellow-green), ß3 tubulin (red). Scale bars: 700 μm (left), 50 μm (right).*

a

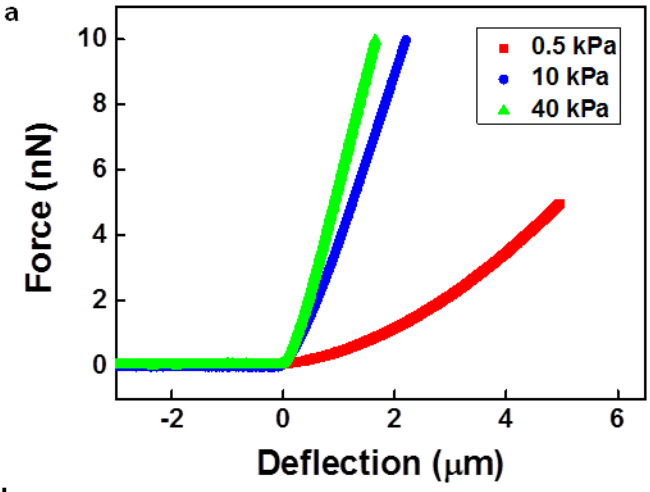

b

Desired Young's Modulus (kPa)	Acrylamide (wt%)	Bis-Acrylamide (wt%)	Measured Young's Modulus (kPa)
0.5	3	0.06	0.6
10	10	0.1	11.2
40	8	0.48	33.18

Figure 3.2 Polyacrylamide gel modulus of elasticity. *a, Force-deflection curves (one of 50 different measurements) obtained on the PA gel with desired Young's moduli of 0.5 (red), 10 (blue), 40 (green). b. A table of the relative concentrations of acrylamide, bis-acrylamide and their desired and measured modulus of elasticity (average of 50 different measurements). Stiffness of PA gels was measured using atomic force microscopy (AFM) as described in ref (22). We fabricated PA gels which had desired stiffness of 0.5, 10 and 40 in order to compare stiffness, and the measured values of Young's modulus were 0.6, 11.2 and 33.18, respectively.*

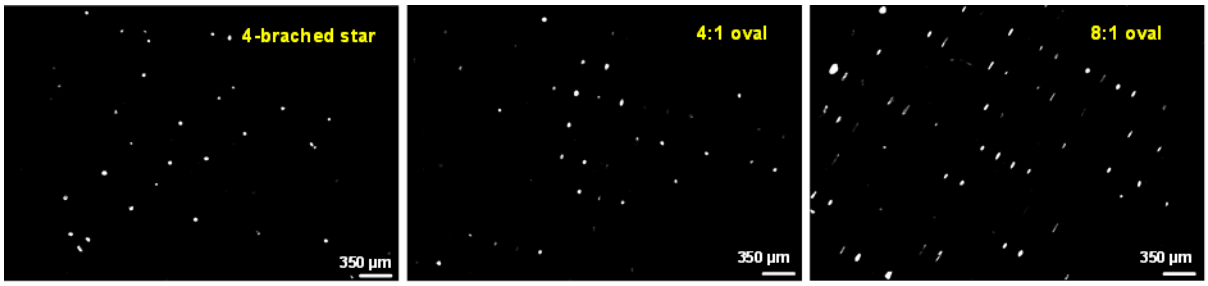

Figure 3.3 Large area matrix protein patterning on soft PA hydrogels. *Representative images of cells on PA gels with patterned adhesion ligands (4-branched star, 4:1 oval, and 8:1 oval shapes). The images obtained from an immunofluorescence microscopy (Zeiss Axiovert 200M inverted research-grade microscope (Carl Zeiss, Inc.)) with with a 5X microscope objective after fluorescence staining of cytoskeletal actin with Alexa Fluor 488-phalloidin.*

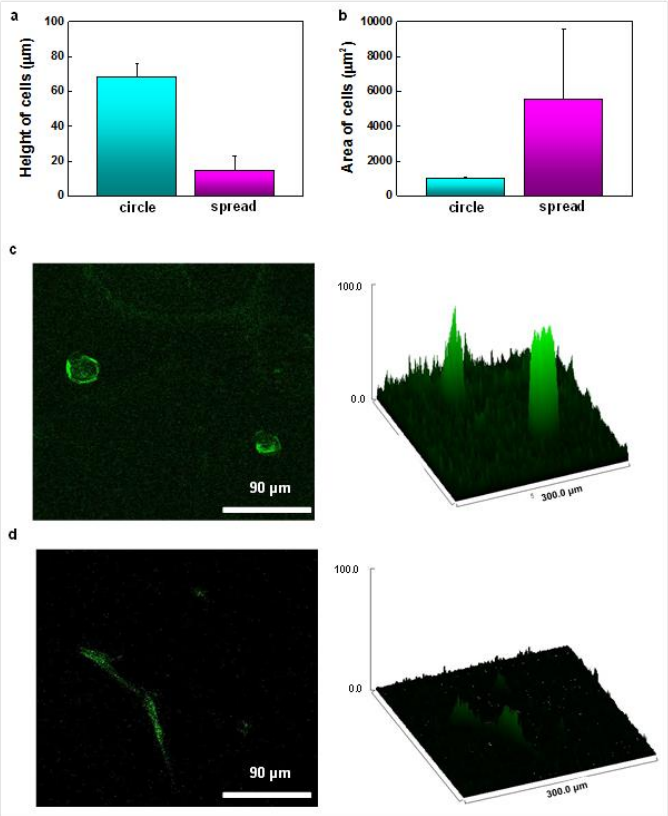

Figure 3.4 Characterizations of MSCs on the gel-protein substrate. *a,b, MSC (a) height and (b) spread area on protein-coated PA gels with the patterned (small circular features-1000 µm2 area) and unpatterned surface after 10 days. c,d, (c) Representative images of MSCs on the features and (d) the unpatterned gel-protein substrate and their z-axis profiles. A Laser Scanning Confocal Microscope (LSCM, Leica Microsystems, TCS SP2 RBB) was employed to characterize average height of MSCs on small circular patterned and unpatterned PA gels. From, confocal 3D Z stack images (5 µm distance of z-axis, 24 images taken), the average height of round or spread MSCs was measured, and the results were about 70 and 15 µm for round and spread cells, respectively. Morphological analysis was performed with the fluorescence images. Since we already knew the total area and number of images and pixels, respectively, we could measure the area of MSCs by counting pixels of patterned or unpatterned MSCs on PA gels (about 1000 and 5000 µm2 for round and spread cells, respectively).*

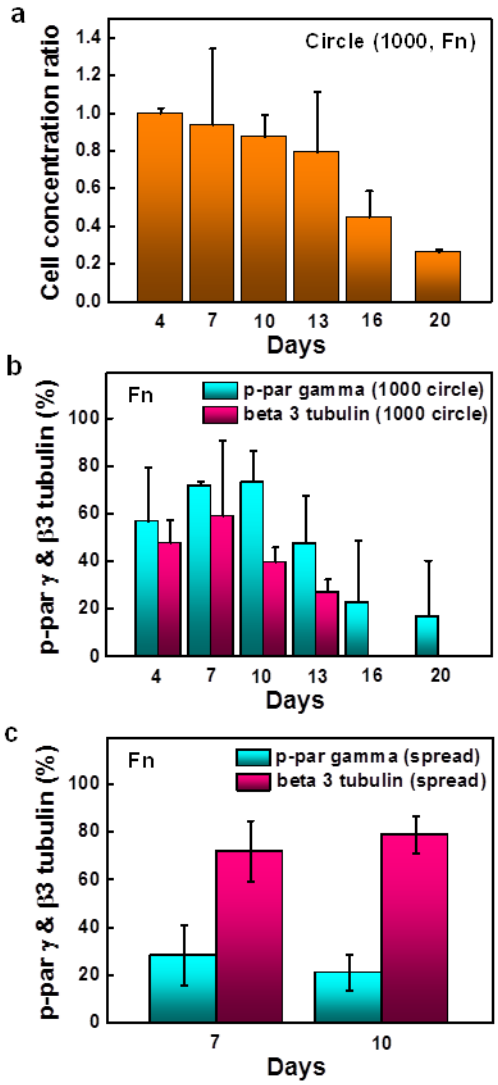

Figure 3.5 Cell viability and lineage marker expression over time on polyacrylamide hydrogels. *a, Cell number studies for several weeks. b,c. Quantitation of the percentage of cells expressing p-par γ and ß3 tubulin on (b) fibronectin coated islands and (c) on unpatterned fibronectin coated substrates. From cell number studies, we saw that cells remained viable and restricted to the islands for 13 days in culture, but cells over 13 days escaped the patterns and proliferated. Immunofluorescence studies of cells at different time in culture were characterized by evaluating the expression of adipogenic (p-par γ) and neurogenic (β3 tubulin) markers using a Zeiss Axiovert 200M inverted research-grade microscope (Carl Zeiss, Inc.). Error bars are standard deviations from two separate experiments with over 200 cells per each condition.*

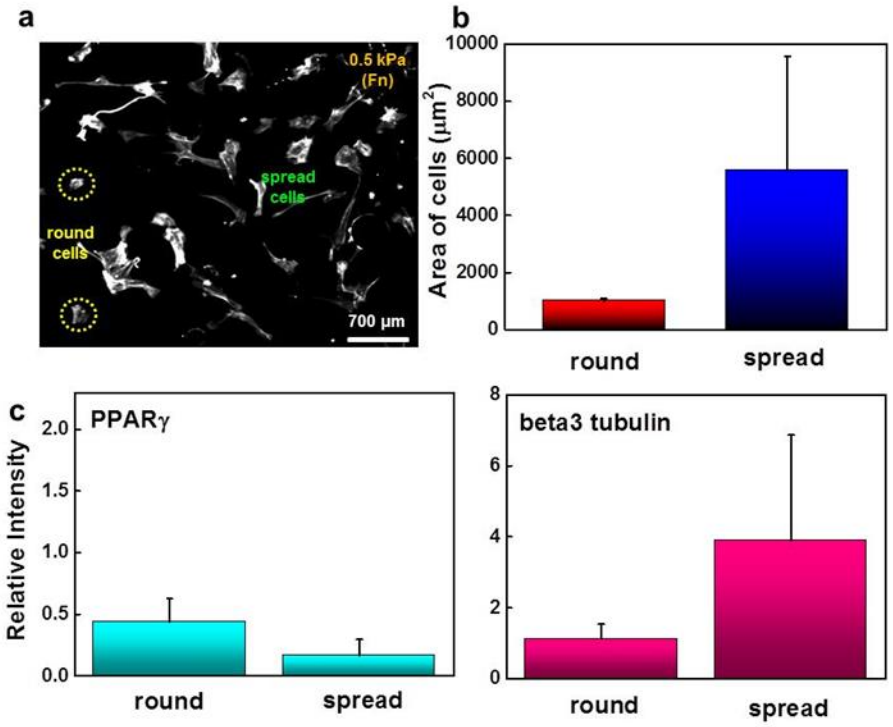

Figure 3.6 Cell spreading influences the degree of adipogenic and neurogenic lineage specification. *(a) Immunofluorescence image of MSCs adherent to the unpatterned fibronectin coated substrates showing cells that display rounded morphology (10-20%). (b) Quantitation of average cell area for those in the population that display a rounded versus spread morphology. (c) Expression of adipogenic (left, p-par γ) and neurogenic (right beta3 tubulin) markers in these populations demonstrating how spreading influences differentiation on soft hydrogel matrices. Error bars are standard deviations of over 70 cells per each condition.*

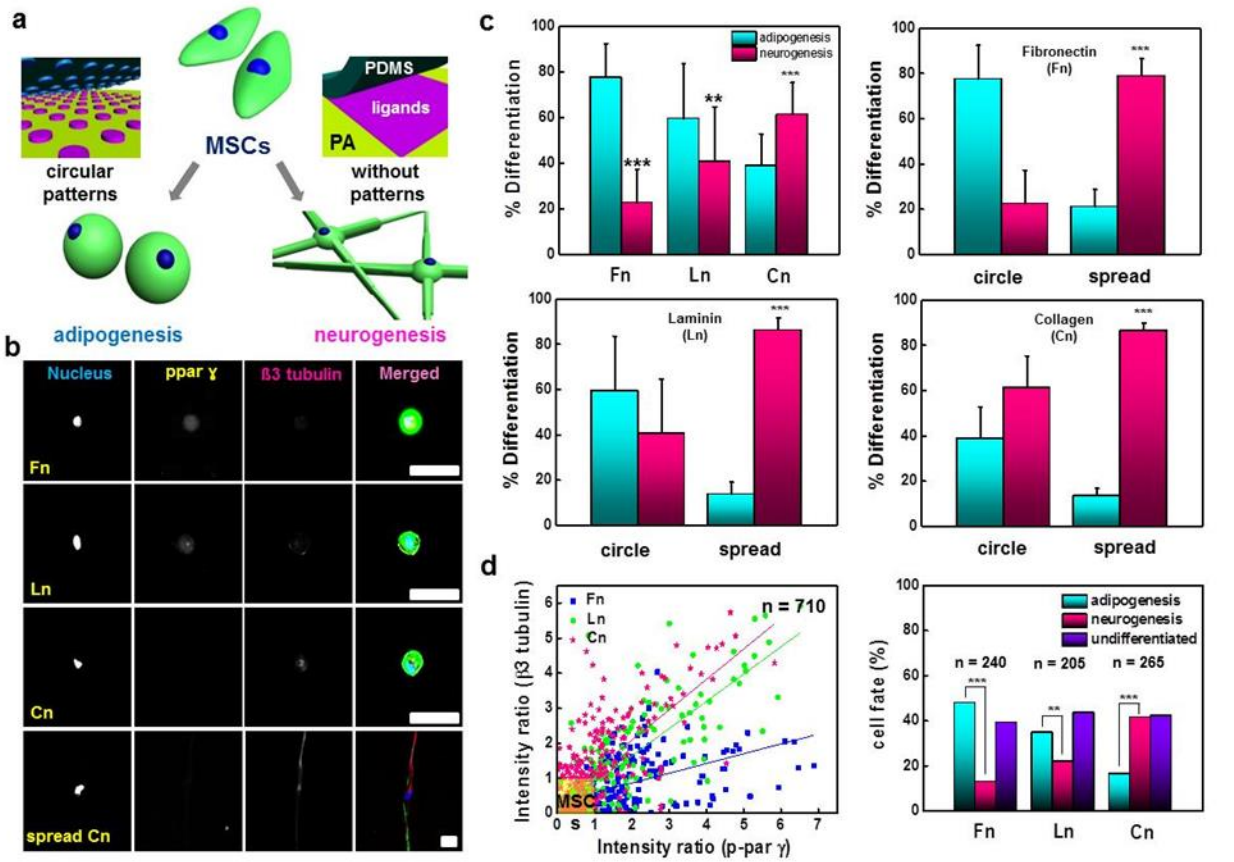

Figure 3.7 Combinations of geometric features and adhesion ligands guide differentiation to adipocyte and neuronal lineages. *(a) Schematic of MSC fate on soft PA hydrogels (0.6 kPa) with and without geometric constraints. (b) Representative immunofluorescence microscopy images of MSCs stained for p-par γ (yellow-green), ß3 tubulin (red) cultured on PA hydrogels of various protein coating (fibronectin (Fn), laminin (Ln), and collagen (Cn)) with different shapes (round or spread) for 10 days; Scale bar 70 μm. (c) Percentage of cells captured on small circular islands or spread on the different matrix proteins, differentiating to adipocyte or neuronal lineages (**P<0.005, ***P<0.0005, Fisher's exact test). (d) Plot of all measured immunofluorescence intensity data (cells cultured on small circular islands) divided by thresholds used to define lineage specification from five different experiments (n=710). The bar graph summarizes a distribution ratio from these cells (**P<0.005, ***P<0.0005, Fisher's exact test). Error bars are standard deviations from five separate experiments with over 200 cells per shape and ligand.*

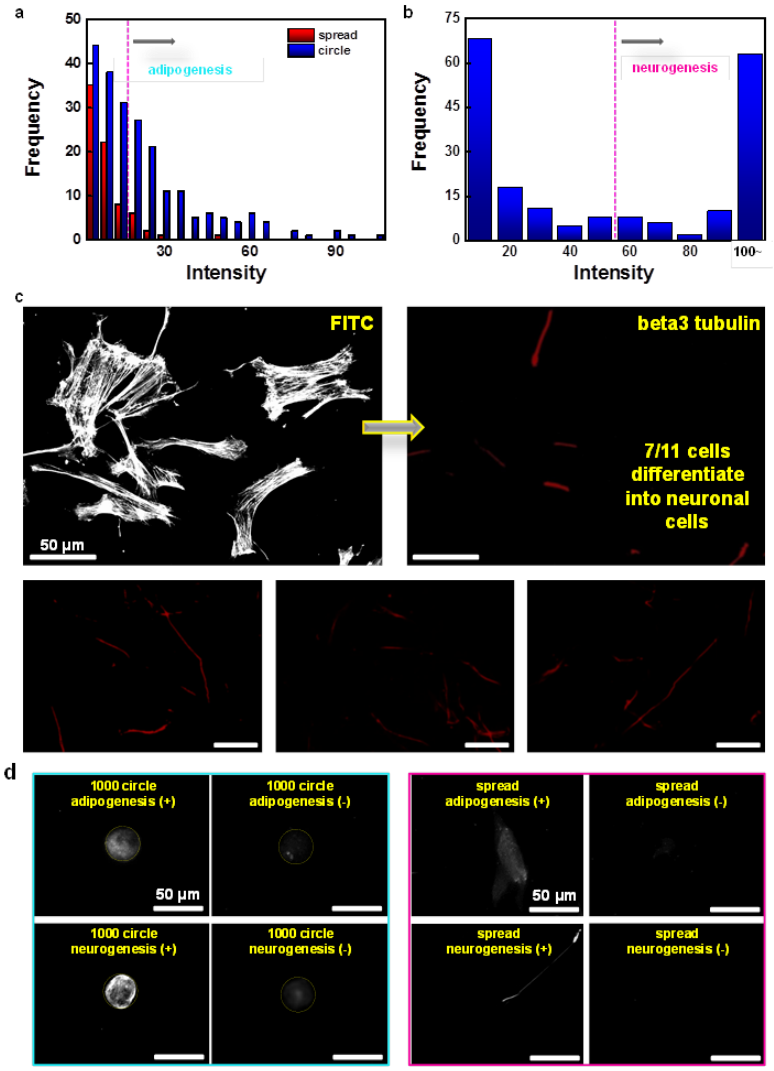

Figure 3.8 Analysis methods for quantitating p-par γ and ß3 tubulin. *a,b, Histograms of (a) p-par γ and (b) beta3 tubulin intensities for MSCs on small circular features or spread MSCs. We assigned thresholds for designating lineage-specific expression. c, Representative Immunofluorescence microscopy images of spread cells showing β3 tubulin-stained. We counted over 100 cells per each matrix proteins and then these cells were categorized into positive or negative bins based on our thresholds. Combination of histograms of spread cells and counting stained spread cells enabled obtaining percentage of cells differentiating to either lineage. d, Representative immunofluorescence images of MSCs to define the thresholds used to categorize lineage specification. Error bars, 50 µm.*

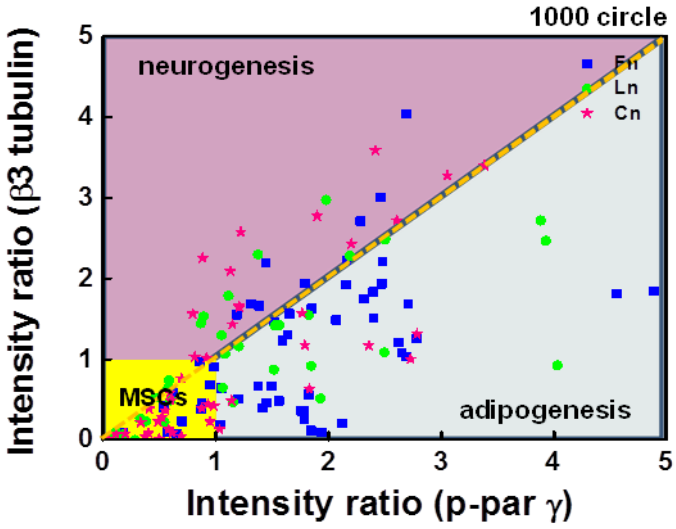

Figure 3.9 Rationale behind the MSC fate decisions. *This graph shows a measured immunofluorescence intensity plot from one individual experiment. Individual intensities (p-par γ and beta3 tubulin) were divided by each threshold used to define lineage specification, and then these cells were categorized into three different groups. First group which had both relative p-par γ and beta3 tubulin intensities below than one was defined as MSCs (undifferentiated cells). Other groups (adipogenesis and neurogenesis) were classified according to lineage specific expression levels.*

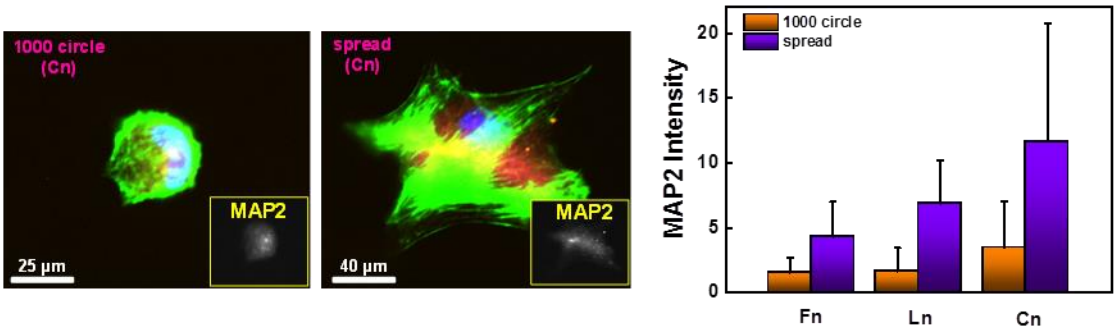

Figure 3.10 Immunofluorescence analysis of MAP2 expression. *In order to confirm the observed immunofluorescence results for adipogenic (p-par γ) and neurogenic (beta3 tubulin) MSCs were also stained for another neurogenic marker, MAP2. The fluorescence images were analyzed by imageJ to measure the fluorescence intensity difference between cytoplasm and nuclei. The results show that the trend is the same as we observed from the beta3 tubulin analysis. These support our results that cells that spread tend to express elevated neurogenic markers. Error bars are standard deviations of over 100 cells per each ligand.*

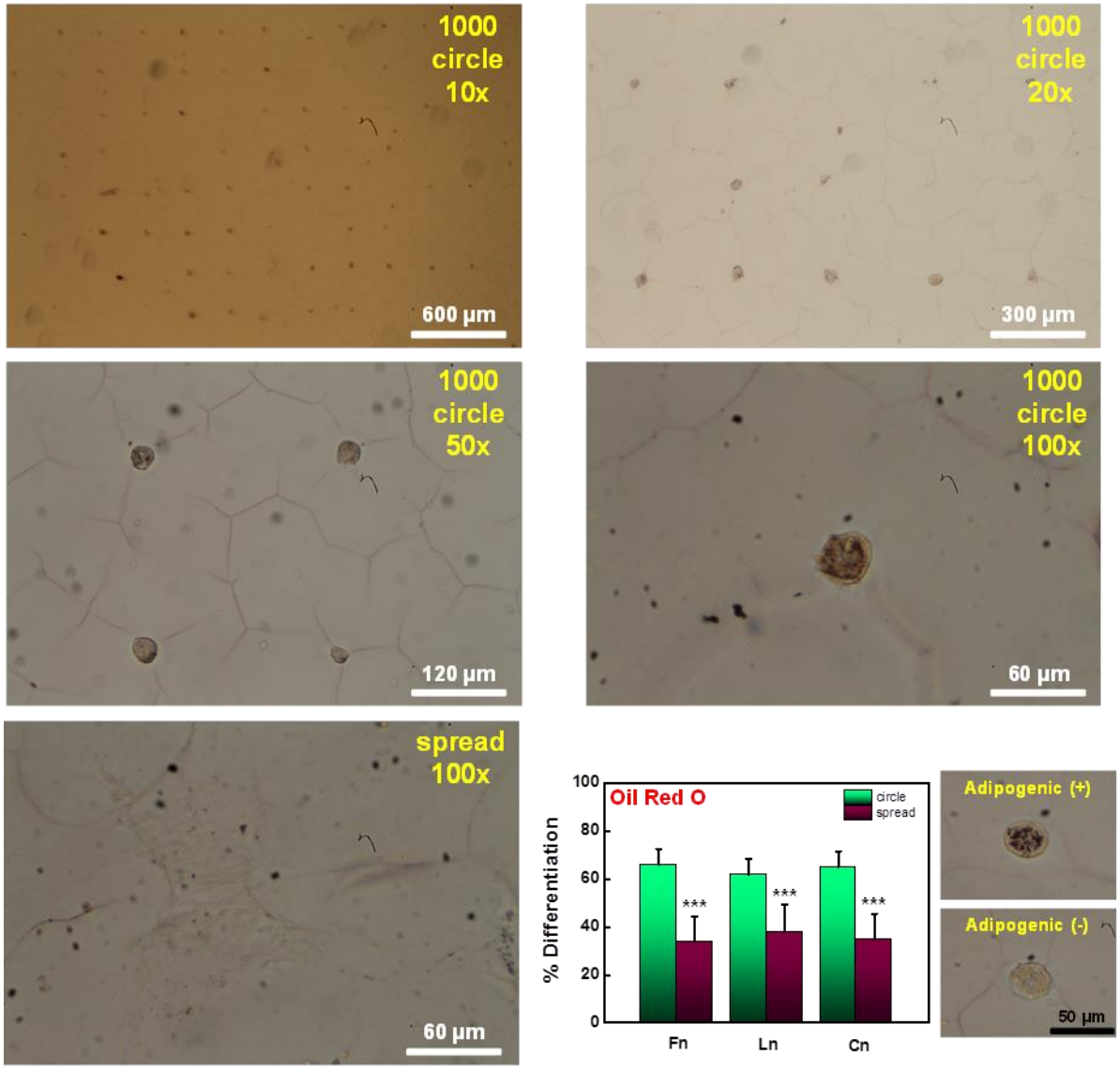

Figure 3.11 Oil Red O of MSCs on polyacrylamide. *Representative optical microscope images show a substantial number of cells on small circular features. In addition, Oil Red O staining study reveals that over 60% of round cells in patterns expressed lipid droplets compared to less than 40% in un-patterned cells on soft PA hydrogels (***P<0.0005, Fisher's exact test), which supports the p-par γ immunofluorescence study. Error bars are standard deviations of 100 cells per each ligand.*

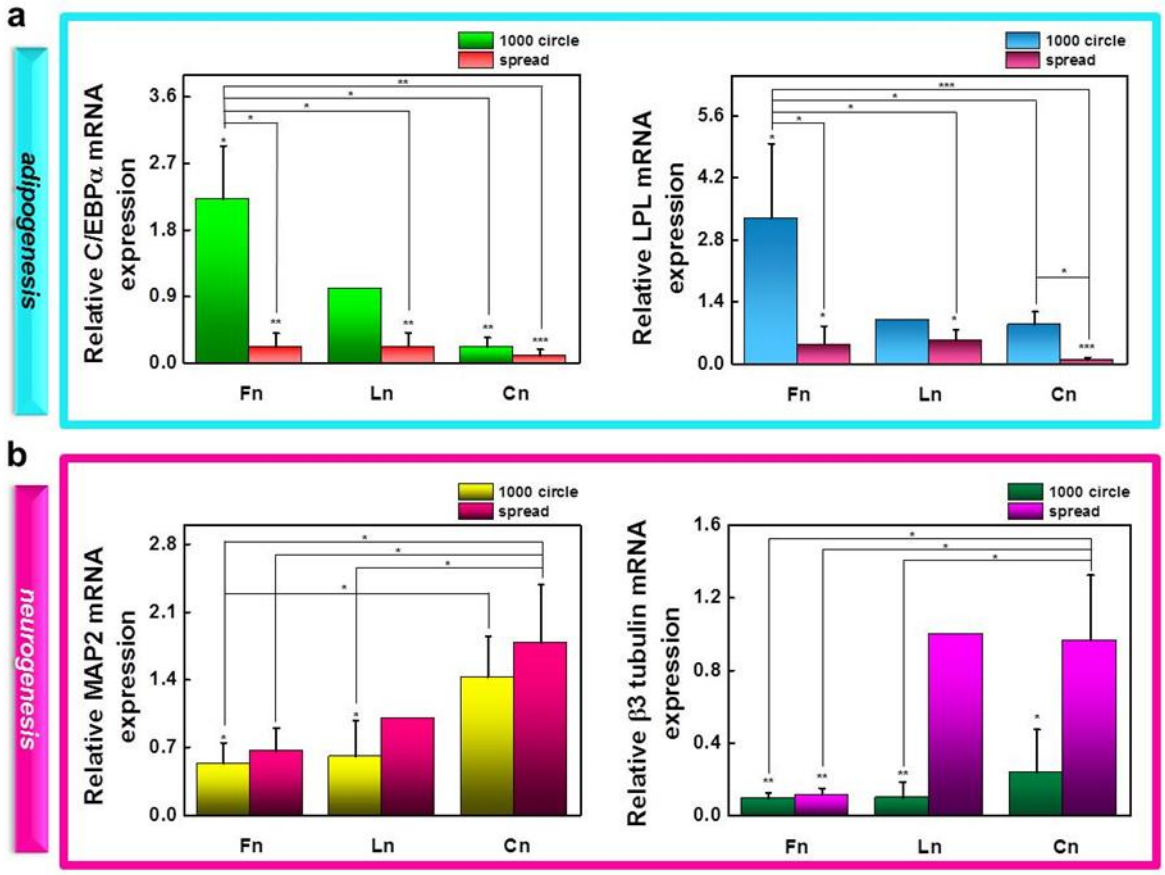

Figure 3.12 Lineage specific gene expression analysis of patterned and unpatterned mesenchymal stem cells. *(a) Results of real-time PCR to measure the gene expression of C/EBP α and LPL as indicators of adipogenesis of MSCs (*P<0.05, **P<0.005, ***P<0.0005, t-test). (b) Results of real-time PCR for quantitation of MAP2 and ß3 tubulin as indicators of neurogenesis mRNA expression of MSCs (*P<0.05, **P<0.005, t-test). Error bars are standard deviations from at least two separate experiments.*

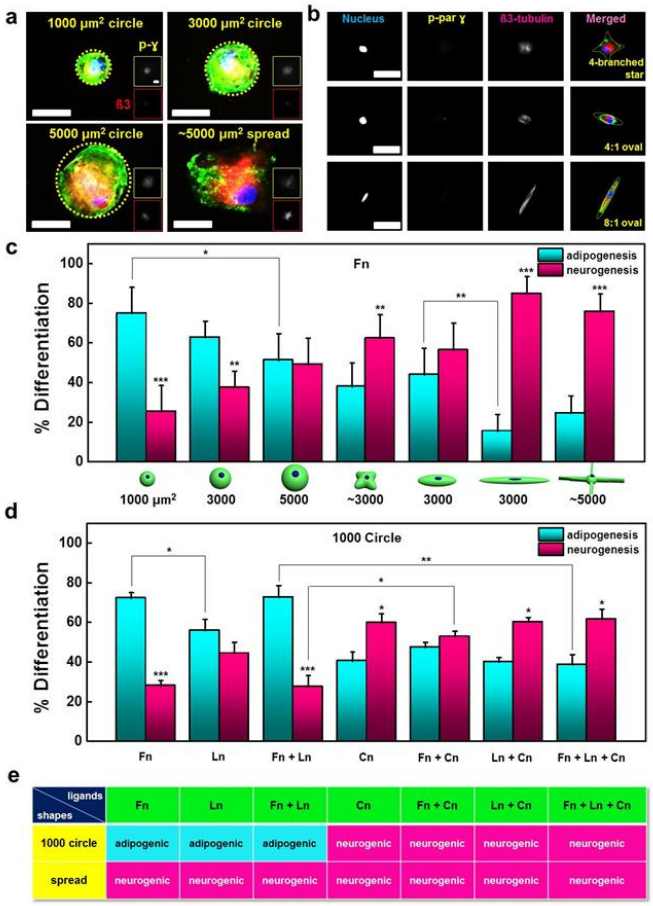

Figure 3.13 Combining geometric cues and matrix protein composition to study adipogenesis and neurogenesis. *(a)-(c) Representative immunofluorescence microscopy images of MSCs cultured in various microengineered geometries for 10 days. Variation in area (scale bar 35 μm) and anisotropic geometric features (scale bar 100 μm). Percentage of cells undergoing adipogenesis or neurogenesis when captured in fibronectin coated geometric islands containing variable area, aspect ratio and branch points (*P<0.05, **P<0.005, ***P<0.0005, Fisher's exact test). (d) Percentage of cells on combination of different matrix proteins, fibronectin (Fn), laminin (Ln), or collagen (Cn), and combinations therof (*P<0.05, **P<0.005, ***P<0.0005, Fisher's exact test). (e) Summary table demonstrating MSC fate decisions depending on the composition of matrix proteins. (c and d) Error bars are standard deviations from three and two separate experiments with over 100 cells per each condition.*

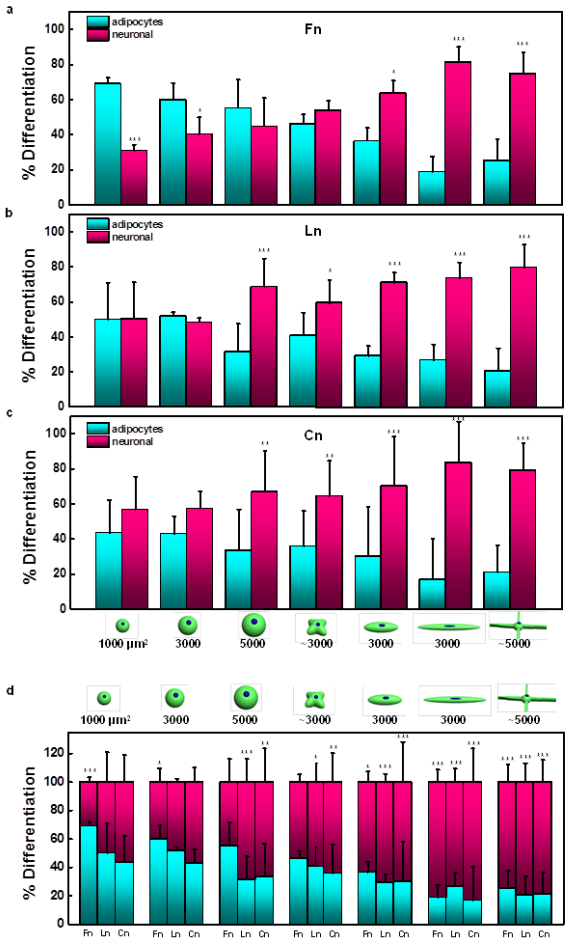

Figure 3.14 Cell fate decisions with combinations of different shapes and adhesion ligands. *a-c, Percentage of cells differentiating to adipocytes or neuronal when cultured on (a) fibronectin, (b) laminin, or (c) collagen coated shapes or flat substrates (*P<0.05, **P<0.005, ***P<0.0005, Fisher's exact test). d, The graph summarizes the results of combination of different shapes and adhesion ligands (*P<0.05, **P<0.005, ***P<0.0005, Fisher's exact test). In most geometric features, there is a trend that fibronectin induce higher level of adipogenesis expression while MSCs on collagen show elevated expression of neurogenesis markers. However, MSCs cultured on laminin do not always display intermediate expression of both markers. For example, MSCs captured in large circles or 4:1 ovals or spread indicate the lowest level of adipogenesis expressions while MSCs on 8:1 oval features show elevated expression of adipogenesis markers. Error bars are standard deviations from two separate experiments with over 100 cells per each shape.*

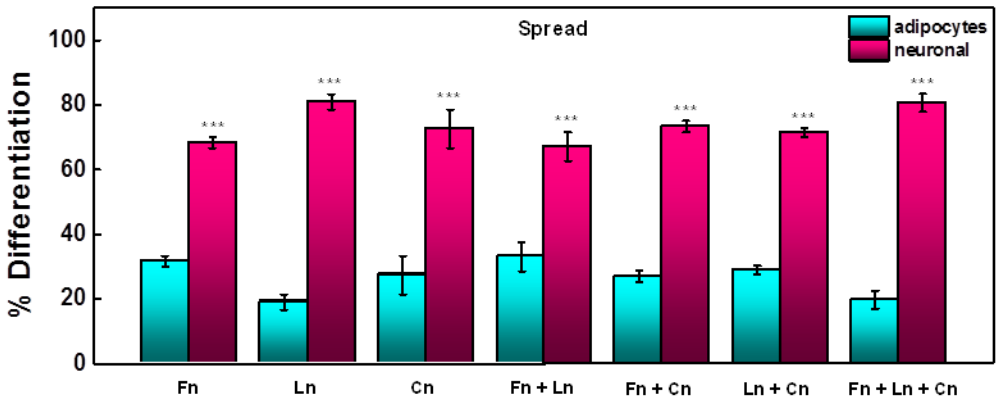

Figure 3.15 Differentiation of spread MSCs on various combinations of matrix proteins. *Percentage of cells (***P<0.0005, Fisher's exact test) shows cell spreading on soft PA hydrogels plays a key role in the neurogenic differentiations of MSCs. However, it is shown that there are subtle differences. Unlike MSCs on laminin patterned small circular features which show higher level of adipogenesis expression, spread MSCs on laminin indicate the highest level of neurogenesis expressions (~81%, Ln (81%) > Fn + Ln + Cn (80%) > Fn + Cn (73%) > Cn (73%) > Ln + Cn (71%) > Fn (68%) > Fn + Ln (67%)). However, the combination of fibronectin and laminin induce higher adipogenesis expressions compared to others (33%). Error bars are standard deviations from two separate experiments with over 200 cells per each condition.*

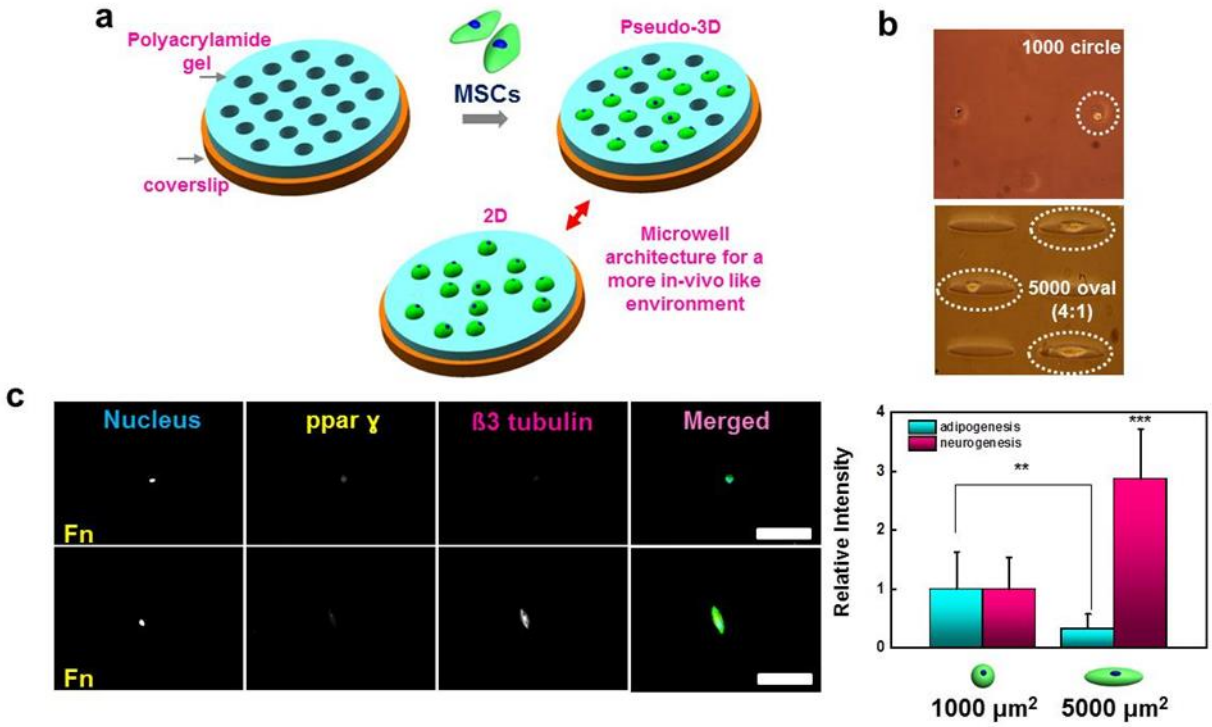

Figure 3.16 Cells encapsulated in pseudo-3D microwells show a similar differentiation dependence to the 2D assays. *(a) Schematic demonstrating the fabrication of protein-conjugated pseudo-3D microwells. (b) Photograph showing cells captured within the wells for small circular patterns and a high aspect ratio/high area geometry. (c) left: immunofluorescence image of MSCs in the microwells stained for adipogenesis (p-par γ) and neurogenesis(ß3 tubulin). Scale bar 70 µm. Right: quantitation of differentiation markers for a population of cells cultured in the microwell arrays.*

CHAPTER 4

CONTROLLING CELL GEOMETRY ON SUBSTRATES OF VARIABLE STIFFNESS CAN TUNE THE DEGREE OF OSTEOGENESIS IN HUMAN MESENCHYMAL STEM CELLS[4]

4.1 Introduction

The development of systems to study the respective roles of different extracellular signals in the cellular microenvironment during stem cell differentiation is an area of significant interest. Cooper-White's group investigated how different matrix proteins grafted to hydrogels with varying mechanical properties will promote different degrees of myogenic and osteogenic signaling in MSCs (22). The results showed that MSC lineage specification can be directed not only by the cells ability to sense the mechanics of the substrate but also by the interaction between specific intergrins and different adhesion proteins. This study more closely mimics the cellular microenvironment by combining multiple ECM cues (stiffness and adhesion ligands). Recent efforts in Chen's group have moved in this direction by micropatterning MSCs on elastomeric microposts to demonstrate how cell shape and substrate stiffness both regulate cell mechanics (97). Using the same platform Chen's group showed how varying micropost spacing and height could be employed to study the synergy between microscale ECM adhesions and substrate rigidity (98). This study showed how adipogenic and osteogenic differentiation are promoted by

[4]This chapter is adapted from the following publication:
Junmin Lee, Amr A. Abdeen, Tiffany H. Huang, and Kristopher A. Kilian, Controlling cell geometry on substrates of variable stiffness can tune the degree of osteogenesis in human mesenchymal stem cells, Journal of the Mechanical Behavior of Biomedical Materials, 2014, 38, 209-218

soft and stiff matrixes, respectively, which means matrix stiffness is directly linked to these MSC fate decisions. These reports demonstrate how the maturation of materials science based tools will lead to new assays for studying multiple extracellular cues independently and together.

In this chapter 4, we control cell shape across hydrogels of different stiffness to explore how cell geometry and influences osteogenesis on lineage-matched substrates. Using microcontact printing of adhesion proteins on soft polyacrylamide (PA) gels, we show that cell shape combined with matrix stiffness can direct the osteogenic differentiation of mesenchymal stem cells. The influence of geometric cues (subcellular curvature and aspect ratio) across the substrate on cell fate decisions is investigated and we show that osteogenesis marker expression can be elevated when cells are confined to shapes that promote increased cytoskeletal tension.

4.2 Materials and Methods

General materials and methods are given in Appendix A.

Materials:

rabbit anti-Runx2, anti-Osteopontin, and anti-myosin IIb were purchased from abcam (ab23981, ab8448, ab204358, respectively).

Immunocytochemistry:

The relative intensity of the fluorescence was determined by picking threshold and then comparing each value to the threshold. For the myosin IIb study, color

histogram generated by measuring an area with different intensities for the heatmaps (averaged intensity of stacked images) of cells stained for myosin IIb in concave and oval shapes was obtained by using imageJ. Total intensity was calculated by the sum of multiplying the area by their intensity. Relative intensity was determined by picking the intensity of circular shape and then comparing each value (concave or elongated cells) to the selected intensity.

Histochemical staining:

To detect alkaline phosphatase activity, fixed cells were incubated in a BCIP/NBT solution (Amresco) one hour at room temperature. Cultures were then rinsed with PBS and imaged with brightfield microscopy.

Atomic Force Microscopy (AFM):

The Young's moduli of the surfaces were obtained using AFM contact force measurements on an atomic force microscope (Asylum Research). The AFM tips (Bruker) were calibrated in air and then in PBS and all force measurements were performed on patterned samples in PBS. At least 9 measurements at different spots were performed for every stiffness condition across 3 samples. The data was fitted into a Hertz model using IGOR PRO software (Wavemetrics). The tip geometry was approximated using a cone architecture to derive the values of Young's modulus.

4.3 Results

Covalent patterning of matrix protein on polyacrylamide hydrogels of different stiffness

To study how changing single cell geometry influences MSC differentiation on hydrogels of different stiffness, we developed a procedure to pattern cells on polyacrylamide hydrogels (Fig. 4.1). We first prepared polyacrylamide (PAAm) hydrogels as previously reported (84). Since it was shown that hydrogels with around 30 kPa stiffness mimic the rigidity of pre-calcified bone tissue (28), we used acrylamide and bis-acrylamide solutions to prepare hydrogels with desired Young's modulus of 10 to 40 kPa (Fig. 4.2). Next, hydrazine hydrate was applied to the PAAm for converting amide groups in polyacrylamide to reactive hydrazide groups. This treatment allows covalent conjugation of the ECM protein fibronectin (via coupling of formed aldehyde groups after oxidation with sodium periodate) to the surface of the hydrogels. The stiffness of the hydrogels was confirmed by atomic force microscopy (AFM) (99). We performed 10 different stiffness measurements, and the results showed that measured Young's modulii of hydrogels with desired stiffness of 10, 20, 30, and 40 kPa were 10, 23, 34, and 40, respectively, in close agreement to the targeted range (Fig. 4.2). To exclude the effects of adhesive ligand, we fixed the amount of fibronectin at 25 μg/mL, and thus we could obtain the influence of only varying stiffness. Microcontact printing was used to transfer fibronectin to the hydrazine treated gels with stiffness ranging from 10 to 40 kPa (Fig. 4.1). First, to fabricate PDMS stamps for microcontact printing, photolithography was employed to obtain patterned structures on the photoresist coated surface of a silicon master. Next, PDMS stamps were prepared by replica molding using liquid PDMS with curing agents over the structured master, and these stamps were employed after oxygen plasma treatment for reducing hydrophobicity on the surface.

To confirm the patterning accuracy of deposited protein on the hydrogel substrates, we incorporated fluorescently labeled (Alexa 546) fibrinogen to the oxidized fibronectin solution prior to patterning to confirm protein patterning on the surface and to check pattern fidelity and optimize the process accordingly (100). Immunofluorescence analysis shows that precise patterning of sophisticated features on hydrogels is highly dependent on curing, drying and contact times. For this reason, we optimized the variables from curing time to the method of protein patterning (see Table. 4.1). For example, hydrogel curing time was fixed at ~20-25 min because this led to full polymerization and easy detachment from a hydrophobic glass slide. In addition, drying times for hydrogels and protein solutions on PDMS were empirically determined to be optimal at ~60-90 min and <5 seconds respectively (See Fig. 4.3a and b). Transferring proteins from the surface of the PDMS stamp to the surface of the hydrogels required complete drying of both surfaces, followed by exposure to trace moisture prior to stamping. Through optimizing all of the variables used in the process, we were able to obtain robust patterning with features resolved down to single microns (Fig 4.4a, b, c, and 4.3d).

Mesenchymal stem cell culture on hydrogel substrates

Cells were seeded on fibronectin coated hydrogels and the morphology of the cells was assessed using phase contrast microscopy. Cells on unpatterned gels adhered randomly and displayed a heterogeneous spread phenotype (Fig. 4.5a). Morphological analysis reveals that the unpatterned cells present a variable spread area dependent on substrate stiffness (10 kPa (~10000 μm^2) to 40 kPa (~15000 μm^2), Fig. 4.5b). On the patterned gels, cells adhered and conformed to the

patterned regions after 4 days in culture (Fig. 4.4d and e). For our initial patterning experiments, we selected geometries that have been shown previously to modulate the degree of cytoskeletal tension while keeping total cell area a constant value (86). The patterned area was chosen to be less than the observed spread area in order to limit proliferation (39) while normalizing the actomyosin contractility state of the single cells across the substrate. Patterned cells adhere to the printed area and show a comparable size to the defined regions (5000 μm^2). In this chapter 4, approximately 60-80% of the patterned cells remained viable and restricted to the islands for 10 days in culture. Moreover, we observed that almost all of the cells in patterns on hydrogels did not divide and stayed single cells over the course of the experiment. Since the patterned cells remain in geometric confinement for timescales that have been shown to promote osteogenesis in a substrate-stiffness dependent fashion, we went on to explore the influence of geometry on expression of osteogenic markers.

Osteogenic differentiation of MSCs on micropatterned hydrogel substrates

Since earlier reports of MSCs undergoing osteogenesis on stiffer matrices used fibronectin as the adhesion protein, we used fibronectin to investigate the degree of osteogenesis on stiffness-tunable hydrogels (~10-40 kPa). Guided by earlier work (38), we hypothesized that elongated shapes and features of local curvature could increase the cytoskeletal tension in MSCs, thus promoting the preference for osteogenesis. To test this we designed a range of geometries: a control condition of circular patterns that should yield a low state of cytoskeletal tension in adherent MSCs, shapes of increasing aspect ratio and shapes that present subcellular

curvature and aspect ratio. We first studied the effect of the confined geometry using the circular features with a moderate area of 5000 μm^2 (Fig. 4.6). Figure 4.6a shows representative immunofluorescence images of cells cultured on circular shapes with different stiffness after 10 days. We investigated the cytoskeletal characteristics in MSCs on the patterns by producing immunofluorescence heatmaps of filamentous actin and myosin IIb generated from 32 and 12 cells, respectively, across the same substrate (Fig. 4.6a). Since this circular shape does not contain features to promote elevated cytoskeletal tension, there was no clear geometric influence on stress fiber formation or focal adhesion architecture and the majority of cells displayed a classical cortical actin network (Fig. 4.6a). To measure the degree of osteogenesis, we chose to immunolabel MSCs with the master regulatory transcription factor Runx2 because it is one of the well-known key transcription factors associated with osteoblast differentiation (101). Immunofluorescent images were analyzed using ImageJ to measure the fluorescence intensity difference between nuclei and cytoplasm. We observed that there was no significant difference in Runx 2 expression between spread and confined cells, and both cases expressed Runx2 with a slight stiffness dependence (maximum at ~30 kPa; Fig. 4.7).

Next, we examined the degree of runx2, osteopontin, and ALP expression in MSCs cultured on a high aspect ratio geometry of the same area (12:1 oval), and a shape with moderate aspect ratio that presents regions of subcellular curvature (Fig. 4.8). For the high aspect ratio shape, cells initially adhered on the patterns without elongation. However, after around two or three days of culture, the cells spread

along the oval shapes and filled the entire area. We observed that as cells elongated along the pattern, the nuclei of cells also deformed and oriented along the elongation direction. Compared to the circular MSCs (Fig. 4.8a), elongated cells displayed large stress fibers concentrated along the long edge of the cells suggesting increased cytoskeletal tension in cells of this geometry (see Fig. 4.8a). Cells captured in the shape with a moderate aspect ratio and concave features fully adhered to the pattern within several days and assembled large stress fibers across the nonadhesive space between points (see Fig. 4.8a). We also performed immunofluorescence staining of the myosin IIb to quantitatively measure contractility. We observed most cells captured on concave or oval shapes or spread on the fibronectin matrix protein showed a higher degree of the marker when they are cultured on around 30 kPa gels for 10 days (Fig. 4.8a) and cells in concave features expressed higher degree of the marker compared to elongated or spread cells, consistent with the protein analysis using immunofluorescence and histogram of heatmaps from myosin IIb (Fig. 4.8b). Although, unlike the immunofluorescence heatmaps of filamentous actin in MSCs confined to concave shape which displayed large stress fibers concentrated along the long edge of the cells suggesting increased cytoskeletal tension, the heatmap of myosin IIb showed higher level of expression in the center than the edge. However, the results clearly show cells in concave shape have higher degree of total myosin IIb intensity in the average of 12 cells per pattern (see Fig. 4.8b). To determine if these shapes would influence MSC osteogenesis, we performed immunofluorescence staining of the osteogenesis marker Runx2, Osteopontin, and ALP staining for patterned (oval and concave shapes) and unpatterned cells after 10 days. Cells cultured on fibronectin show the

highest expression of Runx2 on ~30 kPa gels regardless of their shapes (Fig 4.8b). In addition, for osteopontin study, the highest expression was shown for cells cultured in moderate aspect ratio that presents regions of subcellular curvature and elongated cells (12:1 oval) at around 30 and 40 kPa, respectively. This trend was also shown for ALP staining; nearly 18 (concave) and 15% (oval) of cells expressed the marker on 10 kPa while the highest fraction 36 (concave, ~30 kPa) and 27% (oval, ~40 kPa) was shown. This trend in osteogenic differentiation of MSCs is comparable to previous reports that showed that osteogenesis is directed by the stiffness of the matrix (28). However, patterned cells that present features to increase cytoskeletal tension significantly enhanced the expression of osteogenesis markers. For example, MSCs confined to elongated geometries showed approximately 2-fold enhancement in Runx2 expression (at ~30 kPa) compared to unpatterned cells (p-value < 0.0005). Interestingly, combining aspect ratio with regions of subcellular curvature further enhanced osteogenesis by over 3-fold. These results demonstrate that normalizing cell shape across substrates with optimal mechanics for the osteogenesis program can be used to tune the desired degree of differentiation.

4.4 Discussion

Considerable evidence suggests that MSC lineage specification is influenced by substrate stiffness (2, 24, 25, 28, 78, 102). The tendency for cells to pull against and deform the matrix through specific integrin-mediated interactions with matrix proteins plays a significant role in guiding downstream signal transduction that regulates gene expression (13, 14, 16, 17, 21). Actin filaments anchored at focal

adhesions are important structures for force transmission in order for cells to feel the compliance of their substrate. (34, 38, 93, 103). In this way, stiff matrices give rise to increased cell spreading which has been shown to promote osteogenesis through enhanced actomyosin contractility.

Unlike a 3D niche, 2D surface provides a convenient configuration for deconstructing the niche and allows us to investigate the effects of individual components on stem cell fate decision (104). Micro-contact printing (μCP) has been mainly used for patterning matrix protein on the 2D substrate such as Au (38, 105), polydimethylsiloxane (PDMS) (37, 91), or hydrogels (28, 87, 106). However, few studies showed transferring protein pattern on hydrogels due to their uneven and very soft surface (5, 107). The Shain group showed crossed long line patterns on the hydrogel surface induce neuronal cell growth and attachment (5). These cells can extend their neurite after 72 h in vitro and show viability on the surface more than 4 weeks. To tackle the issues, other approaches to pattern cells on hydrogels have been developed (108–110). Matrix protein patterns can be transferred on the modified glass surface and then hydrogels are fabricated on the patterned glass surface. After peeling gels off, protein patterned hydrogels can be obtained. Likewise, considerable efforts have been made to find better way of patterning cells on the ECM for the study on promoting the differentiation of stem cells to distinct lineages. We have optimized the every single step ranging from curing time to drying and contact times for the precise patterning of sophisticated features on hydrogels.

It is well known that MSCs are heterogeneous when it comes to their differentiation. Although, MSCs cultured in the fixed stiffness are influenced by multiple cues such as geometry, matrix proteins or soluble cues to regulate fate decision, stiffness alone plays a key role in heterogeneity of MSC differentiation. Many studies have showed it by way of the transferring cells to the substrate with different stiffness or dynamic stiffening. For example, heterogeneity is strongly determined by the culture time prior to substrate stiffening. Recently, Burdick's group revealed that the timing of mechanical changes on the fate decision of MSCs using real-time tunable hydrogels undergoing photocrosslingking via UV exposure (90). Cells could sense and respond to the time dependent changes in ECM stiffness by changing the degree of spreading and accompanying traction forces. Cells cultured with ECM stiffening occurring later show an elevated percentage with adipocyte fate while cells placed in earlier ECM stiffening tended to differentiate into osteocytes.

MSCs cultured on hydrogels modified with matrix protein display a range of morphologies. Previously, Mrksich and colleagues have shown how geometric features that promote actomyosin contractility can enhance the ostoegenesis outcome in patterned MSCs that are exposed to lineage-guiding media supplements (38). Here we asked whether normalizing cell shape across hydrogel substrates that promote osteogenesis could influence the differentiation outcome. To test this hypothesis, we patterned MSCs in a circular shape that does not contain geometric cues that promote cytoskeletal tension. MSCs cultured in this shape displayed a disordered cytoskeleton and did not increase the expression of nuclear Runx2 when compared to the population of unpatterned cells. To investigate how shape may

enhance osteogenesis on hydrogels, we explored geometric features that are known to increase actomyosin contractility: a 12:1 aspect ratio oval and a shape with moderate aspect ratio and regions of subcellular concavity. Immunofluorescence heatmaps of filamentous actin in MSCs confined to these geometries indicates the assembly of large stress fibers upon increasing aspect ratio and subcellular concavity, resulting in enhanced cytoskeletal tension compared to circular cells. We see a stiffness dependence in the expression of Runx2, Osteopontin, and ALP irrespective of cell shape with a maximum at ~30 kPa, in agreement with previous reports (28). However, the culture of MSCs in geometries that promote increased cytoskeletal tension show a further enhancement—particularly at the osteogenic stiffness of ~30 kPa—of 2-fold, 1.1-forld, and 1.2-fold (elongated oval shape) and > 3-fold, 2-fold, and 1.6-fold (concave shape) for Runx2, Osteopontin, and ALP expression. Since unpatterned cells display a range of morphologies, the average Runx2 expression measured from this heterogeneous population is variable. Using micropatterning, the cytoskeletal tension of the entire population of cells can be normalized, thus influencing the final degree of osteogenesis.

From the study of myosin IIb staining, the contractility of cells in the concave shape might be dependent on the length between two nearest concave edges. The Mrksich group showed that cell contractility could be localized at concave regions for a star shape with five-edges. However, localization of myosin IIa was shown in the region of larger concave length but not shown in the region of small concave regions (38). Like the study, cells cultured in moderate aspect ratio that presents regions of subcellular curvature might not show a high degree of actomyosin

contractility along the edges but center regions in this work. Interestingly, the degree of myosin contractility can be influenced by the degree of length between concave regions which have nonadhesive regions for cells, meaning that a certain degree of nonadhesive regions is required for the localization of myosin contractility. Thus, instead of the localization of contractility in concave regions, it was shown in the region of center regions of cells. Moreover, for the cells cultured in moderate aspect ratio that presents regions of subcellular curvature, the heatmap of myosin IIb displayed quite different trend compared to the one of F-actin. F-actin showed the localization along both the edge and center regions while myosin IIb preferred to be only center regions. This means the actomyosin contractility is not always influenced by cytoskeletal tension but dependent on the degree of tension and nonadhesive regions.

4.5 Conclusion

Signaling in mesenchymal stem cells is influenced by the physical aspects of the microenvironment including mechanical properties, geometry and topography. In this chapter 4, we show how microengineered hydrogels can be used to combine several of these physical cues to explore MSC differentiation. Cells cultured on protein coated gels show a stiffness dependence in the expression of the master osteoblast regulator Runx2. Patterning single MSCs in isotropic circles show no appreciable difference in Runx2 expression compared to the unpatterned cells. In contrast, MSCs cultured in shapes that present geometric cues to enhance cytoskeletal tension show a significant increase in Runx2, Osteopontin and ALP expression. This result demonstrates how osteogenesis in adherent MSCs can be

controlled by both cell geometry and the mechanics of the substrate. We expect this platform will be broadly applicable across other differentiation events and other stem cell systems that are influenced by the physical microenvironment. This strategy is expected to prove particularly useful in stem cell mechanobiology investigations where control of multiple extracellular parameters will be advantageous to study and direct lineage specification and commitment.

4.6 Tables and Figures

process	Time	Ave. Yield	Additional description
0.5 % APTS	3 min	99%	Surface modification of cover slips
0.5% Glutaraldehyde	30 min	99%	Surface modification of cover slips
Hydrogel curing	~20-25 min (10 to 40 kPa)	95%	Detaching hydrogels on coverslip very gently (In air & room T)
Hydrazine hydrate	2 hours	99%	Surface modification of hydrogels
5% Glacial acid	1 hour	99%	After hydrazine treatment
D.I. water	1 hour	99%	After 5% glacial acid
Drying hydrogels	~60-90 min	97%	Need to be fully dry (see Fig. S2a)
Protein preparation	45 min	99%	Waiting for mixing proteins in PBS
Applying protein solution on PDMS	30 min	99%	Need to be entirely dispersed on PDMS
Drying protein solution on PDMS	few sec with adequate strength	97%	Need to be fully dry (see Fig. S2b)
Transferring proteins to gels	~20-40 sec	80%	Need slight moisture on the surface of PDMS when patterning (with slight pressure) (see fig. S2c)

Table 4.1 Optimized fabrication procedure of patterned hydrogels. *A table of fabrication process with optimized time, an average yield, and the details for each process.*

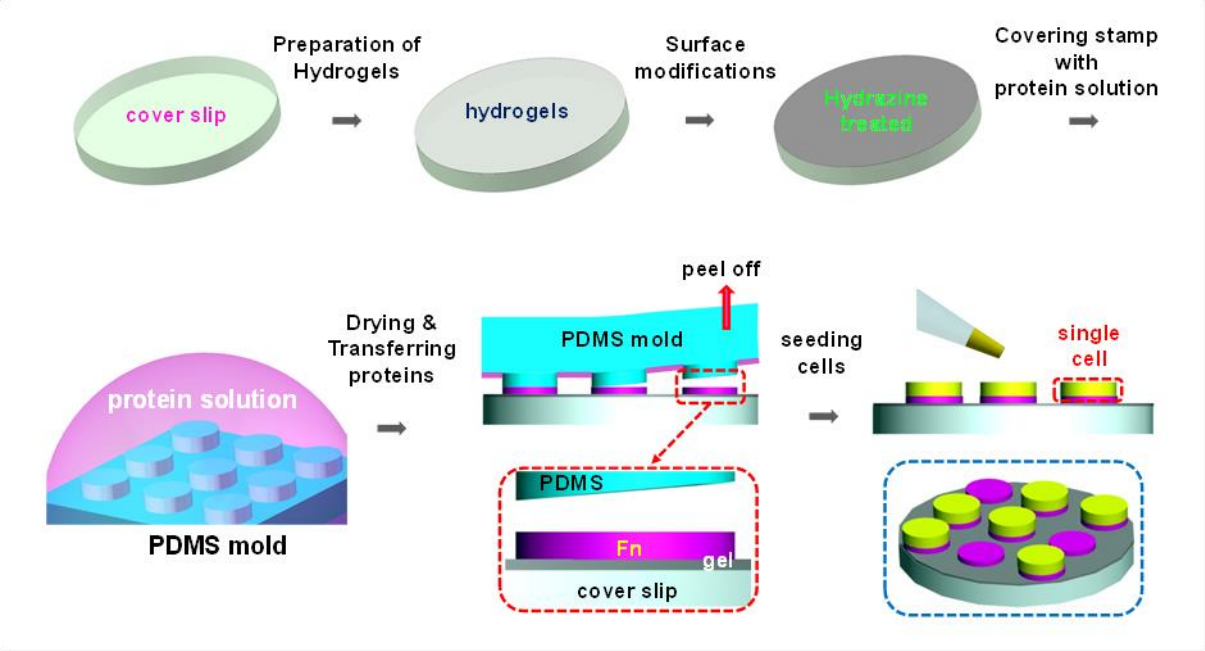

Figure 4.1 Combining geometric cues and substrate stiffness. *Schematic demonstrating the process used to pattern cells on fibronectin coated polyacrylamide hydrogels.*

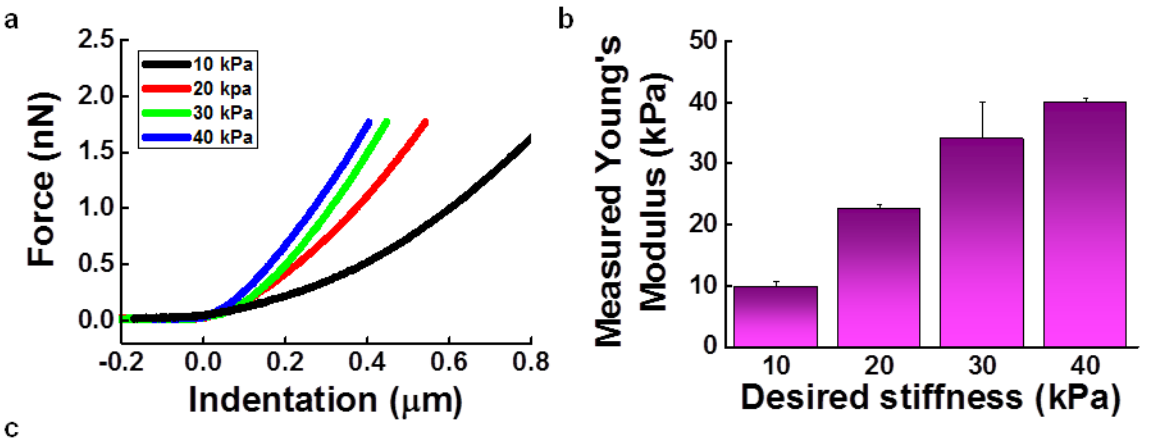

c

Desired Young's Modulus (kPa)	Acrylamide (wt%)	Bis-Acrylamide (wt%)	Measured Young's Modulus (kPa)
10	10	0.100	10 ± 1
20	8	0.264	23 ± 1
30	10	0.250	34 ± 5
40	8	0.480	40 ± 1

Figure 4.2 Characterization of polyacrylamide hydrogels. *a. Force-deflection curves of gels with desired Young's moduli of 10 to 40 kPa (Representative curves). b. Measured Young's modulus of hydrogels with desired stiffness of 10 to 40 kPa. c. A table showing the relative concentrations of acrylamide, bis-acrylamide and their desired and measured Young's modulus.*

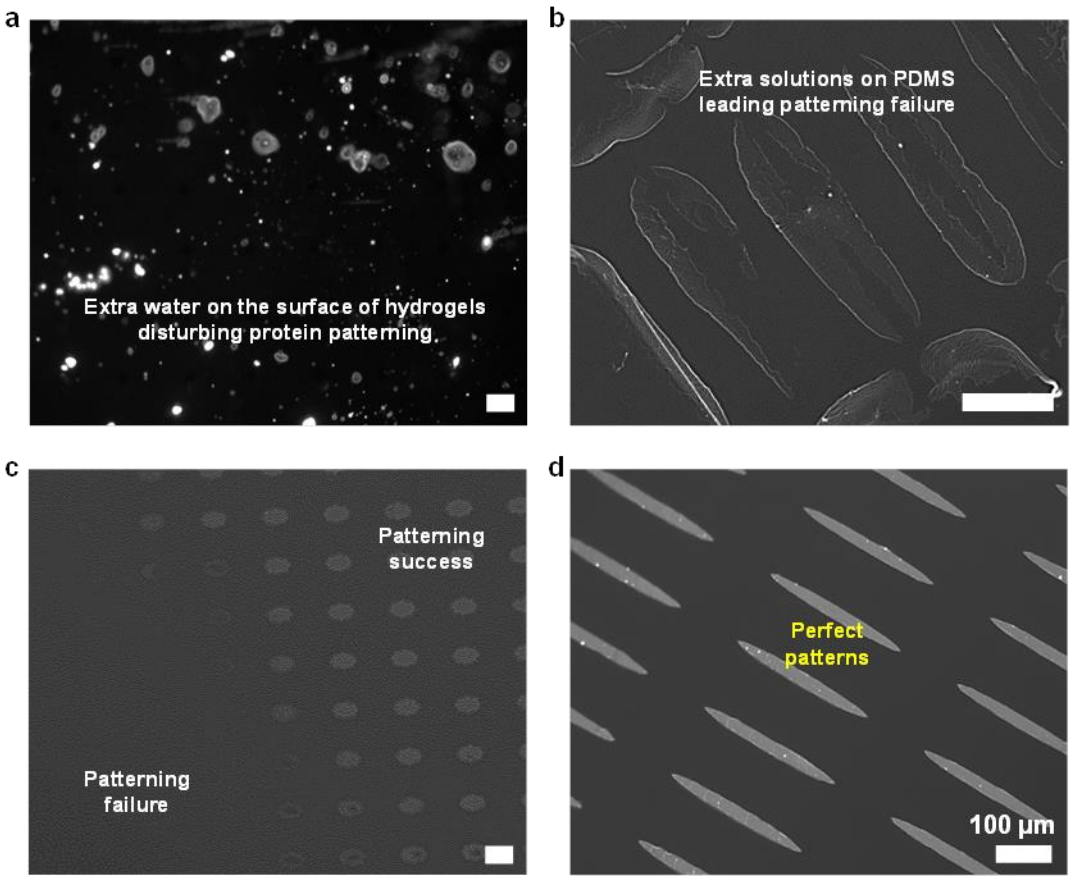

Figure 4.3 Unsuccessful and successful matrix protein patterns on hydrogels. *a-c. Representative fluorescence images of unsuccessful patterned adhesion ligands on hydrogels with fibrinogen due to limited drying for the surface of (a) hydrogels and (b) PDMS molds and (c) lacking moistures between contact surfaces. d. Representative fluorescence images of successful patterns of matrix proteins on hydrogels.*

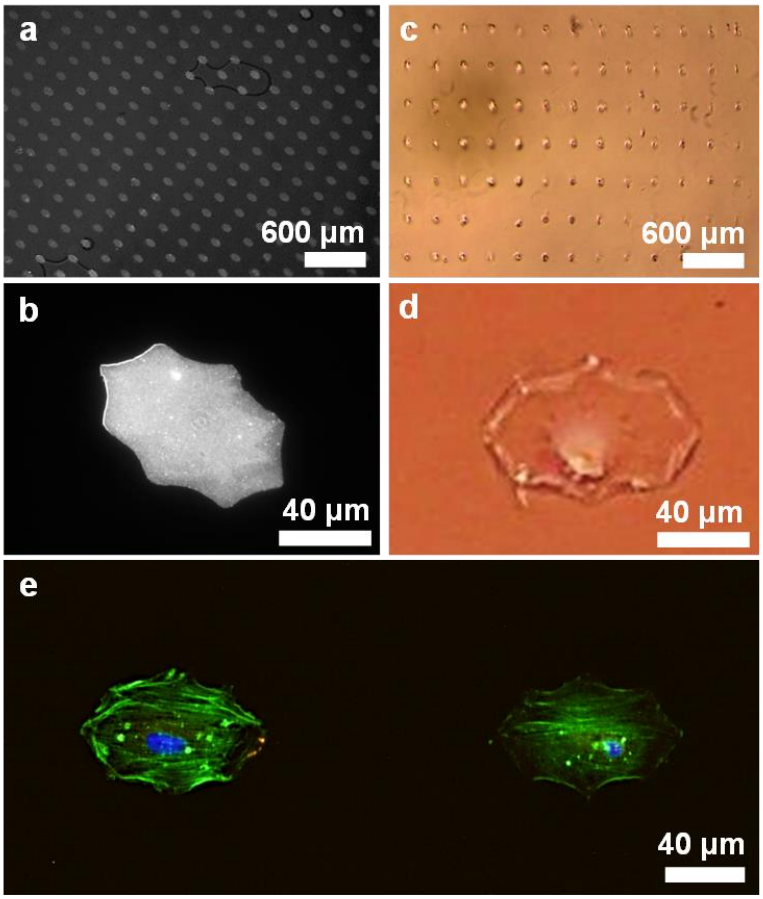

Figure 4.4 Mesenchymal stem cells captured on matrix protein patterned hydrogels. *a-c. Representative fluorescence images of patterned adhesion ligands on PA gels with fibrinogen (concave shapes). d-f. Representative optical images and (g) immunofluorescence images of cells captured to patterned islands (green – actin; blue – nuclei).*

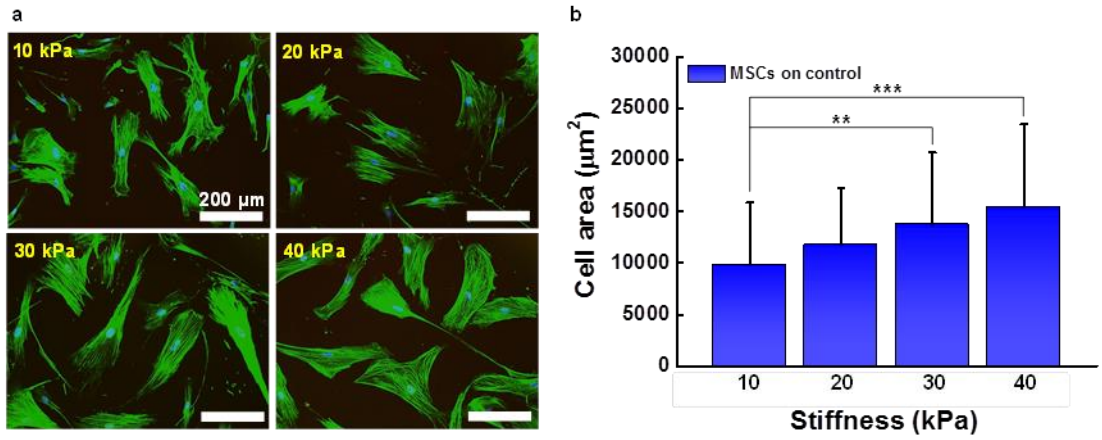

Figure 4.5 Characterizations of mesenchymal stem cells on the gel-protein substrate. *a. Representative images of MSCs on the unpatterned gel-protein substrate. b. MSC spread area on unpatterned protein-coated hydrogels after 10 days (**P<0.005, ***P<0.0005, t-test).*

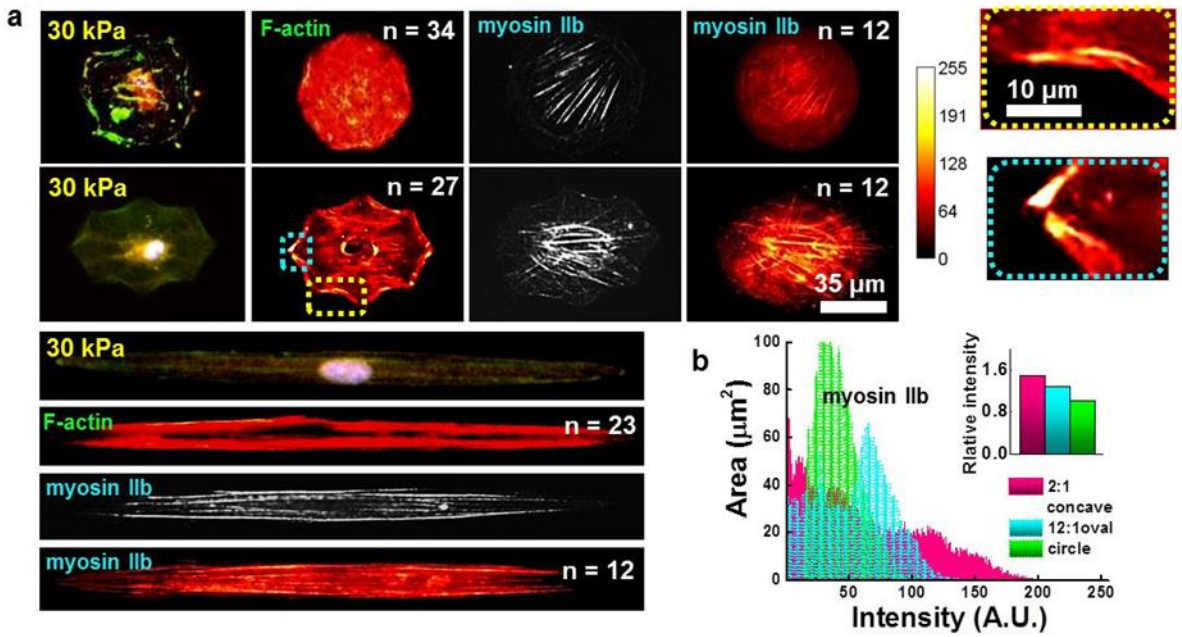

Figure 4.6 Influence of shape on cytoskeleton in mesenchymal stem cells. *a. Representative immunofluorescence microscopy images (F-actin with nuclei, heatmap of F-actin, myosin IIb, and heatmap of myosin IIb) of MSCs cultured in circular, concave, and elongated shapes for 10 days. Blue and yellow images show the regions of highly cytoskeletal tension. b. Comparison of color histogram generated by measuring an area with different intensities for the heatmaps of cells stained for myosin IIb in concave and oval shapes. c. Relative total myosin IIb intensity of the fluorescent heatmaps (12 cells per pattern). The total intensity was calculated by the sum of the product of the area and their intensity. The relative intensity was determined by comparing the total intensity of the concave shaped heatmap to the one of the oval shaped heatmap.*

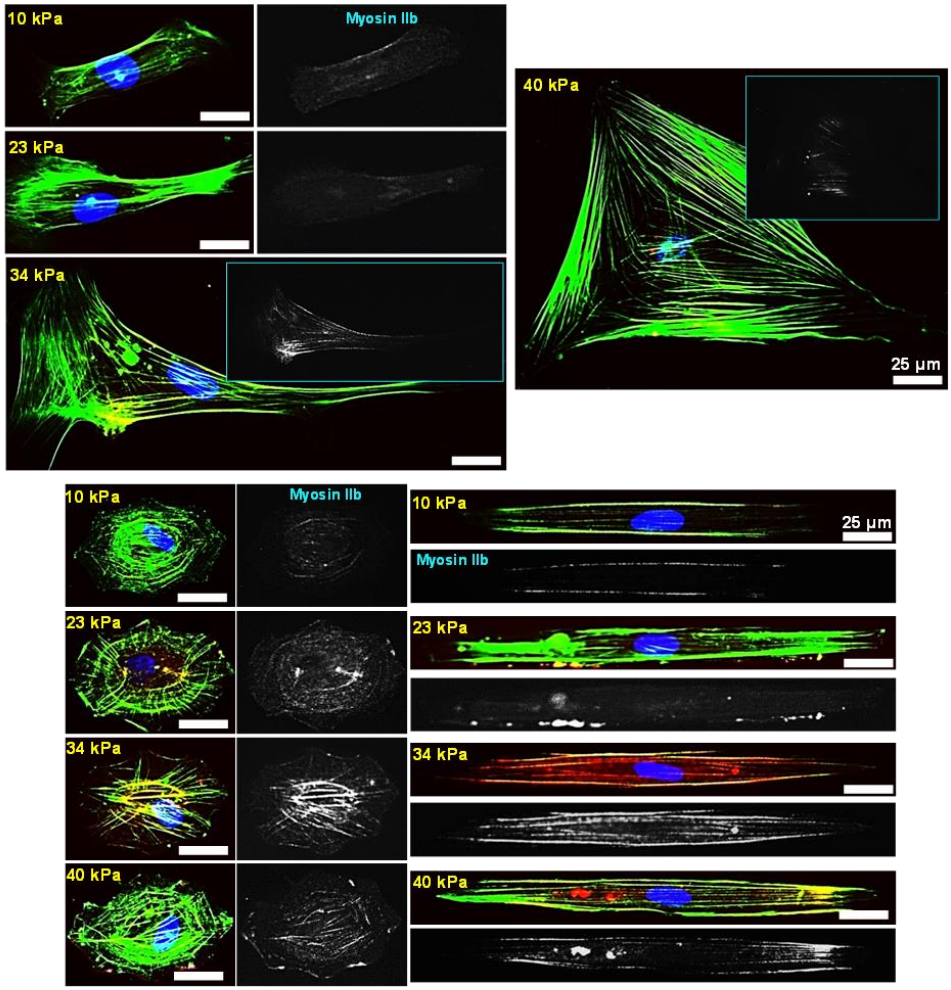

Figure 4.7 Influence of shape on contractility in mesenchymal stem cells. *a. Representative immunofluorescence microscopy images myosin IIb of MSCs cultured in patterns (concave and 2:1 elongated or 12:1 elongated shapes) or unpatterns on 10-40 kPa stiffness of hydrogels for 10 days.*

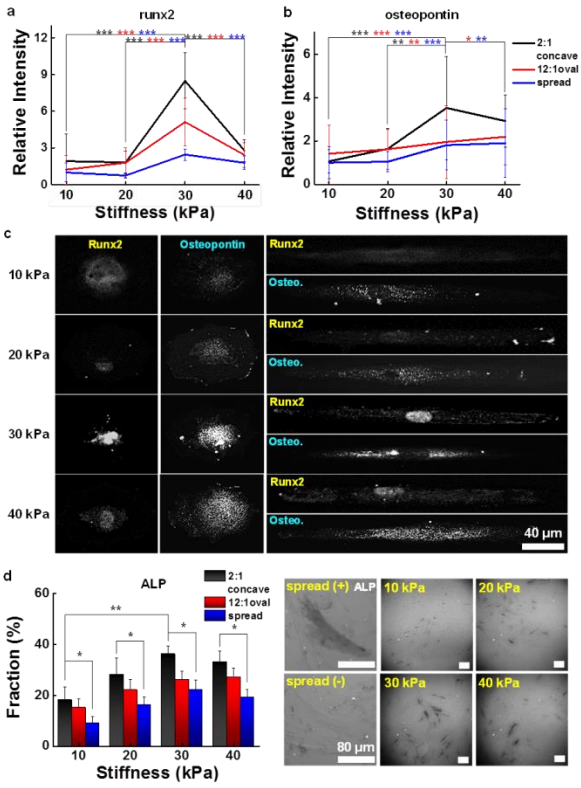

Figure 4.8 Enhanced osteogenesis marker expression in mesenchymal stem cells patterned in contractile geometries. *a. Relative runx2 marker intensity of cells captured on concave or oval shapes or spread on the fibronectin matrix protein, differentiating to osteogenic lineages (***P<0.0005, t-test compared to concave cells on 30 kPa). The relative intensity of the fluorescence was determined by comparing each intensity value to the average intensity of spread cells on 10 kPa. b. Relative osteogenic marker intensity (osteopontin) of cells captured on concave or oval shapes or spread on the fibronectin matrix protein (*P<0.05, **P<0.005, ***P<0.0005, t-test compared to concave cells on 30 kPa). The relative intensity of the fluorescence was determined by comparing each intensity value to the average intensity of spread cells on 10 kPa. c. Representative immunofluorescence microscopy images (Runx2 & Osteopontin) of MSCs cultured in concave or oval shapes for 10 days. d. Percentage of cells captured on concave or oval shapes or spread differentiating to osteoblast lineage. (*P<0.05, **P<0.005, t-test). Representative microscopy images of ALP stained and unstained cells for spread MSCs cultured for 10 days.*

CHAPTER 5

GEOMETRIC GUIDANCE OF INTEGRIN MEDIATED TRACTION STRESS DURING STEM CELL DIFFERENTIATION[5]

5.1 Introduction

Stem cells in their niche are in contact with the extracellular matrix (ECM) which provides multiple structural and biochemical cues to direct their behavior (24, 111–117). Cells adhere to the ECM through several different cell surface receptors including integrins which are involved in mechanosensing and bi-directional transmission of mechanical force (118). This interaction allows cells to sense and respond to their microenvironment via contractile forces and to adaptively remodel tissues with dynamic mechanical forces, guiding broad aspects of their functions such as cell migration, growth, differentiation, and survival (2, 18, 21, 105, 119, 120). For this reason, the careful design of the cellular recognition interface on deformable biomaterials is a critical aspect for the regulation of distinct stem cell functions.

MSCs interact with extracellular matrix proteins though various integrins including α1-6, αV, α11, αX, β1-4, and β7-8 (21, 119). Combinations of two different chains, integrin α and β subunits, define the surface receptors that recognize ECM proteins such as: fibronectin, vitronectin, collagen, and laminin (121, 122). These integrin

---

[5]This chapter is adapted from the following publication:
Junmin Lee, Amr A. Abdeen, Xin Tang, Taher A. Saif, and Kristopher A. Kilian, Geometric guidance of integrin mediated traction stress during stem cell differentiation, Biomaterials, 2015, 69, 174-183

transmembrane receptors act as mechanosensors and mechanotransducers to connect the actin cytoskeleton to the ECM and enable dynamic interactions with the microenvironment through focal adhesions. For example, MSCs primarily bind to fibronectin through the common integrin heterodimers α5β1 or αVβ3 (123). A previous report showed that α5 integrin expression in MSCs was elevated during osteogenic differentiation while cells expressed higher level of α6 integrin during adipogenic lineage specification at 7 days (21). The surface geometry and local biochemical microenvironment of biomaterials have been shown to influence focal adhesions, cytoskeletal tension and differentiation in adherent MSCs (38). However, the relationship between integrin mediated traction stress and MSC differentiation has not been described.

In this chapter 5 we show how control of cell shape can be used to study the relationship between focal adhesion, traction stress, and the differentiation of single mesenchymal stem cells. We use immunofluorescence staining to investigate the protein expression of key markers during osteogenesis and myogenesis. Traction stress measurements are employed to access the force generated by MSCs with different combinations of these cues. We show through immunofluorescence that the expression of early and late osteogenic markers is dependent on the engagement of α5β1 and αVβ3 integrins.

5.2 Materials and Methods

General materials and methods are given in Appendix A.

Materials:

Rabbit anti-Runx2 (ab23981) and anti-Osteopontin (ab8448) were purchased from Abcam. Mouse anti-MyoD (MAB3878) Mouse anti-α5β1 (MAB1969) and αVβ3 (MAB1976Z) were purchased from Millipore. Blebbistatin, Y-27632, FR180204 (ERK inhibitor), SP600125 (JNK inhibitor), and SB202190 (p38 inhibitor) were purchased from Calbiochem.

Immunocytochemistry and histology:

To stain for alkaline phosphatase, surfaces were rinsed with distilled water and incubated for 30 min in BCIP/NBT solution, rinsed well in PBS and imaged in bright field using a Motic trinocular inverted microscope. All experiments were repeated at least three times. Only single cells that were captured in patterns were used in the analysis. The relative intensity of the fluorescence was determined by comparing each intensity value to the average intensity of one condition. The intensity value for single cells was obtained from nuclei (Runx2 and MyoD) or cytoplasmic (Osteopontin) staining intensity minus backgrounds.

Traction stress measurement:

Polyacrylamide gels with desired stiffness (10 and 30 kPa) were fabricated on a glass cover slip (15 mm). To obtain fluorescent bead-infused gels, the polyacrylamide solution was mixed with a 1 μm-bead suspension (Invitrogen, F-8821) at 1:250 and a small amount (1~2 μl) was applied to gel solutions. Upon the placement of the gel surface faced down, beads in a single layer at the same focal plane where imaged using a fluorescent microscope. Matrix proteins were patterned as described above. An Olympus IX81 fluorescent microscope and 20x objective

was used to obtain the live cell images (124). Throughout the experiment, temperature and carbon dioxide levels were maintained at 37°C and 5% respectively. Live cell images on gels embedded with fluorescent beads were captured. Bright field images were firstly taken of the cells to visualize cell shape and location, and then fluorescent images of beads were taken. In order to assess the displacement of beads under the null-force condition, cells were removed from the surface using sodium dodecyl sulfate (SDS, Fisher Inc.), resulting in the gel returning to its relaxed initial state without cells. To characterize the gel displacements, the images before and after cell removal were analyzed using Matlab digital image correlation programs published in (124) to obtain the 2D displacement field (ux, uy). The resolution of the algorithm is 1/10 of pixel size, i.e. ~ 33 nm, and signal-to-noise ratio reaches 40. The detailed procedures of cell traction computation using finite element method can be found in a previous report (124). In brief, our computation employed a mixed boundary condition model, by prescribing zero traction at all nodes outside the cell (Fx=Fy=Fz=0) and the obtained 2D displacement field (ux, uy) as well as Fz=0 at the nodes within the cell boundaries. We did not measure uz during the experiments. Our theoretical derivation suggests that for elastic biomaterial substrates with Poisson's ratio close to 0.5, such as PA gels, prescribing Fz=0 for all surface nodes results in an error of less than 2% in the calculation of in-plane forces Fx and Fy (124).

RNA isolation and RT-PCR:

Adherent cells were lysed directly in TRIZOL reagent (Invitrogen). Chloroform extraction and ethanol precipitation were employed to isolate total RNA. Total RNA

was reverse transcribed using Superscript III® First Strand Synthesis System for RT-PCR (Invitrogen). RT-PCR was achieved linearly by cycle number for each primer set using SYBR® Green Real-Time PCR Master Mix (Invitrogen) on an Eppendorf Realplex 4S Real-time PCR system. Primer sequences were as follows: α1–CTC CTCACTGTTGTTCTACGCT and ATCCAAACATGTCTTCCACCG, α3–CCCACCTGGTGTGACTTCTT and TCCCTGGAGGTGGGTAGC, α5–TGCCGAGTTCACCAAGACTG and TGCAATCTGCTCCTGAGTGG, αv–CATCTTAATGTTGTGCCGGATGT and TCCTTCCACAATCCCAGGCT, α6–CAACTTGGACACTCGGGAGG and ACGAGCAACAGCCGCTT, ß1–CCGCGCGGAAAAGATGAATTT and AGCAAACACACAGCAAACTGA, ß3–TTGGAGACACGGTGAGCTTC and GCCCACGGGCTTTATGGTAA, GAPDH–TGCCTCGATGGGTGGAGT and GCCCAATACGACCAAATCAGA. All reactions were performed linearly by cycle number for each set of primers.

Inhibition assays:

Inhibitors were added to cell culture media at the following concentrations before and after cell seeding and with each media change: Blebbistatin (1 μM) and Y-27632 (2 μM) (Calbiochem). Integrin blocking antibodies (α5β1 and αvβ3) were added to cells in media prior to deposition at 1 μg/mL. MAP kinase inhibition was performed by adding supplemented media of the following molecules at 6 μM after cell seeding and with each media change: FR180204 (ERK1/2), SP600125 (JNK), and SB202190 (p38).

Statistical analysis:

Error bars represent standard deviation and N value is the number of experimental replicates. For statistical analysis one-way ANOVA for comparing multiple groups and two-tailed p-values from unpaired t-test for comparing two groups were employed and values of $P < 0.05$ were considered statistically significant.

5.3 Results

Single cell patterning with adhesive proteins on polyacrylamide hydrogels of different stiffness

We used microcontact printing of adhesive proteins (fibronectin, laminin and collagen) on polyacrylamide (PAAm) hydrogels as a flexible platform to investigate the combinatorial effects of substrate elasticity, matrix composition and cell shape in controlling osteogenesis and myogenesis on protein-coated hydrogels (Fig. 5.1a). Polydimethylsiloxane (PDMS) stamps were fabricated using photolithography and used to pattern adhesive islands of proteins on the surface of chemically modified hydrogels. We employed two different shapes of identical area for patterning the hydrogels, one a simple circle and one approximating a star, where the cell body is expected to span non-adhesive regions (38). PAAm hydrogels with a range of stiffness (10 to 40 kPa) were prepared as previously reported (76). This range of stiffness is physiologically relevant with 10 and 30 kPa stiffness mimicking the rigidity of muscle or pre-calcified bone tissue, respectively (28). The surfaces of PAAm gels were chemically modified with hydrazine hydrate (13), which allows for covalent immobilization between the treated gel surface and an oxidized glycoprotein solution via microcontact printing. After seeding, the mesenchymal

stem cells (MSCs) attached and conformed to the patterned regions. To explore the influence of cell shape on the distribution of the cytoskeleton, we fixed and stained the patterned cultures for filamentous actin. Figure 5.1b shows actin stains and heatmaps of > 30 cells per shape which demonstrates classical cortical actin pattern for MSCs in circles, while MSCs in a star shape show pentagonally organized regions of actin stress fibers. Morphological analysis reveals that the patterned cells that adhere to the printed area show a comparable size to the defined patterns (5000 μm^2) (Fig. 5.1c). Patterned cells stayed viable and maintained adhesion to the islands for 10 days in culture, but a higher number of cells on stiffer substrates and patterns with higher actomyosin contractility escaped from geometric confinement and proliferated (Fig. 5.1d).

The influence of cell shape, matrix stiffness and composition during mesenchymal stem cell differentiation

First we investigated osteogenic and myogenic marker expressions of MSCs cultured in the different shapes on fibronectin-coated hydrogels of varying stiffness (~10 to 40 kPa). We used three different osteogenic markers (Runx2 and ALP as early osteogenic markers; Osteopontin as a late osteogenic marker) and a myogenic marker (MyoD) to compare the degree of osteogenesis and myogenesis specification depending on matrix stiffness and cell shape after 10 days in culture (Fig. 5.2). Cells cultured on substrates with different stiffness express markers associated with osteogenesis and myogenesis in a stiffness dependent manner with a maximum at ~30 to 40 kPa. In addition, cells in star shapes show higher levels of osteogenic and myogenic marker expressions compared to those cultured in circular

shapes. We also explored alternative shapes previously shown to influence actomyosin contractility: oval shapes with different aspect ratios (1:1, 2:1, 4:1, 8:1, and 12:1, 5000 μm^2) (Fig. 5.3). Similar to cells on circle and star shapes, those on shapes that promote higher contractility express higher levels of osteogenic markers. Next we patterned our two shapes using different matrix proteins (fibronectin, laminin and collagen) across surfaces with different stiffness to explore how these cues influence lineage specification when presented in combination (Fig. 5.4). We used representative osteogenic (Runx2) and myogenic (MyoD) transcription factors to assess early differentiation to these lineages. Cells cultured on fibronectin or collagen matrices show increased Runx2 expression as substrate stiffness is increased, while MSCs cultured on laminin did not show a trend in differentiation on account of substrate stiffness. In contrast, MSC myogenesis was shown to be sensitive to substrate stiffness across all matrices. Changing the geometry of single MSCs from a circular shape to that approximating a star led to increased expression of Runx2 (fibronectin and collagen) and MyoD (fibronectin). However, similar to stiffness the shape of single cells on laminin did not influence osteogenesis.

The role of biophysical and biochemical parameters in guiding mesenchymal stem cell traction stress

Micropatterning single cells allows precise control over adhesive structures, and we postulated that the way in which MSCs deform their matrices would be influenced by shape, stiffness and protein composition. First, to explore the relationship between substrate mechanics, adhesion and differentiation, we measured the

traction stress exerted by circular and star-shaped MSCs on hydrogels of two different stiffness (10 and 30 kPa), across three different matrix proteins (fibronectin, laminin, and collagen) (Fig. 5.5). We observed that cells on star shapes on fibronectin matrix showed higher traction stress than those on laminin (2.5-fold on 10 kPa; 7.2-fold on 30 kPa) or on collagen (4.3-fold on 10 kPa; 10.3-fold on 30 kPa). For the same shape and adhesive proteins, matrix stiffness gave rise to different levels of traction stresses; star shaped cells on fibronectin coated 30 kPa substrates displayed 3.2-fold higher traction stresses than those on 10 kPa gels. In addition, MSCs tended to exert higher traction when they were cultured in star geometries on fibronectin matrix (6.4-fold or 7.5-fold higher than circular cells on 10 or 30 kPa, respectively). However, traction exerted by cells on laminin substrates displayed no significant difference (within the limitations of small sample size) even when cultured on different stiffness or in the contractile star geometry. While stiffness influenced the MSCs' ability to exert traction on collagen coated gels, there was no discernible influence of cell shape.

The expression of integrin receptors in response to cell geometry and matrix stiffness

Since MSCs cultured on fibronectin show clear differences in both differentiation and traction stress as a function of matrix stiffness and cell shape, we analyzed the expression of common integrin receptors involved in fibronectin recognition. Cells were cultured for 1 day on matrices of different stiffness (10 or 30 kPa) and in different geometries (circle or star shape) followed by lysis, RNA isolation and RT-PCR. Interestingly, MSCs cultured in the star shape show higher expression than

MSCs cultured in circular shapes on both 10 kPa hydrogels (2.3-fold α1, 3.1-fold α3, 2.1-fold α5, 73-fold αv, 3.3-fold α6, 2.1-fold ß1, 5.5-fold ß3; Fig. 5.6) and 30 kPa (1.2-fold α1, 2.7-fold α3, 2.7-fold α5, 261.3-fold αv, 2.5-fold α6, 2.1-fold ß1, and 2.6-fold ß3; Fig. 5.7). In general integrin expression is higher for cells cultured in the star shape, but in particular integrin αv shows an enormous increase in expression for culture in the star geometry compared to the circle in both 10 and 30 kPa fibronectin conjugated hydrogels.

To further verify the observed trends in integrin expression, we performed immunofluorescence staining of a focal adhesion marker (Paxillin) and two major integrin receptors in fibronectin (α5ß1 and αvß3) (Fig. 5.8 and 5.9). Protein expression by immunofluorescence showed the same trend as the RT-PCR study: higher levels of focal adhesion and integrin expression for MSCs cultured in star shapes compared to those in circular shapes. Since we cultured MSCs for 10 days to study lineage specification and differentiation, we also measured paxillin, α5ß1, and αvß3 at day 10. Similar to cells cultured for 1 day, MSCs cultured for 10 days on star shaped fibronectin substrates displayed higher levels of focal adhesion proteins and integrin receptors.

Blocking integrin receptors and downstream signaling during differentiation of mesenchymal stem cells

MSCs cultured in star shapes show enhanced traction stress, integrin expression, and lineage specification to both osteogenesis and myogenesis programs. To elucidate signal transduction pathways that are involved in linking extracellular

recognition to differentiation, we treated our patterned cultures with mitogen activated protein kinase (MAPK) inhibitors (p38, ERK1/2, and JNK), the Rho-associated kinase inhibitor Y-27632, the non-muscle myosin inhibitor blebbistatin, and integrin blocking antibodies for α5ß1 and αvß3. MSCs were cultured in 5000 μm^2 star geometries with or without 6 μM p38, ERK1/2, and JNK, 2 mM Y-27632, 1 mM blebbistatin, or 1 μg/mL anti-α5ß1 and anti-αvß3 for 10 days. We employed early (Runx2) and late (Osteopontin) osteogenic markers to investigate the effects of inhibitors on different stages of differentiation (Fig. 5.10). The expression of Runx2 shows a modest decrease after treatment with pharmacological inhibitors and blocking antibodies; however, the later marker Ostopontin shows a decreases on account of both blocking integrins and inhibiting downstream signal transduction players. Blocking integrin α5ß1 in particular shows decreased expression of both Runx2 and Osteopontin, which suggests that signaling through this integrin plays a significant role during osteogenesis on these matrices.

5.4 Discussion

Cell surface integrin receptors sense the biophysical and biochemical properties of the extracellular matrix, convey this information to the interior of the cell, and regulate gene expression during stem cell differentiation (21, 119). While the bulk mechanics of the extracellular matrix (ECM) clearly plays a role during lineage specification of stem cells on deformable substrates (22, 28, 87), the identity of the tethered protein will influence the way in which integrin receptors can exert force on the matrix, establish focal adhesions, and transduce this mechanical and biochemical information to the nucleus (27). Discerning the relationship between

integrin mediated traction, focal adhesion, and the mechanochemical signals that direct stem cell differentiation will prove useful for informing the design of the biomaterials interface.

To parse out the relative roles of biophysical and biochemical cues during MSC differentiation, we employed polyacrylamide hydrogels of four stiffness (10 to 40 kPa), three different conjugated matrix proteins (fibronectin, laminin, and collagen I), and two distinct single cell shapes of the same area, but with different geometric cues for guiding subcellular structures (circle and star). In general, cells on stiffer substrates tend to express higher levels of osteogenesis markers. However, when other microenvironment cues are considered, e.g. tethered matrix proteins or control of single cell shapes, our data suggest that the trend in lineage specification can be tuned. For instance, cells on laminin coated surfaces show very little change in osteogenic marker expression regardless of stiffness and geometry. Round cells show similar expression levels of osteogenic markers while cells on star shapes—which coordinate focal adhesion and formation of stress fibers—tend to express higher levels in a stiffness dependent manner. These results show osteogenic differentiation can be modulated with specific combinations of these cues. In contrast, the degree of myogenesis gene expression depends less on single cell geometry and more on stiffness and matrix proteins

Cells in vivo exert a 3D tensional homeostasis which controls diverse biological activities including stem cell differentiation (37, 125). Focal adhesions function as one of the intermediators of tension between cells and the ECM (28, 38). As cells exert traction stresses on deformable matrices, focal adhesions are reinforced and

there have been several reports that size, density and turnover of focal adhesions influence differentiation (23, 126). As cells were cultured on our patterned matrices that differentially affect lineage outcome, we employed traction force microscopy (TFM) to determine the tractions exerted by MSCs by obtaining measurements of the micro-bead displacement within PAAm hydrogels (124). MSCs cultured on fibronectin matrices were able to exert higher traction stress than cells adherent to laminin or collagen. This is consistent with previous reports that demonstrate a higher prevalence of fibronectin-binding integrins expressed in MSCs compared to those associated with laminin or collagen (127). Furthermore, increasing cell perimeter by changing the geometry from a circle to a star leads to enhanced traction on fibronectin. In contrast, the traction exerted by MSCs on laminin and collagen matrices was not altered significantly as stiffness or cell geometry was changed. Coupled with the differentiation results, this study suggests that the ability of MSCs to exert traction through robust focal adhesions on fibronectin can guide the osteogenesis and myogenesis programs.

MSCs express multiple types of integrins involved in adhesion to fibronectin, and we found that cells cultured in star shapes showed higher expression of all integrins analyzed including α1, α3, α5, αv, α6, ß1, and ß3, irrespective of matrix stiffness. Remarkably, expression of integrin αv was 73-fold and 261-fold higher for cells cultured in star shapes on 10 kPa and 30 kPa hydrogels respectively. The enhancement in αv expression with changes in cell shape may be related to geometric guidance of adhesion structures and force transmission to modulate outcome through mechanotransduction (128–130). Immunostaining MSCs in circle

and star shapes for integrin α5ß1 and αvß3 demonstrates an increase in expression at the protein level for both integrins. Therefore we propose that both α5ß1 and αvß3 are likely involved in in vitro focal adhesion formation, traction generation and regulation of differentiation for MSCs cultured on deformable matrices.

To evaluate the role of these integrins in mediating differentiation, we added blocking antibodies to the cell culture media. While inhibition of αvß3 leads to a slight decrease in early osteogenesis marker expression (Runx2), inhibition of α5ß1 shows a large decrease in both early (Runx2) and late (osteopontin) marker expression. Integrins are known to be involved in stem cell lineage specification. For example, integrin α5 promotes osteogenic differentiation of MSCs (21, 131). Integrin α5 was up-regulated during osteogenesis and down-regulated with shRNAs inhibiting osteogenic differentiation, and the osteogenic differentiation enhanced by integrin α5 was related to the focal adhesion kinase/ERK1/2-MAPKs and PI3K signaling pathways (131). Roca-Cusachs et al. reported that two main fibronectin receptors, α5ß1 and αvß3, play a different role in cell adhesion (132). Adhesion strength was dependent on the clustering of integrin α5ß1 while αvß3, which is less stable, mediates mechanotransduction and integrin-cytoskeleton interactions. This result is in line with our data for MSCs with different shapes on fibronectin; cells on star shapes showed higher levels of these integrins and accordingly higher traction stresses and osteogenic outcomes than those on circular shapes. We speculate that both integrins are involved in adhesion, but with disparate roles: αvß3 in mediating focal adhesion assembly through bi-directional force transmission, and α5ß1 in regulating the differentiation program through mechanotransduction. Adding

pharmacological inhibitors of downstream effectors of integrin signaling, including Rho-associated protein kinase, non-muscle myosins, and extracellular related MAP kinases p38, ERK 1 and 2, and c-Jun N-termina kinases, all show some decrease in osteogenesis markers. However, not to the same degree as to when initial adhesion via α5ß1 is perturbed.

5.5 Conclusion

Using micropatterning we can precisely control the shape of single cells, thereby allowing the subcellular adhesive and contractile elements to be modulated. Using this strategy we show how matrix mechanics and adhesive protein composition can influence the way in which MSCs exert traction stresses during differentiation in response to deformable matrices. In particular, MSCs cultured on fibronectin modified hydrogels of increasing stiffness display higher levels of traction, increased expression of integrin receptors, and an increased propensity to differentiate, when they are in geometries that promote enhanced focal adhesion and a contractile cytoskeleton. Using integrin blocking antibodies and pharmacological inhibitors of downstream effectors, we demonstrate that MSCs adhere and deform the fibronectin conjugate matrices through both αvß3 and α5ß1 integrins; however, osteogenesis is directed primarily through integrin α5ß1. By careful control of multiple biochemical and biophysical parameters, the relationship between integrin mediated adhesion, deformation of the extracellular matrix, and regulation of distinct differentiation programs can be discerned, and may find broad applicability across a range of cell systems.

5.6 Figures

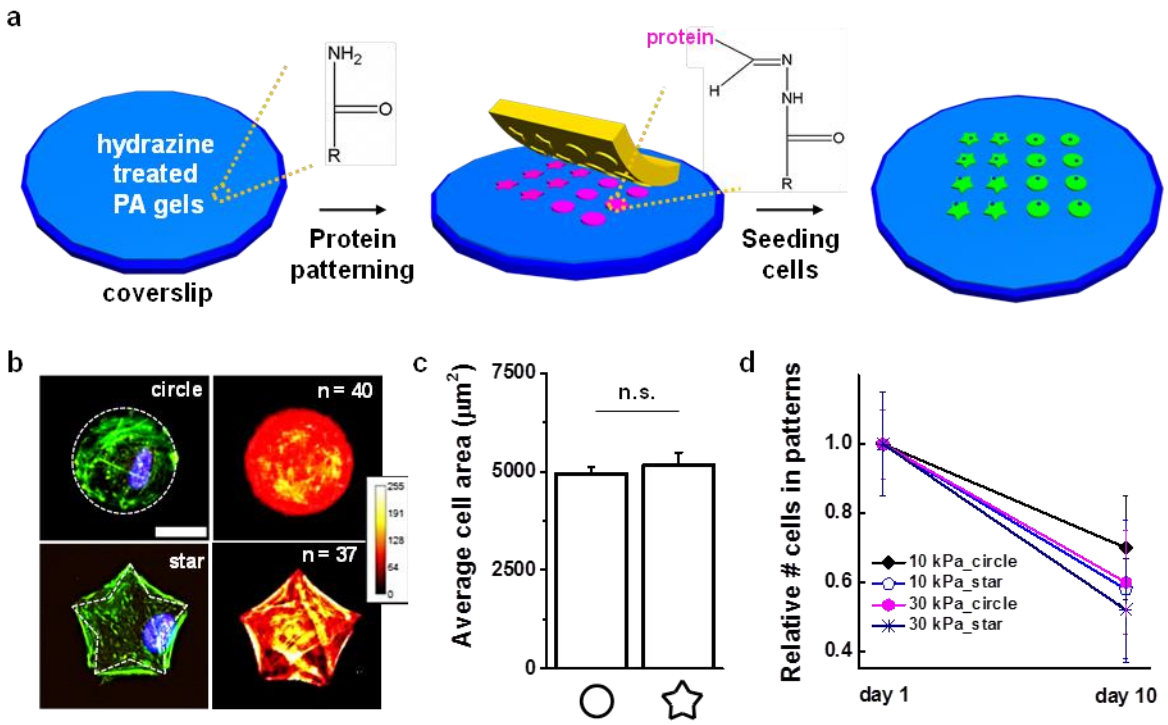

Figure 5.1 Single cell patterning on hydrogels can be achieved by protein immobilization with hydrazine hydrate chemistry. *(a) Schematic of the procedure for patterning cells on polyacrylamide hydrogels. (b) Representative immunofluorescence microscopy images and heat maps of MSCs on circle and star shapes. Staining for MSC nuclei (blue), actin (cyan-green). Scale bar is 40 μm. (c) MSC area on patterned protein-coated hydrogels after 10days. (d) Relative number of cells in patterns after 10 days.*

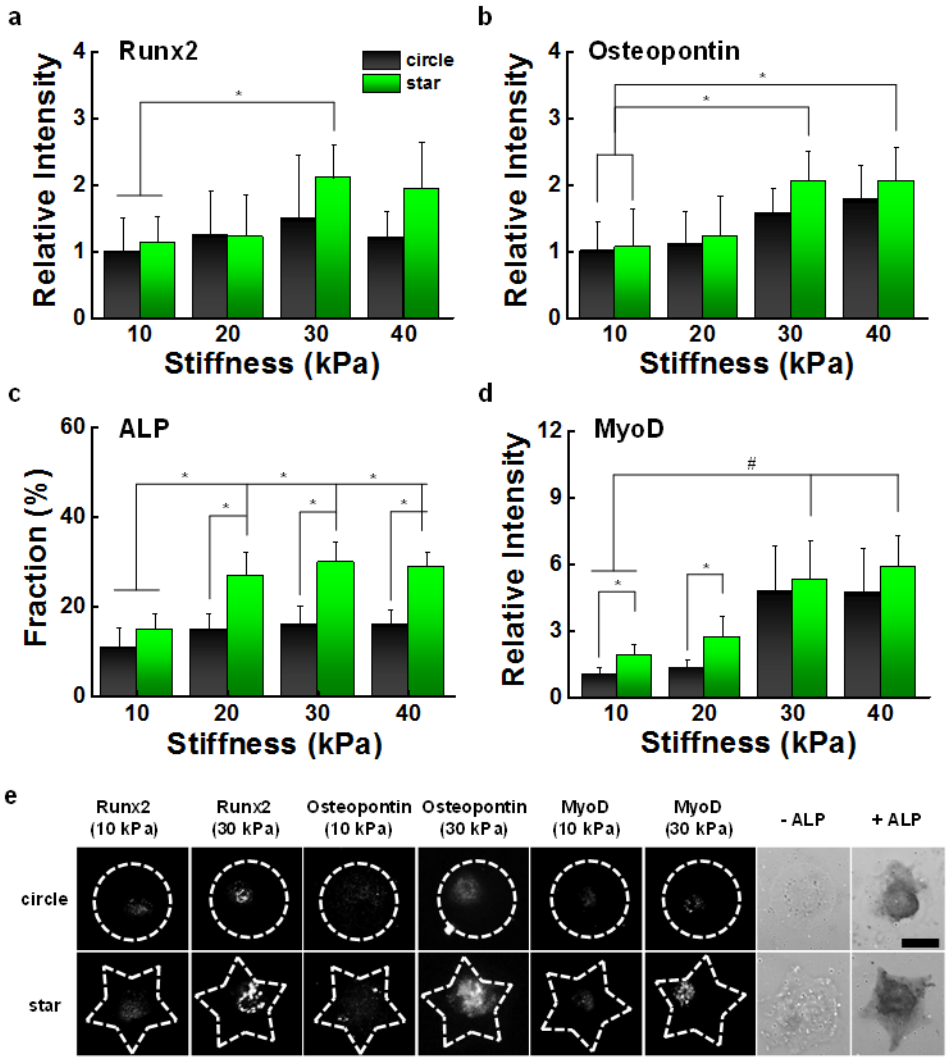

Figure 5.2 Combinations of matrix stiffness and geometric features guide osteogenesis and myogenesis. *Expression of osteogenic (a)-(c) and myogenic (d) markers for cells adherent to the circle or star shape patterned fibronectin coated substrates demonstrating how combinations of matrix stiffness and geometric features influence differentiation. (e) Immunofluorescence image of MSCs stained with Runx2, Osteopontin, ALP, or MyoD. Scale bar is 40 μm. Error bars are standard deviations (N=4). (*P < 0.05 and #P < 0.01, one-way ANOVA)*

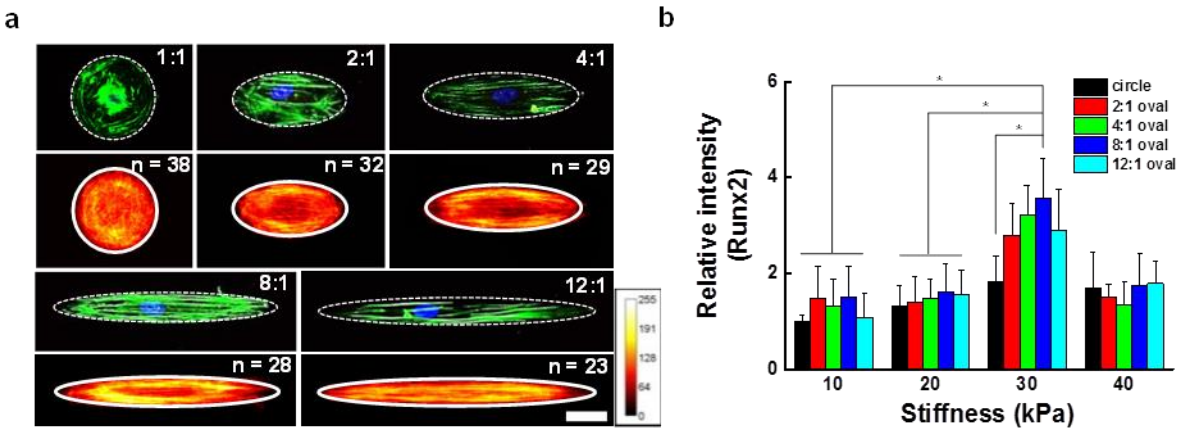

Figure 5.3 Geometric cues with different levels of contractility promote osteogenic lineage specification of MSCs. *(a) Representative immunofluorescence microscopy images and heat maps of MSCs on oval shapes with different aspect ratio (5000 μm^2). (b) Expression of Runx2 for cells adherent to the oval shapes with different aspect ratio patterned fibronectin coated substrates demonstrating how cell contractility caused by geometric features influence osteogenic differentiation. Scale bar is 40 μm. Error bars are standard deviations (N=3). (*P < 0.05, one-way ANOVA).*

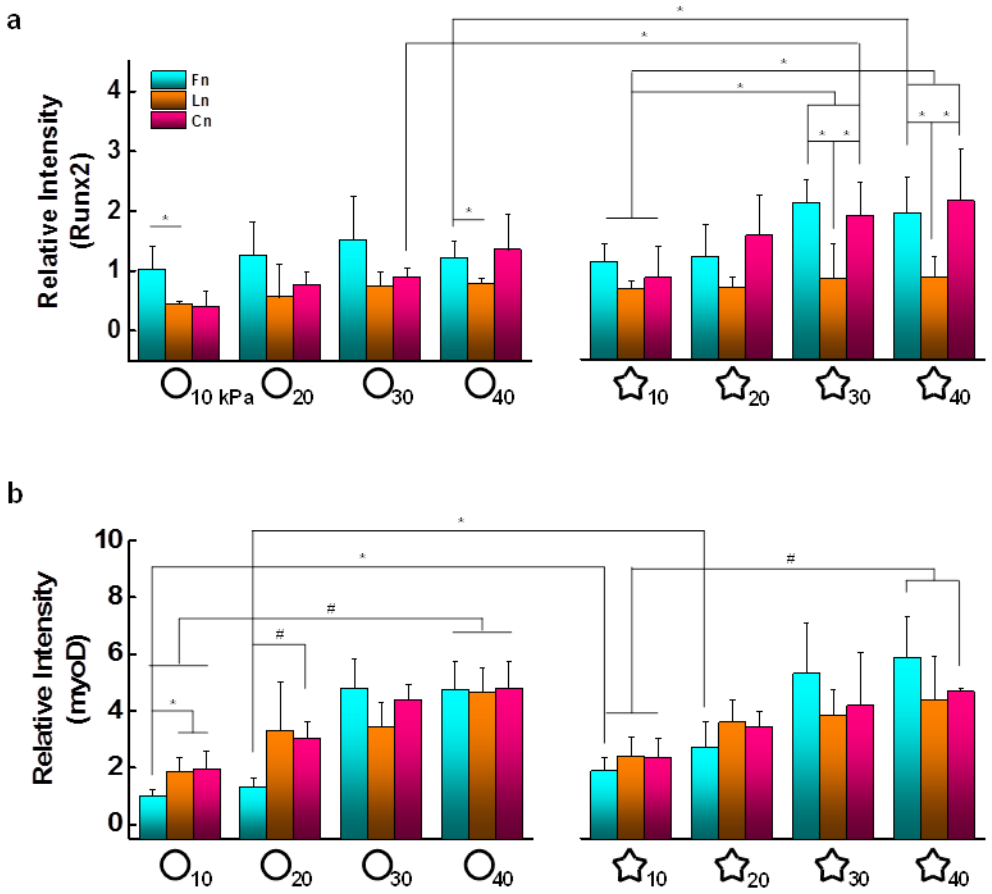

Figure 5.4 Cell shape, matrix elasticity, and composition all influence differentiation. *Quantitation of (a) Runx2 and (b) MyoD markers for patterned cells cultured on different adhesive proteins coated substrates with tunable stiffness for 10 days. Error bars are standard deviations (N=4). (*P < 0.05 and #P < 0.01, one-way ANOVA).*

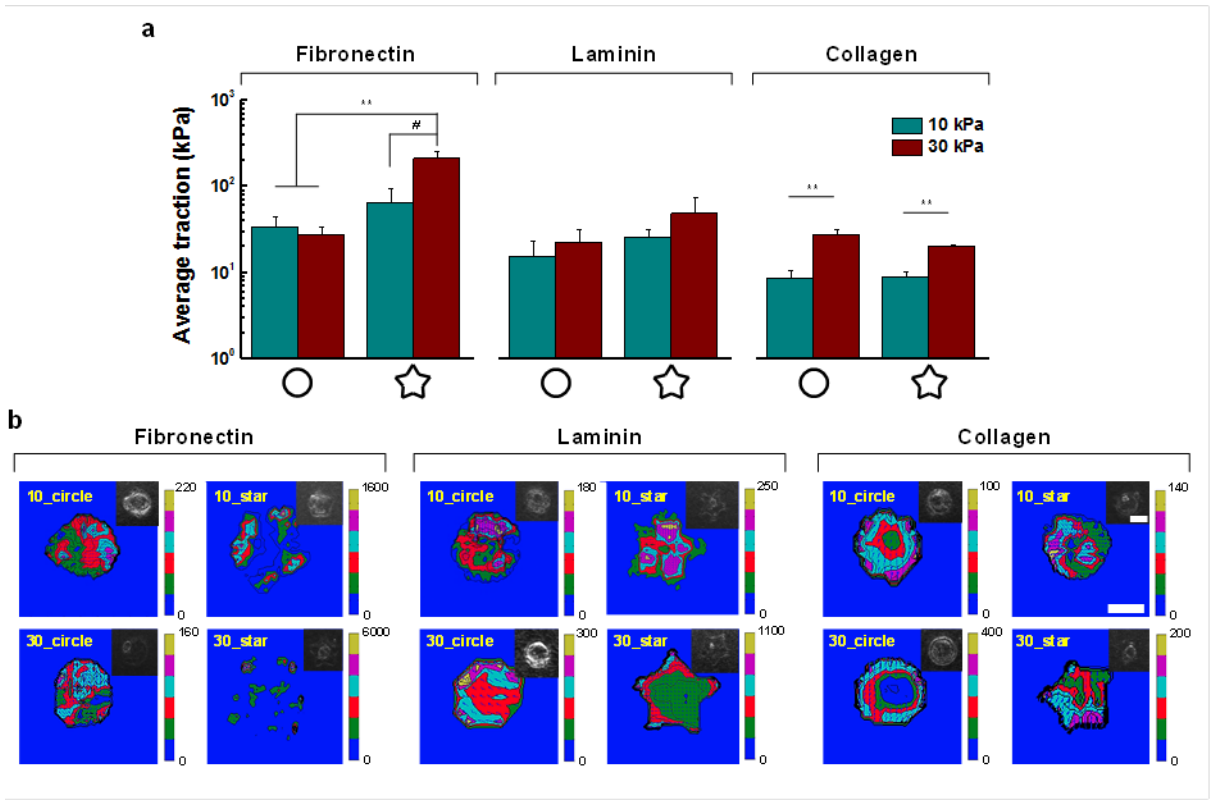

Figure 5.5 Traction stress exerted by MSCs is influenced by combinations of biophysical and biochemical cues. *(a) Average cellular traction stress for MSCs after 1 day of culture. (b) Representative traction map and phase-contrast image (inserted) of MSCs cultured for 1 day. The cells were cultured on combinations of matrix stiffness (10 and 30 kPa), cell shape (circle and star), and adhesive protein (fibronectin, laminin, and collagen). Scale bar is 40 μm. Error bars are standard deviations (N=3). (#P < 0.01 and **P < 0.005, one-way ANOVA).*

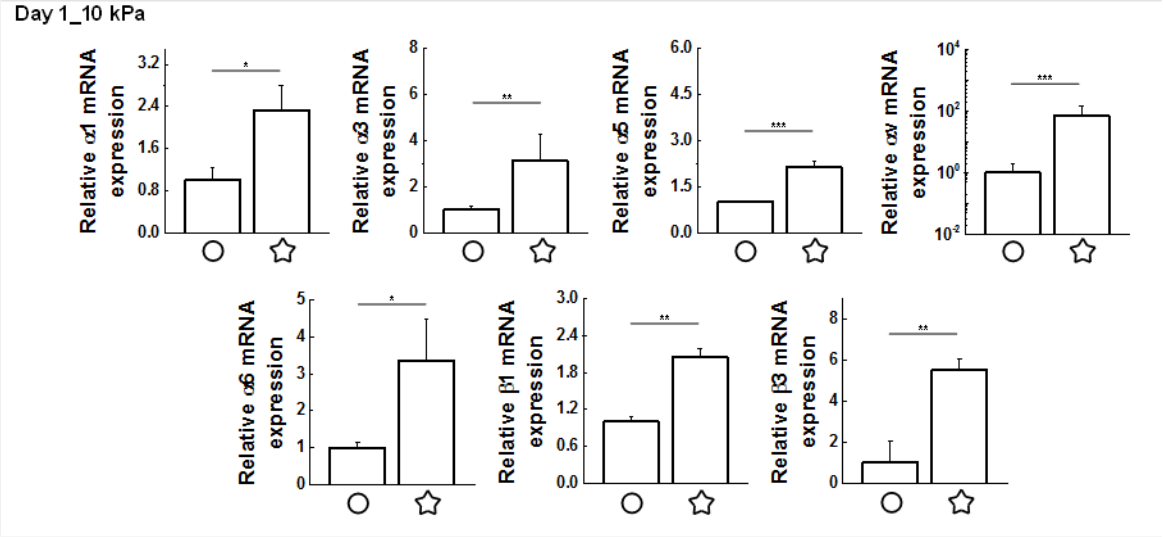

Figure 5.6 Integrin gene expression analysis of patterned mesenchymal stem cells on fibronectin coated 10 kPa substrates. *Results of real-time PCR to measure the gene expression of integrin α1, α3, α5, αv, α6, ß1, and ß3 of MSCs cultured for 1 day Error bars are standard deviations (N=3). (*P < 0.05, **P < 0.005, and ***P < 0.0005, one-way ANOVA).*

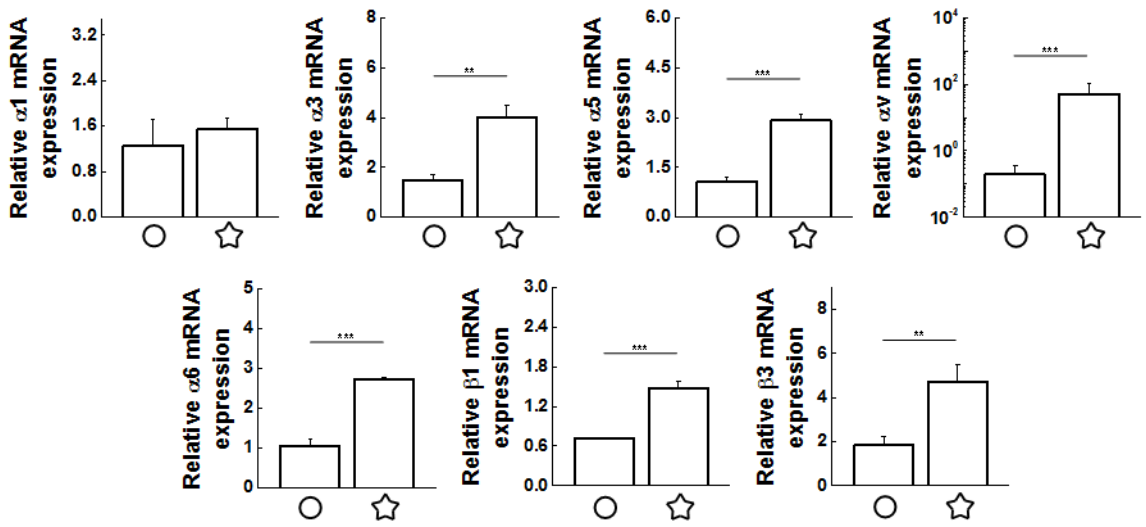

Figure 5.7 Gene expression analysis of integrins for patterned mesenchymal stem cells on fibronectin coated 30 kPa substrates. *Results of real-time PCR to measure the gene expression of integrin α1, α3, α5, αv, α6, ß1, and ß3 of MSCs cultured for 1 day Error bars are standard deviations (N=3). (**P < 0.005 and ***P < 0.0005, one-way ANOVA).*

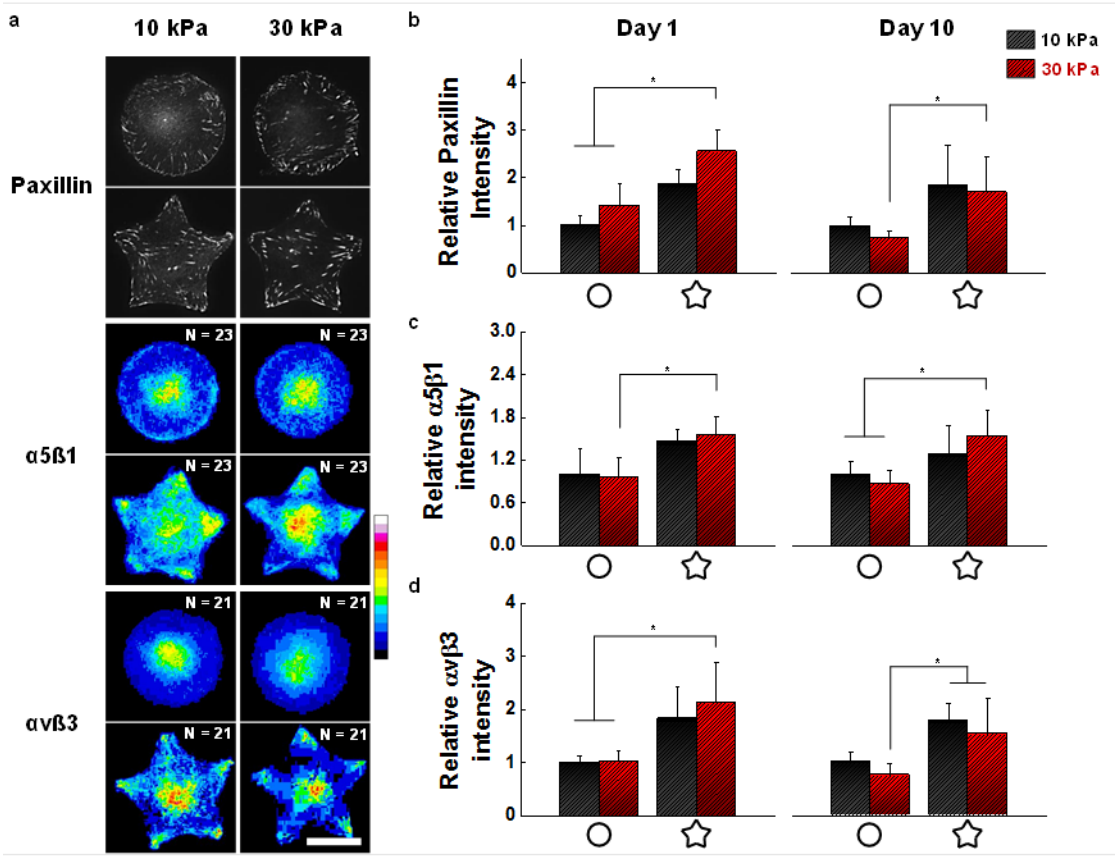

Figure 5.8 Focal adhesion architecture and integrin composition is guided by cell shape and substrate stiffness. *(a) Immunofluorescence image of MSCs cultured for 10 days stained with Paxillin and heat maps of MSCs for integrin α5ß1 and αvß3. Scale bar is 40 μm. (b) Quantitation of Paxillin and integrin α5ß1 and αvß3 markers for patterned cells cultured on fibronectin coated 10 and 30 kPa substrates for 1 and 10 days. Error bars are standard deviations (N=3). (*P < 0.05, one-way ANOVA)*

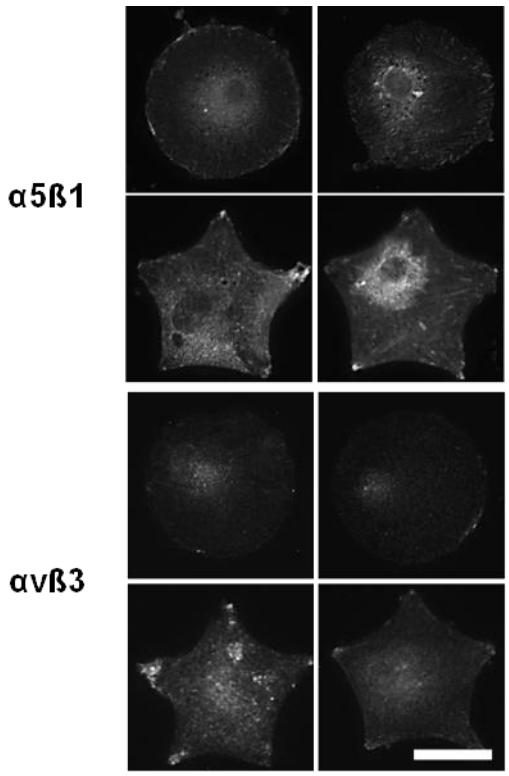

Figure 5.9 Study of integrin receptors in fibronectin. *Immunofluorescence image of MSCs cultured for 10 days stained with integrin α5ß1 and αvß3. Scale bar is 40 μm.*

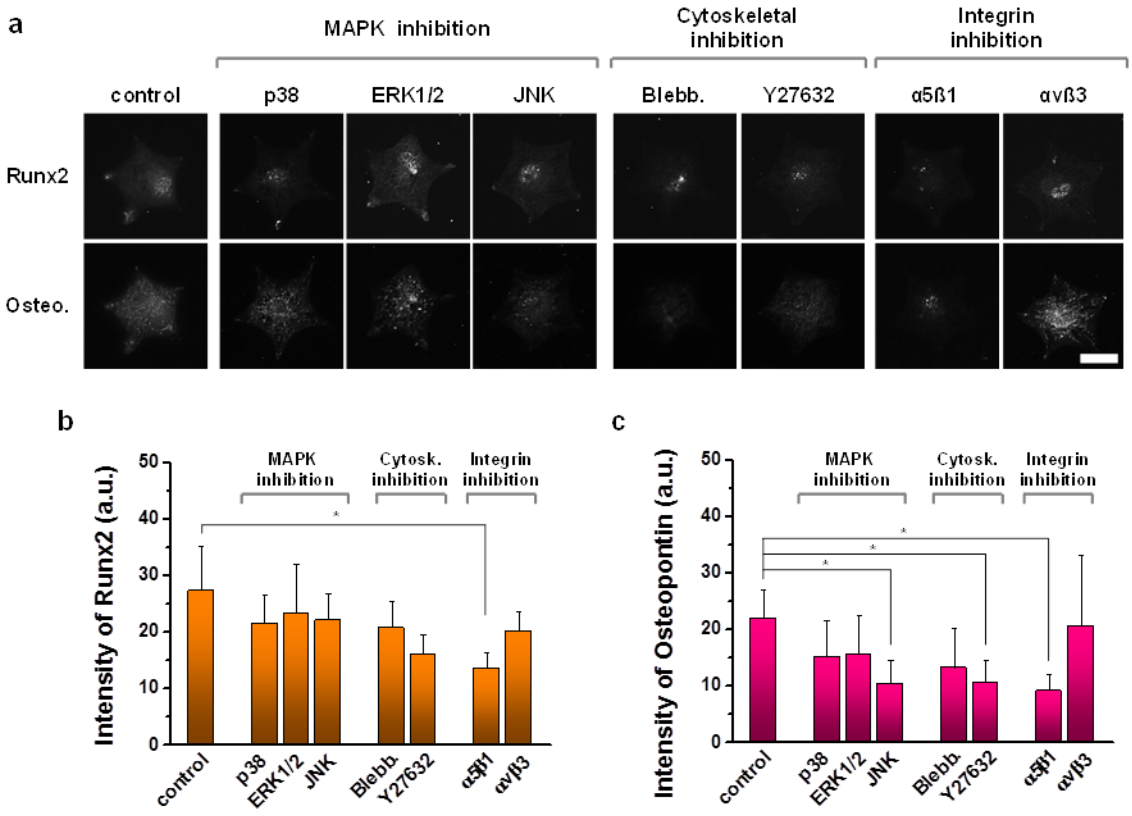

Figure 5.10 Inhibition of integrins and downstream effectors influence differentiation. *(a) Immunofluorescence image of MSCs stained with Runx2 and Osteopontin with or without inhibitors on 30 kPa substrates. Expression of early (Runx2) and late (Osteopontin) osteogenic markers for cells adherent to the star shape of fibronectin patterned substrates displaying how integrin α5ß1 plays a critical role in osteogenic differentiation of MSCs. Scale bar is 40 μm. Error bars are standard deviations (N=3). (*P < 0.05, one-way ANOVA)*

CHAPTER 6

THE INFLUENCE OF BIOPHYSICAL PARAMETERS ON MAINTAINING THE MESENCHYMAL STEM CELL PHENOTYPE[6]

6.1 Introduction

The majority of efforts to control cell programming or reprogramming in the laboratory involve empirically derived media formulations of small molecules and proteins. More recently, the design of synthetic extracellular matrices that convey information from the microenvironment surrounding cells to regulate lineage programs has garnered attention (133, 134). Cells sense their mechanical microenvironment through the interplay of integrin mediated focal adhesions and actomyosin based cellular contractility to direct intracellular signaling programs that regulate cell functions (135–138). This process of mechanotransduction has been shown to play a key role in modulating the lineage specification of MSCs, where the biochemical and biophysical properties of the extracellular matrix are integrated with soluble signals to guide signal transduction cascades that regulate gene expression and cell fate. Model extracellular matrices, where the biochemical and biophysical properties of the cell culture material can be systematically varied, have proved useful in dissecting the importance of microenvironmental signals during cell fate determination (23, 28, 38, 39, 85, 105, 139). For example, human mesenchymal stem cells (MSCs) isolated from bone marrow or adipose tissue, when

[6]This chapter is adapted from the following publication:
Junmin Lee, Amr A. Abdeen, and Kristopher A. Kilian, Rewiring mesenchymal stem cell lineage specification by switching the biophysical microenvironment, Scientific Reports 2014, 4, 5188

cultured on hydrogels of tunable stiffness will specify lineage programs according to native tissue-mimetic stiffness (28, 76, 87, 140). In a report by Gilbert et al., the importance of mechanotransduction in vivo was demonstrated by showing how the engraftment of skeletal muscle stem cells after isolation and expansion is influenced by the stiffness of the in vitro expansion substrate (82). These reports highlight the importance of matrix mechanical properties for in vitro expansion after isolation and when designing a clinically relevant biomaterial.

While most studies aimed at elucidating the biophysical cues that regulate cell fate have involved static in vitro cultures, several recent reports have varied the properties of the substrate during culture (2, 88, 141–143). Burdick and colleagues used an in situ tunable hydrogel system to study how changing matrix stiffness can modulate the degree of adipogenesis and osteogenesis in MSCs exposed to a mixed-media of soluble differentiation cues; increasing the stiffness of a hydrogel earlier will enhance osteogenesis while leaving the gel soft for longer periods promotes adipogenesis (90). Anseth and colleagues used a dynamic softening hydrogel system to explore how the mechanical properties of the substrate are sensed by MSCs and how this information is retained over time (88). They found that the transcriptional activators YAP and TAZ are activated in response to hydrogel stiffness that is reversible after short culture periods; however, after prolonged culture on stiff substrates YAP activation promotes irreversible lineage commitment. This is important because the majority of ex vivo MSC culture is performed on rigid (~GPa) tissue culture plastics, which may adversely affect the multipotency of MSCs (39). Understanding MSC plasticity and the temporal

regulation of lineage specification associated with the biophysical properties of biomaterials—for the canonical lineages and for putative trans-differentiation events—is an important undertaking to define the appropriate conditions to direct differentiation to specific lineages.

In this chapter 6, we use a combination of tunable stiffness hydrogels and single cell micropatterning to explore the plasticity of MSCs when cells are shifted between matrices of very different biophysical properties. Previously it has been shown that MSCs cultured on hydrogel substrates >40 kPa will commit to the osteogenesis lineage while MSCs cultured on hydrogels <1 kPa will express markers associated with trans-differentiation to the neuronal lineage. Here we explore the effect of rigid substrate pre-culture on the expression of neurogenic markers and the effect of soft substrate pre-culture on the expression of osteogenic markers. Monitoring the change in expression of markers associated with distinct stages of lineage commitment reveals reversible expression of early stage markers in response to both substrate stiffness and geometric constraints with less variation in markers associated with mature lineage outcomes.

6.2 Materials and Methods

General materials and methods are given in Appendix A.

Materials

Human MSCs and differentiation media were purchased from Lonza. Rabbit anti-Runx2 was purchased from abcam (ab23981) Technologies, rabbit anti-Osteopontin

was purchased from abcam (ab8448), mouse anti-ß3 tubulin was purchased from Sigma (T8660), and chicken anti-MAP2 was purchased from abcam (ab5392).

Cell culture

For transfer between hydrogels of different stiffness, MSCs cultured for 10 days on 0.5 or 40 kPa substrates were suspended by using 0.25% trypsin and reseeded onto opposite stiffness substrate (0.5 to 40 and 40 to 0.5). After transfer, the cells were cultured for 10 days and media was changed every 3 or 4 days.

Immunocytochemistry

The number of cells measured is over 20 cells per each condition and we confirmed the results three times. We set the threshold exposure time with the condition having lowest intensity among the samples so that we could compare the relative intensities of each condition. The relative intensity of the fluorescence was determined by comparing each intensity value to the average intensity of one condition. Each intensity value was obtained by subtracting actin intensity from nuclei intensity. The absolute value was used for all markers because beta 3 tubulin expression showed mainly on actin instead of nuclei. Cell viability was assessed by using a live/dead (viability/cytotoxicity) staining kit (life technologies) and cell viability was calculated by multiplying % viability before and after mechanical microenvironmental changes.

Statistical analysis

Statistical analysis was performed using one-way ANOVA and student's t-test and values of $p < 0.05$ were considered statistically significant.

6.3 Results

The influence of substrate switching on cell spreading and viability

To explore the influence of stiffness on mesenchymal stem cell (MSC) lineage marker expression, we chose to use polyacrylamide hydrogels which are an established model extracellular matrix (ECM) due to high water content and tunable stiffness by varying the ratio between Acrylamide and Bis-acrylamide. The preparation method is schematically presented in Fig. 6.1a. First, we prepared hydrogels (soft-0.5 kPa and stiff-40 kPa) on glass coverslips and then treated with hydrazine hydrate, modifying the surface chemistry of the gels (76, 87). Subsequently, fibronectin was oxidized and patterned onto the hydrazine treated gels by soft lithography using patterned or unpatterned polydimethylsiloxane (PDMS) stamps. The stiffness of the gels were confirmed using AFM measurements (data not shown). Since matrix stiffness can direct lineage specification of MSCs based on the similarity to the committed cells' native matrix—soft gels (~0.5 kPa) promote the expression of neurogenesis markers and stiff gels (>30 kPa) promote the expression of osteogenesis markers—we asked whether transferring MSCs from a soft to a stiff gel or vice versa would influence the expression of stiffness-directed lineage markers. After culture for 10 days the projected cell area for MSCs were ~4000 μm^2 and ~12000 μm^2 for 0.5 and 40 kPa hydrogel substrates respectively. After trypisinization and transfer between soft and stiff matrices, there were

significant changes in spreading behavior. MSCs that were transferred to stiff substrates after 10 days of culture on soft substrates showed an increase in spread area from ~4000 to ~7000 μm^2 (5 days after transfer) and ~10000 μm^2 (10 days after transfer). MSCs that were transferred to soft substrates after 10 days of culture on stiff substrates showed a reduction in cell area from 12000 to ~8000 μm^2 (5 days after transfer) and ~6000 μm^2 (10 days after transfer) (Fig. 6.2a and b). The final spread area after 10 days from switching was comparable to MSCs cultured on the same stiffness gels without transfer. This suggests that MSC spreading characteristics can recover in response to new mechanical microenvironments. We performed a cell viability assessment before and after the substrate switch (Fig. 6.1c and d). Cells cultured on stiff substrates displayed higher viability than those cultured in soft substrates. In addition, cell viability decreased when cells were transferred to substrate of opposite stiffness (e.g. soft to stiff and stiff to soft) compared to cells cultured with no environment change. Interestingly, cell viability after transfer depended on the mechanics of the final substrate where viability decreased by 15% (soft to stiff) and 8% (stiff to soft). Total cell viability after transfer (stiff to soft, total 20 days culture) showed similar level of viability of cells cultured on soft substrates only for 20 days.

The plasticity of lineage specific marker expression

To assess the expression of lineage specific markers in response to the mechanical properties of our polyacrylamide gels, we chose to immunostain MSCs for early and late stage markers associated with neurogenesis (β3tubulin and MAP2) and osteogenesis (runx2 and osteopontin) (Fig. 6.3 and 6.4). Cells cultured in soft

substrates show elevated expression of neurogenic markers (~6-fold higher for beta3 tubulin and ~3-fold higher for MAP2 than cells cultured on stiff substrates) while cells cultured in stiff substrates tend to express elevated osteogenic markers (~7-fold higher for runx2 and ~2-fold higher for osteopontin than cells cultured on soft substrates), and regardless of stiffness cells stably express the neurogenic and osteogenic markers at nearly constant levels from 10 to 20 days. Since recent studies have demonstrated plasticity in marker expression in response to substrate mechanics (88), we transferred MSCs after culture for 10 days from soft to stiff and stiff to soft, and performed immunofluorescence characterization after 5 days and 10 days culture on the new substrates. Transferred MSCs (stiff to soft) showed decreased levels of osteogenic marker expression and increased expression level of neurogenic markers depending on culture time relative to cells maintained in culture on stiff substrates. However, when cells were transferred to soft gels after 10 days on stiff gels, the expression of nuclear runx2 remained elevated compared to MSCs that were cultured on soft gels for 10 days. In contrast, transferred MSCs (soft to stiff) tended to decrease the expression of β3tubulin and increase the levels of runx2 to levels that are comparable to cells that were cultured on the stiff gels alone. This suggests that stiff gels promote a degree of irreversible runx2 activation that is insensitive to changes in substrate stiffness. We observed the same trends in lineage specification modulation in response to stiffness changes for the late markers osteopontin and MAP2; however the changes were less pronounced. To further verify the observed fluctuations in lineage specification, we performed gene expression analysis using quantitative real-time polymerase chain reaction (PCR) (Fig. 6.5). We observed the same trend as with the immunofluorescence results:

we see a higher degree of neurogenic and lower degree of osteogenic transcript expression for cells (stiff to soft), and elevated levels of osteogenic and lowered levels of neurogenic transcripts for cells (soft to stiff).

The effect of cell shape on modulating the plasticity of lineage specific markers

In the chapter 3, we demonstrated how cell geometry can be controlled across hydrogel substrates using microcontact printing to refine the degree of osteogenesis (76) and neurogenesis (87) in adherent MSCs. Since transferring MSCs from stiff to soft substrates did not lead to a complete lineage reversal, we asked whether transfer to patterned substrates, with shapes that are expected to enhance the stiffness-directed lineage, could further direct the lineage switch. MSCs were cultured on unpatterned soft or stiff substrates for 10 days, and then transferred to different stiffness substrates containing patterns of fibronectin (circle, oval, star, or unpatterned; 5000 μm^2) (Fig. 6.6). As shown in the preceding section, after 10 days of culture the spread cells on the soft substrates show elevated expression of neurogenic markers (β3 tubulin and MAP2) while cells that spread on stiff substrates express elevated osteogenic markers (runx2 and osteopontin). For patterned cells where the mechanical properties change from soft to stiff, the extent of staining for neurogenic or osteogenic markers by circular cells was similar to spread cells (Fig. 6.7a and b). Interestingly, transferred cells (soft to stiff) in oval and star shapes showed higher expression of osteogenic markers compared to cells in other shapes; patterned star shaped cells displayed over 2-fold enhancement in runx2 expression compared to spread or circular cells. In fact, after transfer of MSCs from soft gels to star shapes on stiff gels, runx2 expression is significantly

higher than unpatterned MSCs cultured on stiff gels alone for 10 days. In addition, MSCs that were transferred from soft gels to oval and star shapes on stiff gels—geometries which have previously been shown to enhance neurogenic marker expressions26—displayed a significantly smaller reduction in β3tubulin expression (~1.4-fold) compared to spread or circular cells (> 3-fold declines). When MSCs were transferred from stiff to soft substrates, there was no appreciable difference in osteogenic markers across unpatterned and patterned cells. However, MSCs that were transferred from stiff gels to soft gels patterned with oval and star shapes displayed higher changes in neurogenic marker expression (~6-fold for β3tubulin and ~2-fold for MAP2) compared to cells that were unpatterned or in circle shapes.

Next we analyzed trends in expression for early and late stage markers for differentiation (Fig. 6.8 and 6.9). Fig. 6.10 summarizes the results when MSCs are transferred from soft to stiff or stiff to soft substrates (cultured for 10 days (initial stiffness) + 10 days (final stiffness)) for patterned and unpatterned cells. It is clear that the expression of early markers for neurogenesis (β3tubulin) and osteogenesis (runx2) display significantly more fluctuations compared to late markers (MAP2 for neurogenesis and osteopontin for osteogenesis). For instance, cells transferred from soft to stiff substrates and captured in star shapes showed ~12-fold increase in runx2 compared to a ~3-fold increase in osteopontin. Similarly, cells transferred from stiff to soft substrates and captured in oval shapes show ~6-fold increase in β3tubulin compared to only 2-fold increase in MAP2.

6.4 Discussion

The commitment of adult stem cells to a particular lineage is a complex process involving subtle changes in gene expression patterns as the multipotent cell progresses through intermediate progenitor states. Committed progenitors have also been shown to reprogram to more primitive multipotent states under defined conditions. Lineage specification and reversal in vivo is likely context dependent and guided by combinations of biochemical and biophysical cues in the extracellular microenvironment. Understanding how the properties of in vitro cell culture substrates and prospective cellular delivery materials directs fate-specific differentiation in the laboratory is essential for stem-cell based therapies.

In this chapter we explored the plasticity of lineage specification of mesenchymal stem cells (MSCs) cultured on hydrogels of variable stiffness. Understanding MSC plasticity in vitro is important because these cells are one of the most promising adult stem cell types for regenerative therapies. MSCs have been shown to reverse the specification of lineage specific markers in response to changes in soluble media components (28). Since the physical properties of the MSC microenvironment has been shown to exert an influence on lineage specification, we asked whether changes in the biophysical properties of the substrate over time would redirect the expression of lineage specific markers. We chose to examine two very different MSC fate decisions: the widely studied differentiation of MSCs to osteoblasts, and the more controversial transdifferentiation of MSCs to cells of neuronal lineage. We chose these particular stiffness-directed outcomes because they show the largest difference in native tissue mechanical properties (0.5 kPa for neural tissue and 40

kPa for pre-calcified bone). We employed both early and late markers for neurogenesis (β3-tubulin and MAP2) and osteogenesis (runx2 and osteopontin) to ascertain the degree of which physical cues of the substrate guide lineage specification and reversal after transfer to a new microenvironment. β3-tubulin is a marker for immature neurons that is expressed prior to the neuron-specific protein, microtubule-associated protein 2 (MAP2) (144). Runx2 is an important transcription factor expressed in early osteoblast progenitors that precedes the expression of bone-associated markers like osteopontin (mid/late osteoblast) (57). After culture on soft gels for 10 days, MSCs show reduced area, extension of neuronal-like processes and elevated expression of β3-tubulin and MAP2. In contrast, MSCs cultured on stiff gels show high spreading and elevated expression of runx2 and osteopontin. After culture on soft gels for 10 days, MSCs were transferred to stiff gels and cultured for 5 and 10 days. At both time points there was a decrease in neurogenic markers and an increase in osteogenic markers, where at the 10 day time point expression levels of osteogenic markers were comparable to MSCs that were cultured exclusively on stiff gels for 20 days. In contrast, MSCs that were first cultured on stiff gels and then transferred to soft gels only showed a modest decrease in runx2 after 10 days on the new substrate suggesting that active nuclear runx2 remains operable after the microenvironment switch. This finding is consistent with a recent report by Anseth and colleagues that demonstrated one week culture on rigid surfaces promotes nuclear runx2 expression that remains active after the surrounding matrix is softened (88). There was an increase in the expression of neurogenic markers when MSCs cultured on stiff gels were

transferred to soft gels, albeit not as high as MSCs that were cultured exclusively on soft gels for 20 days.

MSCs cultured on deformable substrates adopt morphologies that are characteristic of cells from lineages with comparable mechanical properties. For instance, MSCs cultured on soft gels will adopt neuronal-like shapes with dendritic processes while MSCs cultured on rigid substrates will adopt cuboidal shapes characteristic of osteoblasts. Controlling the shape of single cells in culture using micropatterning has been shown to influence the mechanosensitivity of MSCs to lineage specification (6, 38, 39, 87, 145). Common to these studies is the apparent importance of geometric features that modulate the degree of actomyosin contractility. For instance, increased aspect ratio and subcellular concave regions at the cell perimeter increase cytoskeletal tension and promote osteogenesis (38, 76). In addition, we have found that anisotropic geometries promote the expression of neurogenic markers (87). From our initial studies the transfer of MSCs from a stiff substrate after 10 days culture to a soft substrate did not lead to a decrease in runx2 comparable to MSCs cultured on the soft substrate alone. Therefore, we investigated whether controlling cell shape across the substrate in features that have been shown to promote neurogenesis and osteogenesis in adherent MSCs would influence the lineage outcome after a microenvironment switch. Cells that were initially cultured on soft or stiff gels and transferred to gels of the opposite stiffness showed a trend in lineage marker expression that was dependent on cell shape. Transfer from soft gels to high aspect ratio ovals and shapes approximating a 5-pointed star on stiff gels led to an enhancement in osteogenic marker

expression, presumably because these shapes have been shown to promote osteogenesis through increased actomyosin contractility compared to isotropic shapes without perimeter curvature (6, 23, 76). Surprisingly, transfer to stiff gels in these geometries led to partial maintenance of neurogenic marker expression, even after 10 days culture, when compared to unpatterned or circular shapes that promoted a significant decrease. MSCs that are initially patterned in oval and star shapes on stiff gels show low levels of β3-tubulin. Taken together, this suggests that transfer of cells that are expressing elevated levels of neurogenic markers to islands displaying anisotropic features may help maintain the neuronal phenotype, even when presented with an antagonistic stiffness. MSCs that are transferred from stiff gels to oval and star shapes on soft gels show an increase in β3-tubulin expression. This finding is consistent with our previous work that demonstrated the importance of anisotropic geometries in guiding the extension of neuron-like processes (87).

6.5 Conclusion

This chapter reveals that lineage specification to diverse outcomes is reversible by switching the biophysical parameters of stiffness and cell geometry. In particular, the early markers for osteogenesis (runx2) and neurogenesis (β3-tubulin), respond more readily to changes in the biophysical characteristics of the substrate, compared to the late markers osteopontin and MAP2. Even after 20 days in culture, there is little variation in the magnitude of expression for both early and late markers. This suggests the biophysical aspects of the cellular microenvironment only promote early differentiation events. Since differentiation in vivo involves the

dynamic temporal regulation of discreet cellular states in response to a host of biophysical and biochemical signals, we speculate that the presentation of physical cues alone serve to prime stem cells to a reversible progenitor state that is poised to receive further signals to guide the progression to full commitment. Selection of appropriate materials that harness lineage specific biophysical conditions may serve as a good starting point for cell-based therapies, where endogenous in vivo signals integrate to direct full differentiation.

6.6 Figures

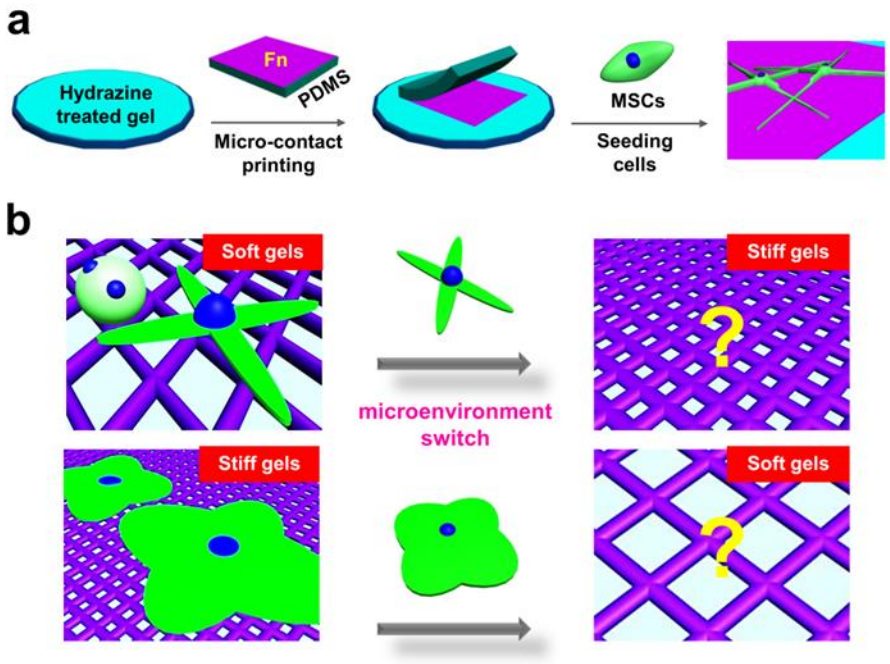

Figure 6.1 Hydrogel fabrication scheme and experimental strategy. *(a) Protocol for fabricating matrix protein conjugated polyacrylamide hydrogels. (b) Schematic illustration of microenvironment switch between soft (0.5 kPa) and stiff (40 kPa) substrates to monitor the dynamic changes of MSC lineage specification.*

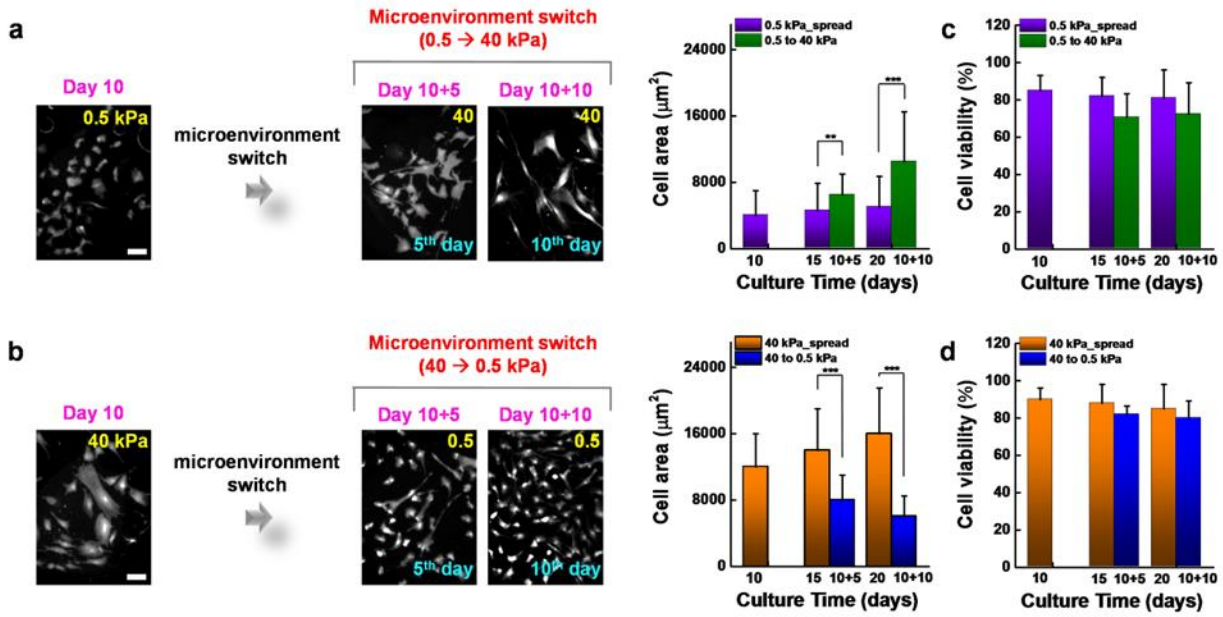

Figure 6.2 Projected cell area and viability are influenced by changing the mechanical properties of the substrate. *(a)-(b) Representative immunofluorescence microscopy images and quantitation of average cell area of MSCs cultured for 10 days and after microenvironment switch (0.5 to 40 kPa); scale bar: 120 μm (**P<0.005, ***P<0.0005, Fisher's exact test). (c)-(d) Cell viability of MSCs before and after substrate switch.*

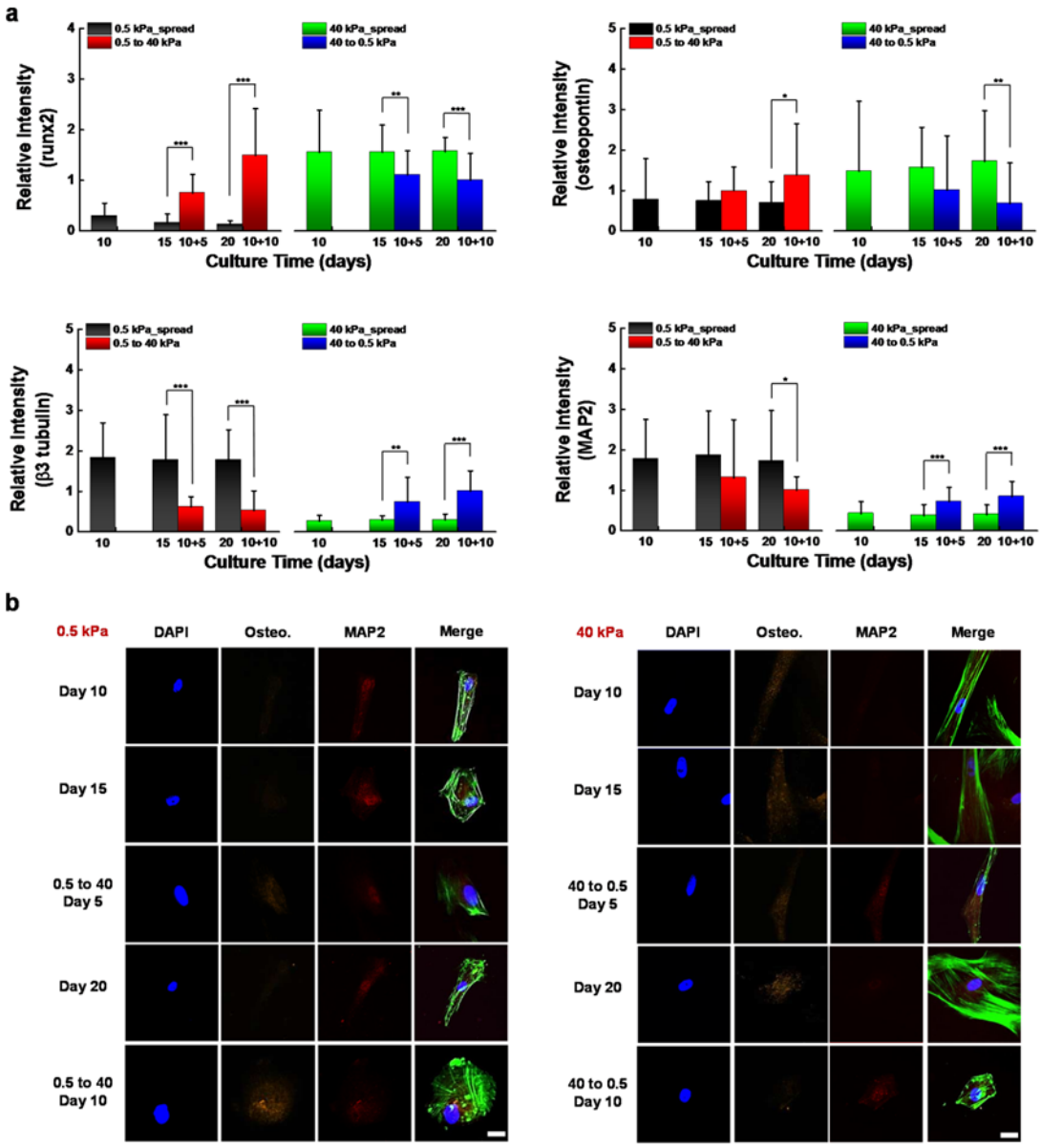

Figure 6.3 Matrix stiffness modulates the degree of MSC lineage specification. *(a) Expression of osteogenic (runx2 and osteopontin) and neurogenic (β-tubulin and MAP2) markers before and after switching the substrate (0.5 40 kPa) (*P<0.05, **P<0.005, ***P<0.0005, Fisher's exact test). (b) Representative immunofluorescence microscope image of MSCs cultured on the unpatterned fibronectin coated substrates after immunostaining for nuclei, osteopontin, MAP2 and filamentous actin; staining for MSC nuclei (blue), actin (cyan-green), osteopontin (orange), MAP2 (red). Scale bar: 35 μm.*

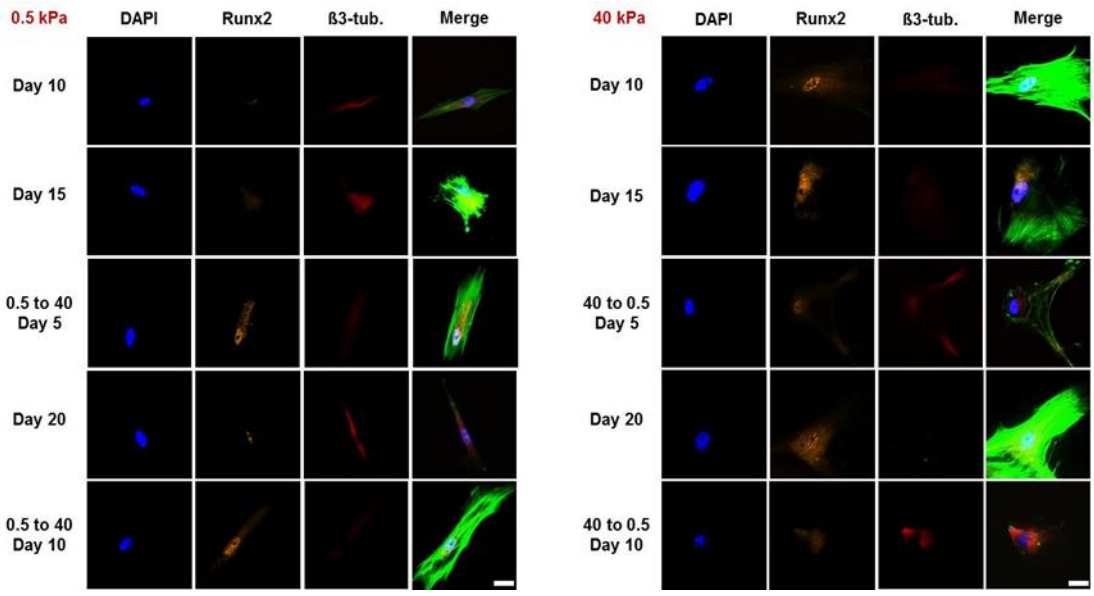

Figure 6.4 *Representative immunofluorescence microscope image of MSCs cultured on the unpatterned fibronectin coated substrates after immunostaining for nuclei, runx2, ß3-tubulin and filamentous actin; staining for MSC nuclei (blue), actin (cyan-green), runx2 (orange), ß3-tubulin (red).*

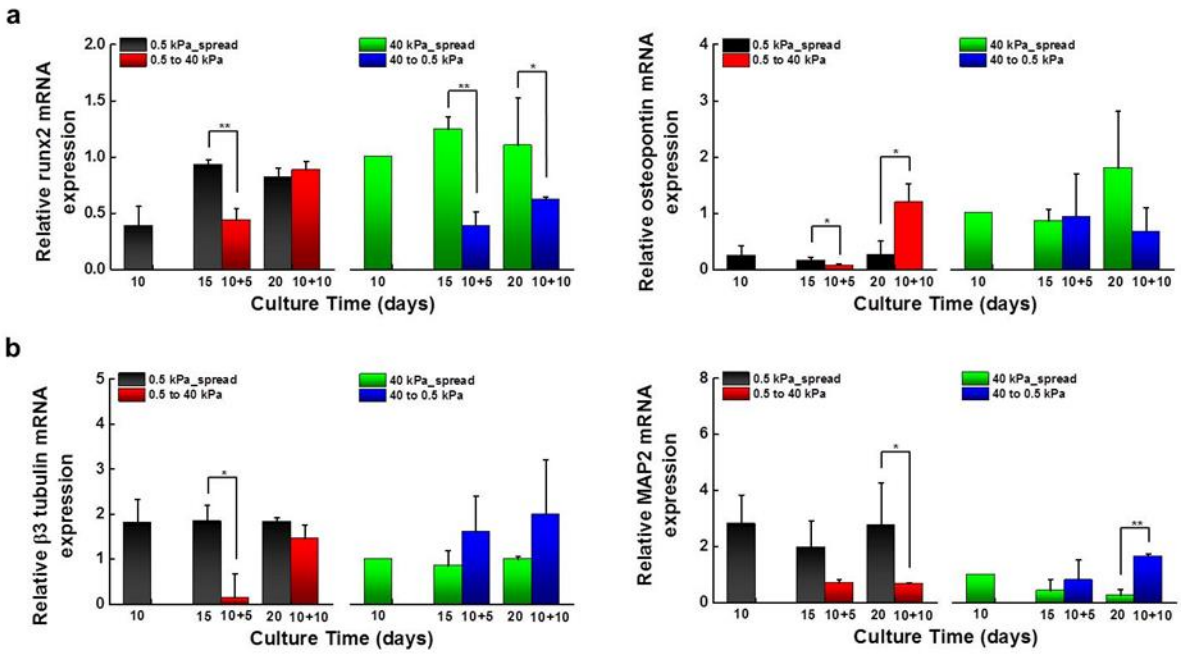

Figure 6.5 Lineage-specific gene expression analysis of MSCs with and without microenvironmental change. *(a) Results of real-time PCR to measure the gene expression of runx2 and osteopontin as early and late indicators of osteogenesis of MSCs, respectively (*P<0.05, **P<0.005, Fisher's exact test). (b) Results of real-time PCR for quantitation of β-tubulin and MAP2 as early and late indicators of neurogenesis mRNA expression of MSCs, respectively (*P<0.05, **P<0.005, Fisher's exact test).*

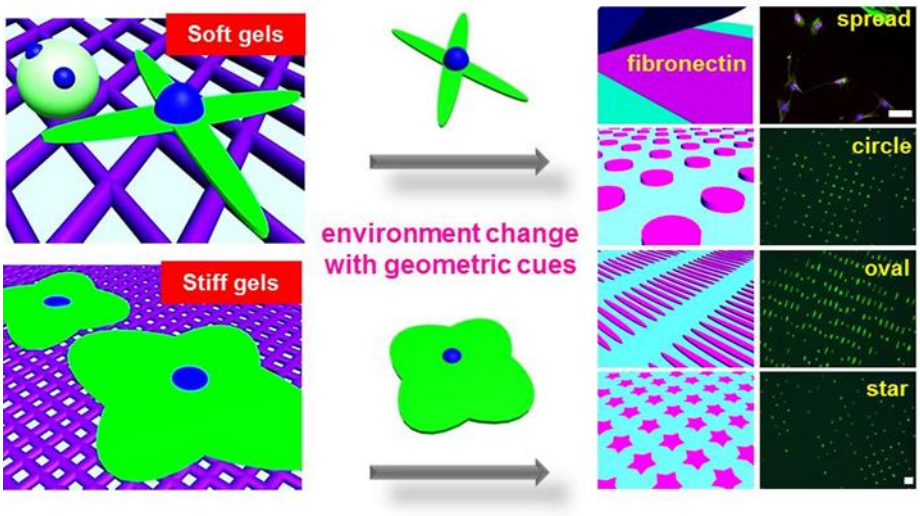

Figure 6.6 Combining matrix stiffness and geometric cues to study stem cell plasticity of lineage specification. *Schematic illustration of mechanical microenvironment changes of MSCs between soft (0.5 kPa) and stiff (40 kPa) substrates with geometric cues to control stem cell lineage commitment; scale bar: 120 μm (top), 700 μm (rest).*

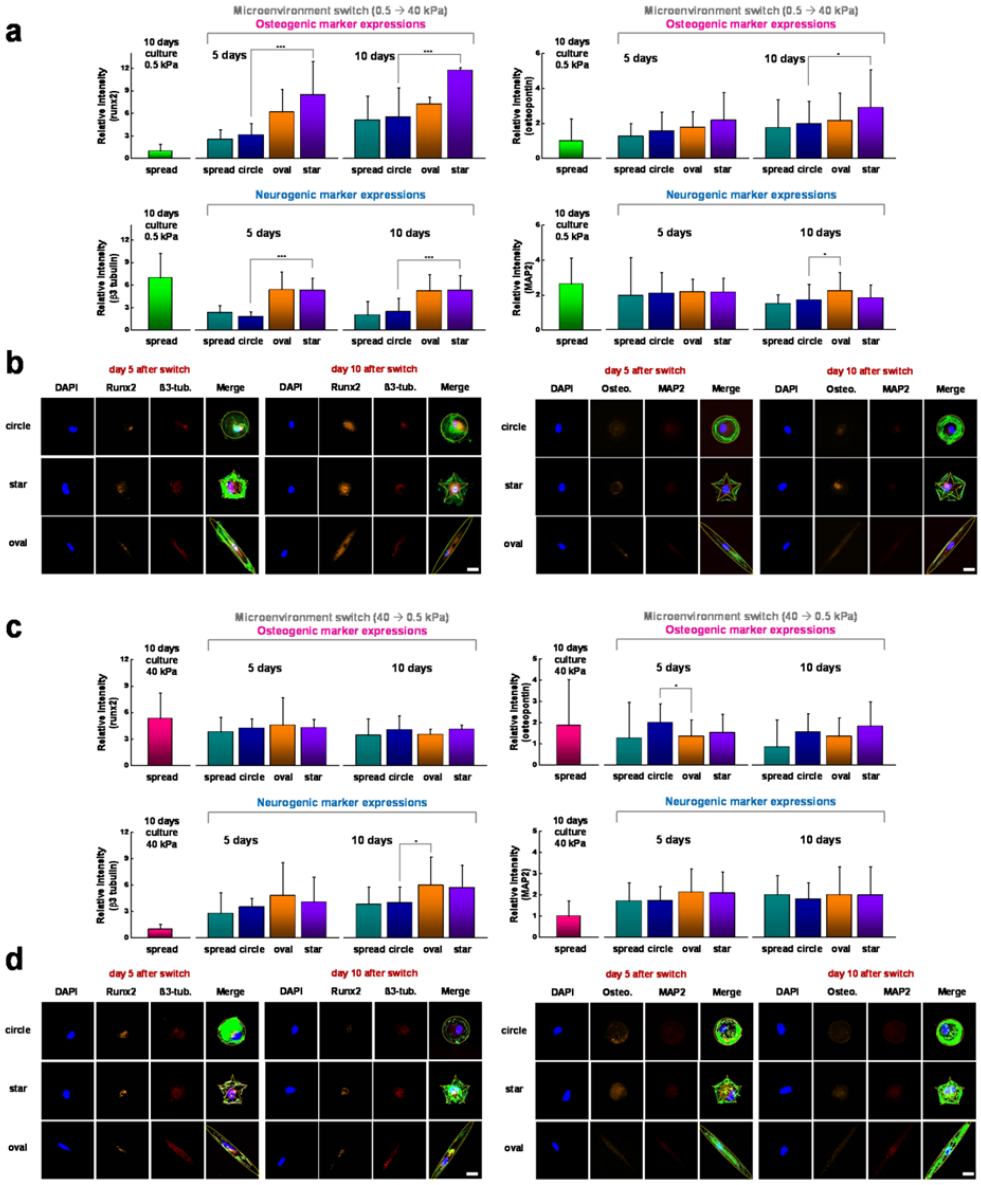

Figure 6.7 Cell shape directs lineage specification of MSCs after microenvironment change. *(a) Quantitation of osteogenic (runx2 and osteopontin) and neurogenic (β-tubulin and MAP2) markers for a population of cells cultured with and without a microenvironment change from soft to stiff. (b) Representative immunofluorescence images. (c) Expression of osteogenic (runx2 and osteopontin) and neurogenic (β-tubulin and MAP2) markers for a population of cells cultured with and without a microenvironment change from stiff to soft. (d) Representative immunofluorescence images; staining for MSC nuclei (blue), actin (cyan-green), runx2 and osteopontin (orange), β-tubulin and MAP2 (red). Scale bar: 35 μm. (*P<0.05, ***P<0.005, Fisher's exact test).*

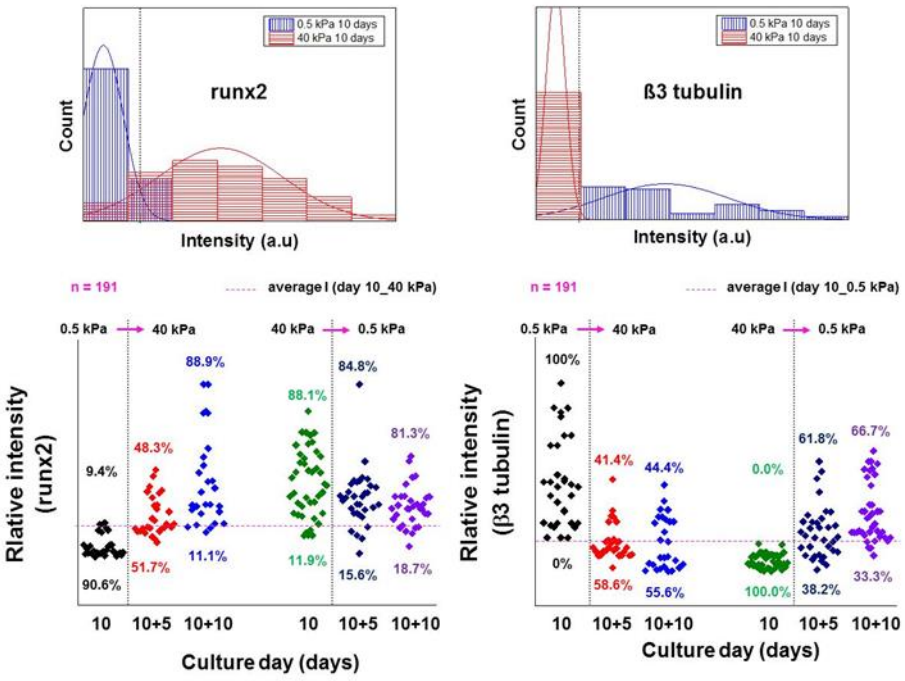

Figure 6.8 *Expression changes of early osteogenic (runx2) and neurogenic (β-tubulin) markers before and after switching the substrate (0.5 to 40 kPa); one of results from three different experiments. Threshold intensities are obtained by comparing histograms between the marker intensity of MSCs on soft and stiff substrates before switching microenvironments.*

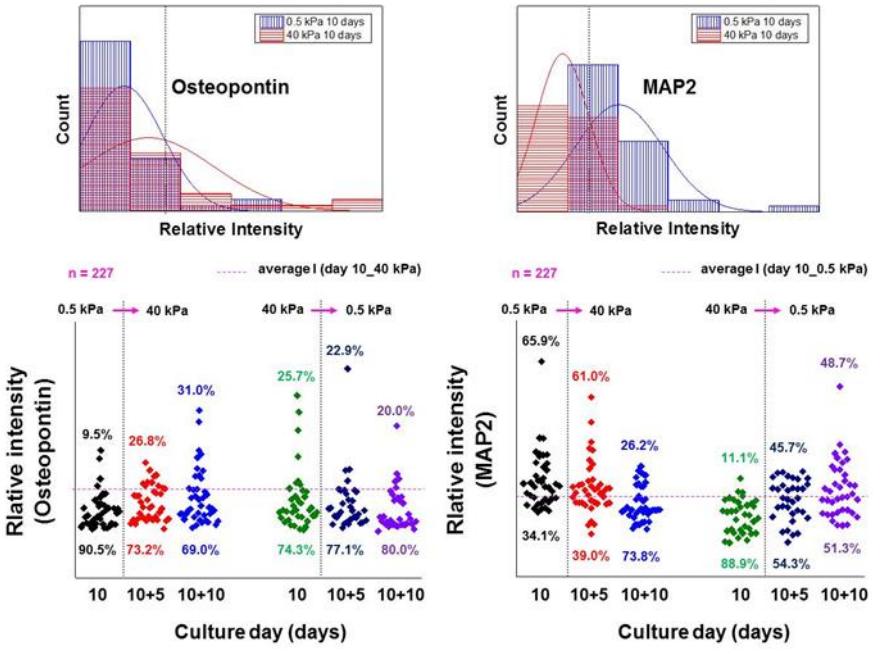

Figure 6.9 *Expression changes of late osteogenic (osteopontin) and neurogenic (MAP2) markers before and after switching the substrate (0.5 to 40 kPa); one of results from three different experiments. Threshold intensities are obtained by comparing histograms between the marker intensity of MSCs on soft and stiff substrates before switching microenvironments.*

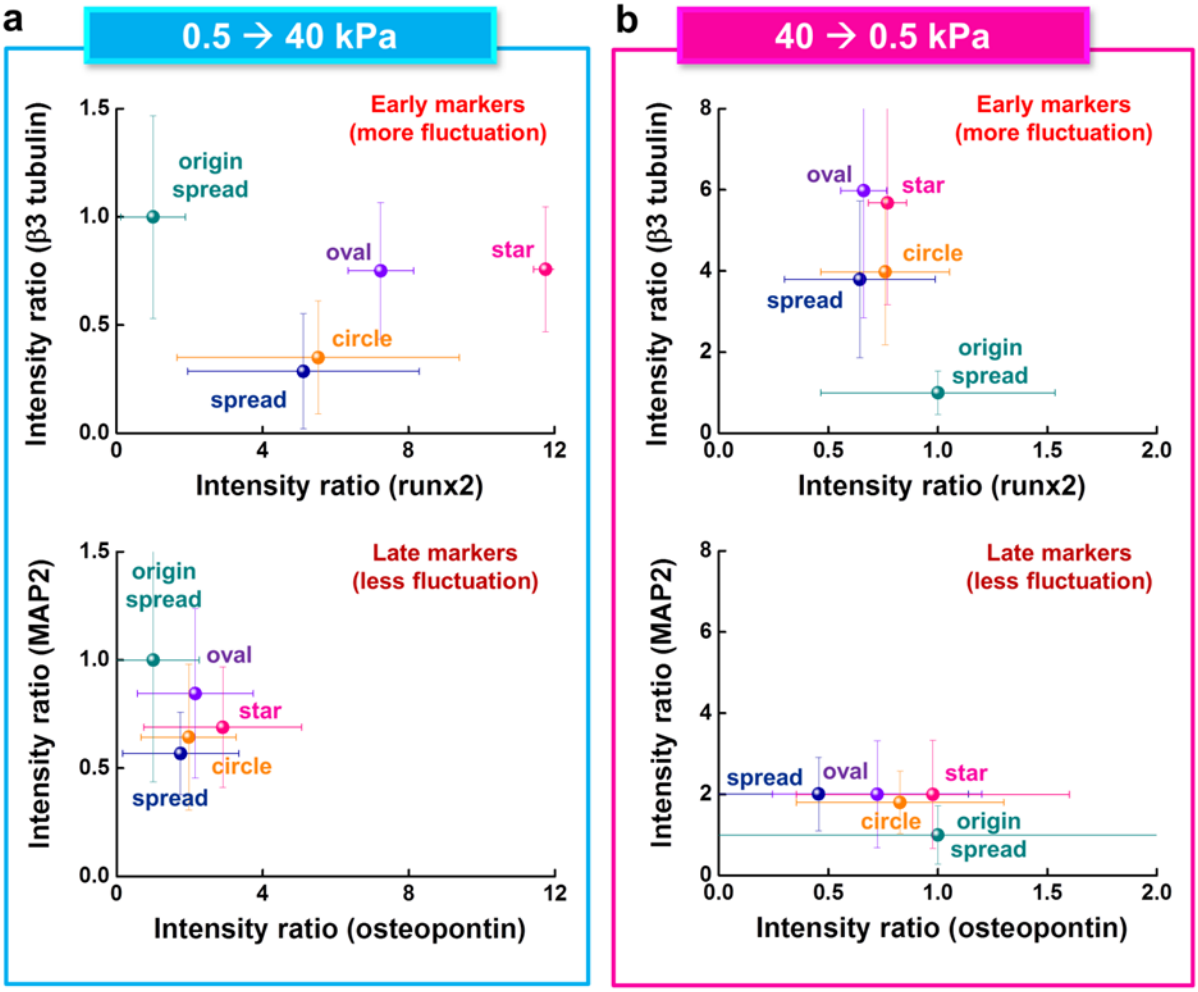

Figure 6.10 *Geometric cues differentially reprogram early and late markers of neurogenesis and osteogenesis for (a) soft to stiff and (b) stiff to soft.*

CHAPTER 7

INTERFACIAL GEOMETRY DICTATES CANCER CELL TUMORIGENICITY[7]

7.1 Introduction

Cancer is a leading cause of death, primarily through the process of metastasis where malignant cells spread to distant organs (146). It is believed that `tumour initiating cells' or ‘cancer stem cells' (herein referred to as CSCs) inherently possess the characteristics necessary for establishing metastases; however, within a tumour mass comprised of billions of cells, usually only a small percentage of cells exhibit a CSC phenotype (147). This same population of cells is believed to be the root cause of recurrence after treatment, because most therapeutic regimens have not been optimized to target CSCs, and there have been multiple examples of CSCs being resistant to therapy (148). Current evidence suggests wide-scale dynamic variation in the presence and function of CSCs across cancers and patients6. Deciphering the cues in the microenvironment that promote the CSC phenotype is a pressing need for understanding disease progression and developing therapeutics that can disrupt the processes involved for induction and survival of CSCs.

In this chapter, by using engineered extracellular matrices, we show that geometric features at the perimeter of tumour tissue will prime a population of cells with a stem-cell-like phenotype. These cells show characteristics of cancer stem cells in

[7] This chapter is adapted from the following publication:
Junmin Lee, Amr A. Abdeen, Kathryn L. Wycislo, Timothy M. Fan, and Kristopher A. Kilian, Interfacial geometry dictates cancer cell tumorigenicity, Nature Materials, 2016, 15, 856-862

vitro, as well as enhanced tumorigenicity in murine models of primary tumour growth and pulmonary metastases.We also show that interfacial geometry modulates cell shape, adhesion through integrin α5ß1, MAPK and STAT activity, and initiation of pluripotency signalling. Our results for several human cancer cell lines suggest that interfacial geometry triggers a general mechanism for the regulation of cancer-cell state. Similar to how a growing tumour can co-opt normal soluble signaling pathways3, our findings demonstrate how cancer can also exploit geometry to orchestrate oncogenesis.

7.2 Materials and Methods

General materials and methods are given in Appendix A.

3D surface preparation

For pseudo-3D microwells, an SU-8 photolithography master displaying the inverse features used in fabricating the PDMS stamps was used as a template to cast PA gels with microwells on the surface. The gels were chemically modified with hydrazine hydrate and the oxidized protein solution was applied. To render the external surface non-adhesive, the top layer of protein-conjugated gels was sheared off by applying an adhesive strip to the surface. In all of our experiments we ensured cells only formed a single monolayer to ensure uniform antibody staining.

For 3D poly(ethylene glycol) (PEG) gels, 10,000 MW PEG (Sigma) was modified to PEGDA as previously reported by the addition of acryloyl chloride (149). Fibronectin

was acrylated by the addition of NHS-Acrylate (Sigma) under basic pH for 4 hours. Matrix metalloprotease (MMP) cleavable peptides were synthesized using solid state peptide synthesis and reacted with PEGDA via Michael addition. 3-(trimethoxysilyl)propyl methacrylate 2% solution in ethanol with 0.3% glacial acetic acid, then baking at 95C for 1 hour35. To encapsulate cells in the degradable hydrogels, 30% (w/v) PEGDA-MMP was mixed with UV-initiator (0.05% Irgacure 2959, Sigma) and cells were centrifuged and re-suspended in this mixture. This solution was sandwiched between the activated coverslip and a hydrophobic coverslip. UV light (5mW/cm^2) was applied for 10 min and the encapsulated cells were detached and placed in cell culture media. For 3D microfluidics PDMS devices, flexible rubber coated wire (200 mm long, 2 mm diameter) was employed to design microfluidic devices with different shapes. The designed wire (line or spiral) was placed on the first layer of PDMS (flat) and the second layer of PDMS was fabricated with the wire inside. After the wire was removed from the PDMS, 0.2 mg/ml sulfosuccinimidyl 6 (4′-azido-2′-nitrophenyl-amino) hexanoate (Sulfo-SANPAH; Pierce), a heterobifunctional protein cross-linker, was used to covalently bind proteins to the PDMS channel inside; exposure of the PDMS in a solution of Sulfo-SANPAH with a UV light source at 365 or 320 nm covalently linked the sulfo-SANPAH to the PDMS (1 h). Sulfo-SANPAH solution was removed from the PDMS channel and the device was washed by gently adding and aspirating PBS until the PDMS channel was transparent again. Fibronectin (25 μg/ml) was conjugated on the surface-modified PDMS inside the channel for 24 h.

Cell source and culture

The cancer cell lines B16F0 and B16F10 (murine melanoma), and PC3 (human prostate) were obtained from American Type Culture Collection (ATCC) and cultured according to the recommended protocols. HELA (human cervical, ATCC) cells were a gift from Andrew M. Smith's laboratory; A549 (human lung, ATCC) cells were a kind gift from Jianjun Cheng's laboratory. For cell culture, media was changed every 3 days and cells were passaged at nearly 90% confluence using 0.25% trypsin (Gibco). B16 cells were tested for mycoplasma contamination.

Inhibition assays

MAP kinase inhibitions (FR180204 (ERK1/2), SP600125 (JNK), and SB202190 (p38)) (Calbiochem) were performed by adding media supplemented with these inhibitors at 6 μM concentration after cell seeding and with each media change. Integrin blocking antibodies (α5ß1) were added to cells in media prior to seeding at 1μg/ml.

Wound-healing assay

B16F0 and B16F10 cells were cultured for 5 days on spiral patterns (with or without p38 inhibitors), non-patterned gels, or glass substrates (12 identical substrates). Cells were trypsinized and re-plated on glass substrates (106 cells per glass) and then cultured under permissive condition to about 90% confluence. A pipet tip was employed to create a linear scratch in the confluent monolayer. Cells were allowed to migrate and close the wound for 12 h, and were observed under phase contrast microscopy. The scratch width per field of view, between the time points 0 and 12 h following wound closure, was determined using imageJ36 and the average

percentage of wound closure, indicated by the shifted width after 12 h, was assessed.

Boyden chamber assay

Invasion of B16F0 and B16F10 cells was examined using 24-well Boyden chambers (Corning) with inserts (8 µm pores) and precoated basement membrane extract (Matrigel, growth factor reduced) (BD Biosciences). Cells were cultured for 5 days on spiral patterns (with or without p38 inhibitors), non-patterned gels or glass substrates (12 identical substrates) and then placed on the inserts in the upper chambers (of each well) and cultured for 12 h. Cells on the upper surface of the membrane filter were removed. Cells that crossed the inserts to the lower surface were fixed with 4% paraformaldehyde and then stained with 4',6-diamidino-2-phenylindole (DAPI). Cells per field of view were imaged under fluorescence microscope (10x) and counted.

Cell labeling and flow cytometry

B16F0 and B16F10 cells cultured for 5 days on spiral patterns or glass substrates (12 identical substrates) were trypsinized and broken down into a single cell suspension. Cells were fixed in 4% paraformaldehyde for 20 min and permeabilized in 0.1% Triton X-100 in PBS for 15 min. Cells were blocked in 1% BSA for 1 h. Cells were stained with primary antibodies in 1% BSA in PBS for 2 h at room temperature. Next, secondary antibodies in 2% goat serum, 1% BSA in PBS were applied for 20 min in a humid chamber (5% CO2 & 37°C). Before every step, cells were washed three times with PBS. Flow cytometry analysis was performed with a

BD LSR Fortessa Flow Cytometry Analyzer. Cells stained without primary antibodies were used as negative controls to set the baseline.

Cell proliferation assay in vitro

BrdU staining was conducted as reported previously (39). Briefly, BrdU labeling reagent (Invitrogen) was added (1:100 v/v) before 24 h of fixing; the reagent was added after seeding, day 2, or day 4 for fixing at days 1, 3, or 5, respectively. Cells were fixed in 70% ethanol for 30 min and then denatured with 2 M HCl for 30 min. Cells were permeabilized with 0.1% Triton X-100 in PBS for 30 min and blocked with 1% BSA in PBS for 15 min and then incubated with mouse anti-BrdU primary antibody (3 h at room temperature) followed by Alexa Fluor 647-conjugated antimouse IgG antibody (20 min in a humid chamber). Cell nuclei were stained with DAPI. For the division rate assay, B16F0 and B16F10 cells cultured for 5 days on spiral patterns or glass substrates (6 identical substrates) were trypsinized and placed on glass.

Ethics statement

All experiments using live animals were in compliance with animal welfare ethical regulations and approved by Institute Animal Care and Use Committee prior to experimentation.

B16 melanoma in vivo models

Six-eight week old female C57BL/6 mice were purchased from Charles River Lab. for Animal Experiment. Primary localized tumors were established by

subcutaneously injecting B16F0 cells (range 250 to 106) grown on pattern, non-pattern (NP) or glass into the right lateral flank (the information of #mice in each experiment is descripted in each figure). Macroscopic tumor growth was serially measured (maximal length and width) with calipers three times a week. Tumor growth was checked every 3 days and experiments were stopped when the first mouse of the respective series had a tumor exceeding 2000 mm^3. The volume of tumor was calculated by V = (L x W2)/2 (L: length, W: width). Experimental metastases were established by injecting 2.5 x 105 (B16F0 grown on pattern/glass or B16F10 grown on glass) or 3.0 x 104 (B16F0 grown on pattern/NP/glass) melanoma cells via lateral tail vein injection. Mice were sacrificed 5, 10, and 16 days (2.5 x 10^5 cells injected) post injection and used to quantify percent tumor surface area within the lung parenchyma or followed for survival analysis. Mice were used for determination of primary tumorigenesis and experimental metastases. No animals or target organ samples (lung tissue) were excluded from analysis. Criteria used for primary tumorigenesis was the formation of subcutaneous tumors which were detectable by visual examination and measurable with calipers. For comparison of primary tumor formation kinetics, mice were evaluated daily until primary tumors exceeded 20 millimeters in diameter, then humanely euthanized. In some experiments evaluating primary tumorigenesis, study endpoints dichotomous in nature, being either tumor formation or no tumor formation after a cumulative lapse of time (60 days). For experimental metastases, the primary endpoint was survival time and mice were monitored daily until reaching criteria for humane euthanasia. Mice were used for determination of primary tumorigenesis and experimental metastases. Inoculation of mice with melanoma cells grown on

different conditions (glass, non-pattern, and pattern) and different cell densities was not performed in a random fashion. Rather, cohorts of mice were predetermined to receive injections of melanoma cells grown under specified conditions and cell densities prior to inoculation. No blinding was done for these animal studies.

Ki67 Immunohistochemistry

Five representative lung sections fixed in 10% formalin per mouse were immunohistochemically stained for Ki67. Within each lung section, 3 randomly selected parenchymal areas completely effaced by melanoma cells were microscopically quantified for Ki67 nuclear positivity and expressed as a percentage using ImageJ software.

Microscopy data analysis

Immunofluorescent images from immunofluorescence microscopy were analyzed using ImageJ software. Multiple cells (over 20 patterns) were imaged for each condition and fluorescence intensity of single cells in patterns (after background subtraction) was used to compare marker expression. For cell curvature analysis, the number of cells in circular patterns (over 20 patterns) with different areas (3,000-100,000 μm^2) were counted, and cell curvature length was calculated based on the length of pattern perimeter and the number of cells at the perimeter. Average curvature angle and intensity of cells at the perimeter of the patterns were measured and plotted. For inhibition studies, positive cells which were above the maximum intensities of the glass control (ImageJ threshold) were counted, and the

numbers were divided by total cells in patterns. For generating immunofluorescence heatmaps, cells cultured on various shapes were imaged on the same day using the same microscope and camera settings. Background intensities of raw fluorescent images were subtracted, and patterns were aligned in image J with the same orientation as cultured across the surface, incorporated into a Z stack and the average intensity calculated for heatmap generation.

For segmentation analysis, cells cultured on each shape in a single monolayer were manually segmented for at least 100 single cells through immunostaining using ImageJ. Since cells predominantly express surface markers at the surface and not within nuclei and junctions, it is possible to segment single cells at the perimeter (line, convex, or concave): (1) we used 20x immunofluorescence images in ImageJ, (2) contrast and brightness were controlled to optimize the image for segmentation analysis, (3) the surface region of each single cell at the perimeter was selected excluding nuclei, (4) the original image was re-opened, and marker intensity of segmented single cells was measured using ImageJ, (5) measured intensity values were subtracted with background intensity.

RNA isolation for microarray experiments

Adherent B16F0 and B16F10 cells cultured for 5 days on spiral patterns, non-patterned gels, or glasses were lysed directly in Trizol reagent (Invitrogen) according to the vendor's instructions. Total RNA from each sample (12 duplicates) was extracted and quantified by photospectrometry using a NanoDrop ND-1000 (ThermoFisher). RNA quality was confirmed by an Agilent Bioanalyzer, and gene

expression profiling performed using Illumina iScan Sentrix® BeachChip technology at the Roy J. Carver Biotechnology Center at the University of Illinois at Urbana-Champaign using standard Illumina protocols (http://support.illumina.com/content/dam/illumina-support/documents/myillumina/3466bf71-78bd-4842-8bfc-393a45d11874/wggex_direct_hybridization_assay_guide_11322355_a.pdf) Illumina gene array data was preprocessed using GenePattern. The background values were subtracted and thresholded. The data was then normalized using the quantile method. Heatmaps of fold changes over Glass in gene expression were visualized using the Gene-E (http://www.broadinstitute.org/cancer/software/GENE-E/) software package. A panel of metastasis genes was selected from a previous report by Clark et al.39. For finding relevant pathways, genes up-regulated in patterns compared to glass were tested in the Database for Annotation, Visualization and Integrated Discovery (DAVID) website (http://david.abcc.ncifcrf.gov/) and genes in each pathway were selected based on DAVID and genes with negligible expression (below 10) were discarded.

Percent tumor surface area

Five representative lung sections fixed in 10% formalin per mouse were microscopically examined at 2 different tissue planes separated by 50 microns. Subgross images (1.25x), including one image containing an imbedded micrometer, were captured for each lung section at both tissue planes using standard microscopy imaging equipment. Images were imported into Adobe Photoshop Creative Cloud 2014 and the imbedded micrometer was used to set a measurement

scale of image pixels to length in mm (1503 pixels = 5.0 mm). Parenchymal surface area of each lung lobe was subsequently measured using the Quick Selection Tool. Regions of B16 melanoma growth were then identified visually and cross-referenced with the histologic slide if necessary, surface area measured using the Magic Wand Tool, summated, and then expressed as a percentage relative to total parenchymal surface area using ImageJ software.

Modeling of cell monolayer

Abaqus software was used to construct and analyze a finite element model of contractile cell monolayers as described previously (47). Briefly, the desired geometry was modeled in 2 layers: an active 20μm thick top layer and a passive 5μm thick bottom layer that is constrained at the bottom surface. The active layer is made to contract isotropically by applying a 5 K temperature drop. The von Mises stress at the bottom surface is reported. We confirmed convergence by testing multiple mesh sizes and layer properties.

Statistical analysis

Data was obtained from 3 independent experiments and expressed as the mean standard deviation (SD) unless otherwise specified. Statistical comparisons between two groups were based on Student's t-test and comparisons of more than two groups were performed by analysis of variance (ANOVA) with Tukey HSD Post-hoc testing to correct for multiple comparisons. Differences were considered significant at $P < 0.05$.

7.3 Results and Discussion

We prepared hydrazine modified polyacrylamide (PA) hydrogels of different elasticity (~1, 10, and 100 kPa) and used soft lithography to conjugate matrix proteins in various patterns with different sizes and shapes (Fig. 7.1). As a model system we selected the murine B16 melanoma cell lines and used putative cancer stem cell molecular markers CD271, CD133 and ABCB520–22. We first measured these markers in B16 melanoma cells cultured for 1, 3 and 5 days on circular patterns of different matrix elasticity and pattern size (Fig. 7.2). Expression of tumorigenic molecular markers strongly depended on culture duration (1-5 days) and colony size with a maximum at the perimeter of circular islands ~3,000 to 100,000 μm^2. The stiffness of the underlying matrix did not exert a significant influence over the expression of CSC markers, thus we fixed the stiffness of our matrices at 10 kPa (Fig 7.3 and 7.4). Analysis of cell morphology at these perimeter features reveals that, with decreasing pattern size, individual cells occupy longer arcs along the pattern perimeter with larger subtended arc angles on average. This correlates with higher ABCB5 expressions in these cells (Fig. 7.4c). For instance, an average cell on the perimeter of a 3,000 μm^2 pattern has an edge curvature ~2.2 times longer with an angle of curvature ~12.7 times larger and shows ~2.6 higher ABCB5 expression than a cell on a 10,000 μm^2. Analysis of cell and nuclear shapes, proliferation characteristics and integrin expression shows marked differences in these parameters which may correlate with enhanced invasiveness (150) (Fig. 7.4c and Fig. 7.5). Since cell-cell adhesion within tissue will regulate the perimeter stress, we designed straight line and torus geometries where curvature and

perimeter/area can be varied. After 5 days of culture we see that both perimeter curvature and perimeter-area ratio (a measure proportional to interfacial energy (125)) exerts an influence on the expression of perimeter CSC markers. In all cases, convex curvature at the exterior of the torus showed higher expression of CSC markers compared to interior concave regions (Fig. 7.4d & 7.6). We designed a range of patterns compromising edges, concave and convex regions, corners of different angles and various radii of curvature, to investigate how combinations of interfacial cues at the perimeter of a population of tumor cells guides cellular organization and the expression of CSC markers (Fig. 7.7). Across all shapes we see higher expression of CSC markers near the periphery, with higher expression localized to convex features and corners. We note a degree of anisotropy in some of our heatmaps, which may be due to uneven initial seeding or patterning artifacts. To further verify our trends in spatial immunofluorescence, we performed segmentation analysis of CSC markers across our pattern features (Fig. 7.8 & 7.9).

To evaluate whether these cells show other characteristics of stem cells, we stained for molecular markers of pluripotency and tumorigenic phenotypes including intermediate filaments (Nestin), chromatin modifying enzymes (Jarid1b) and transcription factors (Oct4, Sox2, Nanog). Strikingly, these markers co-localized with the CSC markers. We used finite element analysis to construct a simple model of relative mechanical stress distribution of a contractile patterned monolayer, and found good correspondence between ’hotspots’ of high CSC marker expression and regions of enhanced mechanical stress within multicellular sheets (Fig. 7.4e, 7.10, and 7.11). Since perimeter features in cell islands, both convex and concave, give

rise to cells with higher expression of CSC markers compared to cells in the interior, we designed a spiral geometry with high interfacial boundary (perimeter/area) that displays an increasing radius of curvature encompassing the range depicted in Figure 7.4d. Cells cultured in the spiral shape demonstrate high expression of markers associated with a CSC state (Fig. 7.4e). We selected cells cultured on this shape for flow cytometry analysis using both B16F0 and B16F10 melanoma cells cultured for 5 days. Similar to the immunofluorescence results, cells cultured in the spiral patterns show higher levels of stem cell and tumorigenicity markers compared to those cultured on non-patterned (NP) surfaces and those on glass (Fig. 7.12 and 7.13).

To gain insight on how interfacial geometry may exert an influence on the CSC state, we performed a full genome expression analysis. B16F0 and B16F10 cells were grown on spiral patterned PA gels, non-patterned PA gels, and glass substrates for 5 days followed by RNA isolation and gene expression analysis. Hierarchical clustering demonstrates segregation of B16F0 and B16F10 cells, as well as those cultured on patterned and non-patterned gels compared to glass. A panel of metastasis related transcripts, mitogen-activated protein kinase cascades (MAPK), and signal transducers and activators of transcription (STAT) show higher levels of expression in both cell lines (B16F0 and B16F10) cultured on the patterns relative to cells cultured on non-patterned gels and glass substrates (Fig. 7.12b and 7.14). Immunostaining for integrin α5β1, Stat1 and Stat3 in patterned B16F0 and B16F10 cells shows elevated expression at the perimeter features similar to the signature found with CSC markers and stem cell transcription factors (Fig. 7.12c and 7.15).

Cells cultured on spiral shapes display elevated expression of genes involved in the MAP kinase pathways linked to mechanotransduction, particularly p38 kinases and extracellular related kinases (ERK). To determine the extent to which MAPK signaling transduces signals within cells along the perimeter curvature, we supplemented our patterned culture with pharmacological inhibitors of MAPK pathways. Addition of a p38 inhibitor and an ERK 1/2 inhibitor led to a decrease in the expression of CSC markers at the perimeter while addition of a JNK inhibitor resulted in more subtle, shape dependent changes (Fig. 7.12d and 7.16a). Since STAT transcriptional activity can be elevated through p38 MAPK signaling cascades (151) and has been shown to play a role in melanoma progression (152), we also explored the ability of p38 inhibition to modulate STAT activity. Supplementing the patterned cultures with p38 inhibitor attenuated Stat1 and Stat3 perimeter localization as determined by both immunofluorescence and flow cytometry (Fig. 7.12e and 7.16b). In addition, introduction of blocking antibodies against α5β1 during culture leads to a partial reduction in the expression of melanoma CSC markers (Fig. 7.12f & 7.8c), suggesting integrin α5β1 plays a role in CSC adhesion. Taken together, we propose that interfacial geometry will modulate cell shape, enhance α5β1 adhesion, MAPK signaling, and STAT activity to promote initiation of self-renewal stem cell networks (Fig. 7.12g).

Recently we demonstrated how switching the biophysical microenvironment could rewire cell state using mesenchymal stem cells as a model system (116). Using this platform we explored whether switching the microenvironments between patterned and glass substrates could rewire the tumorigenic CSC state. Cells were cultured on

both substrates for 5 days followed by transfer of spiral patterned cells to glass and vice versa. Transfer of B16 cells from glass to patterned substrates led to increased expression of CSC markers while cells transferred from patterned to glass substrates maintained some elevation of ABCB5 and CD271 after 5 days suggesting the CSC state remains initially stable after removal from the patterns (Fig. 7.17). In our model 2D tumor microenvironments, interfacial geometry will promote signaling that establishes a tumorigenic CSC state. During tumor growth in vivo, stiffening matrices will similarly present regions of high interfacial tension at the perimeter of the growing tumor (153). To ask whether interfaces in higher dimensional materials—that more closely recapitulate an in vivo environment—can similarly activate a tumorigenic state, we used a templating approach to fabricate pseudo-3D microwells of PA gels (Fig. 7.18a), a 3D microfluidics PDMS device with varying geometry (Fig. 7.18b) or encapsulating groups of cells in 3D poly(ethylene glycol) (PEG) gels, all either coated or conjugated with fibronectin (Fig. 7.18c). After 5 days in culture, cells at the perimeter express higher levels of CSC markers in all of these experimental architectures. The consistent enhancement of CSC markers at the perimeter of our 2D and 3D tumor models gives credence to the idea that interfacial geometry may prove a general driver in coordinating cell state during oncogenesis en route to metastasis (Fig. 7.18d).

To explore the metastatic potential and tumorigenicity of our engineered cells, we performed a number of in vitro and in vivo analyses. Wound healing and Boyden chamber invasion assays demonstrate enhanced migration and invasion characteristics for cells initially cultured on spiral patterns, and p38 inhibition

abrogates these trends (Fig. 7.19a and 7.20). For an in vivo test of tumorigenicity, B16F0 cells were cultured for 5 days on spiral patterned gels, non-patterned gels or glass substrates, followed by subcutaneous injection into 6-8 week old C57BL/6 mice; primary tumor establishment and growth were monitored every three days with calipers.

Primary tumor growth was significantly enhanced for the B16F0 cells cultured on patterned gels compared to cells cultured on non-patterned gels or glass (Fig. 7.19b). To probe the differences in growth rates for the B16s, we cultured cells on spiral shaped patterned gels, non-patterned gels or glass substrates for 5 days, followed by trypsinization and re-seeding on glass. Division rates were similar for both conditions (Fig. 7.19c) suggesting enhanced tumor growth in vivo for the engineered cells is either due to enhanced proliferation in vivo, or on account of better survival characteristics. We performed a limited dilution study to evaluate tumorigenicity, where mice were inoculated with suspensions of 2500, 1000, 500 and 250 cells from our spiral patterned gel and non-patterned gel condition. After 2 months we see that 4 of the 6 mice at the lowest dilution have developed tumors from spiral patterned cells, compared to 1 of 6 in mice injected with cells from non-patterned gels (Fig. 7.19d). This result suggests cells from our patterned hydrogels display enhanced tumorigenicity. With the observed difference for primary tumor growth, we sought to confirm if engineered cells would likewise possess enhanced metastatic potency. We induced experimental metastasis by tail vein injection in C57BL/6 mice of three conditions: B16F0 cells cultured on glass, B16F0 cells cultured on NP gels, and B16F0 cells cultured on spiral patterned gels. After 5 and

10 days, a cohort of mice were sacrificed and histopathology performed on the lungs with metastatic burden calculated as a normalized percent tumor surface area. B16F0 cells cultured on spiral patterns show higher metastatic burden compared with those cultured on glass or NP (Fig. 7.19e and 7.21a and b). Correspondingly, Kaplan-Meier analysis demonstrates that mice inoculated with 3.0 x 104 F0 cells cultured on NP or glass survived the longest, while cells grown on spiral geometries demonstrated truncated survival times (Fig. 7.19f). We measured early stage (Day 10) B16 F0 proliferation after metastasis (2.5 x 10^5 cells) and found similar proliferation albeit slightly higher for cells inoculated from the NP gel condition (Fig. 7.19e and 7.21c).

Considering the significantly higher tumor burden observed in lungs from mice inoculated with patterned cells, this suggests metastatic burden does not arise from increased proliferation, but rather from improved survival characteristics consistent with increased tumorigenicity. We also performed experimental metastasis to compare B16F0 cells with the highly metastatic B16F10 cells cultured on glass. Kaplan-Meier analysis shows that mice inoculated with B16F0 cells survived the longest, with comparable truncated survival times for B16F10 cells and B16F0 cells grown on spiral patterns (Fig. 7.19g and Fig. 7.21d). We have shown how interfacial geometry can activate a stem-cell state in vitro (Fig. 7.9); however, our in vivo experiments with the spiral-patterned gels remain inconclusive as to whether curvature or the sole presence of the interface regulates cancer-cell state. Future work exploring cells patterned in other shapes that isolate positive and negative curvature may prove useful in discerning how subtle changes in perimeter

geometry may guide tumorigenicity. Furthermore, it remains to be demonstrated whether curvature at the interface in a growing tumor will prime a highly metastatic cancer stem-cell state.

To ascertain whether the influence of geometry may prove to serve as a universal tumorigenicity guidance cue, we immunostained several other cancer types for the generation of heatmaps. Similar to murine B16F0 and B16F10 melanoma cells, several human cancers; human HELA (cervical), A549 (lung), and PC3 (prostate) cell lines, all showed similar trends in CSC marker expression on 10 kPa gels (Fig. 7.22). These findings suggest that interfacial geometry may prove to be a general biophysical phenomena underlying cancer cell progression within a microenvironment.

7.4 Conclusion

Our results demonstrate how the interfacial constraints imposed by perimeter geometric features in a population of tumor cells can guide cancer cells towards a stem cell like state. In vivo, the balance between intercellular adhesion and cortical tension act together to specify tissue surface tension (79) which regulates the local behavior of groups of cells (154, 155). Similarly, the state of a tumor cell in a multicellular aggregate may depend on the interplay between force balance, cellular tension, intercellular adhesion and relative position with respect to other cells (156). In line with this hypothesis, we find that perimeter curvature can coordinate the spatial arrangement of cells by modifying interfacial energy, cortical tension, and intercellular adhesion. We show that this coordination can foster a unique

microenvironment where integrin mediated adhesion and mechanotransduction activates a cancer stem cell phenotype. Our findings are in contrast to previous studies where “stemness” is promoted in regions of low mechanical tension (42, 116), which suggests interfacial geometry may play a unique role in cancer through activation of a stem-like cell with a role in metastasis. This finding may help guide clinical analysis of the tumor microenvironment during biopsy or resection, and may lead to advances in the design, development and translation of patient specific models of oncogenesis for personalized therapeutic development.

7.5 Figures

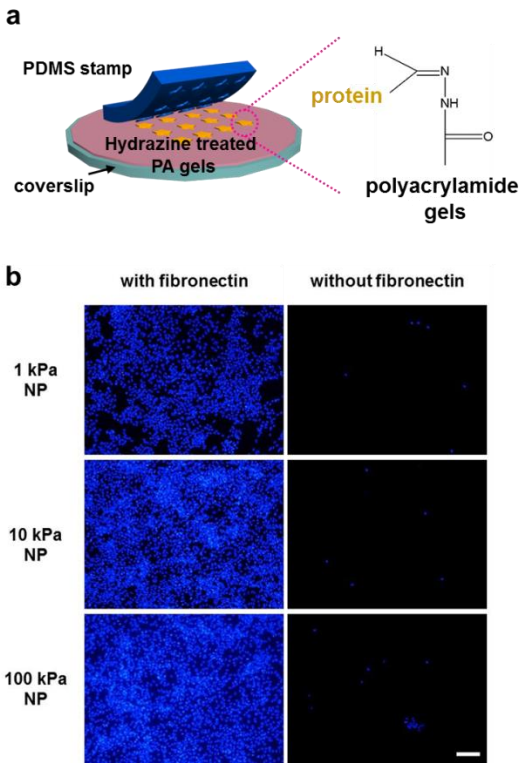

Figure 7.1 Tunable polyacrylamide hydrogel fabrication and conjugation. *a, Proteins are patterned on the surface of hydrazine activated polyacrylamide gels using PDMS stamps. b, Representative immunofluorescence microscopy images of murine B16 cells cultured on polyacrylamide hydrogels with or without protein conjugation. Staining for cell nuclei (blue). Scale bar: 100 μm.*

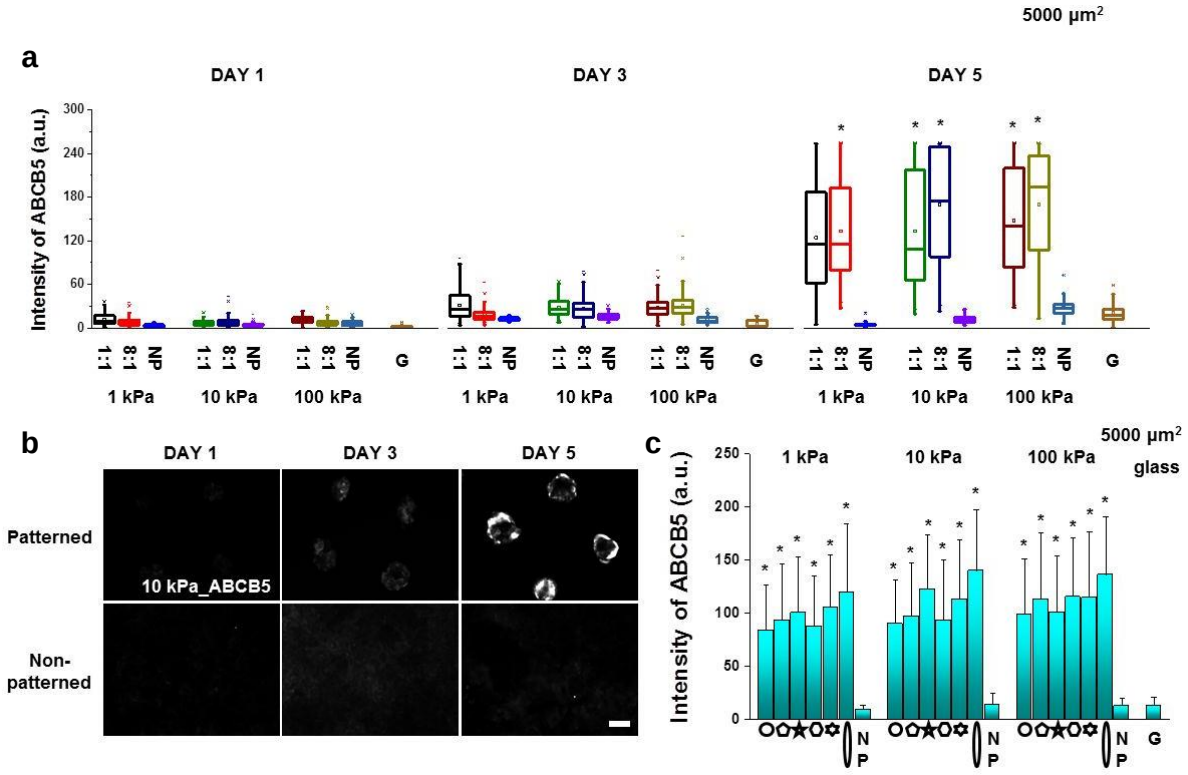

Figure 7.2 Cancer stem cell marker expression of B16 cells is influenced by culture time and geometry. *a, Expression of cancer stem cell marker (ABCB5) depends on culture time for different combinations of matrix stiffness and various geometries (1:1 and 1:8 aspect ratio shapes; 5,000 μm^2). (N=3, * P<0.05, Fisher's exact test compared to glass). b, Representative immunofluorescence microscopy images of ABCB5 expression for B16F10 cells on circular patterns (5,000 μm^2) or non-patterned surfaces with culture days. c, Quantitation of ABCB5 marker expression for B16F10 cells cultured for 5 days on different matrix elasticity and shapes (5,000 μm^2). (* P<0.05, Fisher's exact test compared to the glass control). (N=3, * P<0.05, Fisher's exact test compared to glass). Error bars represent standard deviation. Scale bar: 50 μm.*

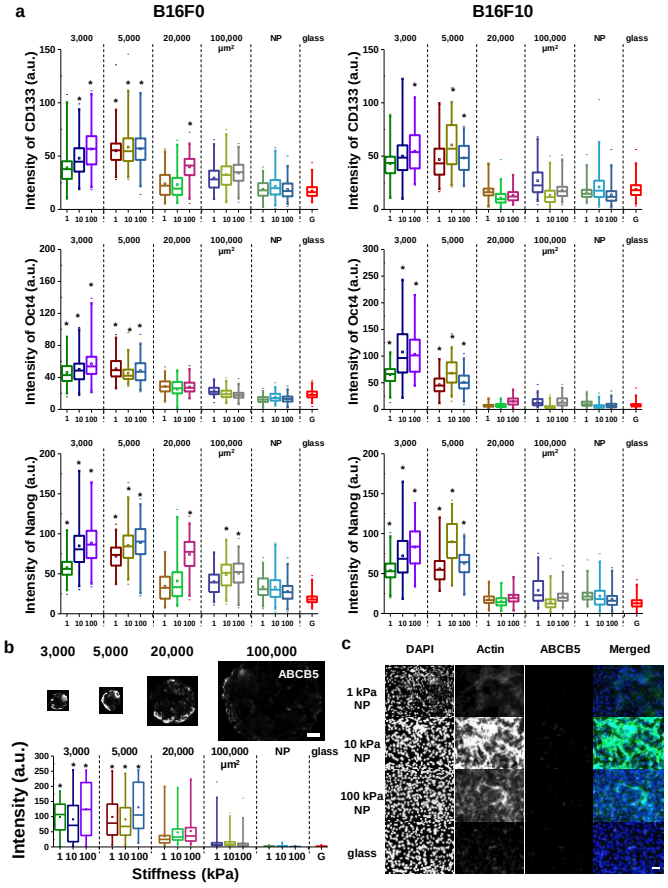

Figure 7.3 Micropatterning tumor cells reveals an optimal size and curvature that guides expression of cancer stem cell and pluripotency markers in B16F0 and B16F10 cells. *a, Expression of cancer stem cell (CD133) and pluripotency (Oct4 and Nanog) markers for B16F0 and B16F10 cells cultured for 5 days on different matrix elasticity and pattern sizes (3,000-100,000 µm^2 and NP). (N=3, * P<0.05, Fisher's exact test compared to glass). b, Representative immunofluorescence images and expression of the cancer stem cell marker ABCB5 for B16F0 cells cultured for 5 days on different size circular patterns (3,000-100,000 µm^2) or non-patterned cells on different stiffness gels (1-100 kPa) and glass. (N=3, * P<0.05, Fisher's exact test compared to glass). c, Representative immunofluorescence microscopy images of B16F0 cells (5 days) on non-patterned surfaces (1-100 kPa) and glass. No significant difference was observed between the non-patterned and glass conditions. (* P<0.05, Fisher's exact test compared to the glass control). Error bars represent standard deviation. Scale bars: 50 µm.*

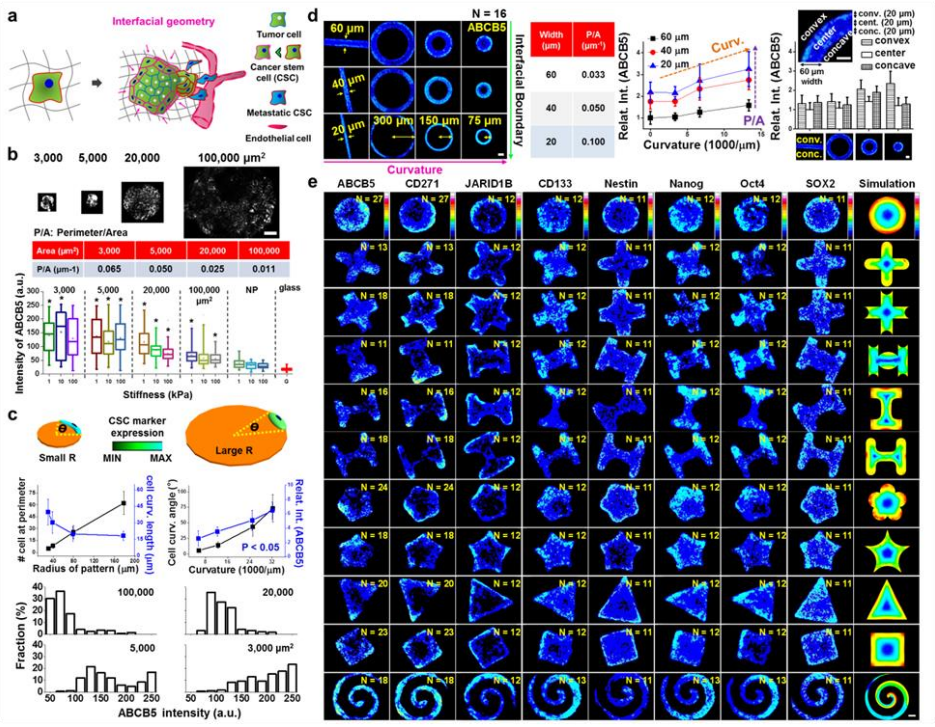

Figure 7.4 Interfacial geometry at perimeter features directs expression of cancer stem cell markers. *a, Schematic depicting how extracellular matrix properties may guide tumorigenicity. b, Increasing micropattern size shows optimal curvature that guides expression of cancer stem cell markers in B16F0 cells (N=3, * P<0.05, Fisher's exact test compared to glass). c, Curvature influences expression of cancer stem cell molecular markers. Intensity of ABCB5 shown as fold change over the NP condition (N=3). (P-value from ANOVA analysis) d, Shapes controlling line width, curvature and perimeter to explore the relationship of interfacial geometry and expression of cancer stem cell markers (N=3). e, Immunofluorescence heatmaps of B16F0 cells cultured in a panel of shapes with variable perimeter geometric features showing semi-quantitative localization characteristics for cancer stem cell surface markers (ABCB5, CD271, CD133), slow-cycling related demethylase enzyme (JARID1B), intermediate filaments (Nestin) and transcription factors (Nanog, Oct4, Sox2). Far right column shows finite element models of perimeter stress in cellular sheets. Scale bar 50 µm. Error bars represent standard deviation.*

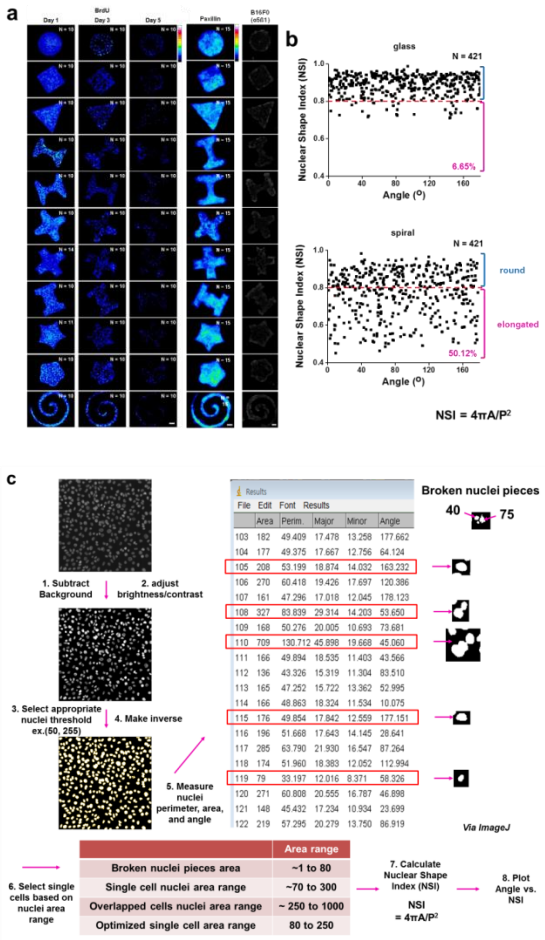

Figure 7.5 Analysis of cell and nuclear shape, proliferation characteristics and integrin expression levels show marked differences in perimeter cells consistent with enhanced invasiveness. *a, Immunofluorescence heatmaps of B16F10 cells cultured in a panel of 2D shapes for > 10 patterns shows a semi-quantitative decrease in proliferation (BrdU) dependent on culture time, no geometric effect on focal adhesion (Paxillin) expression and enhanced expression of α5ß1 integrins on B16F0 cells at the perimeter of geometric features. Scale bar: 50 μm. b, Nuclear shape index (NSI) and alignment of B16F0 and B16F10 cells (N=421 each) cultured on glass or spiral patterned substrates. We quantified nuclear elongation by calculating the NSI according to the formula, NSI = $4\pi A/P^2$, where A is projected nuclear area and P is nucleus perimeter. c, A flow chart to describe how NSI data is filtered by nuclear area.*

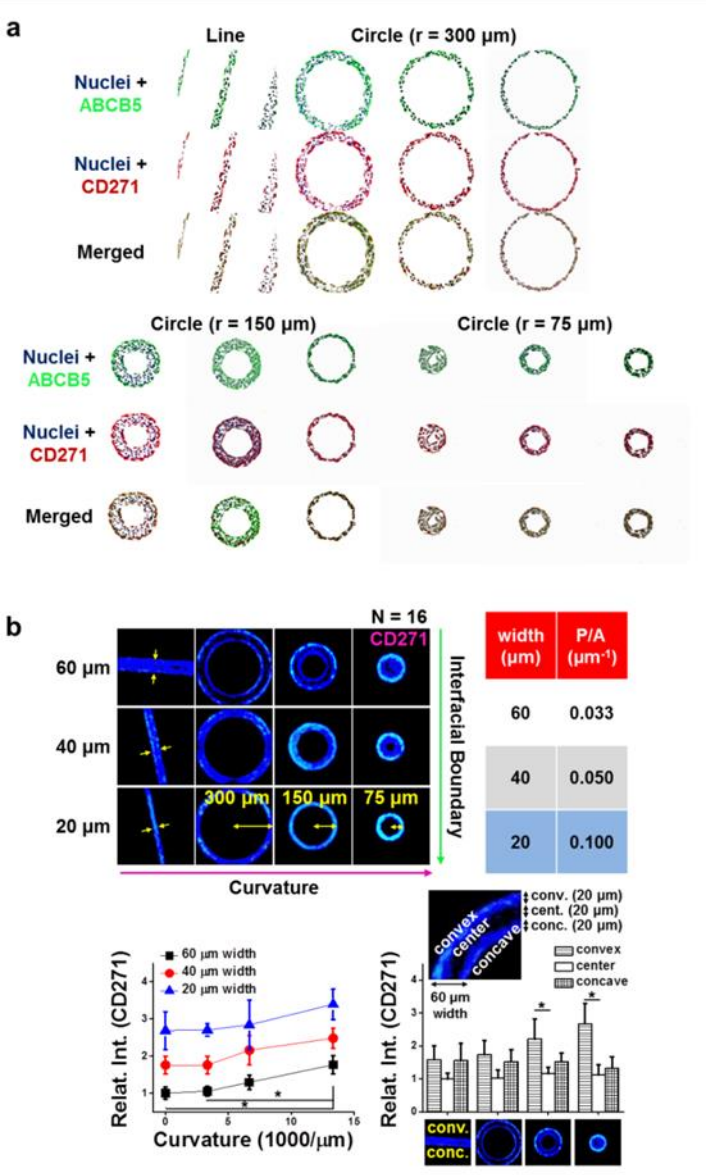

Figure 7.6 Interfacial geometry (interfacial energy, perimeter stress and curvature) influences the expression of cancer stem cell markers. *a. Representative immunofluorescence confocal microscopy images of B16F0 cells cultured for 5 days on polyacrylamide hydrogels with various shapes (circle, flower, H, square, triangle, spiral, and non-pattern) stained with Nuclei (blue), ABCB5 (green), and CD271 (red). b. Effects of interfacial energy and curvature on cancer stem cell marker expressions (CD271). (N=3) *P < 0.05 based on ANOVA with Tukey HSD Post-hoc testing.*

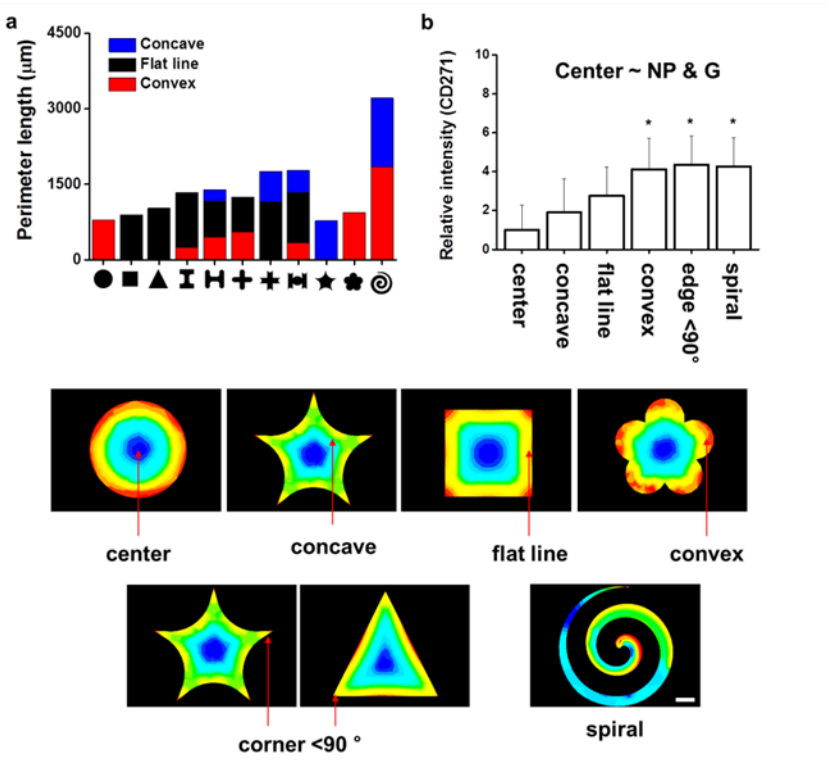

Figure 7.7 Quantitation of perimeter geometric features reveals variable intensity of cancer stem cell markers as a function of region. *a, Perimeter length (50,000 µm^2) and predicted relative contractile stress of shapes consisting of concave and convex curves and flat lines, individually or presented together. b, Relative intensity of cancer stem cell marker expression (CD271) for B16F10 cells cultured for 5 days on different shapes. Intensity of central regions is similar to that of non-patterned cells and the glass controls. (N=3) (* P<0.05, Fisher's exact test compared to center). (NP: Non-pattern, G: Glass) Scale bar: 50 µm.*

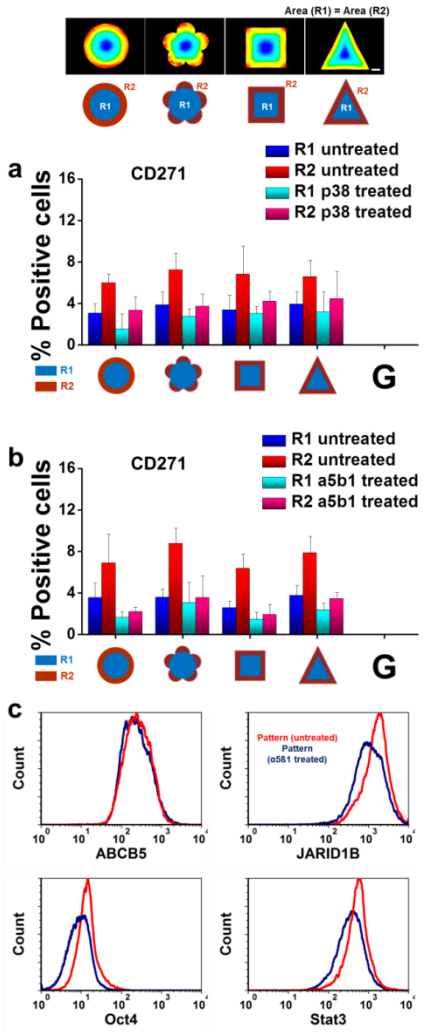

Figure 7.8 Regional analysis of cancer stem cell markers demonstrates enhanced perimeter expression. *a, CD271 expression in B16F0 cells upon treatment with pharmacological inhibitors of the p38 MAPK pathway. (N=3) b, CD271 expression in B16F0 cells upon treatment with antibodies against integrin α5β1. (N=3) c, Flow cytometry characterization of markers associated with cancer stem cell state (ABCB5 and JARID1B), pluripotency (Oct4) and Stat3 in B16F0 cells with or without treatment with antibodies against integrin α5β1.*

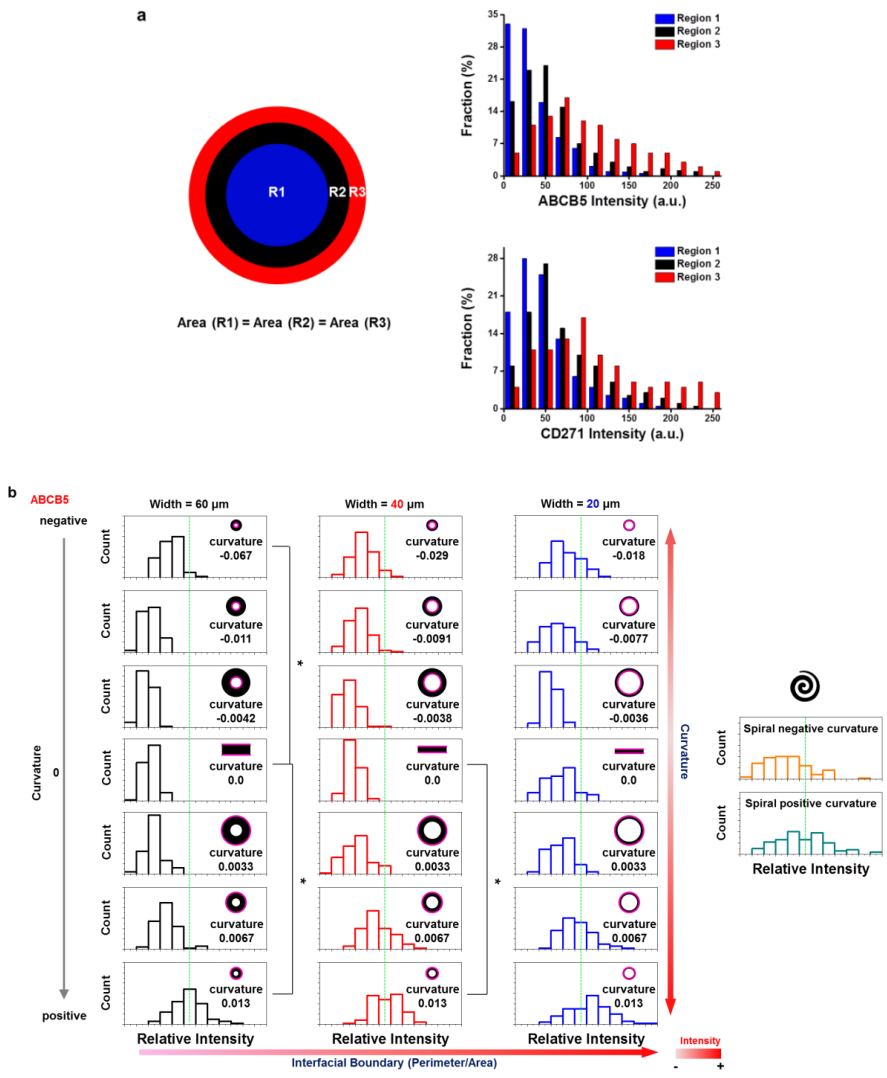

Figure 7.9 Topographically-annotated intensities at the single cell level for B16F0 cells adherent to regions spanning positive and negative curvature. *a. Single cell analysis of ABCB5 and CD271 across three different regions (of the same area) in the 50,000 um^2 circular patterns. b. Single cell analysis of ABCB5 expression in B16F0 cells presented with perimeter regions of positive and negative curvature using torus, line and spiral shapes. c. Single cell analysis of CD271 expression in B16F0 cells presented with perimeter regions of positive and negative curvature using torus, line and spiral shapes. (N=3) d. Comparison of Curvature and Perimeter/Area for spiral and torus geometries. (N=3) e. Segmented single cell analysis of immunofluorescence images of CD133, Jarid1B, Oct4, Nanog, and Stat3 in B16F0 cells presented with perimeter regions of positive and negative curvature using torus (60 um width), line (60 um width) and spiral shapes. (N=3) Intensity versus curvature plots depict average data across line and torus shapes, with the average intensity of the spiral depicted in red. Bottom: representative immunofluorescence images. (* P<0.05, Fisher's exact test compared to straight interface)*

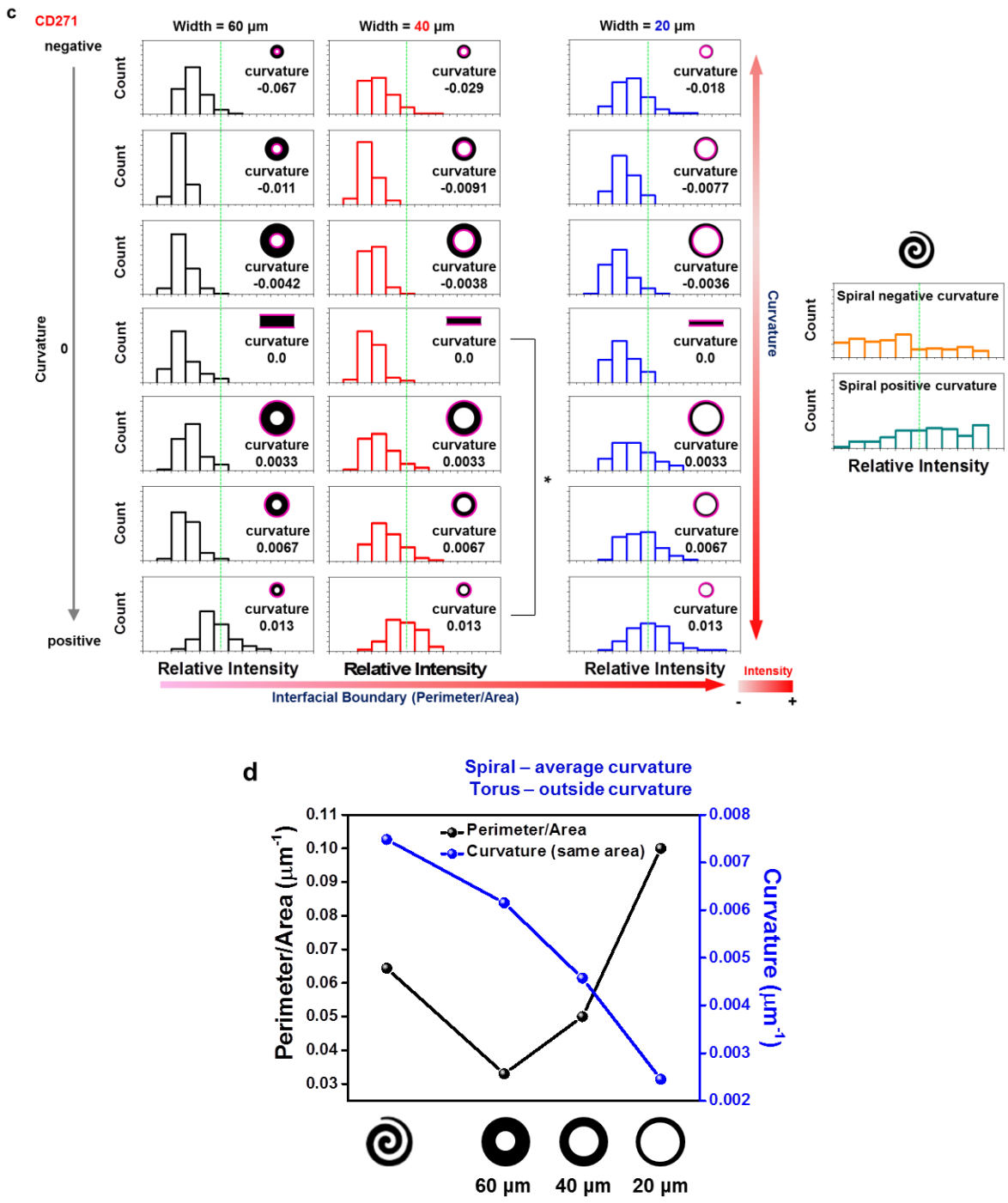

Figure 7.9 (cont.)

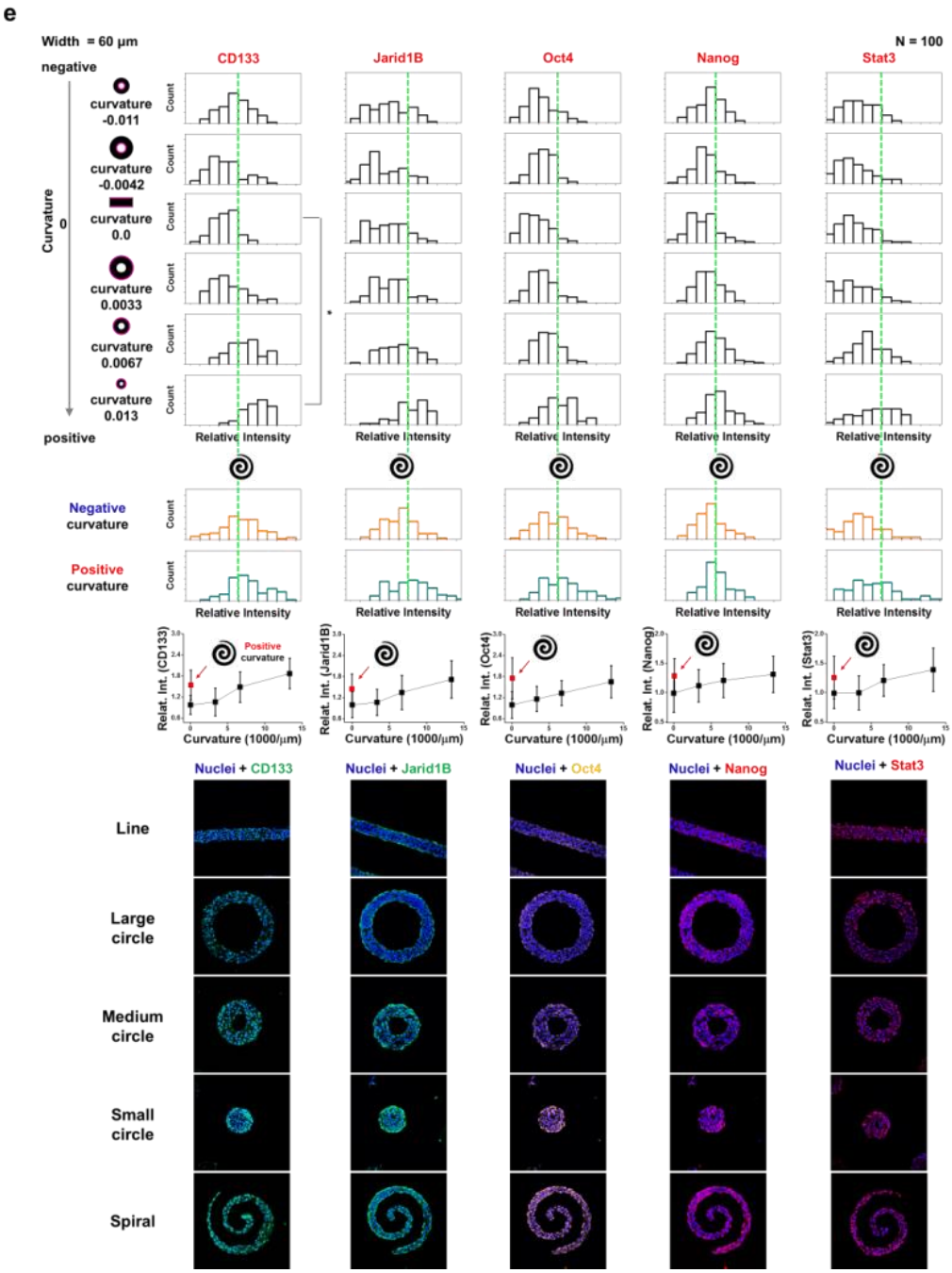

Figure 7.9 (cont.)

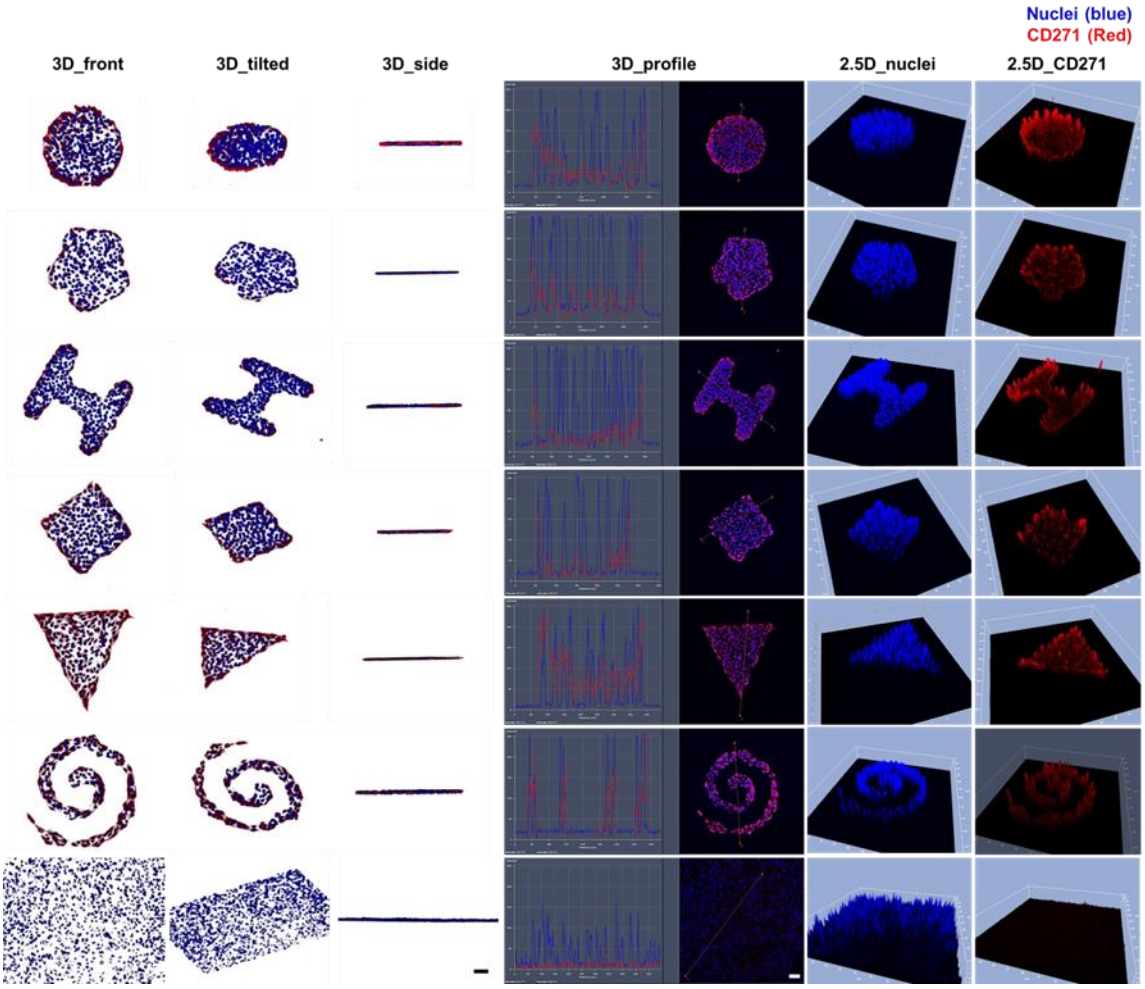

Figure 7.10 Expression of cancer stem cell markers in B16 melanoma cells at the perimeter is not influenced by cell density. *Representative immunofluorescence confocal microscopy images (3D and 2.5D) of B16F0 cells cultured for 5 days on polyacrylamide hydrogels with various shapes (circle, flower, H, square, triangle, spiral, and non-pattern) stained with Nuclei (blue) and CD271 (red). Analysis demonstrates uniform cell density across the geometry with perimeter intensity showing a marked increase at the perimeter. Scale bar: 50 μm.*

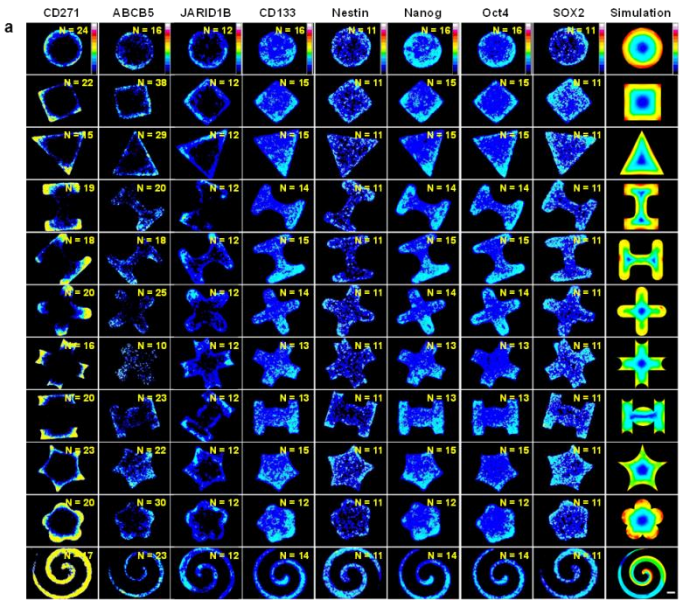

Figure 7.11 Expression of cancer stem cell markers for murine B16 melanoma cells is influenced by perimeter curvature. *a, Immuofluorescence heatmaps of B16F10 cells cultured for 5 days for at least 10 patterns showing semi-quantitative localization characteristics for cancer stem cell surface markers (ABCB5, CD271, CD133), the slow-cycling related demethylase enzyme JARID1B, the intermediate filament Nestin and the transcription factors (Nanog, Oct4, Sox2). Far right column shows finite element models of contractile stress in cellular sheets. b, Representative immunofluorescence microscopy images of B16F10 cells cultured for 5 days on polyacrylamide hydrogels with various shapes stained with Nuclei (blue), Actin (green), ABCB5 (yellow), and CD271 (red) for the left side and Nuclei (blue), CD133 (green), OCT4 (yellow), and Nanog (red) for the right side in merged images. c, Representative immunofluorescence microscopy with differential interference contrast (DIC) images of B16F10 cells stained with Nuclei (light blue), ABCB5 (yellow), and CD271 (Red). d, Representative immunofluorescence microscopy images of B16F10 cells cultured (5 days) on various patterns with different sizes (10,000 μm^2) stained with Nuclei (blue), Actin (green), and the cancer stem cell surface marker ABCB5 (yellow) in merged images. e, Representative immunofluorescence microscopy images of B16F0 cells cultured (5 days) on various patterns stained with Nuclei (blue), Actin (green), ABCB5 (yellow), CD271 (red) for the left side and Nuclei (blue), CD133 (green), OCT4 (yellow), and Nanog (red) for the right side in merged images. Scale bar: 50 μm.*

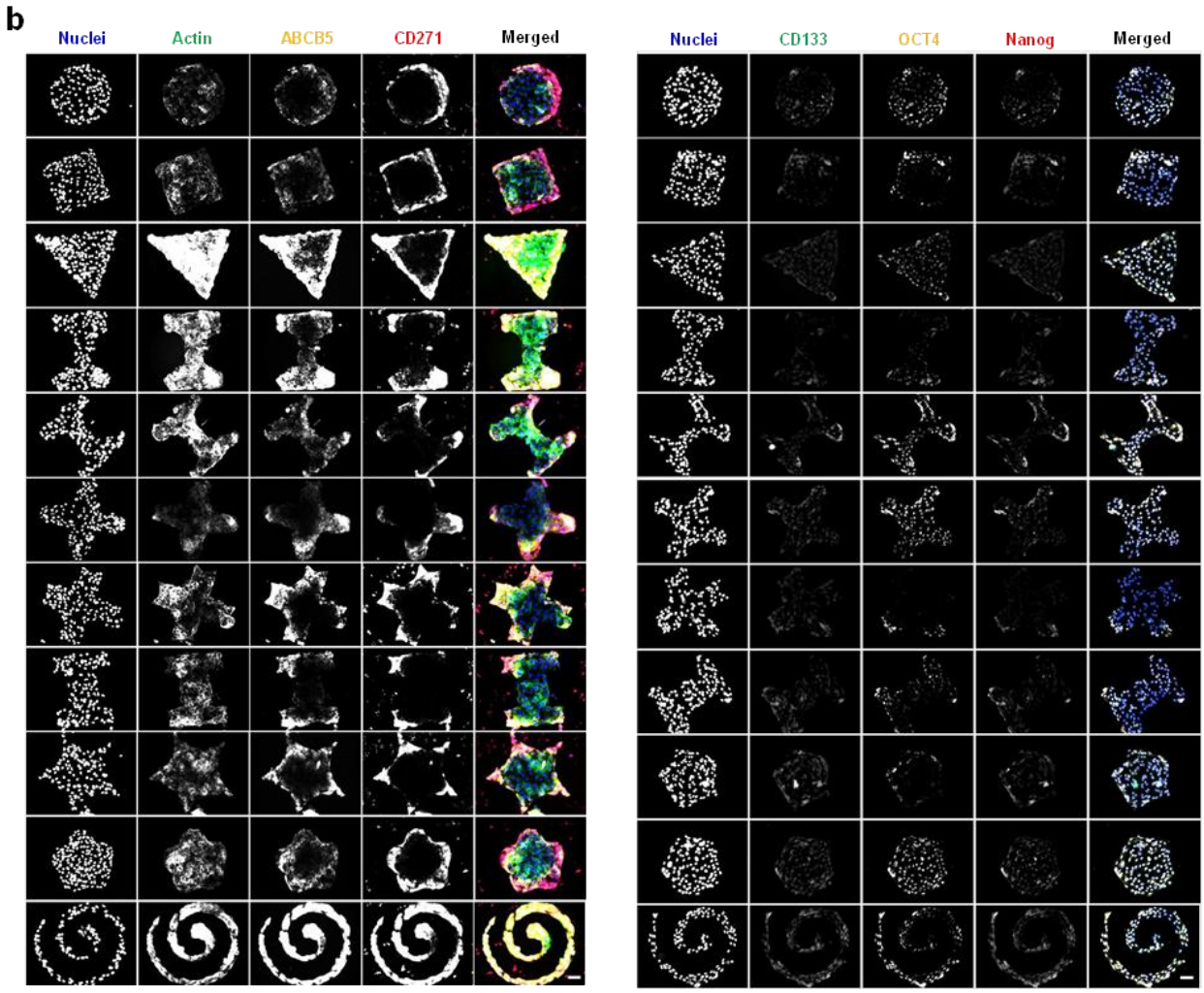

Figure 7.11 (cont.)

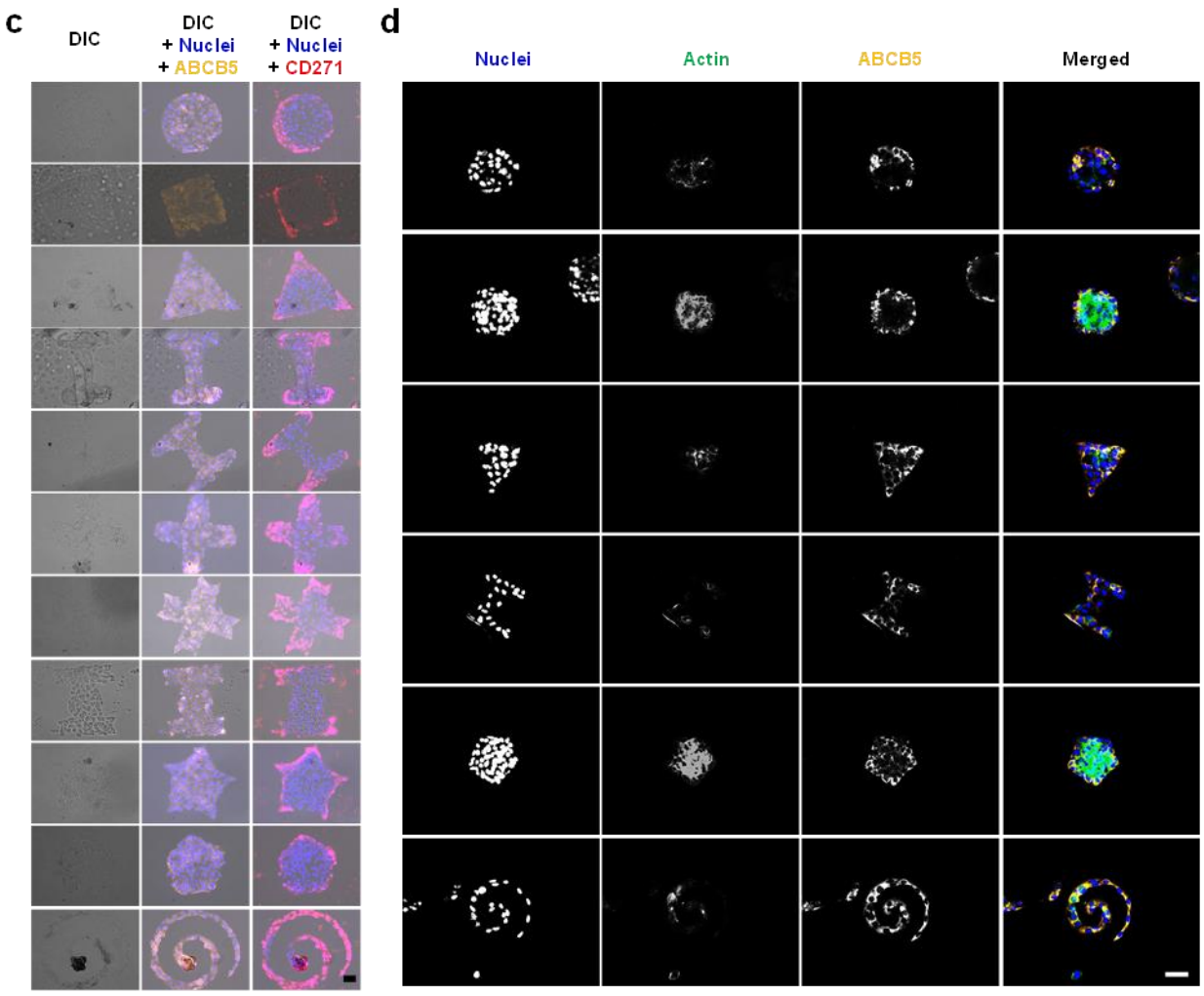

Figure 7.11 (cont.)

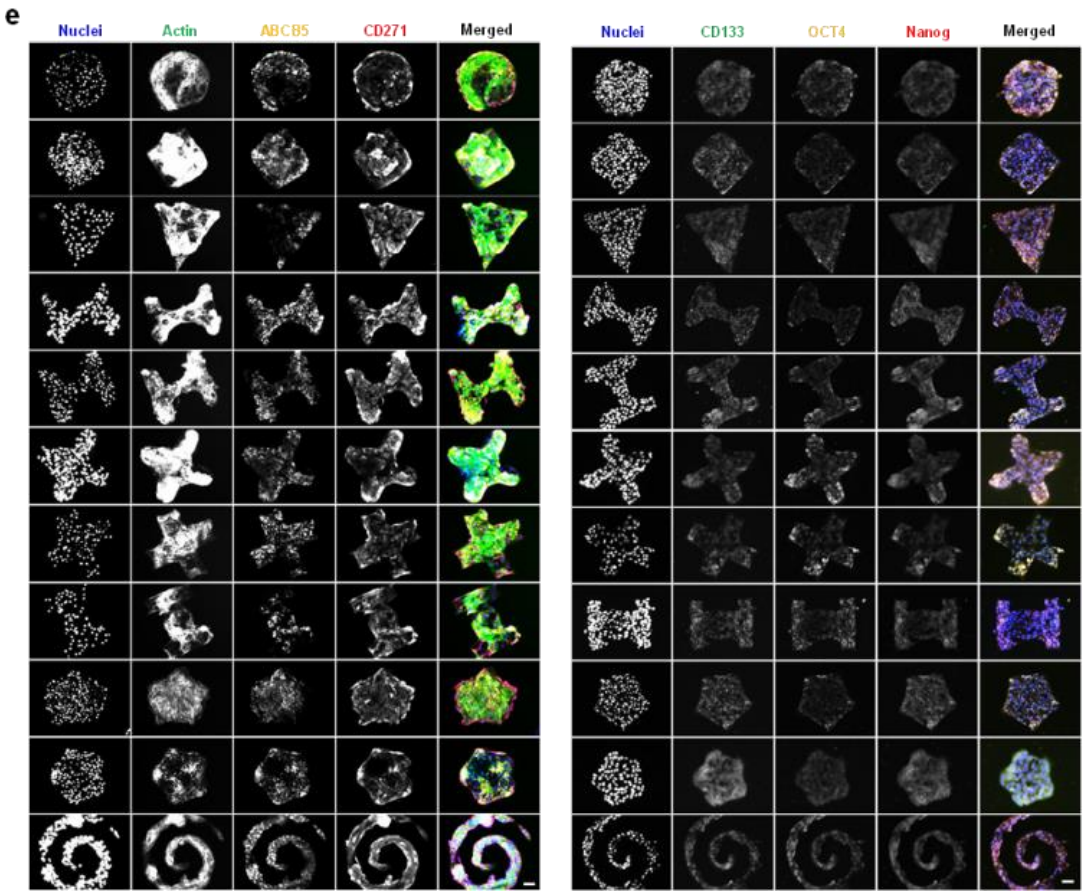

Figure 7.11 (cont.)

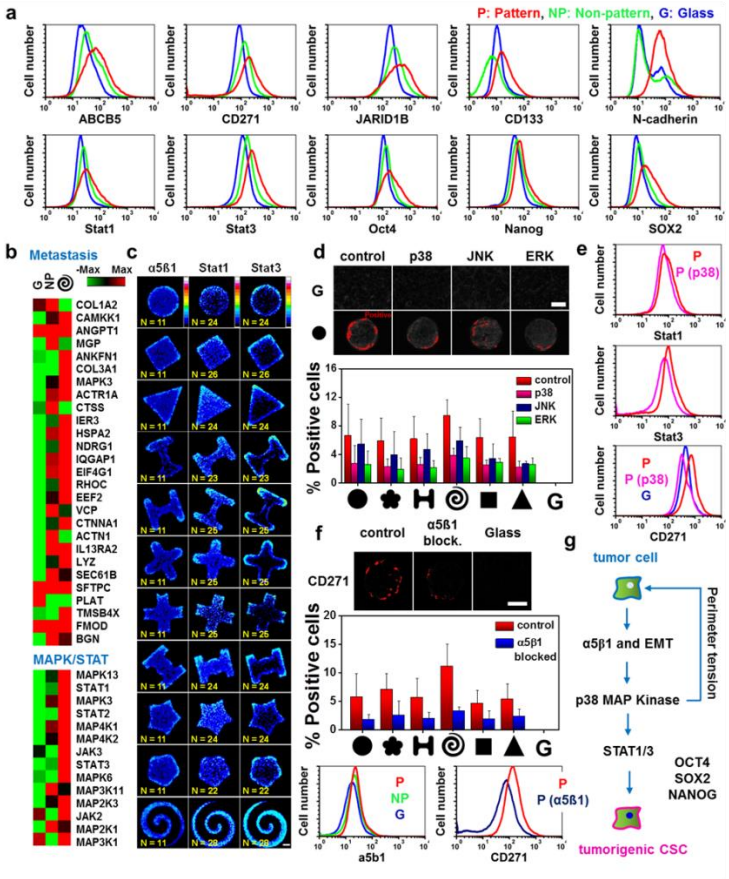

Figure 7.12 Geometric cues activate cancer stem cells at the perimeter through integrin α5β1, mitogen activated protein kinase (MAPK) signaling and regulation of signal transducer and activator of transcription (STAT) pathways. *a, Flow cytometry characterization of markers associated with epithelial to mesenchymal transition, cancer stem cell state and pluripotency in B16F0 cells. b, Gene expression analysis of transcripts associated with metastatic potential and MAPK/STAT signaling for cells cultured on glass (G) non-patterned hydrogel (NP) and spiral patterned hydrogel. c, Immunofluorescence heatmaps of Stat1 and Stat3 for B16F0 cells patterned on our panel of geometries. d, CD271 expression in B16F0 cells upon treatment with pharmacological inhibitors of MAPK pathways (N=3). e, Flow cytometry characterization of CD271, Stat1 and Stat3 positive cells with p38 inhibition. f, CD271 expression in B16F0 cells upon treatment with blocking antibodies against integrin α5β1 (N=3). g, Proposed pathway for interfacial geometry guiding tumorigenicity. Error bars represent standard deviation.*

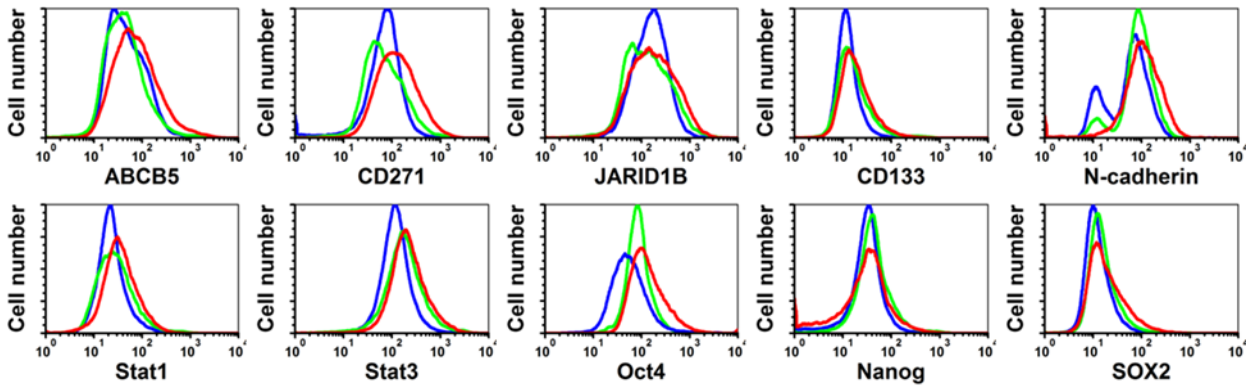

Figure 7.13 B16F10 cells cultured in spiral patterns show enhanced cancer stem cell characteristics in vitro. *Flow cytometry characterization of markers associated with epithelial to mesenchymal transition (N-cadherin), cancer stem cell state (ABCB5, CD271, CD133, JARID1B), pluripotency (Oct4, Nanog, SOX2, Nestin) and Stat1 and Stat3 in B16F10 cells. (P: Pattern (red), NP: Non-pattern (green), G: Glass (blue))*

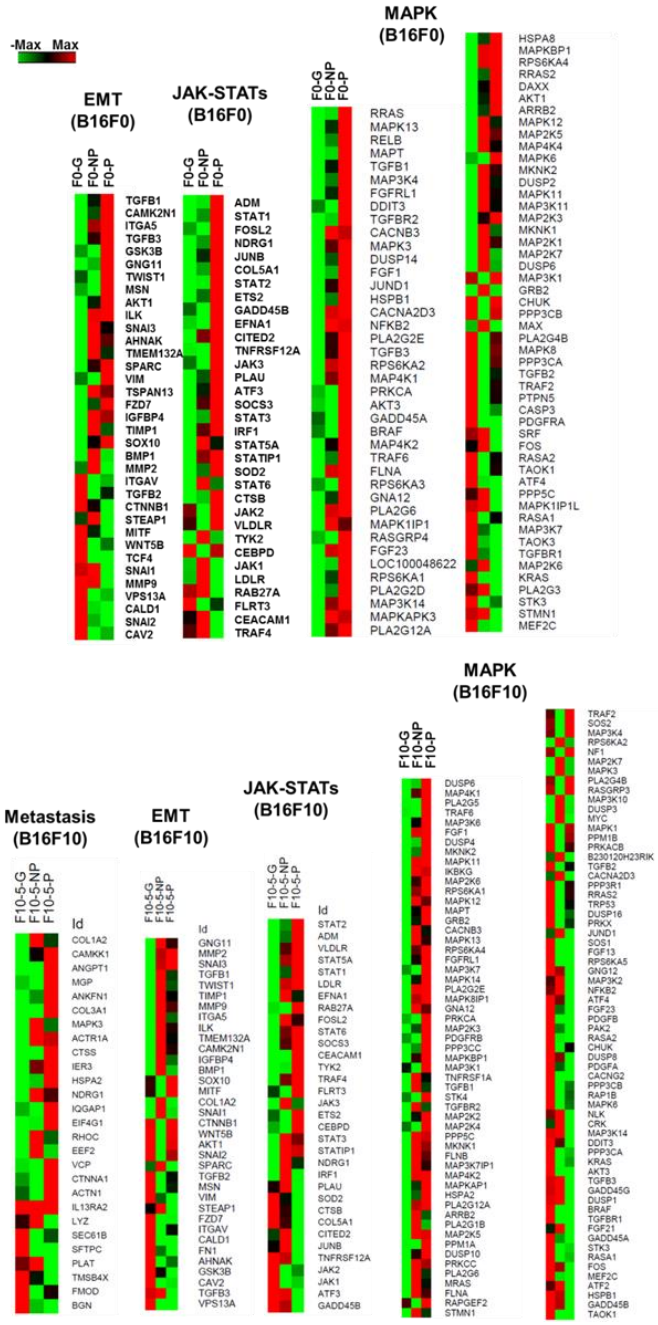

Figure 7.14 Gene expression analysis reveals several pathways influenced by matrix properties and geometry. *Gene expression analysis of transcripts associated with metastatic potential, endothelial to mesenchymal transition (EMT), JAK-STATs and MAPK signaling for B16F0 and B16 F10 cells cultured for 5 days on glass (G), non-patterned hydrogels (NP) and spiral patterned hydrogels.*

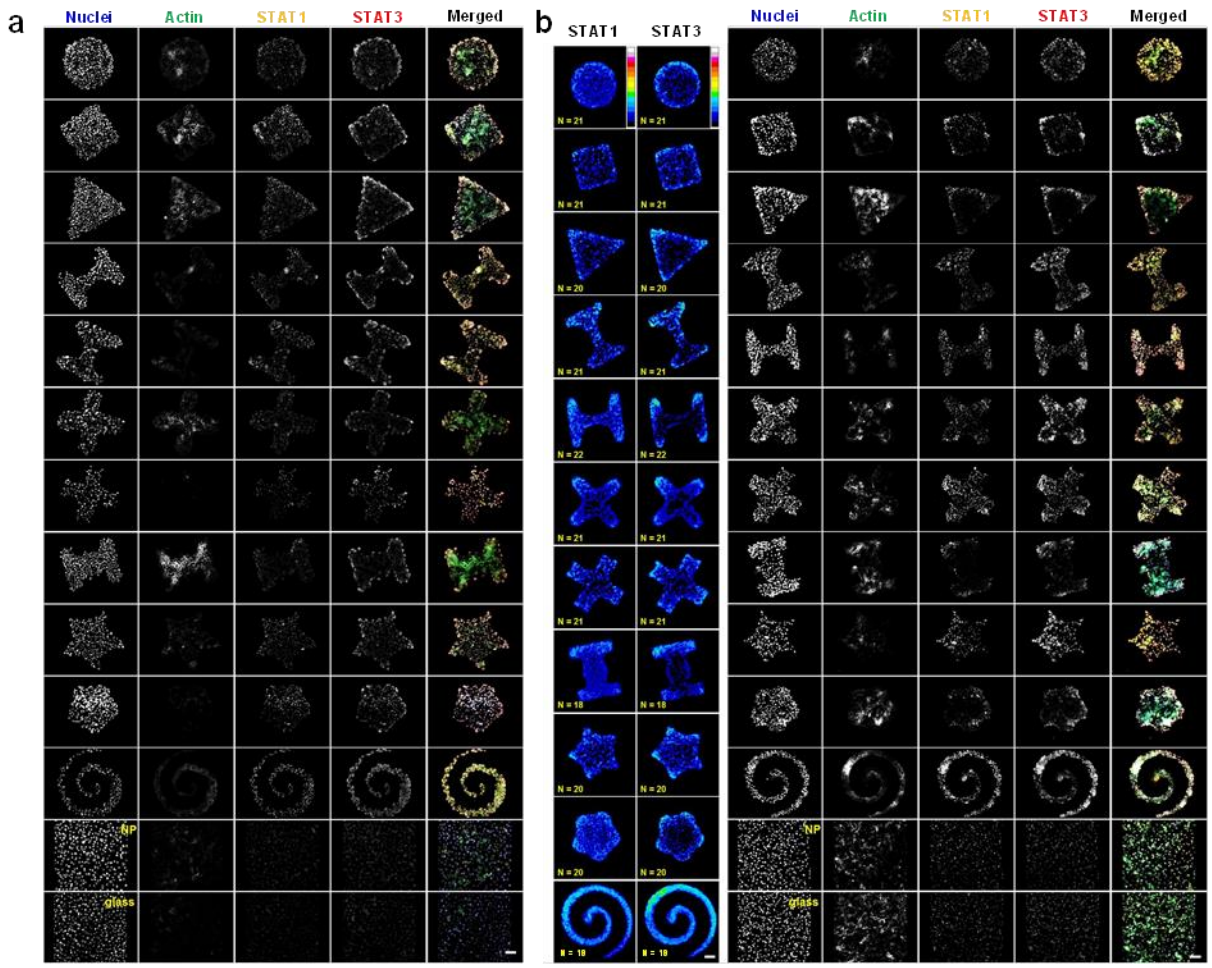

Figure 7.15 Interfacial geometry directs perimeter tumor cells through regulation of signal transducer and activator of transcription (STAT) pathways. *a, Representative immunofluorescence microscopy images of B16F0 cells cultured for 5 days on various geometries stained with Nuclei (blue), Actin (green), STAT1 (yellow), and STAT3 (red). b, Immunofluorescence heatmaps and representative immunofluorescence microscopy images of Stat1 and Stat3 for B16F10 cells patterned on our panel of geometries stained with Nuclei (blue), Actin (green), STAT1 (yellow), and STAT3 (red). Scale bar: 50 μm.*

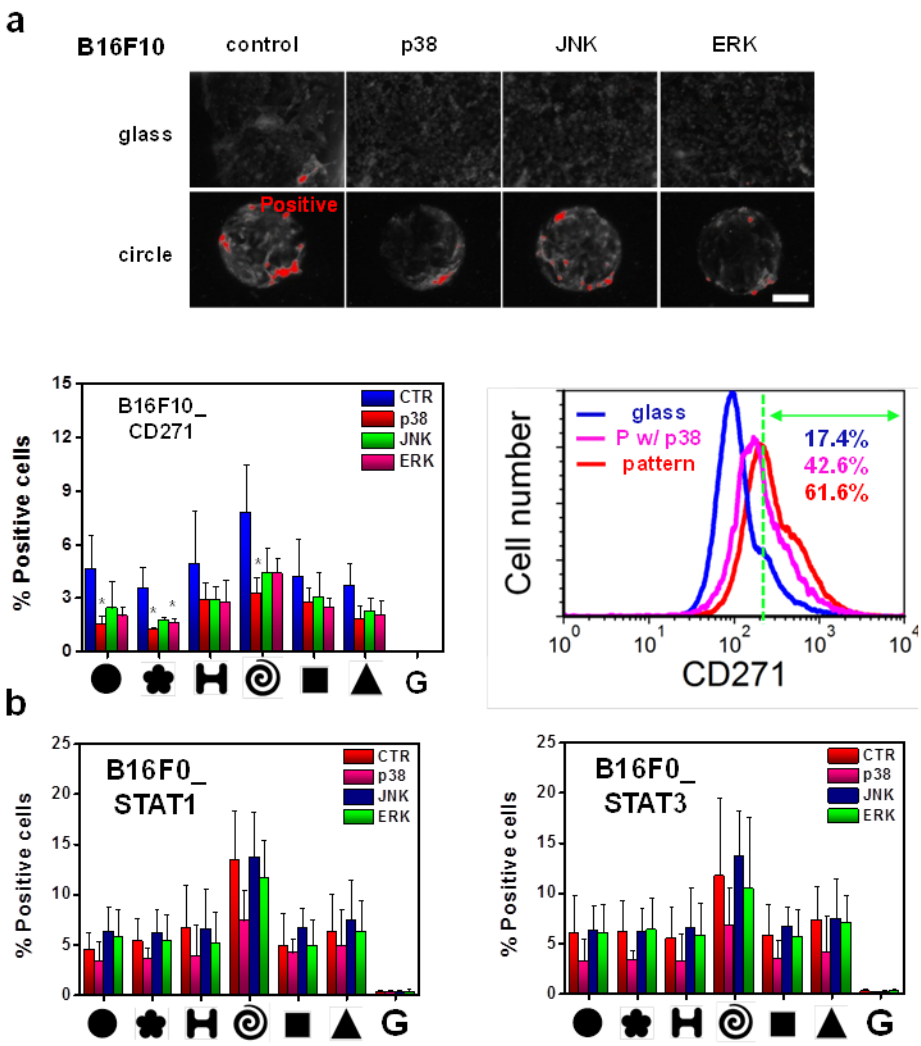

Figure 7.16 Mitogen activated protein kinase (MAPK) signaling and regulation of signal transducer and activator of transcription (STAT) pathways play an important role in the cancer stem cell state of perimeter cells. *a, CD271 expression in B16F10 cells upon treatment with pharmacological inhibitors of MAPK pathways and flow cytometry characterization of CD271 positive cells with MAPK inhibition. (N=3) b, Stat1 and Stat3 expression in B16F0 cells with MAPK inhibition. (N=3) Scale bar: 100 μm.*

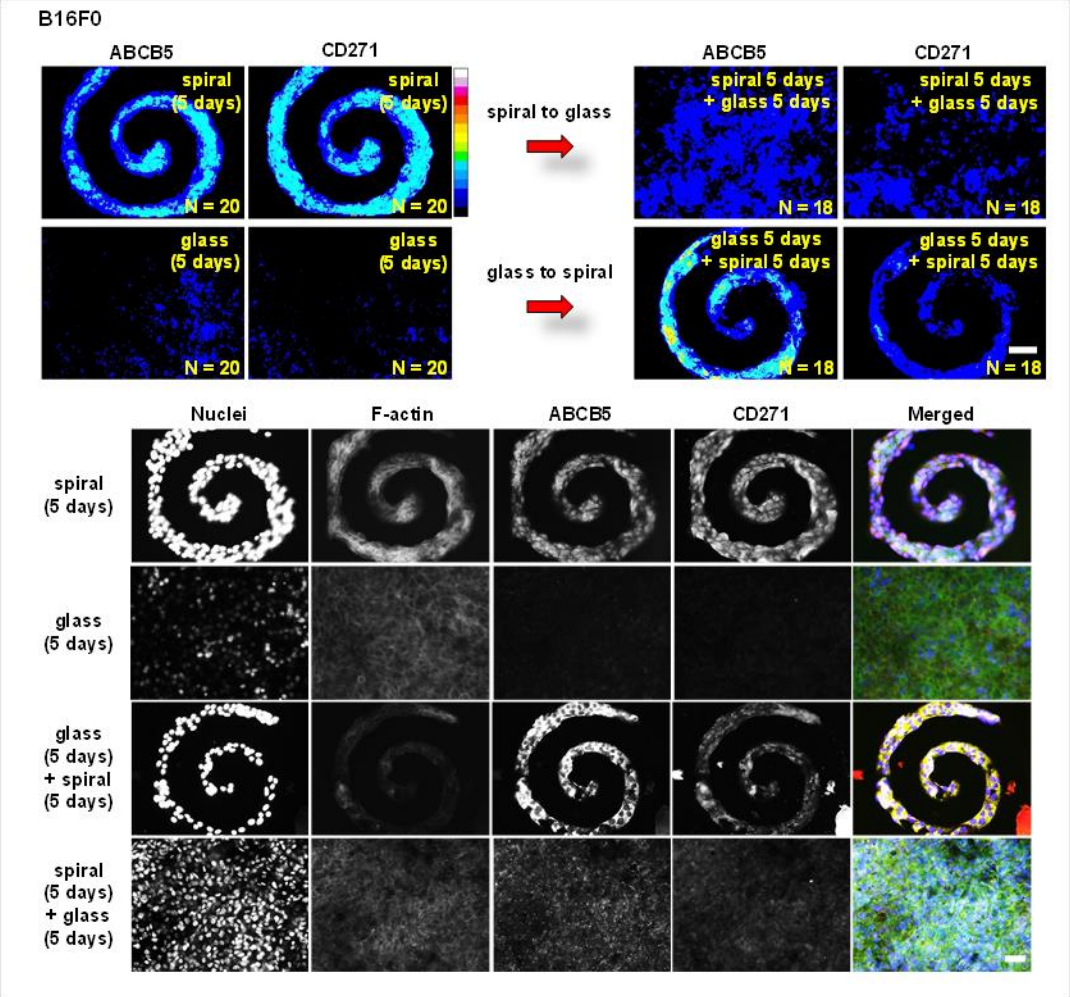

Figure 7.17 Cancer stem cell markers display plasticity when transferred between microenvironments. *(Top) Patterning-induced increase in expression of ABCB5 and CD271 show a partial decrease upon reseeding on glass for 5 days, while cells seeded on glass remain susceptible to perimeter features and demonstrate an increase of ABCB5 and CD271 expression. (Bottom) Representative immunofluorescence images of cells on spiral patterns and glass and of cells reseeded on the alternate condition. Scale bar: 50 μm.*

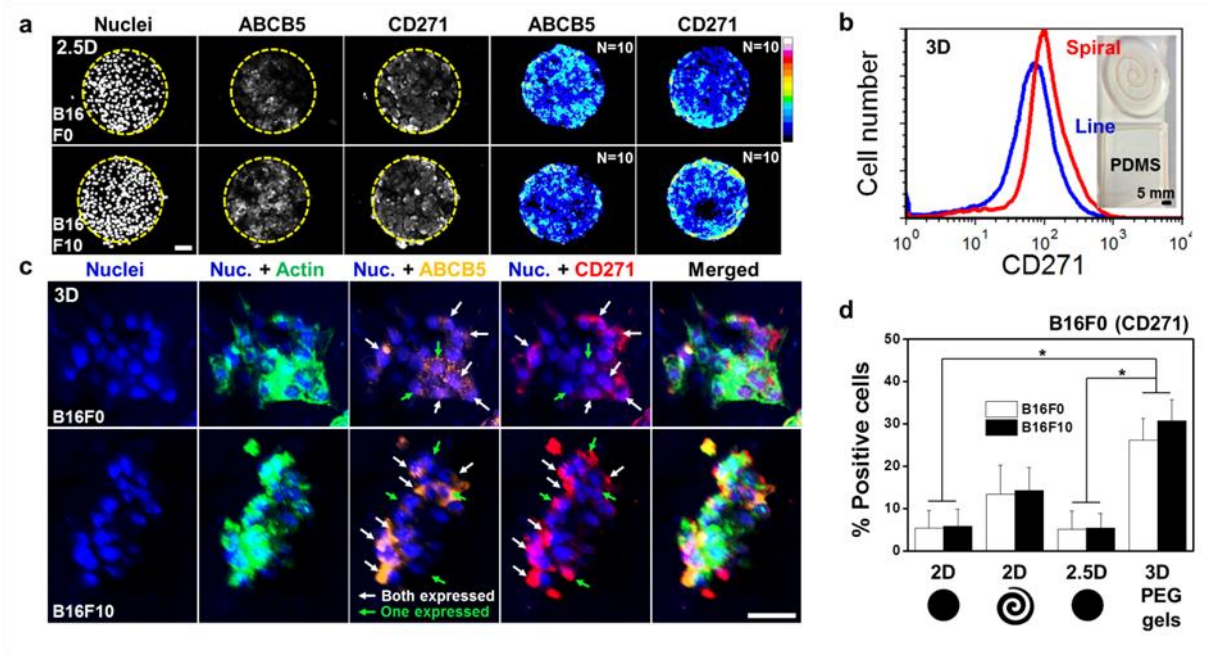

Figure 7.18 Cells encapsulated in model 3D microenvironments demonstrate interfacial regulation of the CSC phenotype. *a, Representative immunofluorescence microscopy images and immunofluorescence heatmaps of B16F0 and B16F10 cells captured within polyacrylamide (PA) 2.5D microwells with large areas (50,000 μm^2). b, Flow cytometry characterization of cancer stem cell markers expressed at the perimeter within a PDMS microfluidic device with 3D spiral and linear channels. c, Encapsulated B16F0 and B16F10 cells in MMP degradable PEG gels showing increased localization of cancer stem cell markers at the perimeter of aggregates. Approximately 30% of cells expressing either ABCB5 or CD271 did not express both cancer stem cell markers at the same time. d, The fraction of B16F0 cells positive for CD271 in different dimensional synthetic model systems. The glass control was used to generate thresholds of the marker intensity for different substrates (N=3). Scale bar 50 μm. (* P<0.05, Fisher's exact test). Error bars represent standard deviation.*

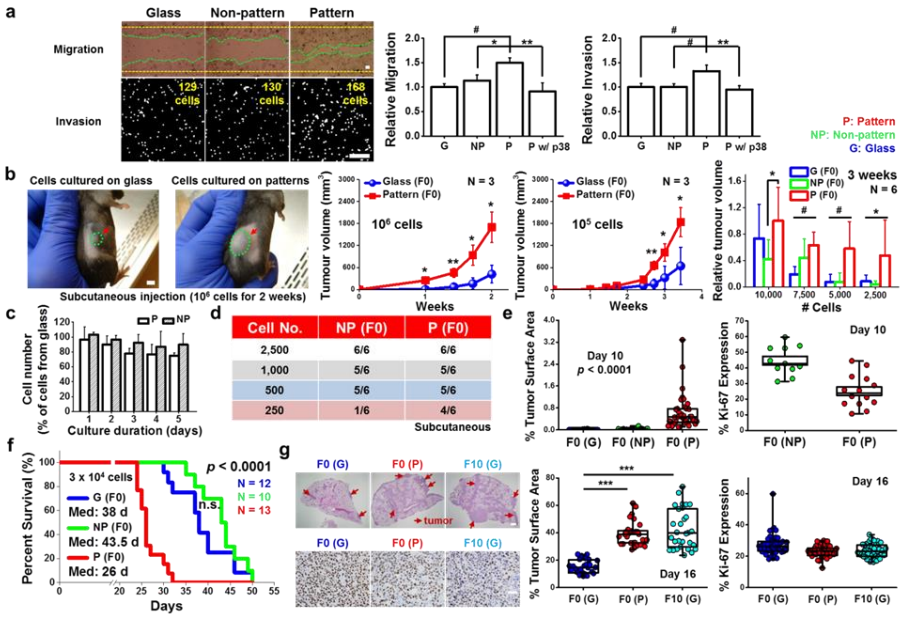

Figure 7.19 Activated cells show higher tumorigenicity and metastatic potency in vivo. *a, Wound healing and Boyden chamber invasion assays for B16F0 cells cultured on glass, non-patterned gels, spiral patterned gels, and on spiral patterned gels with p38 inhibition. Scale bar: 100 μm (N=3, *P < 0.05, #P < 0.01, **P < 0.005 based on ANOVA with Tukey HSD Post-hoc testing). b, Tumor growth characteristics of subcutaneous implanted cells in C57BL/6 mice. Scale bar: 5 mm. c, Proliferation characteristics of patterned and non-patterned cells relative to those cultured on glass (N=3). d, Tumorigenicity results after limited dilutions of B16F0 cells from non-patterned gels or spiral patterned gels after 60 days implantation in C57BL/6 mice. e, Tumor surface area (Day 10) and proliferation assessment through Ki67 staining (Day 10) of excised lung tissue after experimental metastasis. (P-value from ANOVA analysis, N used was # of lung sections) f, Kaplan-Meier analysis of C57BL/6 mice after experimental metastasis. (P-value from ANOVA analysis) g, Histopathology of lung sections after pulmonary metastasis and immunolabeling of excised lung tissue stained for Ki67 markers after tail vein injection of B16F0 cells cultured on glass or in the spiral geometry, compared to the highly metastatic B16F10 cells (positive: brown, negative: blue). (N used was # of lung sections, ***P < 0.0005 based on ANOVA with Tukey HSD Post-hoc testing). Error bars represent standard deviation except for Fig 7.19e & g where boxes represent 25th to 75th percentile and whiskers represent min-max. Scale bar: 1 mm for H&E and 50 μm for Ki67 staining.*

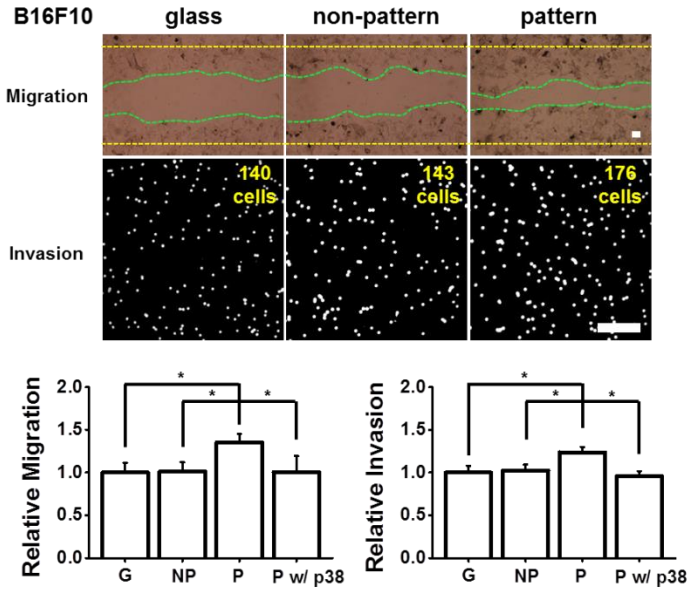

Figure 7.20 Cells from patterned surfaces show functional characteristics of malignant cancer cells in vitro. *Wound healing and Boyden chamber invasion assays for B16F10 cells on glass (G), non-patterned gels (NP), spiral pattern (P), and on spiral pattern with p38 inhibition. (N=3, *P < 0.05, based on ANOVA with Tukey HSD Post-hoc testing). Scale bar: 100 μm.*

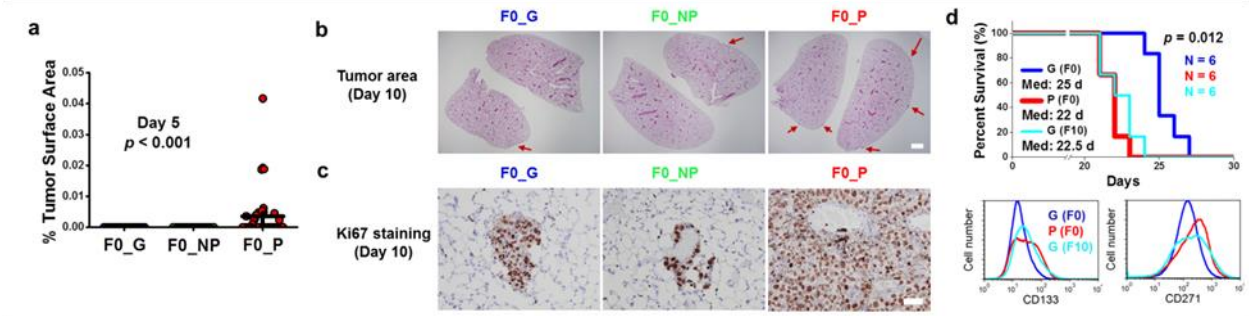

Figure 7.21 Patterned B16F0 cells show higher tumorigenicity in vivo. *a, Tumor surface area (Day 5) of excised lung tissue after experimental metastasis. (N used was # of lung sections, P < 0.001 based on ANOVA analysis) b, Histopathology of lung sections after pulmonary metastasis (Day 10). Scale bar: 1 mm. c, Immunolabeling of excised lung tissue stained for Ki67 markers (Day 10) (positive: red, negative: blue). Scale bar: 50 µm. d, Kaplan-Meier analysis of C57BL/6 mice survival characteristics after tail vein injection of B16F0 cells cultured on glass or in the spiral geometry, compared to the highly metastatic B16F10 cells. (P: Pattern, NP: Non-pattern, G: Glass)*

a

Cell line	Degree of spreading	Spreading difference in two regions (edge vs. center)	CSC markers (perimeter effect)	special note
B16F0 (mouse melanoma)	++	++	ABCB5(+), CD133(+), CD271(++), JARID1B(++)	Forming colony in center after confluence (~5dyas)
B16F10 (mouse melanoma)	++	+++	ABCB5(+), CD133(+), CD271(+++), JARID1B(+++)	Forming colony in center after confluence (~5dyas)
HELA (human cervical)	+	+	CD44(+), CD133(+)	Escape from patterns right after confluence
A549 (human lung)	+	+	CD44(+), CD133(+)	Forming multilayers after confluence
PC3 (human prostate)	+	+	CD44(+), CD133(+)	Forming multilayers after confluence

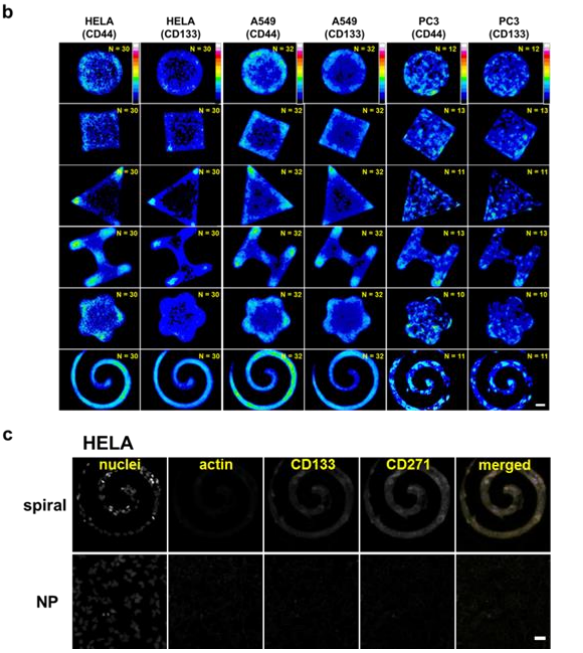

Figure 7.22 Interfacial geometry promotes increase in the expression of cancer stem cell markers at the perimeter of several human cancer cell lines. *a, A table showing different spreading characteristics for different cell lines. b, Immuofluorescence heatmaps of human cancer cell lines (HELA, A549 , PC3) cultured for 5 days for at least 10 patterns showing semi-quantitative localization characteristics for the cancer stem cell surface markers CD44 and CD133. b, Representative immunofluorescence images of HELA cells on spiral pattern and non-patterned gels. Scale bar: 50 μm.*

CHAPTER 8

MICROENVIRONMENT-MEDIATED HISTONE MODIFICATION PREDICTS PHENOTYPIC ALTERATION OF MELANOMAS[8]

8.1 Introduction

Epigenetics, defined as heritable change in gene expression occurring independent of changes in primary DNA sequence, is highly implicated in the underlying mechanisms of cell development and progression (157). Unlike the previous idea that cancer was initially recognized as a completely genetic disease, microenvironment-mediated epigenetic regulation of cancer-related gene expression through DNA methylation, histone modification, and chromatin compartments is also now believed to take part in a broad spectrum of the cancer behaviors ranging from initiation to phenotypic alteration (158). Histone modifications, including methylation, phosphorylation, and acetylation are covalent post-translational modifications to histone proteins. These modifications allow histones to alter the structure of chromatin, resulting in transcriptional activation or repression, affecting changes in cell behavior. For example, histone H3 lysine 4 di/tri-methylation (H3K4me2/3) and histone H3 acetylation (H3ac) are generally associated with gene activation (159), whereas H3K27me, which marks active cis-regulatory elements, is associated with gene inactivation (160).While the detection of cancer-specific changes through histone modifications as epigenetic biomarkers

[8] This chapter is adapted from the following publication:
Junmin Lee, Christopher Seward, Amr A. Abdeen, Huimin Zhang, Lisa J. Stubbs, and Kristopher A. Kilian, Microenvironment-mediated histone modification predicts phenotypic alteration of melanomas, (2017) *in preparation.*

has potential for clinical prediction, diagnosis, and therapeutic development, it remains elusive.

Malignant melanoma-initiating cells (MMICs) are sub-populations of cells in melanoma tumors with self-renewal potential and tumor initiating capacities (161). Unlike the clonal evolution model describing how a single cell accumulates genetic and epigenetic changes until becoming a cancer tumor cell, the cancer stem cell (CSC) model suggests a hierarchical organization (unidirectional) of cancer cells according to their tumorigenic potential that has important implications for cancer therapy with CSC-specific treatment regimens (147). However, accumulating evidence surrounding cancer plasticity supports a new emerging model of tumorigenecity, in which the potential for non-CSC reversion to CSC phenotypes exists due to epigenetic alterations which confer phenotypic plasticity to the tumor cell population (162). Recently, we and other groups have shown that cancer cells are more plastic than previously thought and non-CSC-to-CSC conversions are influenced by microenvironment-mediated epigenetic regulation such as pH (163), geometry (164), radiation (165), stiffness (166), and hypoxia (167). Hence we hypothesize that if non-MMICs could be activated into MMIC phenotypes at the margin topology of microenvironments, we might be able to identify specific histone modifications differentially regulated by activated cells and use those modifications to investigate potential mechanism underlying phenotypic alteration toward MMIC phenotypes.

8.2 Materials and Methods

Inhibition assay and siRNA:

Histone deacetylase (HDAC) inhibitors, valproic acid (VPA, Sigma-Aldrich (P4543)) sodium butyrate (NaB, Bio Vision (1609-1000)), or Trichostatin A (TSA, Sigma-Aldrich (T8552)) were added to cells in media before seeding and after changing media at 1 μg/ml, respectively. MAP kinase inhibitors for ERK1/2 (FR180204) and p38 (SB202190) (Calbiochem) were supplemented in the media at 6 μM after seeding cells and changing each media. Blocking integrin α5ß1 was performed by adding the antibodies to cells in media before seeding at 1μg/ml.

The siRNAs for Jarid1B (ID 75605, Trilencer-27 Mouse siRNA, siRNA A: SR422988A, siRNA B: SR422988B, and siRNA C: SR422988C) or scrambled siRNAs (SR30004) were purchased from OriGene. Transfection was performed according to the vendor's instructions. Lipofectamine 2000TM was employed for higher transfection efficiency. Cells cultured for 5 days in patterned substrates were treated with siRNA twice at day 1 and day 3.

RNA isolation and RT-PCR:

Adherent cells on patterned gels (12 identical substrates for each condition) were lysed directly in TRIZOL reagent (Invitrogen). Total RNA was isolated by chloroform extraction and ethanol precipitation and amplified using TargetAmpTM 1-Round aRNA Amplification Kit 103 (Epicentre) according to vendor protocols. Superscript III® First Strand Synthesis System for RT-PCR (Invitrogen) was employed to reversely transcribe total RNA. RT-PCR was performed using SYBR® Green Real-

Time PCR Master Mix (Invitrogen) on an Eppendorf Realplex 4S Real-time PCR system. All reactions were performed linearly by cycle number for each set of primers.

Cell labelling and flow cytometry:

B16F0 cells cultured for five days on spiral-patterned or non-patterned gels (12 identical substrates for each condition) were isolated from substrates by trypsin, followed by breaking down into a single cell suspension. Cells were fixed in 4% paraformaldehyde for 20 min and then permeabilized in 0.1% Triton X-100 in PBS for 30 min. After blocking cells in 1% BSA in PBS for 1 h, Cells were stained with primary antibodies in 1% BSA in PBS overnight at 4°C and then secondary antibodies in 2% goat serum, 1% BSA in PBS for 20 min in a humid chamber (5% CO2 and 37°C). Before every step, cells were rinsed at least three times with PBS. A BD LSR Fortessa Flow Cytometry Analyzer was used to perform flow cytometry analysis. To set the baseline, negative controls were prepared by staining cells without primary antibodies.

Microscopy data analysis:

Confocal images were analyzed using ImageJ software. Multiple cells were imaged for each condition and fluorescence intensities of single cells in different regions of patterns (after background subtraction) were used to compare marker expression. For generating immunofluorescence heatmaps, cells cultured on various shapes were fixed, stained, and imaged on the same day using the same settings. After subtraction of background intensities of raw fluorescent images, patterns were

aligned in ImageJ with the same orientation as cultured across the surface, followed by incorporating into a Z stack with the average intensity calculated for heatmap generation.

Chromatin immunoprecipitation and sequencing (Chip-seq):

H3K4me2 and H3K9ac ChiP samples were prepared from B16 melanoma cells cultured on patterned or non-patterned substrates, and ChiP DNA quality was verified as previously described (168). Cultures of B16 melanoma cells for five days were fixed with 1% formaldehyde final concentration for 10 min at room temperature. Fixations were quenched by glycine (125 mM), followed by washing cells with cold 1x PBS two times. Cells were treated with hypotonic lysis buffer for 10 min (20 mM HEPES at pH 7.9, 10 mM KCl, 1 mM EDTA at pH 8, 10% glycerol, 1 mM DTT, 0.5 mM PMSF, 0.1 mM sodium orthovanadate, and Roche protease inhibitors) and lysed by dounce homogenization (using pestle B). Collected nuclear pellets were lysed in in 1× RIPA buffer (10 mM Tris-Cl at pH 8.0, 140 mM NaCl, 1% Triton X-100, 0.1% SDS, 1% deoxycholic acid, 0.5 mM PMSF, 1 mM DTT, 0.1 mM sodium orthovanadate, and Roche protease inhibitors). Nuclear lysates were sonicated with a Branson 250 Sonifier (output 20%, 100% duty cycle) to shear the chromatin to ~1 Kb in size. Clarified lysates were incubated overnight at 4°C with anti-H3K4me2 or H3K9ac antibodies. Protein–DNA complexes were precipitated, immunoprecipitates were washed three times in 1× RIPA, once in 1× PBS, and then eluted from the beads by addition of 1% SDS, 1× TE (10 mM Tris-Cl at pH 7.6, 1 mM EDTA at pH 8), and incubation for 10 min at 65°C. Cross-links were reversed overnight at 65°C. Purification for all samples were performed by treatment first

with 200 μg/mL RNase A for 1 h at 37°C, then with 200 μg/mL Proteinase K for 2 h at 45°C, followed by extraction with phenol:chloroform:isoamyl alcohol and precipitation at −70°C with 0.1 volume of 3 M sodium acetate, 2 volumes of 100% ethanol, and 1.5 μL of pellet paint coprecipitant. ChIP DNA prepared from 1×10^7 cells was resuspended in 50 μL of ultrapure water. Sequencing was performed at the Roy J. Carver Biotechnology Center at the University of Illinois at Urbana-Champaign using standard Illumina protocols (http://support.illumina.com/content/dam/illumina-support/documents/myillumina/3466bf71-78bd-4842-8bfc-393a45d11874/wggex_direct_hybridization_assay_guide_11322355_a.pdf).

Statistical analysis:

Data were obtained at least three independent experiments. Error bars represent standard deviation around the mean. For comparing statistics between two groups or more than two groups, student's t-test or analysis of variance (ANOVA) with Tukey HSD Post-hoc testing, respectively, were employed. Differences were considered significant at $P<0.05$.

8.3 Results and Discussion

To classify histones linked to 'epigenetic switching' from non-MMIC to MMICs, we employed engineered biomaterials to generate MMIC phenotypes with topological cues such as curvature and perimeter/area ratio (Fig. 8.1 and 8.2). Cells cultured for five days at the periphery of geometries expressed higher levels of MMIC and stemness markers, giving them MMIC-like characteristics in vitro and in vivo (164).

Given this clue, we first investigated possible candidates for histone methylation. Histone H3 lysine 4 methylations (mono, di, and tri) were employed because these are known as active histone marks (159). In addition, Jarid1B (gene name: KDM5B) which is the histone lysine demethylase for H3K4me3/2/1 and has been known to play a distinct role in different cancer types (169). For example, overexpression of Jarid1B in the MDA-MB 231 breast cancer cells suppressed malignant characteristics such as cell migration and invasion ability (170), while overexpression of Jarid1B in melanoma (40) or immortalized normal breast cancer cells (MCF10A) (171) were found to enhance metastatic progression or cell invasion, respectively. Another representative histone associated with transcriptional activation, histone H3 lysine 36 methylation (H3K36me2), and a histone correlated with transcriptional repression, histone H3 lysine 9 methylation (H3K9me3), were also employed.

To investigate potential histone methylations to regulate phenotypic changes of melanomas, we cultured cells for five days in five different geometries with the same area (50,000 μm^2) or non-patterned substrates and stained for histone methylation markers (Figs. 8.3 and 8.4). Interestingly, H3K4me2 and H3K36me2 expression co-localized with MMIC phenotypes at the periphery of the geometries. We selected cells cultured for five days in the spiral shape for flow cytometry analysis because this shape was designed for a high interfacial boundary (perimeter/area) while taking advantages of a high curvature (164). Similar to immunofluorescence results, cells cultured in the spiral patterns display higher levels of H3K4me2 and H3K36me2 expressions compared to those cultured on non-patterned surfaces (Fig. 8.3B). To gain understanding into the spatial distribution of

histone markers, cells were grown in circular shapes, and then the expression of these histone markers in two different regions (outside and inside) with the same area in the geometry was quantified. We found that cells cultured at the perimeter (circular shape) displayed significantly higher levels of H3K4me2 compared to those cultured at central regions (Fig. 8.3C), revealing that phenotypic change of melanomas into MMIC phenotypes could be linked to H3K4 dimethylation. To investigate the role of Jarid1B, a known MMIC marker (40) and demethylase, into the MMIC state, we cultured B16F0 cells in spiral geometries with small interfering RNA (siRNA) of Jarid1B or scrambled (control). After five days in culture, we performed gene expression analysis using real-time polymerase chain reaction (RT-PCR) of a panel of markers associated with MMIC (CD271) and stemness (Sox2, Oct4, and Nanog). We see a lower degree of transcript expression of stemness markers for cells cultured with Jarid1B siRNA, but we found concentration dependent changes for transcript expression of CD271 (Fig. 8.3D and 8.5), suggesting the contribution of Jarid1B to the promotion of MMIC states. To evaluate the contribution of Jarid1B to demethylation of H3K4me 3/2/1 in the different geometric regions, we performed immunofluorescence staining of H3K4me 3/2/1 for cells cultured in circular shapes, treated with Jarid1B or scrambled siRNA. We saw Jarid1B demethylated H3K4me 3/2/1, however, the efficiency was different; ~10% for H3K4me1, ~20% for H3K4me2, and ~40% for H3K4me3 regardless of region in circular geometries (Fig. 8.6). Interestingly, cells expressed higher levels of H3K4me2 at the periphery regardless of the Jaid1B or scrambled siRNA treatment, consistent with the identification of potential histone methylations using immunofluorescence. These results indicate that Jarid1B probably has a dual

opposite function in activated melanoma cancers; on the one hand, it may enhance pluripotent states by significant demethylation of H3K4me3 known to be enriched at tumor suppressors (172), on the other hand, it may suppress MMIC states through the demethylation of H3K4me2 which correlates to MMIC phenotypes.

Because histone acetylation may be also linked to the phenotypic change of melanoma cancers in geometries (173), we selected some candidates such as histone deacetylases (HDAC) acting on lysine residues to remove acetyl groups and cause the compaction of chromatin and suppression of gene transcription. In addition, we also employed global acetylation of lysines (AcK), and histone H3 lysine 4 and 9 (H3K4ac and H3K9ac) associated with gene activation. By applying the same process for identifying the methylation histone, we found that cells cultured at the periphery of different shapes expressed higher levels of HDAC1, AcK, H3K4ac, and H3K9ac compared to those cultured at central regions, like the signature found with MMIC characteristics (Fig. 8.7A and 8.8). Flow cytometry of cells cultured in spiral patterns or non-patterned substrates verified immunofluorescence results (Fig. 8.7B). Regional study dividing cells in two regions by area, central or outer, reveals that cells cultured at the periphery of shapes exhibit significant levels of H3K9ac. All acetylation markers (AcK, H3K4ac, and H3K9ac) were highly expressed by cells at the perimeter while those expressed similar (HDAC2) or lower (HDAC3) levels of HDACs (except for HDAC1). Interestingly, we also see a lower degree of transcript expression of HDAC1 for cells cultured with Jarid1B siRNA (Fig. 8.5), this may be because HDAC1 is linked to the domains of Jarid1B (169) and is one of the EMT-inducing genes (Snail) when

complexed with HDAC2 (67). Based on these results, we hypothesized that histone acetylation may play a significant role in the enhancement of gene transcription for MMIC states. To verify our hypothesis, we supplemented our patterned cultures with the representative HDAC inhibitors valproic acid (VPA), sodium butyrate (NaB), or Trichostatin A (TSA). Addition of HDAC inhibitors led to an increase in not only histone acetylation but also MMIC and stemness marker expression (Fig. 8.7D and 8.9). The complicated roles of HDAC inhibitors may give rise to marker dependent variations; however, our hypothesis that histone acetylation augments MMIC states remains viable in general and corresponds to a previous report that showed HDAC inhibition played an important role in CSCs and epithelial to mesenchymal transition (EMT) (68). Since we observed elevated levels of H3K9ac for cells cultured at margin topology and a previous study suggested H3K9 deacetylation is dependent on HDAC3 (174), we also explored these markers' expressions when cultured in straight line and torus geometries where curvature and perimeter/area ratio can be varied. Interestingly, after five days in culture, we see cells express higher levels of H3K9ac with increasing of both perimeter curvature and P/A, while those show higher levels of HDAC3 expressions with decrease in both factors, corresponding the potential effect of HDAC3 deletion on H3K9ac (Fig. 8.7E).

After identifying histone modifications linked to phenotypic alterations of B16 melanomas (Fig. 8.7F), we hypothesized that there may be a relationship between levels of these selected histone modifications (H3K4me2/H3K9ac) and expression of representative MMIC and stemness markers. As expected, cells with tumor periphery activation showed elevated levels of MMIC (Jarid1B and CD271) and

stemness (Oct4 and Sox2) marker expressions with culture days, which corresponds the high levels of H3K4me2/H3K9ac for cells cultured at margin topology (Fig. 8.7G). We also observed similar results through comparison of cells cultured on spiral geometry and non-patterned substrates (Fig. 8.7H). Interestingly, the levels of histone expressions decreased with culture days when cells were cultured on non-patterned substrates or central regions of circular shape (which were surrounded by others), corresponding to lower expression levels of MMIC and stemness markers with time (Fig. 8.10 and 8.11). This suggests that cell-cell contact suppresses histone modification and we observed that cells showed lower levels of H3K4me2 expressions with increasing cell-cell contact (Fig. 8.12). Taken together, we conclude that identified histone modifications (H3K4me2/H3K9ac) are directly associated with the expressions of representative markers for MMIC phenotypes, enhanced by curvature, and suppressed by cell-cell contact.

To understand the possible mechanisms underlying phenotypic alterations by histone modifications, B16 melanoma cells were grown on spiral patterned (activated) or non-patterned (non-activated) substrates for five days, followed by chromatin immunoprecipitation and DNA sequencing (ChiP-seq). ChiP assays specific for the identified histones (H3K4me2/H3K9ac) were performed and the sequencing peaks were cut by 2-fold changes (Fig. 8.13 and 8.14). Higher levels of peaks linked to H3K4me2 (57.3%)/H3K9ac (77.8%) were shown for activated cells cultured in spiral geometries. To gain insights into the identification of DNA-binding transcription factors that cooperate or compete, we also performed the motif enrichment analysis. We found that differential peaks between patterned and non-

pattered cells enriched for distinct genes; ERG (ETS)/Pit1/Sox2/9 (activated cells) or ETS1/TcFap2e1/USF2 (non-activated cells) for H3K4me2 peaks and ERG (ETS)/Sox10/MITF (activated cells) or RBPJ/Nur77/Nkx2 (non-activated cells) for H3K9ac peaks. ETS genes are known to be linked to p38/ERK mitogen-activated protein kinases (MAPK) signaling for tumor growth and progression (175). For example, ETS1 could promote the development and invasion of malignant melanoma (176), and when it associated with RhoC (this gene is also upregulated for cells in spiral patterned substrates), melanoma cells could be progressive and metastatic (177). Although the ETS family was also top ranked for H3K4me2 peaks in non-patterned cells, the enriched annotations suggest they have distinct roles from those for cells activated at the tumor periphery (Fig. 8.14 and 8.15). Pit1 is also known to upregulate Snai1, leading to tumor EMT and their growth and metastasis (178). Similar trends were observed for H3K9ac peaks but it has more distinct and specific differences between cells cultured on patterned and non-patterned substrates (Fig. 8.14). Sox10, a neural crest stem cell marker, is one of the top motifs for cells cultured at the marginal topology. Previous studies revealed that Sox10 played an important role in melanoma cell survival, proliferation, and metastasis (179). It was also reported that the CD271 expression for malanoma, one of representative MIC markers, was directly related to the expression of Sox10 (180). In addition, previous studies showed that MITF which could function as a melanoma oncogene was associated with melanoma progression (181) and Sox10 has known to act upstream of MITF (182). Interestingly, the enriched mouse phenotype annotations related to Sox10 family in H3K9ac peaks for patterned cells suggest that increased tumor incidence and tumorigenesis are involved in their

mouse phenotype and Nanog and Sox2 targets may be perturbed by the Sox10 family, suggesting the importance of Sox10 in the tumor periphery activation. To further confirm the association between the high ranked genes (ERG (ETS), Sox10, and MITF for activated cell upregulating H3K9ac peaks) and regulation downstream of promoter genes, we collected H3K9ac differential peaks between two different conditions (activated and non-activated cells). As expected, upregulation of Sox10 and ETS1/2 were observed. Interestingly, peaks for downstream genes associated with cancer growth and progression were also upregulated, suggesting the entire process may be caused by the interaction between the Sox10/ETS/MITF families and downstream genes associated with melanoma progression. Taken together, we propose that tumor periphery activation will modulate malignancy phenotypes by H3K9ac and H3K4me2 modifications through integrin α5ß1 adhesion and p38/ERK MAPK signaling (Fig. 8.16), guiding MAPKs/ETS or Sox/MITF signaling pathways (Fig. 8.17).

8.4 Conclusion

In this chapter, we have provided evidence that changes in specific histone modifications of cancers are predictive of phenotypic alteration by employing immunofluorescence and chromatin immunoprecipitation (ChIP) sequencing. The mechanistic basis of such changes may be related to the response of tumors to their microenvironment where various factors such as cell-cell contact and mechanical cues exist, proving to be indicative of the alteration of tumor malignancy and metastasis with tumor periphery activation at the invasive regions. These findings may help guide researchers in further exploring epigenetic

signatures for tumor malignancy, and the development of novel strategies to prevent, diagnose, and treat malignant cancers.

8.5 Figures

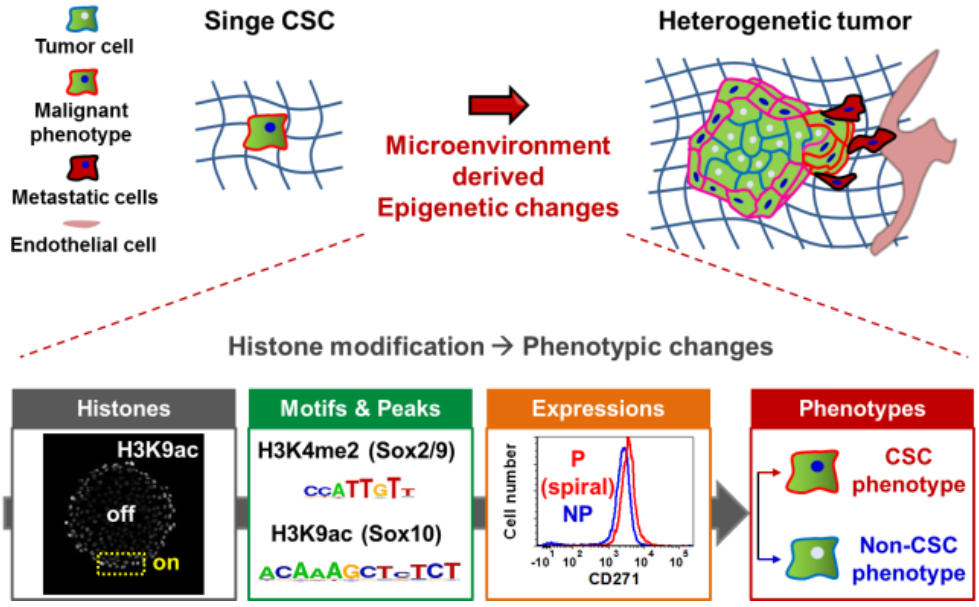

Figure 8.1 *Phenotypic alterations caused by histone modifications in response to microenvironment derived epigenetic changes.*

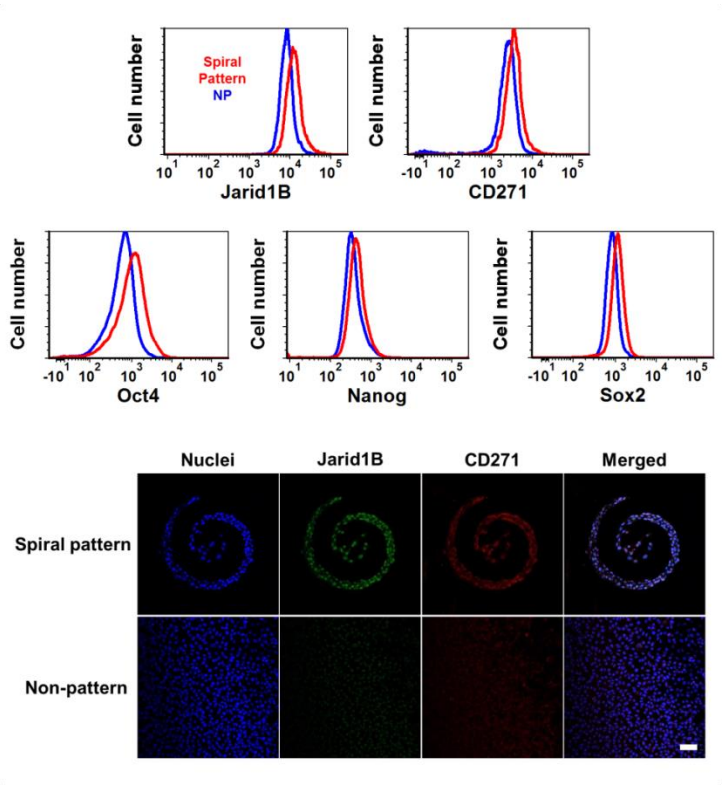

Figure 8.2 *Flow cytometry characterization of MMIC (Jarid1B and CD271) and stemness (Oct4, Nanog, and Sox2) markers in B16F0 cells cultured on spiral patterned or non-patterned substrates. Representative confocal images of Jarid1B and CD271 for B16F0 cells cultured on spiral patterned or non-patterned substrates.*

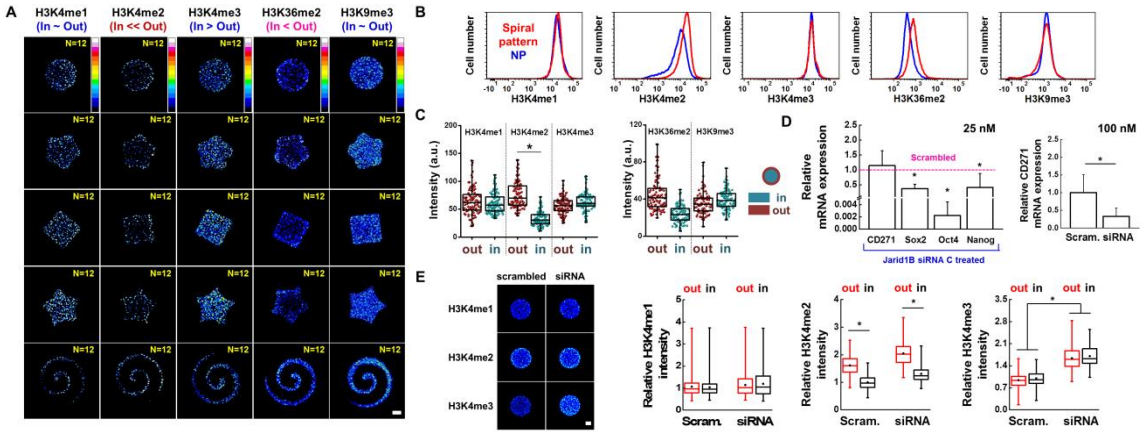

Figure 8.3 *Chromatin histone methylation points out tumor periphery activation at the invasive region. (a) Immunofluorescence heatmaps of H3K4me3/2/1, H3K36me2, and H3K9me3 for B16F0 cells cultured in a panel of shapes. (b) Flow cytometry characterization of histone methylation in B16F0 cells. (c) Single cell analysis of histone expression of methylation markers in B16F0 cells cultured in perimeter or central regions of circular geometry (N=3). (d) Results of real-time PCR to measure the gene expression of CD271, Sox2, Oct4, and Nanog for B16F0 cells cultured on spiral geometries for 5 days with Jarid1B or scrambled siRNAs (N=5). (e) Jarid1B regulates the levels of demethylation of H3K4me3/2/1 with different efficiencies (N=3). Boxes represent 25th to 75th percentile and whiskers represent minimum-maximum. Horizontal lines and points within boxes represent the median and mean respectively for three duplicates. Scale bars, 50 μm. Error bars represent s.d.*

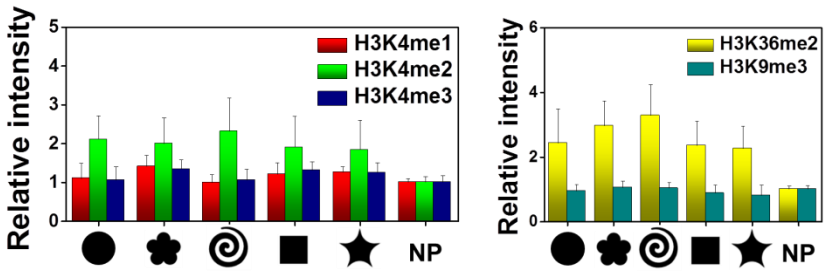

Figure 8.4 *Histone expressions of methylation markers for B16F0 cells cultured in a panel of shapes or non-patterned substrates (N=3). Error bars represent s.d.*

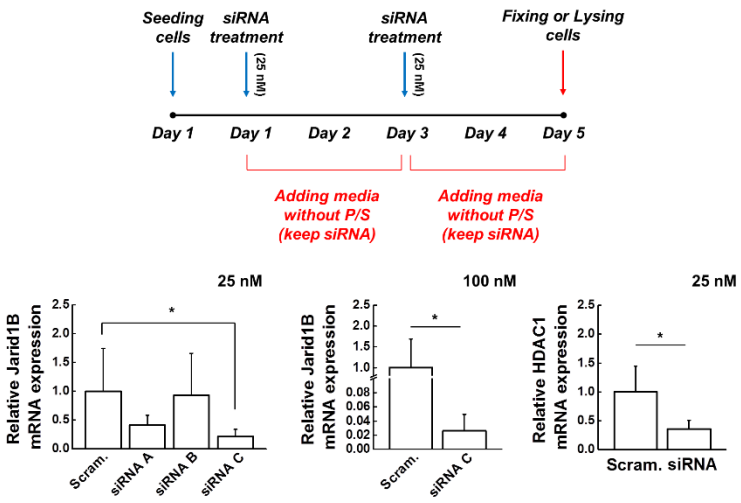

Figure 8.5 *Media conditions for normal, inhibition, or siRNA transfection. Results of real-time PCR to measure the gene expression of Jarid1B (three different sequences of Jarid1B siRNAs (A, B, and C) with different concentrations (25 or 100 nM)) and HDAC1 for cells cultured on spiral geometry for 5 days with Jarid1B or scrambled siRNAs (N=5). Error bars represent s.d.*

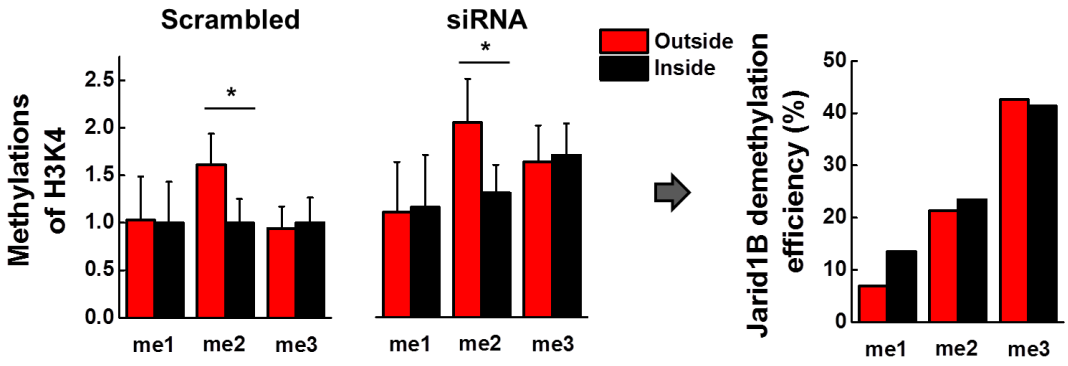

Figure 8.6 *Results of real-time PCR to measure the gene expression of Jarid1B for cells cultured on spiral geometry for 5 days with Jarid1B or scrambled siRNAs (N=3). The efficiency of demethylation of H3K4me3/2/1 (calculated by (siRNA/scrambled) x 100). Error bars represent s.d.*

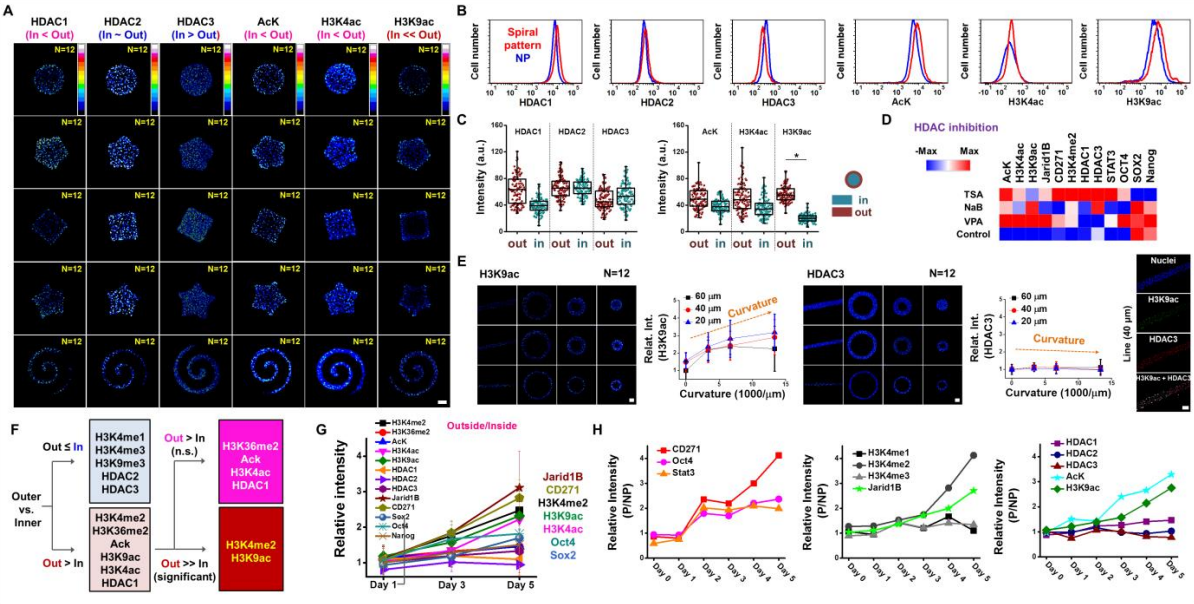

Figure 8.7 *Chromatin histone acetylation and deacetylation identify epigenetic-mediated phenotypic changes in melanomas. (a) Immunofluorescence heatmaps of histone acetylation and deacetylation expressions for B16F0 cells cultured on our panel of geometries. (b) Flow cytometry characterization of histone acetylation and deacetylation in B16F0 cells. (c) Single cell analysis of histone expressions of acetylation and deacetylation markers in B16F0 cells cultured in two different regions of circular shape (N=3). Boxes represent 25th to 75th percentile and whiskers represent minimum-maximum. Horizontal lines and points within boxes represent the median and mean respectively for three duplicates. (d) Immunofluorescence expression analysis of histone acetylation and deacetylation, MMIC surface marker (CD271), transcriptional factors related to stemness and MMIC state for cells cultured with/without HDAC inhibitors (N=3). (e) Shapes regulating curvature and perimeter/area to explore the relationship between H3K9ac and HDAC3 (N=3). (f) Flow chart of the identification of histone modifications linked to phenotypic alterations toward malignant phenotypes. Expression of Histones, MMIC markers, transcriptional factors related to stemness and MMIC state depending on culture time for cells cultured on (g) different regions (outside/inside ratio) of circular shape or (h) spiral geometry over those cultured on non-patterned substrates (N=3). Scale bars, 50 μm. Error bars represent s.d.*

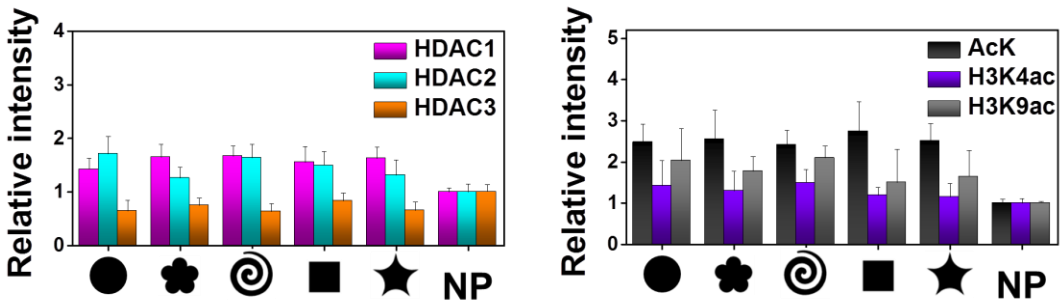

Figure 8.8 *Histone expressions of acetylation markers for B16F0 cells cultured in a panel of shapes or non-patterned substrates (N=3). Error bars represent s.d.*

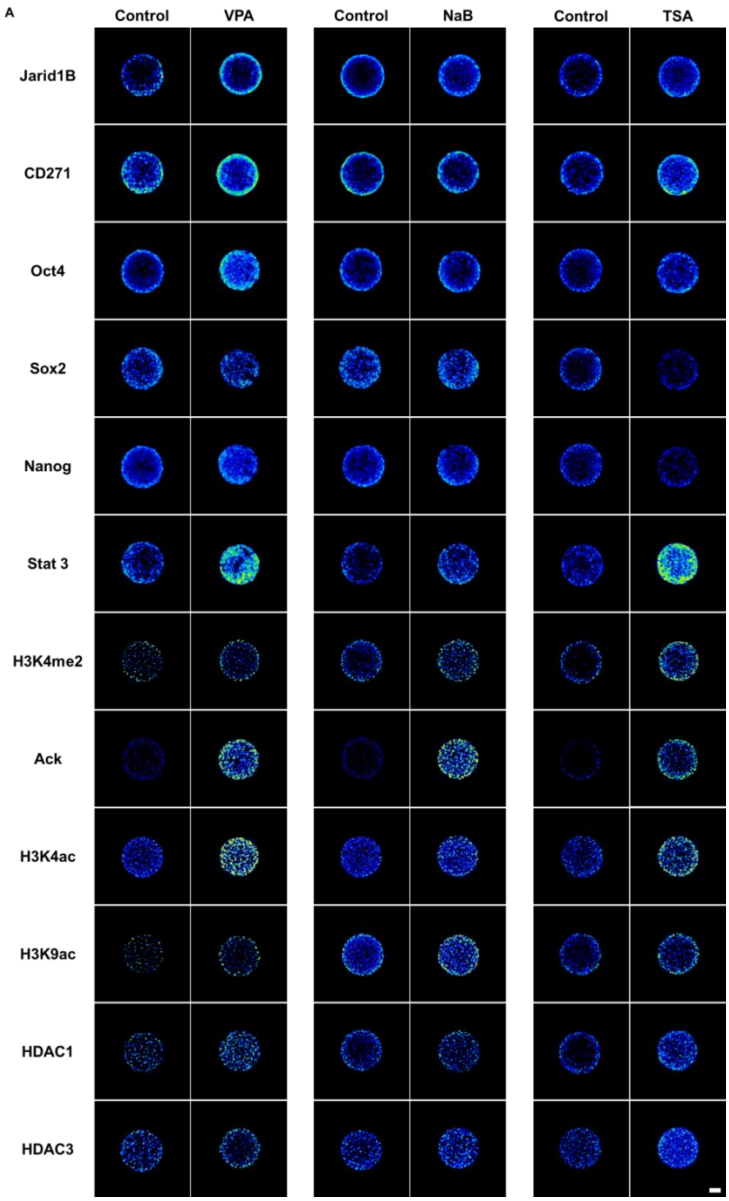

Figure 8.9 *(a) Immunofluorescence heatmaps of histone acetylation and deacetylation, CSC surface marker (CD271), transcriptional factors related to stemness and CSC state for B16F0 cells cultured in circular shapes. (b) Relative immunofluorescence intensity of the markers we selected for cells cultured in spiral geometry with/without HDAC inhibitors (N=3). (c) Flow cytometry characterization of the markers in B16F0 cells. Scale bars, 50 μm. Error bars represent s.d.*

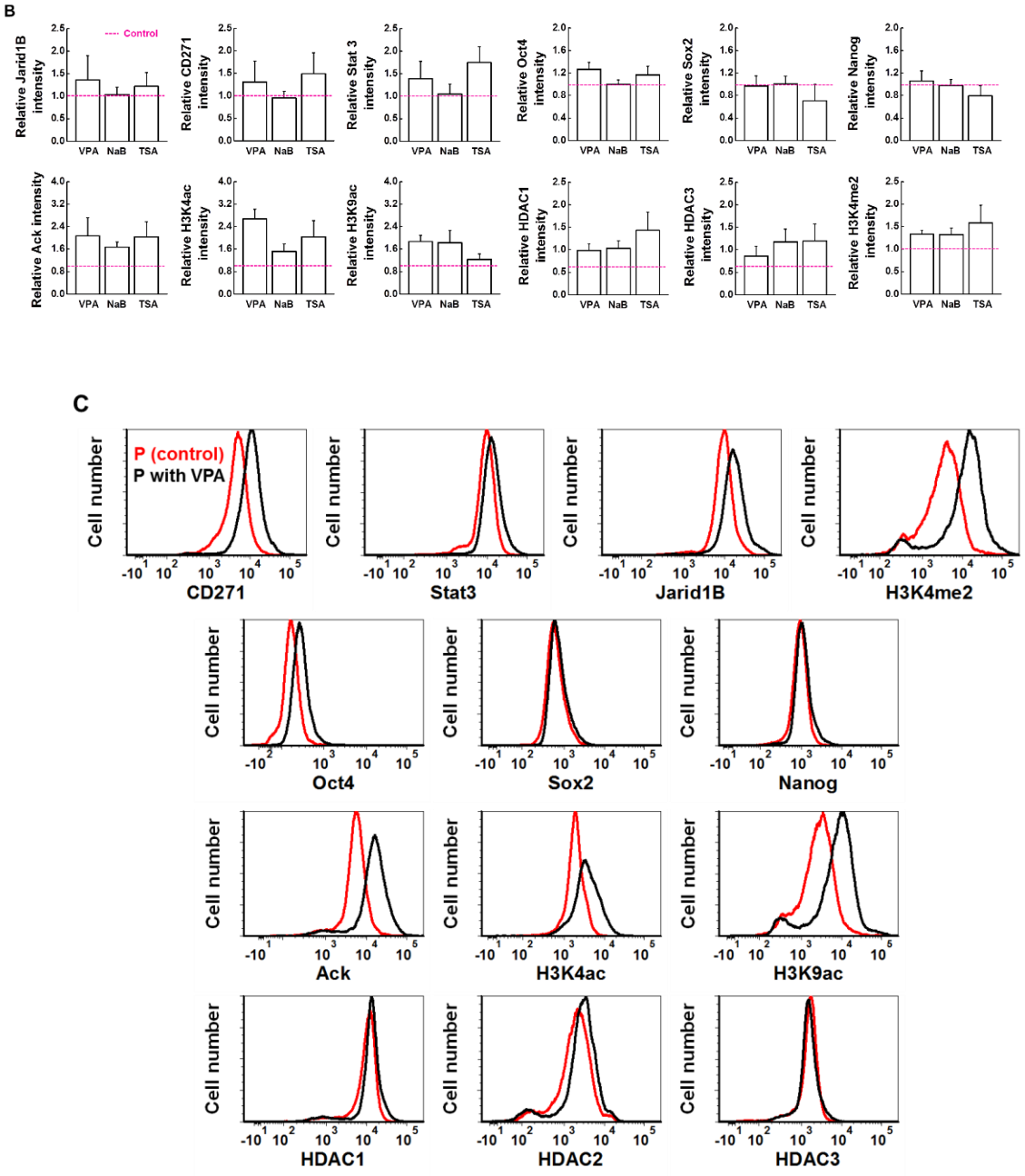

Figure 8.9 (cont.)

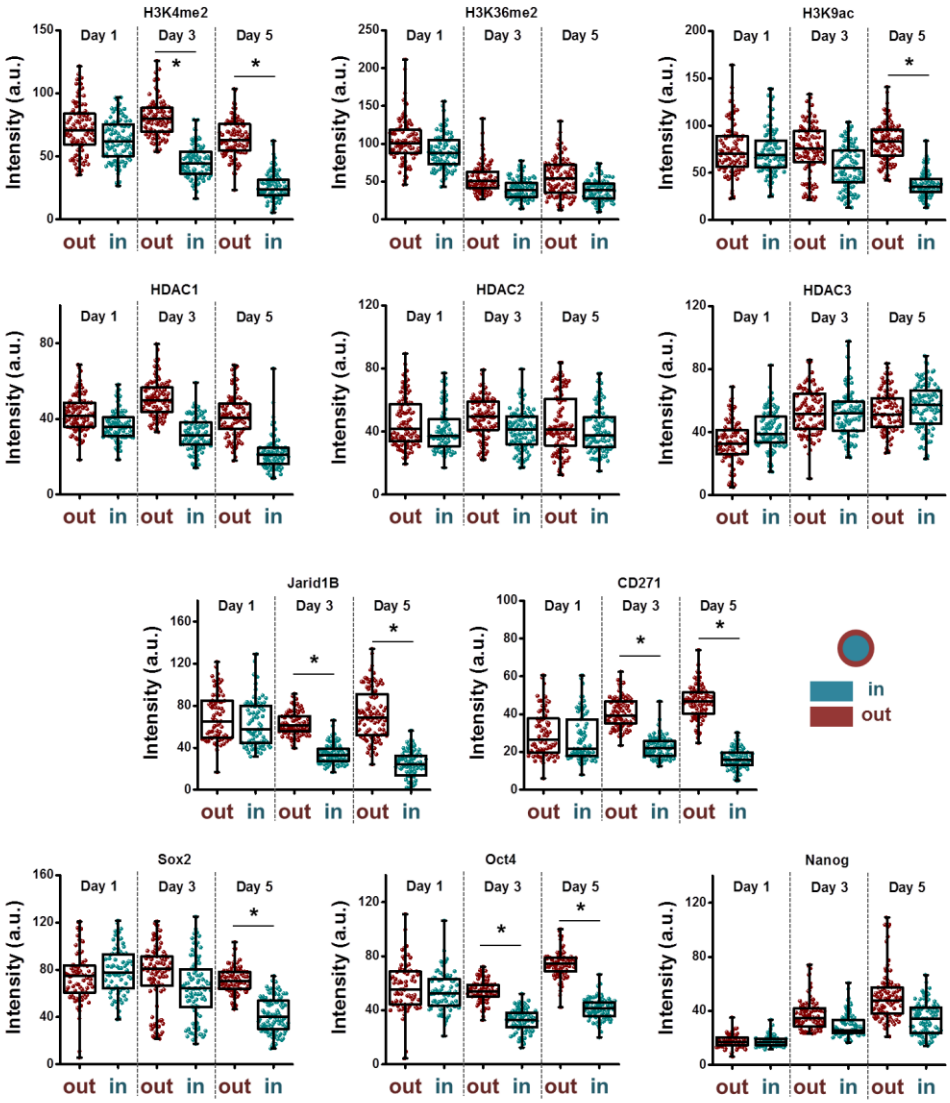

Figure 8.10 *Expression of Histone modifications (H3K4me2, H3K36me2, H3K9ac, and HDAC1/2/3), MMIC markers (Jarid1B and CD271), and transcriptional factors related to stemness and MMIC state (Sox2, Oct4, and Nanog) depending on culture time (day 1, 3, and 5) for cells cultured on different regions (outside/inside ratio) of circular shape (N=3). Error bars represent s.d.*

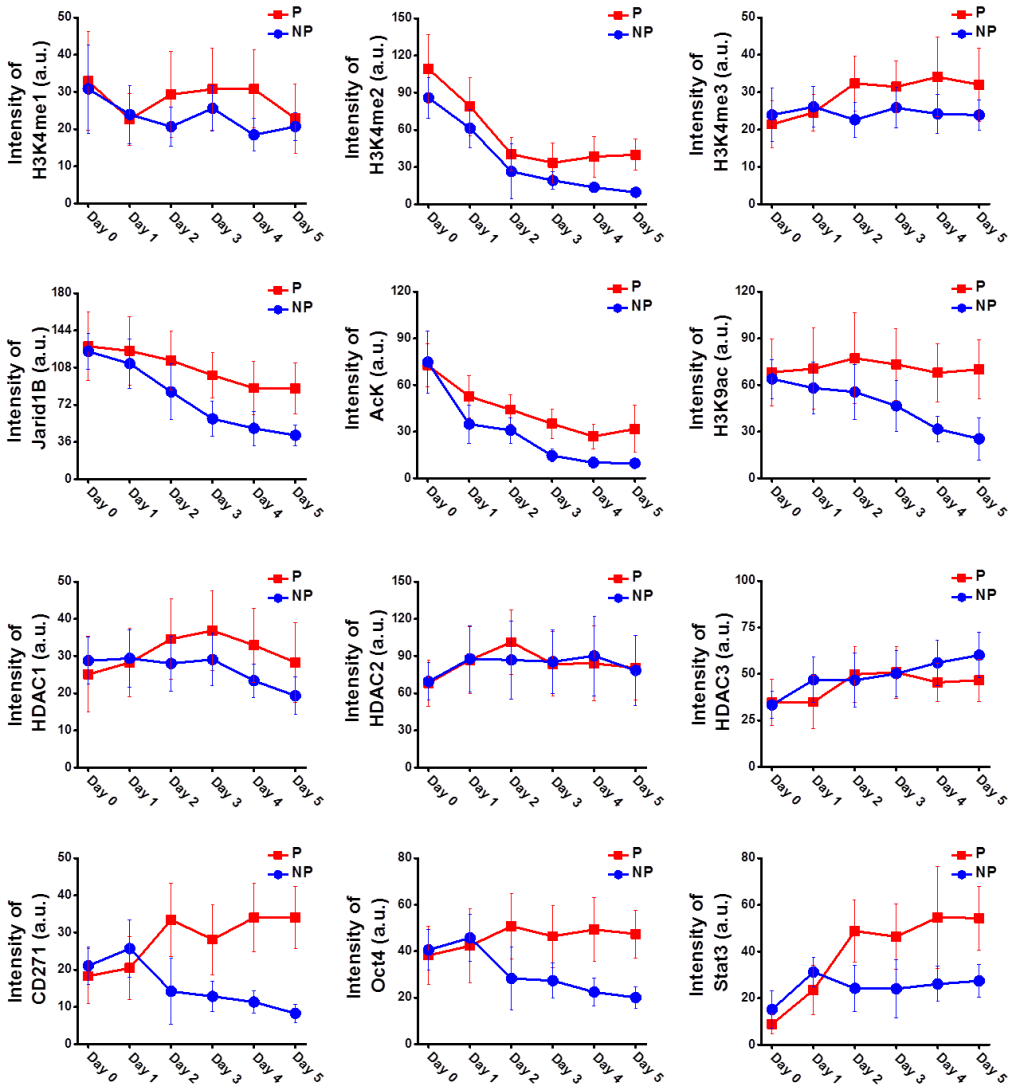

Figure 8.11 *Expression of Histone modificationss (H3K4me3/2/1, H3K9ac, AcK and HDAC1/2/3), MMIC markers (Jarid1B and CD271), and transcriptional factors related to stemness and MMIC state (Oct4 and Stat3) depending on culture time (each day for 5 days) for cells cultured on spiral shapes or non-patterned substrates (N=3). Error bars represent s.d.*

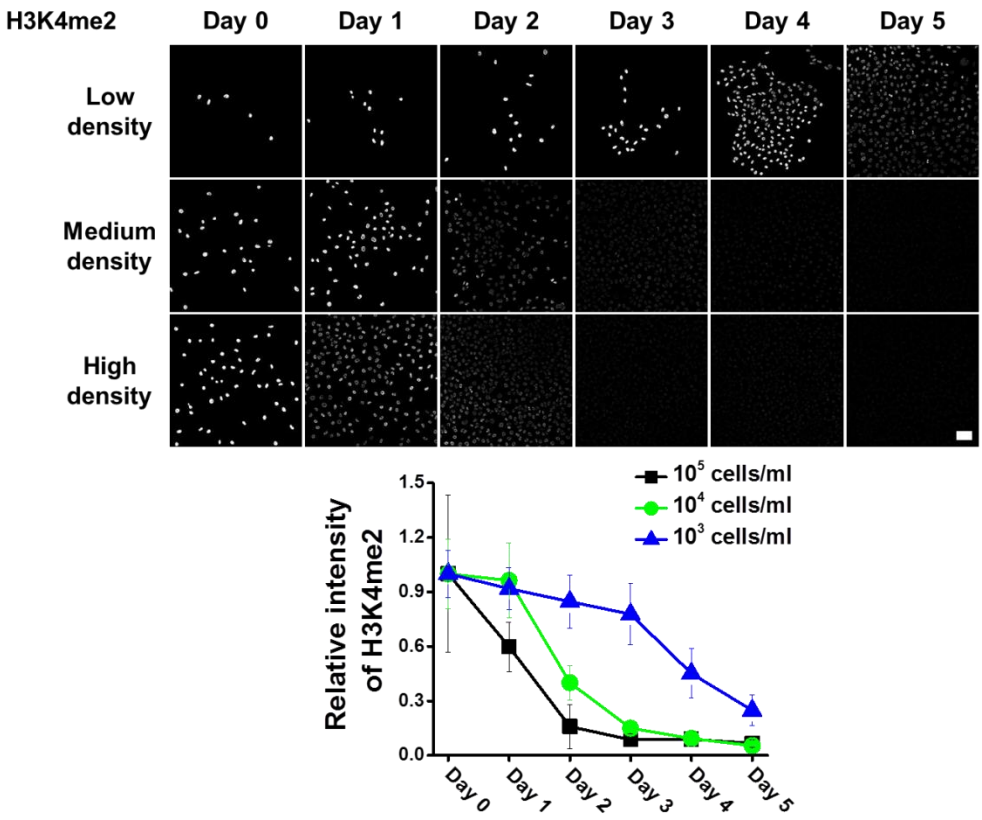

Figure 8.12 *Representative confocal images and expressions of H3K4me2 histones depending on culture time for B16F0 cells cultured on non-patterned substrates with different initial seeding density. Scale bars, 50 μm. Error bars represent s.d.*

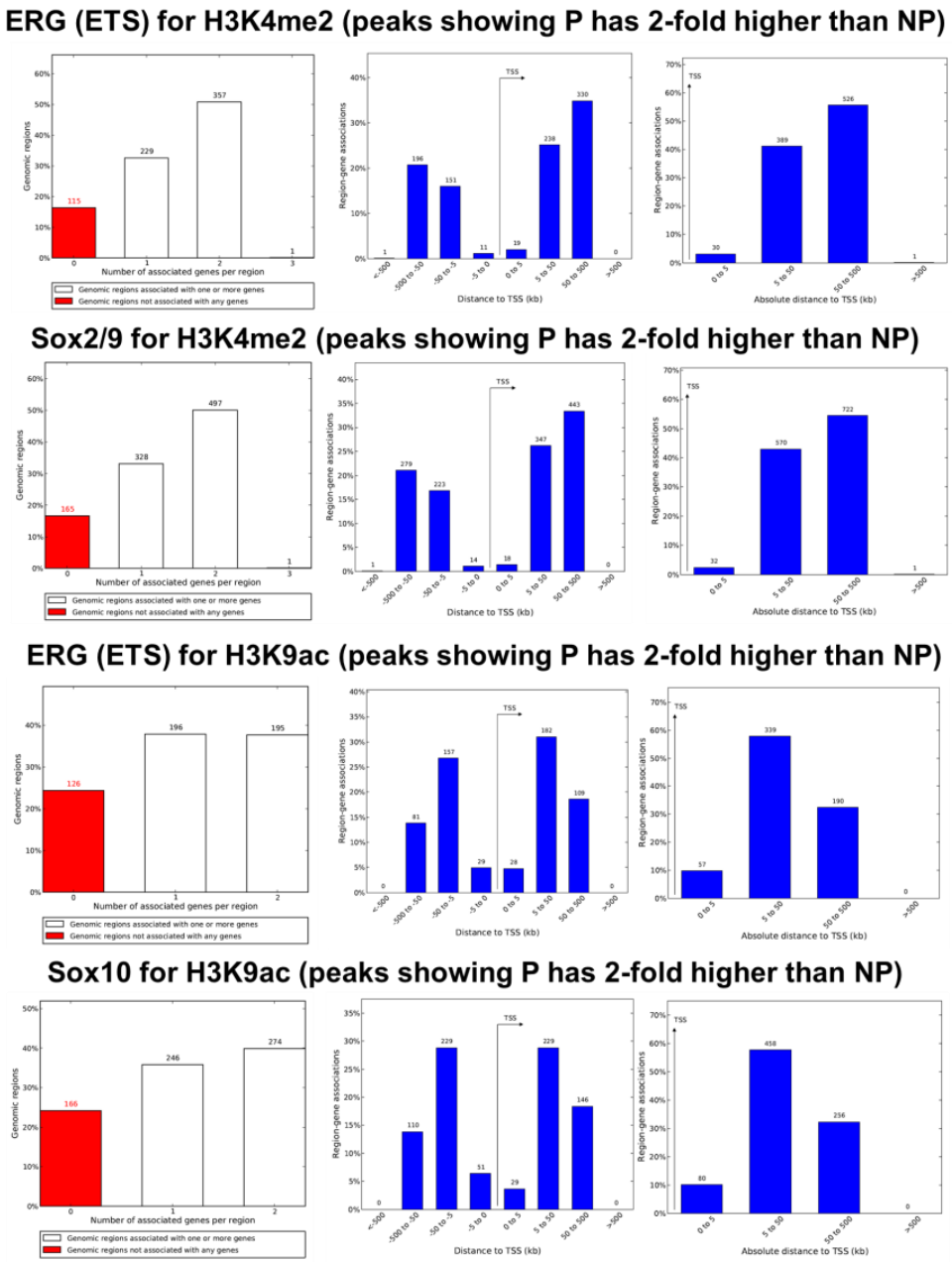

Figure 8.13 *Number of associated gene per region and binned by distance (with orientation or absolute value) to generate enriched annotations (GREAT) of genes for cells cultured on spiral patterns that contain a specific motif (Sox or ETS family) within the promoter.*

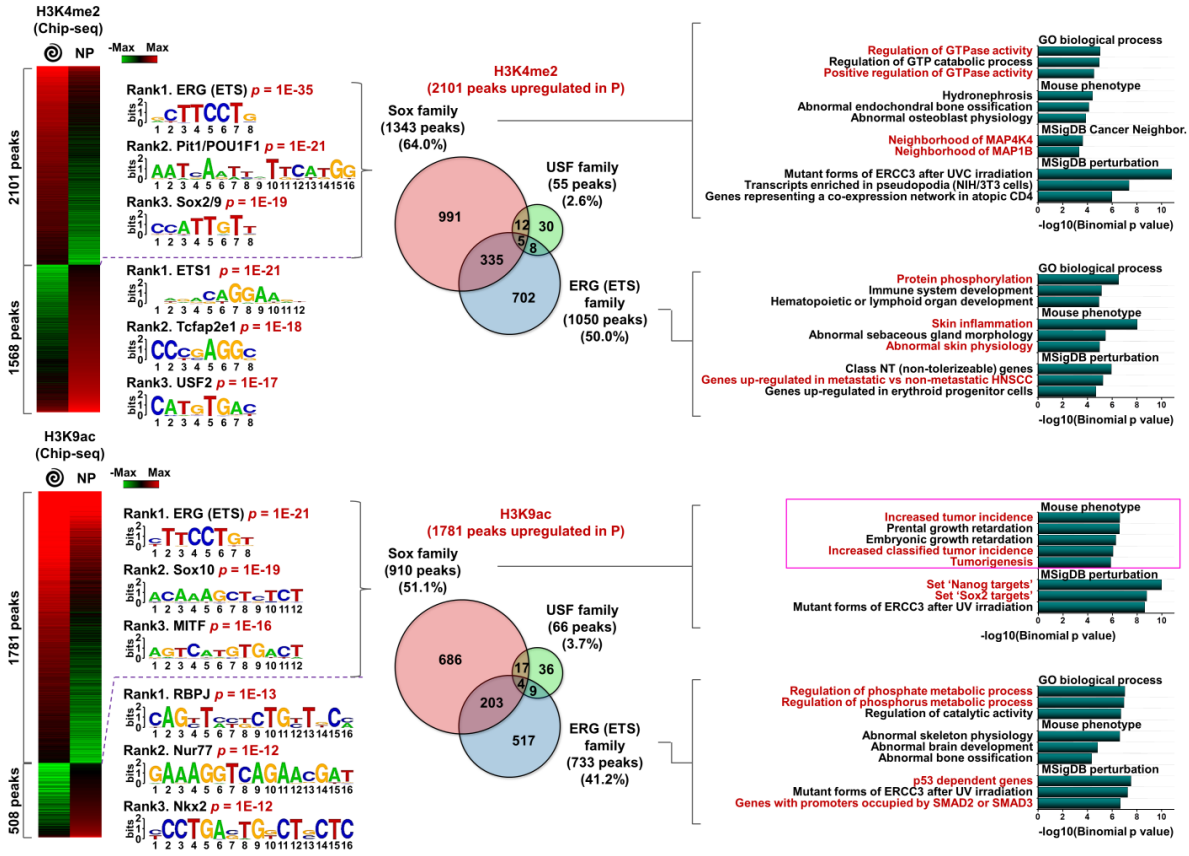

Figure 8.14 *H3K4me2/H3K9ac-regulated gene panels predict phenotypic alterations of melanoma cancers. Heatmap of H3K4me2 and H3K9ac ChiP-seq signal for cells cultured on spiral geometry or non-patterned substrates. The top three predictive transcription factor motifs with p-values. Enriched annotations of genes for cells cultured on spiral patterns that contain a specific motif (Sox or ETS family) within the promoter. Venn diagram showing the number of upregulated genes for cells cultured on spiral patterns linked to Sox, ETS, and USF families among H3K4me2/H3K9ac-marked genes.*

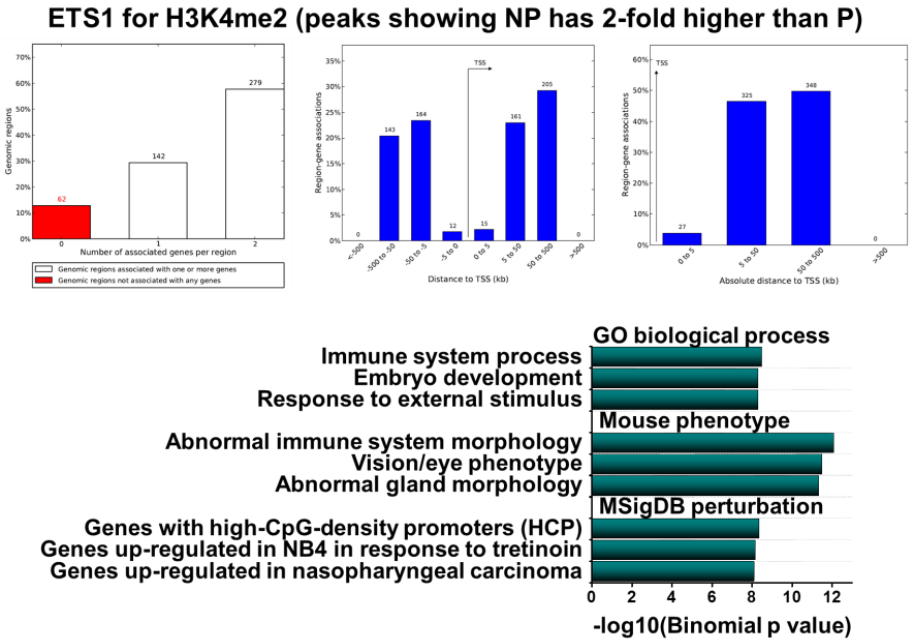

Figure 8.15 *Number of associated gene per region and binned by distance (with orientation or absolute value) to generate enriched annotations (GREAT) of genes for cells cultured on non-patterned substrates that contain a specific motif (ETS1 family) within the promoter, and the enriched annotation results.*

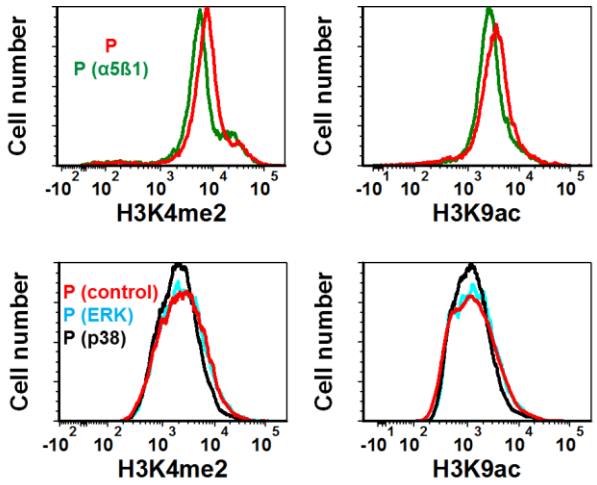

Figure 8.16 *Flow cytometry characterization of markers associated with histone modifications (H3K4me2 and H3K9ac) in B16F0 cells with or without treatment with antibodies against integrin α5ß1 and inhibitors of the p38 or ERK MAPK pathway.*

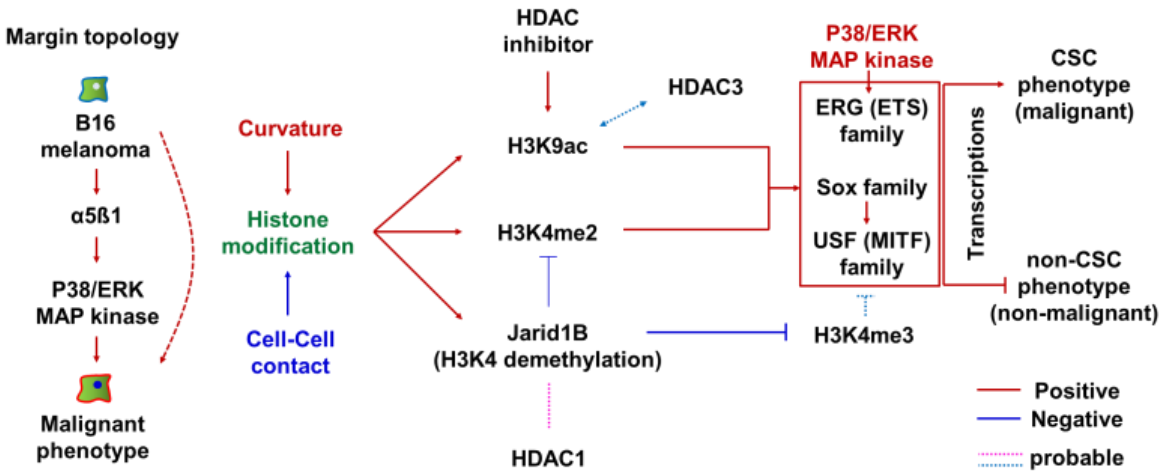

Figure 8.17 *Proposed pathway for marginal topology guiding phenotypic alteration of B16 melanomas toward malignant phenotypes through histone modifications.*

CHAPTER 9

MELANOMA CANCER CELL ANGIOGENESIS BY TUMOR PERIPHERY ACTIVATION[9]

9.1 Introduction

The cancer microenvironment is a spatially and temporally heterogeneous assortment of cells and extracellular matrix components that guide cellular fate and the process of oncogenesis (153). The role of the microenvironment during the initiation and progression of tumors has been recognized to be of critical importance for understanding fundamental principles of cancer behaviors (183). Tumor initiating cells or cancer stem cells (herein referred to as CSCs) are a subpopulation of cancer cells critical for cancer progression through promotion of tumorigenicity and metastasis (147, 184, 185). These CSCs also have stem-like properties and tend to resist chemo- and radiotherapy, which causes tumor recurrence (148). Growing evidence surrounding the plasticity of cancer cells suggests that highly tumorigenic CSCs can be created through the crosstalk between tumor cells and their surrounding microenvironment (42, 66, 162). Thus, understanding the interactions of CSCs with their microenvironment would be of utmost importance for developing rational treatment approaches for the prevention of adaptive strategies for cancer cells to survive and progress.

---

[9] This chapter is adapted from the following publication:
Junmin Lee, Amr A. Abdeen, Jamila Hedhli, Kathryn L. Wycislo, Timothy M. Fan, Wawrzyniec L. Dobrucki, and Kristopher A. Kilian, Melanoma cancer cell angiogenesis at the periphery of tumor, (2017) *in preparation.*

Angiogenesis, the formation of new blood vessels, is also essential for cancer development, growth, and progression (12, 186, 187). This process is regulated by the balance of signals both positive, like vascular endothelial growth factor (VEGF) (188), and negative, like tissue inhibitors of metalloproteinases (TIMP) (189). Most studies have focused on how hypoxia, or low oxygen tension, plays a critical role in promoting vessel growth via upregulating multiple pro-angiogenic pathways including hypoxia-inducible factors (HIFs) (190–192). For instance, studies report that hypoxia activates signal transducer and activator of transcription 3 (STAT3), a VEGF promoter, which induces upregulation of HIF1α (another VEGF promoter),enhancing VEGF expression, which mediates angiogenesis (193, 194). However, emerging evidences suggest that the conventional theory where the HIF pathway mediated by hypoxic conditions is a master regulator of angiogenesis may not be always true (195, 196). For cancer cells at the periphery of the tumor in normoxia, an increased level of VEGF production was observed in many types of tumors (197, 198). In addition, even single cells or small sized aggregates have the capacity to induce the beginning of microvessel formation (199, 200). However, underlying mechanisms of how tumor angiogenesis can be regulated by CSCs at the invasive regions of tumors remains to be elucidated.

In the chapter 7 we demonstrated how geometric features at the interface of tumor tissue can guide cancer cells toward CSC-like phenotypes (164). When cultured on patterned substrates with high curvature and interfacial boundary, melanoma cells not only undergo epithelial to mesenchymal transition (EMT) and express elevated CSC and stemness markers, but also show upregulation of genes related to the MAP

kinases and JAK-STAT signaling pathways in vitro. In addition, when injected into mice subcutaneously and intravenously, these CSC phenotypes show higher tumorigenicity and metastasis, respectively, compared to non-CSC phenotypes. In addition, bone morphogenetic proteins (BMPs) were also investigated for the CSC states of B16F0s when cultured with different peptides on the substrates. However, it is unclear whether these CSC phenotypes have different levels of angiogenic potential relative to non-CSC phenotypes and through which signaling pathways CSCs actually mediate angiogenesis in non-hypoxic conditions. To elucidate the role of CSCs located at the periphery of tumors in angiogenesis, we use micro-patterning to pattern populations of tumor cells on soft hydrogels to generate CSC phenotypes. Then, we explore how these CSCs influence pro-angiogenic potential upon endothelial cells in vitro and in vivo.

9.2 Materials and Methods

In vitro tubulogenesis assay:

The in vitro tubulogenesis assay was performed as described previously (77). Briefly, 25μL of thawed reduced growth factor matrigel (Trevigen) was employed to cover the bottoms of 48 well plates and then allowed forming gels for 30 min at 37°C. After the gelation, 15,000 hMVECs were seeded per well in 100μL of unsupplemented EBM-2 media (Lonza) and 200μL of B16F0 conditioned media (media from day 3-5) was added to each well. A negative or positive control was generated with unsupplemented or fully supplemented EBM-2 media respectively. After 8 hours of tube formation, hMVECs were imaged using a Rebel T3 Camera

(Canon) at 25x and tube area quantified using imageJ. For co-culture experiments, pre-cultured B16F0s were additionally seeded at 5,000 cells/well. Tube areas were analyzed using ImageJ by thresholding fluorescent images.

Angiogenic cytokines array:

For cytokine analysis in the conditioned media we used mouse antibody angiogenesis array membrane (Abcam – ab139697, 24 target proteins) as per manufacturer instructions. Conditioned media samples were incubated with blocked membranes overnight with the membranes at 4°C. Prepared membranes were exposed to x-ray film and developed for the protein detection. Films were scanned and analyzed using the ImageJ plugin 'Protein array analyzer' (written by Gilles Carpentier, 2010, available at http://rsb.info.nih.gov/ij/macros/toolsets/Protein%20Array%20Analyzer.txt)

Immunofluorescence:

Cells (B16F0s and hMVECs) were fixed using 4% paraformaldehyde for 20 minutes and permeabilized with 0.1% Triton-X100 for 30 min at room temperature. 1% bovine serum albumin was used to block cells for 15 min and then cells were stained with appropriate primary and secondary antibodies. Before every step, cells were rinsed at least twice with PBS. Imaging was done using an LSM 700(Carl Zeiss, Inc.) four laser point scanning confocal microscope with a single pinhole for confocal imaging or an IN Cell Analyzer 2000 (GE healthcare) for fluorescence imaging. Red and green cell trackers (Invitrogen) were used for co-culture experiments on pre-cultured B16F0s and hMVECs, respectively as per manufacturer

instructions. These cells with cell trackers were fixed as above without the rest steps for staining and imaged.

Inhibition assay and siRNA:

Integrin-blocking antibodies α5ß1 (Millipore) or αvß3 (Santa Cruz) were added to cells in media before seeding and after changing media at 1 μg/ml. MAP kinase inhibitions (FR180204 (ERK1/2), SP600125 (JNK), and SB202190 (p38)) (6 μM) (Calbiochem), cytoskeletal inhibitions (Blebbistatin (1 μM) and Y-27632 (2 μM) (Calbiochem)), BMP inhibition (Noggin) (5 ng/ml) (Prospec),GSK-3 inhibition (CHIR) (10 nM) (Calbiochem), HIF-1 inhibition (10 nM) (Santa Cruz), hydrocortisone (0.5 mM) (Tocris), heparin sodium salt (0.1 mg/ml) (Tocris) were performed by adding media supplemented with these inhibitors at concentration after cell seeding and with media change. For inhibition assay, cells cultured for three days with inhibitors were washed twice with PBS and then cultured with fresh media without inhibitors to prevent the effect of the inhibitors in conditioned media on tubulogenesis of hMVECs.

The siRNAs for Jarid1B (ID 75605, Trilencer-27 Mouse siRNA) or scrambled siRNAs were purchased from OriGene. Transfection was performed according to the vendor's instructions (100 nM). Lipofectamine 2000TM was used for higher transfection efficiency. Similar to inhibition assay, cells were washed twice with PBS at day 3 and cultured with fresh media for the preparation of conditioned media.

Cell labelling and flow cytometry:

B16F0 cells cultured for five days on spiral-patterned or non-patterned gels (12 identical substrates) were detached from the substrates by trypsin and broken down into a single cell suspension. Cells were fixed in paraformaldehyde for 20 min. Cells were permeabilized in 0.1% Triton X-100 in PBS for 30 min and blocked in 1% BSA in PBS for 1 h. Primary antibodies in 1% BSA in PBS were applied overnight at 4°C. Cells were stained with secondary antibodies in 2% goat serum, 1% BSA in PBS for 20 min in a humid chamber (5% CO2 and 37°C). Before every step, cells were washed at least three times with PBS. Flow cytometry analysis was performed with a BD LSR Fortessa Flow Cytometry Analyzer. For negative controls to set the baseline, cells stained without primary antibodies were used.

Ethics statement:

All experiments using live animals (mice) were in compliance with animal welfare ethical regulations and approved by the Institute Animal Care and Use Committee before experimentation, following the principles outlined by the American Physiological Society on research animal use.

Chick chorioallantoic assay:

Embryonated chicken eggs at Day 10 were obtained from the University of Illinois poultry farm (Urbana, IL). A rectangle-shaped hole with around 20mm width and 10mm length was drilled and B16F0 cells cultured on non-patterned PA gels or spiral-patterned PA gels with/without blocking integrin α5ß1or inhibiting ERK were placed on the chorioallantoic membrane (CAM), face down. The hole was completely covered with scotch tape and the eggs were incubated for 5 days (37°C

and ~50% humidity). After five days in culture, embryos were fixed with 4% paraformaldehyde overnight. CAMS containing hydrogels with cells were excised and washed with distilled water at least for tree times. The explants were imaged and the area covered with blood vessels over the gels was quantified using ImageJ as described for the in vitro tubulogenesis assays above.

B16F0 melanoma in vivo models:

For the in vivo study, around six to eight-week-old female C57BL/6 mice were purchased from Charles River Laboratories for Animal Experiment. To form primary localized tumors, B16F0 cells (5 x 105 cells in 100 µl of HBSS) cultured on spiral-patterned (P) or non-patterned (NP) PA gels were subcutaneously injected with or without matrigel (50% volume ratio) into the right lateral flank (N=specified in each figure). Experiments were stopped after seven days in culture.

In vivo molecular imaging of angiogenesis:

One week after xenograft Initiation as well as two, and three weeks after, all animals were anesthetized with 1-3% isoflurane, the neck area was shaved, and the left jugular vein was isolated for placement of a PE-50 polyurethane catheter to facilitate injection of the radiotracer. The animals were injected with 80 µCI of {64}Cu-NOTA-PEG_4-cRGD_2 targeted to αvβ3 (a well characterized marker of angiogenesis). Imaging was performed using a hybrid small animal microPET-CT scanner (Inveon, Siemens Healthcare, USA). The animals were placed on the animal bed and 60 min after radiotracer injection a 15 min microPET imaging session was performed. This was followed by a high-resolution anatomical microCT

imaging (360 projections, 80 keV/500μA energy). The microPET and microCT images were reconstructed using OSEM/3D algorithm (Siemens Healthcare USA) and cone-beam technique (Cobra Exim), respectively.

PET-CT image analysis:

PET-CT images of tumor bearing animals were analyzed using Inveon Research workplace. Volumes of Interest (VOIs) were created by manually tracing tumors on CT, which were clearly visible, with numerous 2-D axial ROIs, followed by interpolation of those 2-D regions to yield the tumor VOIs. Standard uptake values (SUV) were then calculated for each tumor.

Immunohistochemistry:

Formalin-fixed, melanoma tumors from Pattern and Non-Pattern groups were trimmed and processed into paraffin-embedded tissue blocks. Tissue sections cut from the blocks for immunohistochemistry (IHC) were mounted onto glass slides, deparaffinized in xylene, and rehydrated in ethanol. Trypsin 0.1% was used as a pretreatment, followed by blocking of endogenous peroxidase activity with Peroxidazed 1 (PX968) for 5 minutes and blocking of non-specific background staining with Background Punisher (BP974) for 10 minutes. Blocked slides were incubated with polyclonal rabbit anti-human Von Willebrand Factor antibody (Dako A0082) at 1:1000 for 30 minutes. The slides were then incubated with a rabbit-on-canine horseradish peroxidase (HRP) secondary antibody (RC542) for 30 minutes. The chromogen ImmPACT NovaRED (Vector Labs SK-4805) was applied for 10 minutes to develop slides, followed by nuclear counterstaining with Cat hematoxylin

(CATHE) for 5 minutes. Individual steps were followed by washing in either wash buffer or deionized water, if necessary. Negative controls were processed identically as above, but in the absence of primary antibody. Mouse spleen was used a positive control.

Quantification of Microvessel Density:

Single tumor tissue sections stained for Von Willebrand Factor (Factor VIII) were evaluated for both Pattern and Non-Pattern groups. For each tumor, microvessel density was quantified microscopically by averaging the number of individualized, intratumoral vascular elements enumerated within 3 separate vascular "hotspots" at 200x. Vascular hotspots were identified visually by scanning the entire tumor tissue section at 100x. All tissue sections were evaluated by a single veterinary pathologist (K.L.W.).

Microarray data analysis:

Microarray data was obtained from previous study (GSE79085). Genes in VEGF signaling was selected based on the Database for Annotation, Visualization and Integrated Discovery (DAVID) website (http://david.abcc.ncifcrf.gov). A panel of genes regulated by HIF-1 was selected from a previous report by Semenza and colleagues. Genes with negligible expression (below ten) and difference between conditions (below 1.5-fold) were not included in the analysis. Heatmaps for fold changes over glass in gene expression were generated by using the Gene-E (http://www.broadinstitute.org/cancer/software/GENE-E) software package.

Statistical analysis:

Data was obtained at least three independent experiments. Error bars represent standard deviation (s.d., immunofluorescence study of B16F0s) or standard error (s.e., tube area study of hMVECs) around the mean. Student's t-test was used for statistical comparisons between two groups, and analysis of variance (ANOVA) with Tukey HSD Post-hoc testing was employed for multiple comparisons. Differences were considered significant at $P<0.05$.

9.3 Results

Regulating Tubulogenesis with Distinct Cancer Phenotypes.

We modified the surface chemistry of polyacrylamide (PA) hydrogels by employing hydrazine chemistry, and soft-lithography was used to conjugate matrix proteins in various patterns on the hydrazine treated surface of gels (87). Since we had previously shown that the effect of matrix stiffness on the CSC or stemness marker expressions was negligible compared to the effect of subcellular geometry (164), the elasticity of gels was fixed at 10 kPa. As a model system, we selected the murine B16 melanoma cells (B16F0s) and used a representative putative cancer stem cell molecular marker, CD271. To assess whether CSC phenotypes enriched at interfacial areas might influence the process of vessel formation of endothelial cells (Fig. 9.1a), B16F0 melanoma cells were grown on spiral patterned PA gels, non-patterned PA gels, and glass substrates for 5 days. Following culture, conditioned medium from B16F0s in different conditions was collected and added to matrigel human microvascular endothelial cells (hMVECs) in 3D matrigel culture. After 8

hours, hMVECs were fixed and the degree of tubulogenesis was imaged, and the tube areas were analyzed after normalizing cell number across conditions (Fig. 9.2).

First, we compared the tube formation of hMVECs with conditioned medium from patterned B16F0s or a positive control containing an empirically derived cocktail of growth factors. We see tubulogenesis displays no significant difference for these two conditions (Fig. 9.3). Interestingly, tubulogenesis with conditioned medium collected from B16F0s cultured on spiral patterned gels exhibited a more elongated morphology and higher hMVEC tube area relative to those with conditioned medium collected from B16F0s cultured on non-patterned gels and glass substrates, which corresponds to the trend of CD271 expressions with a correlation coefficient of around 0.99 (Fig. 9.1b). Next, we co-cultured B16F0s and hMVECs in 3D matrigel to investigate interactions between populations. B16F0s cultured on spiral patterned or non-patterned PA gels for 5 days were trypsinized and same number of cells re-cultured with hMVECs in matrigel for 8 hours without conditioned media. A similar trend was observed in the degree of tubulogenesis to that with conditioned media (Fig. 9.1c). To deconstruct the effect of interfacial geometry on this enhancement of tubulogenesis, we employed straight line and torus geometries where curvature and perimeter/area ratio can be varied. As we had shown previously (164), B16F0s cultured on higher curvature and smaller width displayed higher CD271 marker expressions (Fig. 9.1d & 9.3b). Interestingly, we see the degree of tubulogenesis with conditioned media collected from B16F0s cultured on these straight line and torus geometries corresponds to the expression of CD271 marker (Fig. 9.1e & 9.3c). When the correlation between tubulogenesis and CD271

marker expressions was analyzed with shape widths, cells cultured in shapes with 20 μm width show the highest correlation (~0.94) relative to those cultured in wider shapes (40 μm: 0.77 & 60 μm: 0.91) (Fig. 9.1f). In addition, when co-cultured with hMVECs in 3D matrigel, B16F0s cultured on small torus shapes 20 μm wide displayed higher tubulogenesis than those cultured in shapes 60 μm wide (Fig. 9.4).

Mechanisms for Cancer Cell Activation Guiding Angiogenic Potential.

We previously showed B16F0s cultured in a spiral shapes containing higher interfacial boundary (perimeter/area) expressed higher levels of CSC and stemness markers at perimeter features in other geometries, both convex and concave (164). Thus, we employed spiral-patterned and non-patterned PA gels to explore the angiogenic potentials of CSC and non-CSC phenotypes. To compare angiogenesis related gene expression for B16F0s cultured in spiral-patterned or non-patterned gels or glass substrates, a panel of VEGF signaling and genes regulated by hypoxia-inducible factor (HIF-1) were analyzed (Fig. 9.5a). The results show higher levels of expression in cells cultured on spiral patterned gels relative to those cultured on non-patterned gels and glass substrates. Previously, we revealed that integrin α5β1, the MAPK pathway, and STAT activity play an important role in melanoma cancer cell plasticity influencing their metastatic and tumorigenic characteristics when cultured in interfacial regions. To explore possible pathways for enhancing angiogenic potential of cells cultured on patterns, we treated cells with blocking antibodies to integrins α5β1 or αvβ3 and inhibitors for cytoskeletal tension (Blebbistatin & Y27632), MAPK (p38, ERK, JNK), BMPs (Noggin), or glycogen

synthase kinase-3 (GSK-3) (CHIR). To prevent the effects of these blocking antibodies or inhibitors on the tube formation of hMVECs, B16F0s were treated for an initial 3 days of culture, and fresh media was added after washing twice with PBS, then we collected the fresh conditioned media after the remaining two days of culture (Fig. 9.6). Among these treatments, tube formation significantly decreased with blocking antibodies to integrins α5β1 (~0.45-fold) or αvβ3 (~0.59-fold) and treatment of patterned cells with Y27632 (~0.60-fold) or ERK (~0.64-fold) (Fig. 9.5b). Based on these results, we speculate that these integrins or inhibitiors for cytoskeletal tension or ERK pathways which suppress the angiogenic potential of B16F0s may be associated with CSC states. Thus, we cultured cells for five days on patterned gels with or without treatments (α5β1, αvβ3, Y27632, ERK) for flow cytometry analysis to compare CD271 and STAT3 expressions. Similar to tube formation results, treated cells cultured in spiral patterns show lower levels of CD271 and STAT3 compared to untreated, treatment-dependent changes (Fig. 9.5c). To confirm the effect of Jarid1B which is known as one of the melanoma CSC markers, we employed short interfering RNA (siRNA) to silence gene expression. The results show cells cultured with Jarid1B siRNAs lead to decreased levels of the angiogenic potential (Fig. 9.5d). Since genes regulated by HIF-1 were upregulated for cells cultured on patterned gels, we employed a HIF1α inhibitor to explore its effect on the angiogenic potential of B16F0s. Moreover, hydrocortisone and heparin sodium salt (HSS) were used because they were previously used as angiogenesis inhibitors and inducing endothelial character (reducing mesenchymal). Patterned cells treated with HIF1α (~0.55-fold) or hydrocortisone (~0.61-fold) showed a significantly reduced angiogenic potential but not for HSS (~0.75-fold) (Fig. 9.5e).

The Influence of Interfacial Geometry on the Melanoma Secretome.

We investigated the influence of interfacial geometry on the pro-angiogenic secretory profile of B16F0s by using protein arrays. The relative concentrations of a panel of 24 different angiogenic cytokines in the conditioned media of B16F0s cultured on spiral-patterned gels to those cultured in the same shapes with integrin α5ß1 blocking or an ERK 1/2 inhibitor or non-patterned gels were investigated (Fig. 9.5f). A heat map of protein expression was normalized to cell number and we see an increase in expression of pro-angiogenic proteins secreted from spiral-patterned cells across the broad spectrum of cytokines compared to molecules secreted from non-patterned cells, especially from IL-1 to Leptin (arranged in descending order (left to right) of –fold change for patterned cells over non-patterned cells). However, interestingly, when patterned cells are supplemented with inhibitors of α5ß1 and ERK 1/2, the molecules which secreted more in patterned cells relative to those cultured in non-patterned gels (IL-1 to Leptin) showed decreased levels of expressions while pro-angiogenic proteins were up-regulated in non-patterned cells (G-CSF to IGF-2) displayed elevated expression levels. Moreover, TIMP-1 expression was elevated for cells on spiral-patterned gels treated with the ERK inhibitor (~1.53-fold higher) compared to those from other conditions. Taken together, interfacial geometry modulates not only tumorigenicity but also the angiogenic potential of cancer cells through enhancing α5ß1 and αvß3 adhesion, MAP/ERK kinase signaling and STAT3 or HIF1α activity, which may lead to the secretion of various molecules promoting angiogenesis at the invasive regions.

Interfacial Regulation of the CSC phenotype in 3D microenvironments.

To explore higher-dimensional materials which more closely mimic the tumor microenvironment in vivo, we encapsulated groups of cells in 3D poly(ethylene glycol) (PEG) gels. After five days in culture, B16F0s cultured in 3D PEG gels express higher levels of CD271 marker relative to those cultured in 2D spiral patterned PA gels, and conditioned media collected from those cultured in 3D PEG gels promote tubulogenesis in hMVECs cultured in matrigel (Fig. 9.7a). Tube formation decreases when B16F0s cultured in 3D PEG gels with blocking of integrin α5ß1 or inhibiting ERK MAP kinase signaling, which is corresponding to a decrease in CD271 marker expressions with a correlation coefficient of around 0.96.

In Ovo Pro-Angiogenic Potential of the CSC Phenotype.

To explore whether CSC-like B16F0s at the interfacial geometry will reveal pro-angiogenic activity in ovo, we employ a chick chorioallantoic membrane (CAM) assay. We placed 2D PA gels containing B16F0s cultured on non-patterned or spiral-patterned gels with/without blocking integrin α5ß1or inhibiting ERK signaling on the CAMs of 10-day old chick embryos (face down). After five days in culture, we analyzed the formation of new vessels and the results reveal enhanced vessel formation in CAMs which are much bigger and more mature after administration of spiral patterned B16F0s, when compared to untreated (~3.78-fold) or B16F0s cultured in non-patterned gels (~1.80-fold) or spiral patterns with α5ß1 blocking (~1.68-fold) or ERK inhibition (~1.48-fold) (Fig. 9.7b). This demonstrates that B16F0s cultured in geometries which contain curvature and interfacial boundaries show an enhanced pro-angiogenic potential when applied to the CAM system, and

thus we asked whether we could see the similar trend for angiogenesis in vivo to relate to the observations in vitro and in ovo.

In Vivo Tumorigenicity and Angiogenesis of the Activated Cells.

To verify the tumorigenicity and angiogenic potential of our engineered cells in vivo, we cultured B16F0s for five days on spiral patterned or non-patterned gels, followed by subcutaneous injection into 6-8-week-old C57BL/6 mice and observed for 3 weeks. Primary tumor growth (monitored every week with calipers) was enhanced for the B16F0 cells cultured on spiral patterned gels relative to those cultured on non-patterned gels (Fig. 9.8a). Those tumors derived from patterned cells had higher levels of angiogenesis, with enhanced vessel formation around the tumors (Fig. 9.8b). With the observed differences for primary tumor growth and angiogenesis, we sought to confirm if these activated cells would likewise give rise to a higher degree of angiogneic signaling in vivo. We measured the signal of Cu64-cRGD targeting to the integrin αvβ3 which is highly expressed on activated endothelial cells during angiogenesis (201, 202) and found higher levels of Cu64-cRGD signaling (~1.26-fold_1 week, ~1.35-fold_2 weeks, ~1.37-fold_ 3 weeks) on the periphery of patterned cells where the new vascular network was formed (Fig. 9.8c and d). Next, we matrigelencapsulated cells in matrigel when subcutaneously injecting into mice because tumors could grow stably and angiogenesis occurs through the matrix inside, allowing us to quantitatively analyze the vessel density by sectioning tumors in matrigel. After seven days in culture, we confirmed primary tumor establishment in both conditions and we analyzed the blood vessel formation by staining for endothelial cells around the tumor for mice injected with B16F0s in

matrigel (Fig. 9.8e). The vessel density per tumor mass was enhanced for the B16F0s cultured on spiral patterned gels compared to those cultured on non-patterned gels (~ 4.6-fold) (Fig. 9.8f). Overall, our in vivo results were consistent with our observations in vitro and in ovo.

9.4 Discussion

In the present chapter, we provide evidence that geometries which contain curvature and interfacial boundaries regulate not only melanoma cancer cell tumorigenicity but also their angiogenic potential. We showed that CSC-phenotypes at the interface which express elevated levels of CD271 also have higher levels of angiogenic potential relative to non-CSC-phenotypes. Furthermore, we found adhesion through integrin α5ß1 and MAPK signaling especially ERK play an important role in higher vessel formation of endothelial cells by these CSC-phenotypes at the interface in both 2D and 3D model systems. The results from in ovo CAM and in vivo mice models supported the understanding of the mechanisms that regulate angiogenesis from CSCs at the interface of tumors.

Tumor angiogenesis is considered one of the most essential strategies for tumor growth and progression, and most studies have focused mainly on angiogenesis in the hypoxic microenvironment (191). In general, HIF1 which is one of the most important angiogenic transcriptional factors regulating a lot of genes involved in cancer invasion, differentiation, metabolism, and apoptosis could be activated by hypoxia (190, 192). HIF1 mainly consists of an oxygen-regulated subunit (HIF1α) and a constitutively expressed subunit (HIF1ß). HIF1α could be degraded for cells in

non-hypoxic conditions through ubiquitin-proteasome pathways while those in hypoxic conditions could have the stable HIF1α subunit which interacts with coactivators and regulates the expression of target genes, promoting angiogenesis (192). However, recent studies have shown some evidences of hypoxia-independent mechanisms of tumor angiogenesis (195, 196). The fact that HIF1 could be also regulated in an oxygen-independent manner by various factors such as cytokines (203), growth factors (204), environmental stimuli (205), and other signaling molecules (206) suggests hypoxia may not the only way to regulate HIF1. In melanoma cancer, there is evidence showing some signaling pathways such as BRAF/MEK/ERK (207) and PI3K (208) could give rise to the stabilization and activation of HIF1α protein levels in non-hypoxic conditions. Furthermore, MAPK signaling has been reported to be able to stimulate HIF1 activation regardless of oxygen tension (209). In the current study, we found that the MAPK (especially ERK 1/2) pathway is significantly involved in melanoma angiogenic potential in non-hypoxic conditions, and thus we questioned whether HIF1α would be highly associated with their angiogenic activity. The fact that when B16F0s were inhibited with HIF1α, tube area of hMVECs with B16F0 conditioned media was significantly suppressed relative to untreated suggests HIF1α, which may be activated by ERK-MAPK signaling in normoxia, also plays an important role in the angiogenic potential of melanoma cells in non-hypoxic conditions.

VEGF is one of the most potent endothelilar-specific mitogens to regulate angiogenesis and also known to be regulated by HIF-1 and STAT3 (193, 194). For instance, VEGF expression could be enhanced by hypoxia via HIF1α induced by

increased STAT3 activities (193). In addition, a previous report showed STAT3 directly contributes to the overexpression of VEGF (210). In the current study, we see genes related to VEGF signaling or regulated by HIF-1 are upregulated for B16F0s cultured on spiral-patterned gels compared to those cultured on non-patterned gels or glass substrates. This may be supported by STAT3 activity in normoxia, because, previously, we showed STAT3 is downstream of these integrin α5ß1 and of the MAPK pathway (mainly p38 and ERK) for promoting CSC-phenotypes at the interface. In this study, we also found that STAT3 expressions was regulated by integrin α5ß1 and αvß3, ERK pathway, or cytoskeletal tension (Y27632) and VEGF expressions decreased with blocking α5ß1 and inhibition of ERK pathway in the protein array. This suggests that activated STAT3 activities caused by the signaling through integrin α5ß1and ERK may increase the angiogenic potential of CSC-like B16F0s.

TIMP-1 which can inhibit the activities of matrix metalloproteinases (MMPs) is known as a suppressor of melanoma growth, invasion, metastasis, tumorigenesis, and angiogenesis (189). In this study, B16F0s cultured on spiral-patterned gels with an ERK inhibitor show elevated levels of TIMP-1 expression compared to those cultured on non-patterned gels or spiral-patterned gels (untreated or blocking integrin α5ß1), suggesting ERK may also play a significant role in promoting melanoma malignant activity via suppression of TIMP-1. Taken together, unlike the traditional concept showing hypoxic conditions are required for tumor angiogenesis, hypoxia-independent drivers such as ERK may be able to activate angiogneic factors by enhancing STAT3 activities and suppress TIMP-1. Based on the fact that

melanoma CSC phenotypes activated at the perimeter may have similar pathways for being highly tumorigenic and promoting angiogenesis at the same time, blockade of the integrin α5ß1 and ERK pathway is a novel therapeutic approach for the prevention of progression and angiogenesis of melanoma CSCs.

3D in vitro models can span the gap between 2D cultures and whole animal systems. In this study we cultured B16F0s not only on the 2D surface of PA gels but also encapsulated them in 3D PEG gels to study the angiogenic potential in response to their microenvironments. Similar to the results from our previous study (164) showing B16F0s cultured in 3D microenvironments displayed higher CD271 marker expressions relative to those cultured on spiral-patterned gels, these cells in 3D also showed higher levels of tubulogenesis of hMVECs. Despite dramatic increases in the angiogenic potential in 3D cultures, blocking adhesion through integrin α5ß1 and inhibiting ERK pathway also suppressed tube formation of hMVECs with condition media from B16F0s. The consistent effect of these treatments of our 2D and 3D tumor models on the angiogenic potential of B16F0s indicate that adhesion through integrin α5ß1 and ERK pathway may also prove a general driver for activated melanoma cells at the perimeter in promoting angiogenesis by modulating angiogenic factors.

Animal studies help confirm the relevance of the in vitro results and could support the understanding of the underlying mechanisms. We employed an in ovo CAM assay and murine model of primary tumor growth to investigate the role of activated CSC-like cells at the periphery in promoting angiogenesis. Like previous studies showing that CSC phenotypes sorted by CD133 for glioma cells (211) or

CD105 for renal cell carcinoma (212) could promote tumor angiogenesis in vivo, activated cells cultured on interfacial geometry without sorting by CSC markers could promote higher levels of angiogenesis in both the in ovo CAM assay and in vivo mice models. For the in ovo CAM studies, the vessel area was higher for B16F0s cultured in spiral geometries than those cultured on non-patterned substrates, and blocking α5ß1 and inhibiting ERK pathway played an important role in promoting angiogenesis, which is consistent with in vitro results. For in vivo mice studies, we saw higher levels of angiogenesis, with Cu64-cRGD incorporation indicating the formation of new vascular networks, and increased vessel density around tumors derived from cells cultured in spiral geometries, which also support the hypothesis that a population of cells with a stem-cell-like phenotype at the interface promotes higher levels of tumor angiogenesis.

9.5 Conclusion

Our results show that the angiogenic potential of melanoma cells can be modulated by a unique microenvironment where CSC phenotypes can be activated through integrin-mediated adhesion and mechanotransduction. These CSC phenotypes can promote higher degrees of tubulogenesis in hMVECs in vitro 2D and 3D tumor models and angiogenesis in an in ovo CAM model and an in vivo mouse model relative to non-CSC phenotypes. In addition, unlike the traditional concept that tumor angiogenesis occurs under hypoxic conditions due to low nutrient concentrations, our data underscores the concept that hypoxia may not be a pre-requisite for tumor angiogenesis, suggesting that CSCs at the interfaces of tumors may initiate angiogenesis and that it could be accelerated by hypoxic conditions at

the certain time points. Although molecular mechanisms of melanoma cell secretion to promote angiogenesis remains to be defined, we reveal specific signaling pathways associated with angiogenesis in melanoma CSC phenotypes. Therefore, targeting of adhesion through α5ß1 and the ERK pathway which are highly involved in enhanced HIF1α and STAT3 activities, and suppressed TIMP-1 levels may represent a novel approach to controlling the angiogenesis of melanoma cancers at early time points. Our results may also have important implications for different approaches to preventing angiogenesis from different stages of tumors with increased specificity and efficiency in targeting of CSCs at the invasive regions of tumors.

9.6 Figures

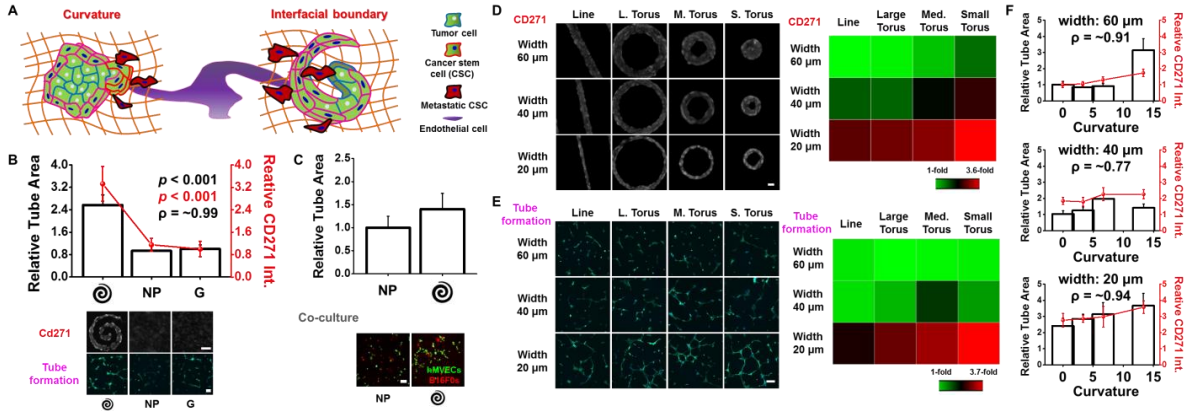

Figure 9.1 *Interfacial geometry at perimeter features regulate angiogenic potential. (a) Schematic depicting how interfacial geometry containing curvature and interfacial boundaries may guide tumorigenicity and angiogenesis. (b) CD271 marker expression of B16F0s cultured on spiral-patterned gels, non-patterned gels, or glass substrates, and tube area formed by hMVECs after being treated with conditioned media from the B16F0s. Representative immunofluorescence images of B16F0s for CD271 and hMVECs for tube formation (green). Correlation coefficient (ρ) is around 0.99. Scale bar: 100 μm. (N=5). (c) Quantitation of relative tube area of hMVECs co-cultured with B16F0s pre-cultured on spiral-patterned or non-patterned gels. Representative immunofluorescence images of hMVECs tube formation (green) and B16F0s (red) when co-cultured on matrigel for 8 hours. Scale bar: 100 μm. (N=5). (P-value from ANOVA analysis). (d) Representative immunofluorescent images of patterned B16F0s showing CD271 expression in line and torus geometries with different curvature and width. Heat map comparing the CD271 marker expressions across the shapes. Scale bar: 50 μm. (N=5). (e) Representative immunofluorescent images of hMVECs showing tube formation (green) after being treated with conditioned media from patterned B16F0s. Heat map comparing tube area of hMVECs across the shapes of B16F0s. Scale bar: 100 μm. (N=5). (f) Curvature with different width of torus shape influences both CD271 marker expression of B16F0s and tube formation of hMVECs cultured in matrigel for 8 hours with conditioned media of the B16F0s. Correlation coefficients (ρ) are around 0.91 (60 μm width), 0.77 (40 μm width), 0.94 (20 μm width).*

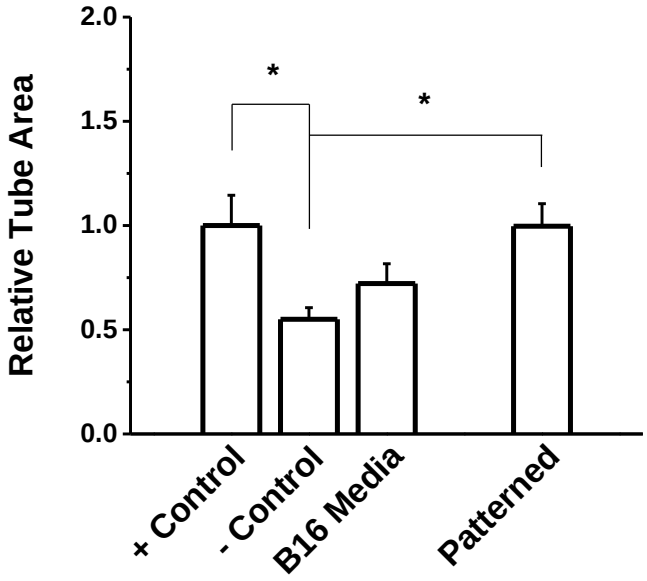

Figure 9.2 *Relative tube area of hMVECs with conditioned media from B16F0s cultured on spiral-patterned PA gels compared to those cultured with positive or negative control media or B16F0s media. (P-value from Student's t-test, *P<0.05).*

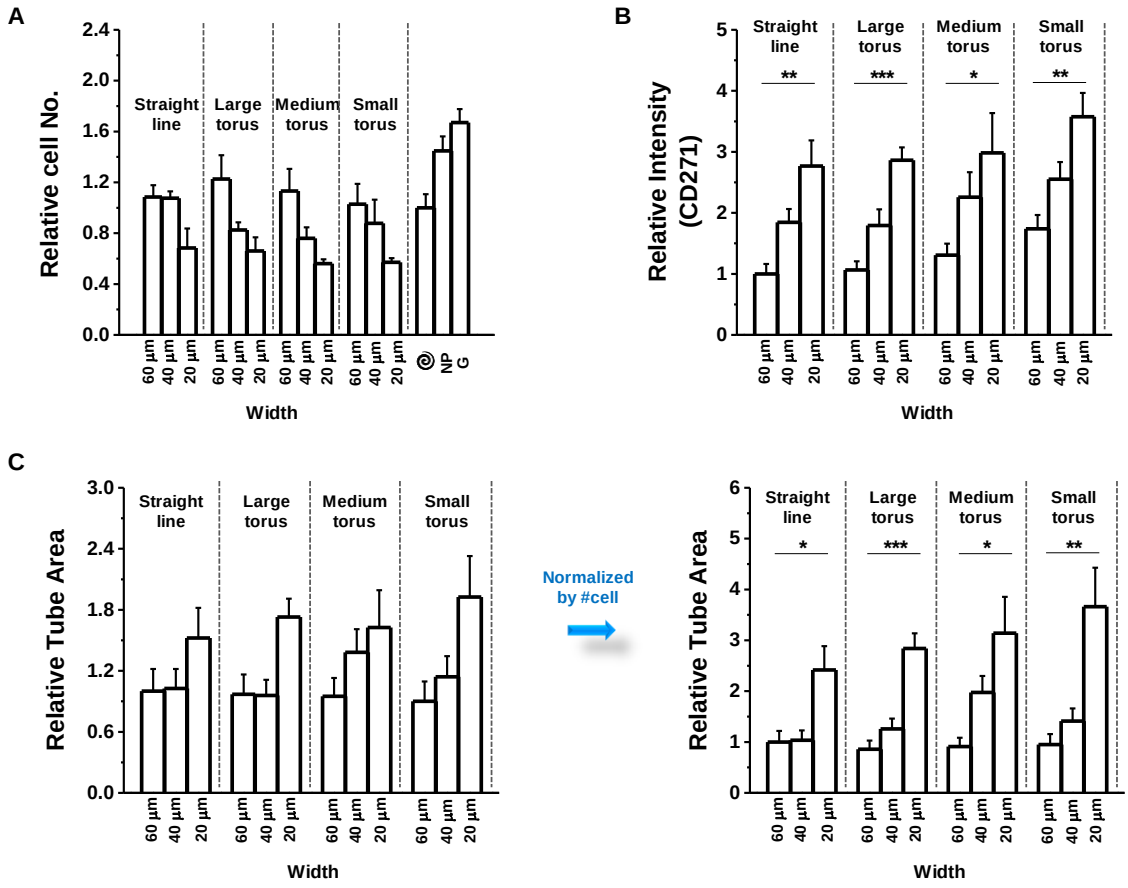

Figure 9.3 *(a) Relative numbers and (b) immunofluorescence intensity (CD271) of B16F0s in different patterns, non-patterns, or glass substrates. (c) Relative tube area of hMVECs cultured with different conditioned medias before and after normalization by cell numbers. (N=5). (P-value from ANOVA analysis).*

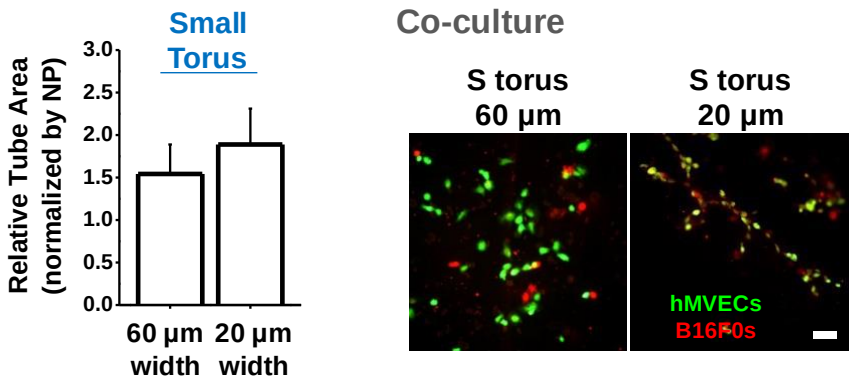

Figure 9.4 *Quantitation of relative tube area of hMVECs co-cultured with B16F0s pre-cultured on torus-patterned (60 or 20 μm width) gels. Representative immunofluorescence images of hMVECs tube formation (green) and B16F0s (red) when co-cultured on matrigel for 8 hours. Scale bar: 100 μm. (N=5).*

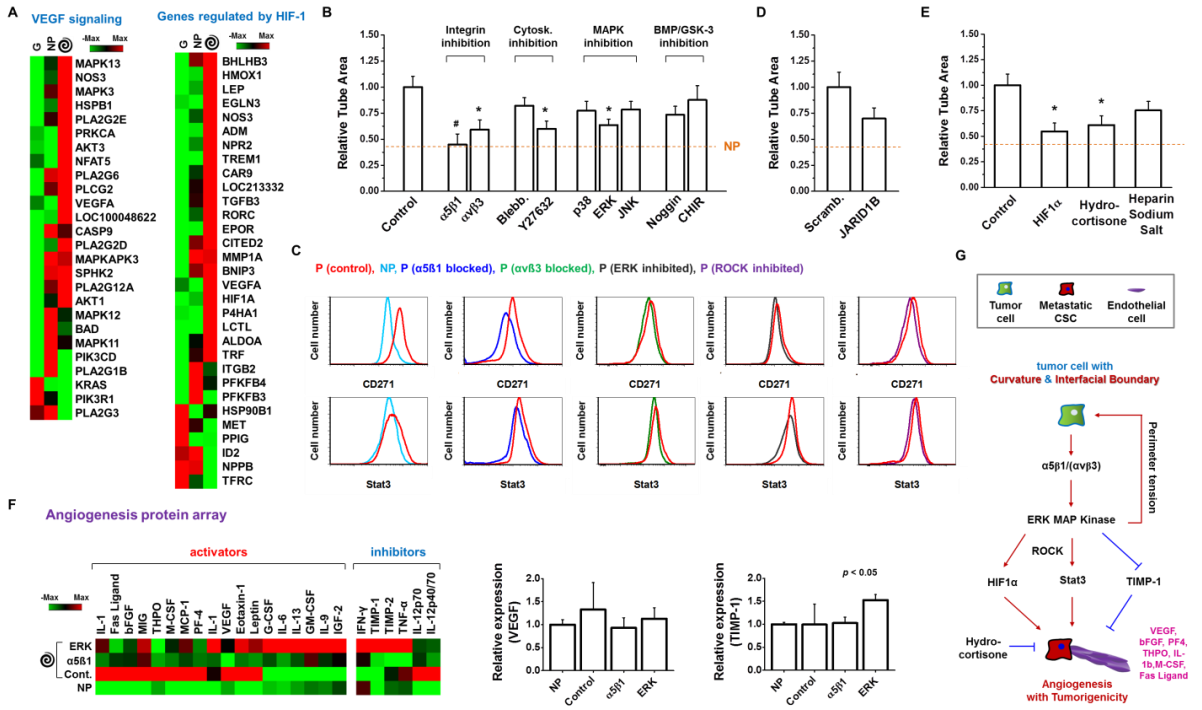

Figure 9.5 *Interfacial geometry activates CSCs and their angiogenic potential through integrin α5ß1 (αvß3), mitogen-activated protein kinase (MAPK) signalling and regulation of signal transducer and activator of transcription (STAT) or hypoxia-inducible factor-1 α (HIF-1α) pathways. (a) Gene expression analysis of transcripts associated with VEGF signaling and genes regulated by HIF-1 for cells cultured on glass substrates (G), non-patterned gels (NP), and spiral-patterned gels. (b) Effect of treatment of spiral-patterned B16F0s with blocking antibodies to integrins α5ß1 and αvß3 or inhibiting cytoskeletal tension (Blebbistatin & Y27632), MAPK pathways (p38, ERK, JNK), BMPs pathway (Noggin), or GSK-3 (CHIR) to B16F0s conditioned media on tube formation of hMVECs (N=5). (P-value from Student's t-test, *P<0.05, #P<0.01). (c) Flow cytometry characterization of CD271 or STAT3 in B16F0s when treated with α5ß1 or αvß3 blocking, an ERK inhibitor, or a ROCK inhibitor (Y27632). (d) Effect of interfering Jarid1B RNAs for B16F0s to their conditioned media on tube formation of hMVECs. (N=5). (e) Effect of HIF1α inhibition, hydrocortisone, or heparin sodium salt for B16F0s to their conditioned media on tube formation of hMVECs. (N=5). (f) Heat map of cytokine expression (24 proteins) in conditioned media of B16F0s cultured in non-patterned gels or spiral-patterned gels with/without α5ß1 blocking or ERK inhibition. (N=4). (P-value from ANOVA analysis). (g) Proposed pathway for interfacial geometry regulating angiogenic potential of B16F0s.*

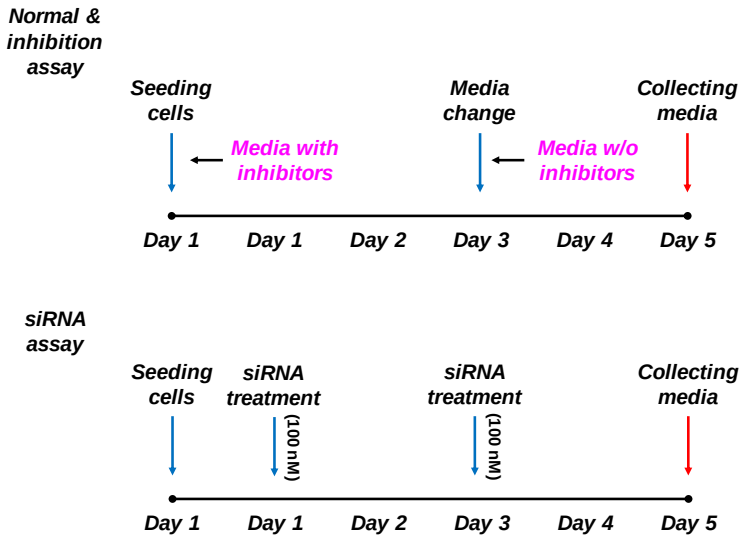

Figure 9.6 *Media conditions for normal, inhibition, or siRNA transfection.*

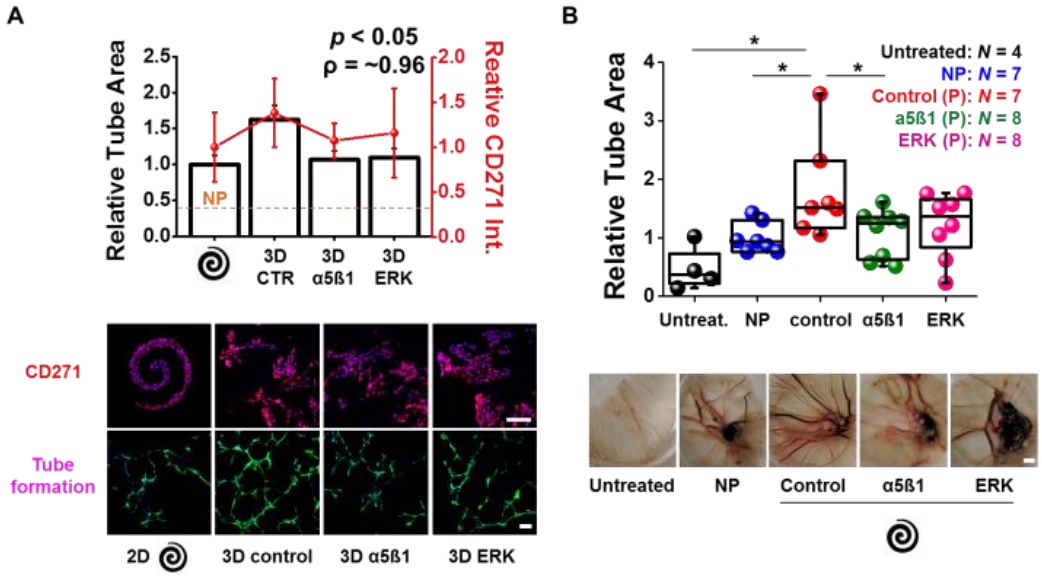

Figure 9.7 *Interfacial geometry regulates the CSC phenotype and angiogenic potential in 3D microenvironments and enhances in ovo angiogenesis. (a) CD271 marker expression of B16F0s cultured in spiral-patterned gels (2D) or incorporated in PEG gels (3D) with/without α5ß1 blocking or ERK inhibittion, and tube area formed by hMVECs after being treated with conditioned media from the B16F0s. Representative immunofluorescence images of B16F0s (blue: nuclei) for CD271 (red) and hMVECs for tube formation (green). Correlation coefficient (ρ) is around 0.96. Scale bar: 100 μm. (N=5). (P-value from ANOVA analysis). (b) Relative tube area (normalized to cell number) on CAMs with implanted PA hydrogels with B16F0s non-patterned or spiral-patterned with/without α5ß1 blocking or ERK inhibition. Representative images of CAMs from different conditions. Scale bar: 2mm. (P-value from Student's t-test, *P<0.05).*

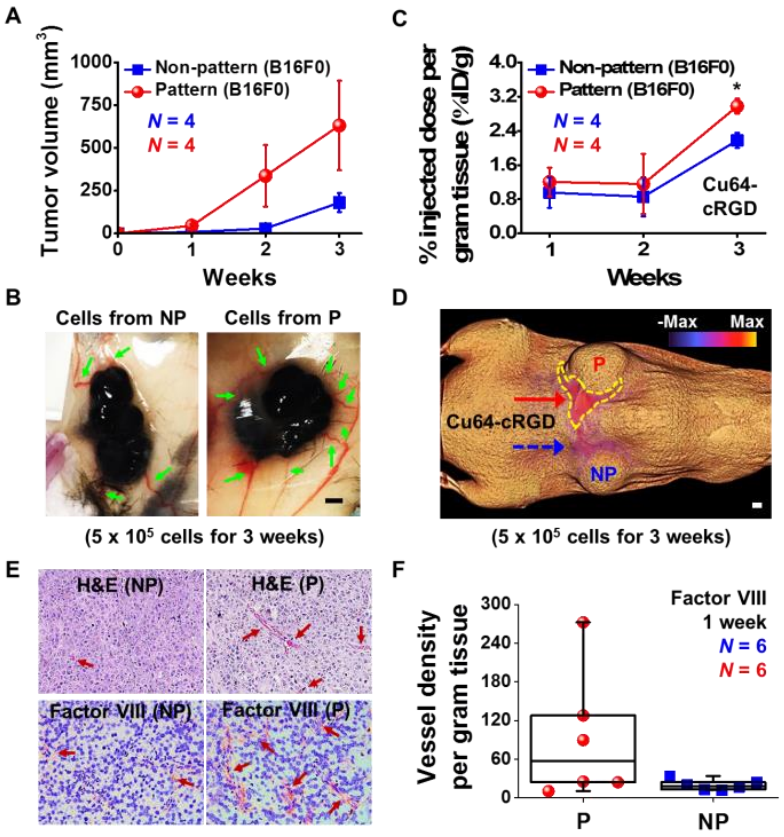

Figure 9.8 *CSC like cells display higher tumorigenicity and angiogenic potency in vivo. (a) Tumor growth characteristics of subcutaneous implanted cells (patterned or non-patterned) in C57BL/6 mice. Error bars represent s.e. (b) Representative images of tumors and angiogenesis after culturing of the subcutaneous implanted cells cultured for 3 weeks. Scale bar, 2 mm. (c) Percent of injected dose per gram of tissue (%ID/g) (avb3 integrin targeting using Cu64-cRGD) for subcutaneous implanted cells. Error bars represent s.e. (d) 3D color map from a PET/CT scan of a representative mouse for Cu64-cRGD signals (targeting to avb3) 3 weeks after subcutaneously implanted with patterned (Left) and non-patterned (Right) cells. (e) Histopathology of tumor sections after subcutaneous injection and Immunolabelling of excised sections of tumors tissue (with matrigels) stained for Factor VIII after subcutaneous implantation of B16F0 cells cultured in the spiral geometry or non-patterned substrates. Scale bar, 50 μm. (f) Vessel density per gram tissue of C57BL6 mice after experimental tumorigeneicity (Factor VIII). N is the number of tumor sections used. Boxes represent 25th to 75th percentile (50th for center line) and whiskers represent minimum–maximum.*

CHAPTER 10

CONCLUDING REMARKS AND FUTURE PROSPECTIVES

10.1 Concluding Remarks

In this work we have shown that ECM properties can have a profound impact on cell programming and reprogramming. We show in Chapter 2-5 that biophysical (elasticity, geometry) and biochemical (matrix composition) cues can influence MSC fate decision especially differentiation. These results may prove useful in the design of tailored hydrogel biomaterials that more efficiently direct distinct differentiation outcomes without the guidance of specific cocktails for promoting MSC lineage specification.

In Chapter 6, we focus on whether changing the biophysical aspects of the substrate could modulate the degree of MSC lineage specification. We revealed that MSCs remain susceptible to the biophysical properties of the extracellular matrix—even after several weeks of culture—and can redirect lineage specification in response to changes in the microenvironment. These results may help us understand the timescales and plasticity underlying stem cell fate determination and is important for fundamental biology as well as for establishing appropriate in vitro culture conditions to direct a desired outcome.

In this study, we hypothesized that properties of the extracellular matrix, such as elasticity, composition, and cell/tissue geometry, can be used to guide reprogramming as well as programming. We demonstrated the possibility of rewiring MSC lineage specification by switching the biophysical microenvironment in

Chapter 6, which highlights the degree of cellular plasticity in response to microenvironmental cues. Emerging evidence suggests that in addition to physiologically normal cells, cancer cells in solid tumors may exhibit more plasticity than originally anticipated, and may be influenced through biophysical cues in the tumor microenvironment. Hence, in Chapter 7-9 we leveraged microengineered biomaterials to deconstruct and study the effects of these parameters on guiding cellular processes, in particular the reprogramming of cancer cells. Combinations of biophysical and biochemical properties exerted an influence on cell state to help us gain a fundamental understanding of the role of the tumor microenvironment during metastasis.

We explored the role that tumor geometry and mechanical properties play in guiding cancer stem cell phenotype and investigated the mechanism in which biophysical properties guide the melanoma cancer stem cell state. We showed that our finding based on 2D biomaterials—the role of interfacial geometry in guiding the cancer stem cell phenotype—can be applied not only to tumor-mimetic pseudo-3D and 3D architectures, but also to in vivo using a well-characterized murine model of primary tumor growth and pulmonary metastases. In addition, we provide evidence that histone H3 lysine 4 di-methylation and lysine 9 acetylation are preferentially activated by cancer stem cell phenotypes of malignant melanoma at the periphery of tumors. This discovery may help detect cancer-specific epigenetic changes which could be used as epigenetic biomarkers for clinical prediction, diagnosis, and therapeutic development. Furthermore, we explored angiogenesis signaling in proximity to reprogrammed cancer cells to understand the underlying mechanism

which promotes angiogenesis and dissemination, which has important implications for future research in developing rational treatment strategies for metastasis.

Overall these works provide several insights into how cell programming or reprogramming can be modulated via combinations of biophysical and biochemical properties. However, in order to realize the benefits of this work for practical therapies, further work is required: for MSCs, showing the in-vivo applicability for MSC differentiation and, for cancers, understanding the different characteristics between distinct cancers and their possible mutations in vivo, which leads to the limitation of targeted cancer therapies. This would enable more precise control for clinical prediction, diagnosis, and therapeutic development.

10.2 Future Perspectives

In the past several decades, a substantial number of biomaterial systems have been designed to present physiologically relevant physical and chemical properties to understand how complex natural microenvironments guide fate decision of both stem and cancer cells. The model system presented here patterning different types of matrix proteins with various geometries on the hydrogel substrates with tunable stiffness is one representative 2D model system which has a significant impact on understanding cellular behavior for biomedical applications. However, it is undeniable that complex dynamic 3D substrates would be more relevant to in vivo tissue microenvironments. Owing to their physiological relevance, 3D model systems would have a strong impact on predicting and understanding the cellular response of real organisms. Nevertheless, studies employing 3D microenvironments

with multiple factors would be complicated without precisely understanding each factor. For tackling this issue, we may need to develop standard protocols and quantitative analysis methods. However, a myriad of obstacles must be overcome to achieve these goals; first, standardization could take several years to be fully developed, and second, for the analysis in complex 3D systems, different results may be obtained in different laboratories without standardized and quantitative analysis methods. Thus, we may need to design and develop tailored model systems bridging 2D and 3D comprising multiples cues together to supplement or replace animal models. The process of exploring how interfacial geometry promotes cancer stem cell phenotypes in 2D, 3D, and mice in vivo studies in chapter 7-9 is a key example of providing a bridge between 2D cell cultures and complicated 3D in vivo microenvironments. This means not only investigating specific roles of individual cues in a simple 2D system but also integrating these cues in complex 3D microenvironments. This makes it possible to bridge the gap between findings in 2D cell culture systems and in vivo tissue cultures.

In the last several decades, traditional therapies including chemo- and radio-therapies against cancer have several limitations that give rise to treatment failure and cancer recurrence. These limitations are associated with systemic and local toxicity, yet treatment failure and cancer relapse may be owing to the existence of cancer stem cell (CSC) phenotypes defined as cells with a small fraction within a tumor which have the capacity to self-renew, and are associated with cancer initiation, maintenance, metastasis, chemo-resistance and recurrence. Thus, developing efficient treatments including drug discovery that can specifically target

and eradicate CSCs have been fast becoming an essential part of clinical development for long-term patient survival. Consequently, separating pure CSC populations or developing a useful tool to be able to reprogram cancer cells into CSC phenotypes by promotion of the epithelial to mesenchymal transition (EMT) would play a crucial role in gaining in-depth knowledge about cancer heterogeneity and understanding plasticity of CSC phenotypes. CSC identification is a complicated process and it is highly dependent on different strategies such as expression of specific surface markers, in vitro tumor sphere assays, and in vivo limited dilution assays. One of biggest struggles to isolate and study CSCs is due to the rarity of this population within the tumor tissue. Developing cell and tissue engineering approaches as a way to model cancer based on reprogramming a CSC state may prove a facile strategy for mimicking progression as a tool for drug development. Accumulated evidence has supported the possibility of cancer reprogramming; first, many cancer cell types such as breast (213, 214), prostate (215), lung cancers (216, 217), leukemia (218, 219), and melanoma (220, 221) have shown characteristics of reprogramming, second, multiple studies have revealed that several specific signaling pathways such as Wnt (222, 223), mTOR/PI3K/Akt (224), MAP kinase (225) or Notch (226) pathways involved in CSC phenotype signaling could be associated with reprogramming of cancers and targeted to prevent the reprogramming, and third, several ways to reprogram cancers into CSC phenotypes such as induced pluripotent stem cell technology with Yamanaka factors (64, 227), employing microRNA highly expressed in ESCs (228), hypoxic condition (229), and microenvironmental factors (230) have been investigated.

In the last several decades, conventional cancer cell lines cultured on dishes have been used for in vitro drug screening and development owing to being convenient and easy to use (231). However, these cancer cell lines are not representative of complicated tumor heterogeneity for each patient, and there exist lots of alterations during the process of generating them such as biological properties, genetic information, and general characteristics including growth and invasion properties (232, 233). Therefore, the use of cancer cell lines for preclinical drug development seems like an inappropriate strategy for potential application in personalized medicine. In general, personalized medicine categorizes patients into unique cancer subgroups, allowing for individualized therapy with tailored treatment and follow-up for each patient according to disease aggressiveness and the tendency to response to a certain treatment (234). For instance, patient-derived tumor xenograft (PDX), which is based on the transfer of primary tumors from the patient into an immunodeficient mouse, has been of great interest to researchers over the past several decades because of a high level of correlation between clinical results in patients and these models (235). These transferred tumors show very similar characteristics like heterogeneity and molecular diversity of the patients, but there may be some limitations to be tackled such as the lack of functional immune system in these models, the selection of the most appropriate tissue from patients and the best strategy of engraftment in mice, or interval between engraftment time for PDX models and treatment schedules for patients (236). Thus, novel approaches to reprogram cancer cells into CSC phenotypes still seem required to investigate health and disease and aid drug discovery efforts in the pharmaceutic industry. For example, unlike most previous cancer treatments predicated on targeting mainly

tumor cells cultured on plastic-ware, we have developed a simple way to generate higher fraction of cancer stem cell phenotypes at the interfacial geometry using 2D engineered biomaterials. These advances may allow us to tackle some issues raised in the current systems ranging from a rare population to reproducibility. Although further studies are required to explore the relevance of CSCs in vitro model systems, it is possible to use these systems for clinical applications. For instance, as a tool for personalized medicine, cancer cells from different patients could be reprogrammed through EMT by using the model system containing interfacial geometry, and then these reprogrammed CSC phenotypes could be targeted by multiple drugs to find the best one for each patient or by pathways activated during cancer reprogramming. These could help us to guide further therapeutic steps and the tailored design of preclinical and clinical trials.

REFERENCES

1. Shin H et al. (2005) Osteogenic differentiation of rat bone marrow stromal cells cultured on Arg-Gly-Asp modified hydrogels without dexamethasone and beta-glycerol phosphate. *Biomaterials* 26:3645–54.

2. Khetan S et al. (2013) Degradation-mediated cellular traction directs stem cell fate in covalently crosslinked three-dimensional hydrogels. *Nat Mater* 12:1–8.

3. Benedetto F Di, Biasco A, Pisignano D, Cingolani R (2005) Patterning polyacrylamide hydrogels by soft lithography. *Nanotechnology* 16:S165–70.

4. Khetan S, Burdick J A. (2011) Patterning hydrogels in three dimensions towards controlling cellular interactions. *Soft Matter* 7:830–8.

5. Hynd MR, Frampton JP, Dowell-Mesfin N, Turner JN, Shain W (2007) Directed cell growth on protein-functionalized hydrogel surfaces. *J Neurosci Methods* 162:255–63.

6. Peng R, Yao X, Cao B, Tang J, Ding J (2012) The effect of culture conditions on the adipogenic and osteogenic inductions of mesenchymal stem cells on micropatterned surfaces. *Biomaterials* 33:6008–19.

7. Saha K et al. (2008) Substrate modulus directs neural stem cell behavior. *Biophys J* 95:4426–38.

8. Wilson A, Trumpp A (2006) Bone-marrow haematopoietic-stem-cell niches. *Nat Rev Immunol* 6:93–106.

9. Banerjee A et al. (2009) The influence of hydrogel modulus on the proliferation and differentiation of encapsulated neural stem cells. *Biomaterials* 30:4695–9.

10. Lee JN, Park C, Whitesides GM (2003) Solvent compatibility of poly(dimethylsiloxane)-based microfluidic devices. *Anal Chem* 75:6544–54.

11. Dusseiller MR, Schlaepfer D, Koch M, Kroschewski R, Textor M (2005) An inverted microcontact printing method on topographically structured polystyrene chips for arrayed micro-3-D culturing of single cells. *Biomaterials* 26:5917–25.

12. Ingber DE, Folkman J (1989) Mechanochemical switching between growth and differentiation during fibroblast growth factor-stimulated angiogenesis in vitro: role of extracellular matrix. *J Cell Biol* 109:317–30.

13. Damljanović V, Lagerholm BC, Jacobson K (2005) Bulk and micropatterned conjugation of extracellular matrix proteins to characterized polyacrylamide substrates for cell mechanotransduction assays. *Biotechniques* 39:847–51.

14. McGarry JP et al. (2009) Simulation of the contractile response of cells on an array of micro-posts. *Philos Trans R Soc - Ser A Math Phys Eng Sci* 367:3477–97.

15. Janmey PA, Miller RT (2011) Mechanisms of mechanical signaling in development and disease. *J Cell Sci* 124:9–18.

16. Kurpinski K, Chu J, Hashi C, Li S (2006) Anisotropic mechanosensing by mesenchymal stem cells. *Proc Natl Acad Sci U S A* 103:16095–100.

17. Aydin D et al. (2010) Polymeric substrates with tunable elasticity and nanoscopically controlled biomolecule presentation. *Langmuir* 26:15472–80.

18. Gallant ND, Michael KE, Garcı J (2005) Cell adhesion strengthening : contributions of adhesive area , integrin binding , and focal adhesion assembly. *Mol Biol Cell* 16:4329–40.

19. Kushiro K, Chang S, Asthagiri AR (2010) Reprogramming directional cell motility by tuning micropattern features and cellular signals. *Adv Mater* 22:4516–9.

20. Gopalan SM et al. (2003) Anisotropic stretch-induced hypertrophy in neonatal ventricular myocytes micropatterned on deformable elastomers. *Biotechnol Bioeng* 81:578–87.

21. Frith JE, Mills RJ, Hudson JE, Cooper-White JJ (2012) Tailored integrin-extracellular matrix interactions to direct human mesenchymal stem cell differentiation. *Stem Cells Dev* 21:2442–56.

22. Rowlands AS, George PA, Cooper-white JJ (2008) Directing osteogenic and myogenic differentiation of MSCs : interplay of stiffness and adhesive ligand presentation. *Am J Physiol Cell Physiol* 295:1037–44.

23. Kilian KA, Mrksich M (2012) Directing stem cell fate by controlling the affinity and density of ligand-receptor interactions at the biomaterials interface. *Angew Chem Int Ed Engl* 51:4891–5.

24. Guilak F et al. (2009) Control of stem cell fate by physical interactions with the extracellular matrix. *Cell Stem Cell* 5:17–26.

25. Higuchi A, Ling Q, Chang Y, Hsu S, Umezawa A (2013) Physical cues of biomaterials guide stem cell differentiation fate. *Chem Rev* 113:3297–328.

26. Abdeen AA, Lee J, Kilian KA (2016) Capturing extracellular matrix properties in vitro : Microengineering materials to decipher cell and tissue level processes. *Exp Biol Med* 241:930–8.

27. Huebsch N et al. (2010) Harnessing traction-mediated manipulation of the cell/matrix interface to control stem-cell fate. *Nat Mater* 9:518–26.

28. Engler AJ, Sen S, Sweeney HL, Discher DE (2006) Matrix elasticity directs stem cell lineage specification. *Cell* 126:677–689.

29. Keung AJ, Asuri P, Kumar S, Schaffer DV (2012) Soft microenvironments promote the early neurogenic differentiation but not self-renewal of human pluripotent stem cells. *Integr Biol* 4:1049–58.

30. Flanagan LA, Ju Y, Marg B, Osterfield M, Paul A (2002) Neurite branching on deformable substrates. *Neuroreport* 13:2411–2415.

31. Lee J, Abdeen AA, Tang X, Saif TA, Kilian KA (2016) Matrix directed adipogenesis and neurogenesis of mesenchymal stem cells derived from adipose tissue and bone marrow. *Acta Biomater* 42:46–55.

32. Abdeen AA, Lee J, Bharadwaj NA, Ewoldt RH, Kilian KA (2016) Temporal Modulation of Stem Cell Activity Using Magnetoactive Hydrogels. *Adv Healthc Mater* 5:2536–44.

33. Cho S-W et al. (2004) In vitro study of osteogenic differentiation of bone marrow stromal cells on heat-treated porcine trabecular bone blocks. *Biomaterials* 25:527–35.

34. Trappmann B et al. (2012) Extracellular-matrix tethering regulates stem-cell fate. *Nat Mater* 11:642–9.

35. Hudalla GA, Murphy WL (2011) Chemically well-defined self-assembled monolayers for cell culture: toward mimicking the natural ECM. *Soft Matter* 7:9561–71.

36. Klim JR, Li L, Wrighton PJ, Piekarczyk MS, Kiessling LL (2010) A defined glycosaminoglycan-binding substratum for human pluripotent stem cells. *Nat Methods* 7:989–96.

37. McBeath R, Pirone DM, Nelson CM, Bhadriraju K, Chen CS (2004) Cell shape, cytoskeletal tension, and RhoA regulate stem cell lineage commitment. *Dev Cell* 6:483–95.

38. Kilian KA, Bugarija B, Lahn BT, Mrksich M (2010) Geometric cues for directing the differentiation of mesenchymal stem cells. *Proc Natl Acad Sci U S A* 107:4872–7.

39. Zhang D, Kilian KA (2013) The effect of mesenchymal stem cell shape on the maintenance of multipotency. *Biomaterials* 34:3962–9.

40. Roesch A et al. (2010) A temporarily distinct subpopulation of slow-cycling melanoma cells is required for continuous tumor growth. *Cell* 141:583–94.

41. Liu J et al. (2012) Soft fibrin gels promote selection and growth of tumorigenic cells. *Nat Mater* 11:734–41

42. Tan Y et al. (2014) Matrix softness regulates plasticity of tumour-repopulating cells via H3K9 demethylation and Sox2 expression. *Nat Commun* 5:4619.

43. Kumar S, Weaver VM (2009) Mechanics, malignancy, and metastasis: The force journey of a tumor cell. *Cancer Metastasis Rev* 28:113–27.

44. Discher DE, Janmey P, Wang Y-L (2005) Tissue cells feel and respond to the stiffness of their substrate. *Science* 310:1139–43.

45. Swift J et al. (2013) Nuclear lamin-A scales with tissue stiffness and enhances matrix-directed differentiation. *Science* 341:1240104.

46. Ingber DE (2005) Mechanical control of tissue growth: function follows form. *Proc Natl Acad Sci U S A* 102:11571–2.

47. Nelson CM et al. (2005) Emergent patterns of growth controlled by multicellular form and mechanics. *Proc Natl Acad Sci U S A* 102:11594–9.

48. Friedl P, Gilmour D (2009) Collective cell migration in morphogenesis, regeneration and cancer. *Nat Rev Mol Cell Biol* 10:445–57.

49. Nelson CM, Vanduijn MM, Inman JL, Fletcher D a, Bissell MJ (2006) Tissue geometry determines sites of mammary branching morphogenesis in organotypic cultures. *Science* 314:298–300.

50. Murphy WL, Mcdevitt TC, Engler AJ (2014) Materials as stem cell regulators. *Nat Mater* 13:547–57.

51. Gomez EW, Chen QK, Gjorevski N, Nelson CM (2010) Tissue geometry patterns epithelial-mesenchymal transition via intercellular mechanotransduction. *J Cell Biochem* 110:44–51.

52. Boghaert E et al. (2012) Host epithelial geometry regulates breast cancer cell invasiveness. *Proc Natl Acad Sci U S A* 109:19632–7.

53. Komarova NL (2013) Principles of regulation of self-renewing cell lineages. *PLoS One* 8:e72847.

54. Chen X et al. (2007) Extracellular matrix made by bone marrow cells facilitates expansion of marrow-derived mesenchymal progenitor cells and prevents their differentiation into osteoblasts. *J Bone Miner Res* 22:1943–56.

55. Gregorio GB Di et al. (2001) Attenuation of the self-renewal of transit-amplifying osteoblast progenitors in the murine bone marrow by 17 β - estradiol. J Clin Invest 107:803–12.

56. Thomas D, Kansara M (2006) Epigenetic Modifications in Osteogenic Differentiation and Transformation. *J Cell Biochem* 769:757–69.

57. Frith J, Genever P (2008) Transcriptional control of mesenchymal stem cell differentiation. *Transfus Med Hemotherapy* 35:216–27.

58. Cantone I, Fisher AG (2013) Epigenetic programming and reprogramming during development. *Nat Struct Mol Biol* 20:282–9.

59. Cherry ABC, Daley GQ (2012) Perspective Reprogramming Cellular Identity for Regenerative Medicine. *Cell* 148:1110–22.

60. Hajkova P Epigenetic reprogramming — taking a lesson from the embryo. *Curr Opin Cell Biol* 22:342–50.

61. Krabbe C, Zimmer J, Meyer M (2005) Neural transdifferentiation of mesenchymal stem cells – a critical review. *APMIS* 113:831–44.

62. Bishi, D. K. et al. Trans-differentiation of human mesenchymal stem cells generates functional hepatospheres on poly(L-lactic acid)-co-poly(ε-caprolactone)/collagen nanofibrous scaffolds. *J. Mater Chem B* 1, 3972–84.

63. Zipori D (2004) Mesenchymal stem cells : harnessing cell plasticity to tissue and organ repair. *Blood Cells Mol Dis* 33:211–5.

64. Takahashi K, Yamanaka S (2006) Induction of pluripotent stem cells from mouse embryonic and adult fibroblast cultures by defined factors. *Cell* 126:663–76.

65. Li R et al. (2010) A mesenchymal-to-Epithelial transition initiates and is required for the nuclear reprogramming of mouse fibroblasts. *Cell Stem Cell* 7:51–63.

66. Gupta PB, Chaffer CL, Weinberg RA (2009) Cancer stem cells: mirage or reality? *Nat Med* 15:1010–2.

67. von Burstin J et al. (2009) E-cadherin regulates metastasis of pancreatic cancer in vivo and is suppressed by a SNAIL/HDAC1/HDAC2 repressor complex. *Gastroenterology* 137:361–71.

68. Giudice FS, Pinto DS, Nor JE, Squarize CH, Castilho RM (2013) Inhibition of histone deacetylase impacts cancer stem cells and induces epithelial-mesenchyme transition of head and neck cancer. *PLoS One* 8:e58672.

69. Shackleton M, Quintana E, Fearon ER, Morrison SJ (2009) Heterogeneity in cancer: cancer stem cells versus clonal evolution. *Cell* 138:822–9.

70. Lee J, Abdeen AA, Wycislo KL, Fan TM, Kilian KA (2016) Interfacial geometry dictates cancer cell tumorigenicity. *Nat Mater* 15:856–62.

71. Chaffer CL et al. (2013) Poised chromatin at the ZEB1 promoter enables breast cancer cell plasticity and enhances tumorigenicity. *Cell* 154:61–74.

72. Sarrio D et al. (2008) Epithelial-mesenchymal transition in breast cancer relates to the basal-like phenotype. *Cancer Res* 68:989–97.

73. Hennrick KT et al. (2007) Lung cells from neonates show a mesenchymal stem cell phenotype. *Am J Respir Crit Care Med* 175:1158–64.

74. Keating A (2012) Mesenchymal stromal cells: new directions. *Cell Stem Cell* 10:709–16.

75. Tse JR, Engler AJ (2011) Stiffness gradients mimicking in vivo tissue variation regulate mesenchymal stem cell fate. *PLoS One* 6:e15978.

76. Lee J, Abdeen AA, Huang TH, Kilian KA (2014) Controlling cell geometry on substrates of variable stiffness can tune the degree of osteogenesis in human mesenchymal stem cells. *J Mech Behav Biomed Mater* 38:209–18.

77. Abdeen AA, Weiss JB, Lee J, Kilian KA (2014) Matrix composition and mechanics direct proangiogenic signaling from mesenchymal stem cells. *Tissue Eng Part A* 20:2737–45.

78. Winer JP, Janmey PA, McCormick ME, Funaki M (2009) Bone marrow-derived human mesenchymal stem cells become quiescent on soft substrates but remain responsive to chemical or mechanical stimuli. *Tissue Eng Part A* 15:147–54.

79. Lee J, Abdeen AA, Kilian KA (2014) Rewiring mesenchymal stem cell lineage specification by switching the biophysical microenvironment. *Sci Rep* 4:5188.

80. Khalil AS, Xie AW, Murphy WL (2014) Context clues: the importance of stem cell-material interactions. *ACS Chem Biol* 9:45–56.

81. Ghaemi SR, Harding FJ, Delalat B, Gronthos S, Voelcker NH (2013) Exploring the mesenchymal stem cell niche using high throughput screening. *Biomaterials* 34:7601–15.

82. Gilbert PM et al. (2010) Substrate elasticity regulates skeletal muscle stem cell self-renewal in culture. *Science* 329:1078–81.

83. Skardal A, Mack D, Atala A, Soker S (2013) Substrate elasticity controls cell proliferation, surface marker expression and motile phenotype in amniotic fluid-derived stem cells. *J Mech Behav Biomed Mater* 17:307–16.

84. Tse JR, Engler AJ (2010) Preparation of hydrogel substrates with tunable mechanical properties. *Curr Protoc Cell Biol* 47:10.16.1–10.16.16.

85. Dalby MJ et al. (2007) The control of human mesenchymal cell differentiation using nanoscale symmetry and disorder. *Nat Mater* 6:997–1003.

86. Kilian KA, Bugarija B, Lahn BT, Mrksich M (2010) Geometric cues for directing the differentiation of mesenchymal stem cells. *Proc Natl Acad Sci USA* 107:4872–7.

87. Lee J, Abdeen AA, Zhang D, Kilian KA (2013) Directing stem cell fate on hydrogel substrates by controlling cell geometry, matrix mechanics and adhesion ligand composition. *Biomaterials* 34:8140–8.

88. Yang C, Tibbitt MW, Basta L, Anseth KS (2014) Mechanical memory and dosing influence stem cell fate. *Nat Mater* 13:645–52.

89. Re F et al. (1994) Inhibition of anchorage-dependent cell spreading triggers apoptosis in cultured human endothelial cells. *J Cell Biol* 127:537–46.

90. Guvendiren M, Burdick JA (2012) Stiffening hydrogels to probe short- and long-term cellular responses to dynamic mechanics. *Nat Commun* 3:792.

91. Ruiz SA, Chen CS (2008) Emergence of patterned stem cell differentiation within multicellular structures. *Stem Cells* 26:2921–7.

92. Sart S, Tsai AC, Li Y, Ma T (2014) Three-dimensional aggregates of mesenchymal stem cells: cellular mechanisms, biological properties, and applications. *Tissue Eng Part B* 20:365–80.

93. Fu J et al. (2010) Mechanical regulation of cell function with geometrically modulated elastomeric substrates. *Nat Methods* 7:733–6.

94. Suri S, Schmidt CE (2010) Cell-laden hydrogel constructs of hyaluronic acid, collagen, and laminin for neural tissue engineering. *Tissue Eng Part A* 16:1703–16.

95. Park JS et al. (2011) The effect of matrix stiffness on the differentiation of mesenchymal stem cells in response to TGF-β. *Biomaterials* 32:3921–30.

96. Mariman ECM, Wang P (2010) Adipocyte extracellular matrix composition, dynamics and role in obesity. *Cell Mol Life Sci* 67:1277–92.

97. Tan JL et al. (2003) Cells lying on a bed of microneedles: an approach to isolate mechanical force. *Proc Natl Acad Sci U S A* 100:1484–9.

98. Singh A et al. (2013) Adhesion strength-based, label-free isolation of human pluripotent stem cells. *Nat Methods* 10:438–44.

99. Rotsch C, Jacobson K, Radmacher M (1999) Dimensional and mechanical dynamics of active and stable edges in motile fibroblasts investigated by using atomic force microscopy. *Proc Natl Acad Sci U S A* 96:921–6.

100. Tseng Q et al. (2011) A new micropatterning method of soft substrates reveals that different tumorigenic signals can promote or reduce cell contraction levels. *Lab Chip* 11:2231–40.

101. Komori T et al. (1997) Targeted disruption of Cbfa1 results in a complete lack of bone formation owing to maturational arrest of osteoblasts. *Cell* 89:755–64.

102. Flanagan LA, Ca Y, Marg B, Oster M, Janmey PA (2002) Neurite branching on deformable substrates. *Neuroreport* 13:2411–5.

103. Yim EK, Darling EM, Kulangara K, Guilak F, Leong KW (2010) Nanotopography-induced changes in focal adhesions, cytoskeletal organization, and mechanical properties of human mesenchymal stem cells. *Biomaterials* 31:1299–306.

104. DeForest CA, Anseth KS (2012) Advances in bioactive hydrogels to probe and direct cell fate. *Annu Rev Chem Biomol Eng* 3:421–44.

105. Chen CS, Mrksich M, Huang S, Whitesides GM, Ingber DE (1997) Geometric control of cell life and death. *Science* 276:1425–8.

106. Lee J, Silberstein MN, Abdeen AA, Kim SY, Kristopher A (2016) Mechanochemical functionalization of disulfide linked hydrogels. *Mater Horiz* 3:447–51

107. Choi WS, Kim M, Park S, Lee SK, Kim T (2012) Patterning and transferring hydrogel-encapsulated bacterial cells for quantitative analysis of synthetically engineered genetic circuits. *Biomaterials* 33:624–33.

108. Rape AD, Guo W-H, Wang Y-L (2011) The regulation of traction force in relation to cell shape and focal adhesions. *Biomaterials* 32:2043–51.

109. Li Y, Kilian KA. (2015) Bridging the gap: from 2D cell culture to 3D microengineered extracellular matrices. *Adv Healthc Mater* 4:2780–96.

110. Tang X et al. (2012) Attenuation of cell mechanosensitivity in colon cancer cells during in vitro metastasis. PLoS One 7: e50443.

111. Li L, Xie T (2005) Stem cell niche: structure and function. *Annu Rev Cell Dev Biol* 21:605–31.

112. Jones DL, Wagers AJ (2008) No place like home: anatomy and function of the stem cell niche. *Nat Rev Mol Cell Biol* 9:11–21.

113. Wang Y-K, Chen CS (2013) Cell adhesion and mechanical stimulation in the regulation of mesenchymal stem cell differentiation. *J Cell Mol Med* 17:823–32.

114. Yao X, Peng R, Ding J (2013) Cell-material interactions revealed via material techniques of surface patterning. *Adv Mater* 25:5257–86.

115. Mitragotri S, Lahann J (2009) Physical approaches to biomaterial design. *Nat Mater* 8:15–23.

116. Lee J, Abdeen AA., Kim AS, Kilian KA. (2015) Influence of biophysical parameters on maintaining the mesenchymal stem cell phenotype. *ACS Biomater Sci Eng* 1:218–26

117. Huang C, Dai J, Zhang XA. (2015) Environmental physical cues determine the lineage specification of mesenchymal stem cells. *Biochim Biophys Acta - Gen Subj* 1850:1261–6.

118. Na S et al. (2008) Rapid signal transduction in living cells is a unique feature of mechanotransduction. *Proc Natl Acad Sci U S A* 105:6626–31.

119. Gronthos S, Simmons P., Graves S., G. Robey P (2001) Integrin-mediated interactions between human bone marrow stromal precursor cells and the extracellular matrix. *Bone* 28:174–81.

120. Shao Y, Sang J, Fu J (2015) On human pluripotent stem cell control: The rise of 3D bioengineering and mechanobiology. *Biomaterials* 52:26–43.

121. Hynes RO (1992) Integrins: versatility, modulation, and signaling in cell adhesion. *Cell* 69:11–25.

122. Humphries JD, Byron A, Humphries MJ (2006) Integrin ligands at a glance. *J Cell Sci* 119:3901–3.

123. Goessler UR et al. (2008) Integrin expression in stem cells from bone marrow and adipose tissue during chondrogenic differentiation. *Int J Mol Med* 21:271–9.

124. Tang X, Tofangchi A, Anand SV, Saif TA. (2014) A novel cell traction force microscopy to study multi-cellular system. *PLoS Comput Biol* 10:e1003631.

125. Manning ML, Foty RA, Steinberg MS, Schoetz E-M (2010) Coaction of intercellular adhesion and cortical tension specifies tissue surface tension. *Proc Natl Acad Sci U S A* 107:12517–22.

126. Frith JE, Mills RJ, Cooper-White JJ (2012) Lateral spacing of adhesion peptides influences human mesenchymal stem cell behaviour. *J Cell Sci* 125:317–27.

127. Hidalgo-Bastida LA, Cartmell SH (2010) Mesenchymal stem cells, osteoblasts and extracellular matrix proteins: enhancing cell adhesion and differentiation for bone tissue engineering. *Tissue Eng Part B Rev* 16:405–12.

128. Humphrey JD, Dufresne ER, Schwartz MA (2014) Mechanotransduction and extracellular matrix homeostasis I E r. *Nat Rev Mol Cell Biol* 15:802–12.

129. Oakes PW, Gardel ML (2014) Stressing the limits of focal adhesion mechanosensitivity. *Curr Opin Cell Biol* 30:68–73.

130. Riveline D et al. (2001) Focal contacts as mechanosensors: Externally applied local mechanical force induces growth of focal contacts by an mDia1-dependent and ROCK-independent mechanism. *J Cell Biol* 153:1175–85.

131. Hamidouche Z et al. (2009) Priming integrin alpha5 promotes human mesenchymal stromal cell osteoblast differentiation and osteogenesis. *Proc Natl Acad Sci U S A* 106:18587–91.

132. Roca-Cusachs P, Gauthier NC, Del Rio A, Sheetz MP (2009) Clustering of alpha(5)beta(1) integrins determines adhesion strength whereas alpha(v)beta(3) and talin enable mechanotransduction. *Proc Natl Acad Sci U S A* 106:16245–50.

133. Sun Y, Chen CS, Fu J (2012) Forcing stem cells to behave: a biophysical perspective of the cellular microenvironment. *Annu Rev Biophys* 41:519–42.

134. Yim EKF, Sheetz MP (2012) Force-dependent cell signaling in stem cell differentiation. *Stem Cell Res Ther* 31:41.

135. Chien S (2007) Mechanotransduction and endothelial cell homeostasis : the wisdom of the cell. *Am J Physiol Heart Circ Physiol* 292:H1209–24.

136. Mammoto A, Mammoto T, Ingber DE (2012) Mechanosensitive mechanisms in transcriptional regulation. *J Cell Sci* 125:3061–73.

137. Eyckmans J, Boudou T, Yu X, Chen CS (2011) Perspective A Hitchhiker ' s Guide to Mechanobiology. *Dev Cell* 21:35–47

138. Ross TD et al. Integrins in mechanotransduction. *Curr Opin Cell Biol* 25:613–8.

139. Engler A et al. (2004) Substrate Compliance versus Ligand Density in Cell on Gel Responses. *Biophys J* 86:617–28.

140. Young DA, Choi YS, Engler AJ, Christman KL (2013) Biomaterials Stimulation of adipogenesis of adult adipose-derived stem cells using substrates that mimic the stiffness of adipose tissue. *Biomaterials* 34:8581–8.

141. Burdick JA, Murphy WL (2012) Moving from static to dynamic complexity in hydrogel design. *Nat Commun* 3:1269.

142. Kloxin AM, Tibbitt MW, Anseth KS (2010) Synthesis of photodegradable hydrogels as dynamically tunable cell culture platforms. *Nat Protoc* 5:1867–87.

143. Levental KR et al. (2009) Matrix crosslinking forces tumor progression by enhancing integrin signaling. *Cell* 139:891–906.

144. Tondreau T et al. (2004) Bone marrow-derived mesenchymal stem cells already express specific neural proteins before any differentiation. *Differentiation* 72:319–26.

145. Gao L, McBeath R, Chen CS (2010) Stem cell shape regulates a chondrogenic versus myogenic fate through Rac1 and N-cadherin. *Stem Cells* 28:564–72.

146. Mehlen P, Puisieux A (2006) Metastasis: a question of life or death. *Nat Rev Cancer* 6:449–58.

147. Visvader JE, Lindeman GJ (2008) Cancer stem cells in solid tumours: accumulating evidence and unresolved questions. *Nat Rev Cancer* 8:755–68.

148. Dean M, Fojo T, Bates S (2005) Tumour stem cells and drug resistance. *Nat Rev Cancer* 5:275–84.

149. Chang C-W, van Spreeuwel A, Zhang C, Varghese S (2010) PEG/clay nanocomposite hydrogel: a mechanically robust tissue engineering scaffold. *Soft Matter* 6:5157–64.

150. Sil H, Sen T, Chatterjee A (2011) Fibronectin-integrin (alpha5beta1) modulates migration and invasion of murine melanoma cell line B16F10 by involving MMP-9. *Oncol Res* 19:335–48.

151. Roux PP, Blenis J (2004) ERK and p38 MAPK-activated protein kinases: a family of protein kinases with diverse biological functions. *Microbiol Mol Biol Rev* 68:320–44.

152. Nicholas C, Lesinski GB (2010) The Jak-STAT signal transduction pathway in melanoma. (2009) *INTECH* Chapter 14.

153. Lu P, Weaver VM, Werb Z (2012) The extracellular matrix: A dynamic niche in cancer progression. *J Cell Biol* 196:395–406.

154. Lecuit T, Lenne P-F (2007) Cell surface mechanics and the control of cell shape, tissue patterns and morphogenesis. *Nat Rev Mol Cell Biol* 8:633–44.

155. Kollmannsberger P, Bidan CM, Dunlop JWC, Fratzl P (2011) The physics of tissue patterning and extracellular matrix organisation: how cells join forces. *Soft Matter* 7:9549–60.

156. Hegerfeldt Y, Tusch M, Bröcker E-B, Friedl P (2002) Collective cell movement in primary melanoma explants. *Cancer Res* 62:2125–30.

157. Goldberg AD, Allis CD, Bernstein E (2007) Epigenetics: A Landscape Takes Shape. *Cell* 128:635–8.

158. Feinberg AP, Tycko B (2004) The history of cancer epigenetics. *Nat Rev Cancer* 4:143–53.

159. Leightone J. Core, Josua J. Waterfall JTL (2008) Nascent RNA Sequencing Reveals Widespread Pausing and Divergent Initiation at Human Promoters. *Science* 322:1845–8.

160. Schuettengruber B, Chourrout D, Vervoort M, Leblanc B, Cavalli G (2007) Genome Regulation by Polycomb and Trithorax Proteins. *Cell* 128:735–45.

161. Schatton T et al. (2008) Identification of cells initiating human melanomas. *Nature* 451:345–9.

162. Meacham CE, Morrison SJ (2013) Tumour heterogeneity and cancer cell plasticity. *Nature* 501:328–37.

163. Hjelmeland AB et al. (2011) Acidic stress promotes a glioma stem cell phenotype. *Cell Death Differ* 18:829–40.

164. Lee J, Abdeen AA, Wycislo KL, Fan TM, Kilian KA (2016) Interfacial geometry dictates cancer cell tumorigenicity. *Nat Mater* 15:856–62.

165. Lagadec C, Vlashi E, Della Donna L, Dekmezian C, Pajonk F (2012) Radiation-induced reprogramming of breast cancer cells. *Stem Cells* 30:833–44.

166. Pang MF et al. (2016) Tissue stiffness and hypoxia modulate the integrin-linked kinase ilk to control breast cancer stem-like cells. *Cancer Res* 76:5277–87.

167. Heddleston JM, Li Z, McLendon RE, Hjelmeland AB, Rich JN (2009) The hypoxic microenvironment maintains glioblastoma stem cells and promotes reprogramming towards a cancer stem cell phenotype. *Cell Cycle* 8:3274–84.

168. Hartman SE et al. (2005) Global changes in STAT target selection and transcription regulation upon interferon treatments. *Genes Dev* 19:2953–68.

169. Klein BJ et al. (2014) The histone-H3K4-specific demethylase KDM5B binds to its substrate and product through distinct PHD fingers. *Cell Rep* 6:325–35.

170. Li Q et al. (2011) Binding of the JmjC demethylase JARID1B to LSD1/NuRD suppresses angiogenesis and metastasis in breast cancer cells by repressing chemokine CCL14. *Cancer Res* 71:6899–908.

171. Yoshida M et al. (2011) PLU1 histone demethylase decreases the expression of KAT5 and enhances the invasive activity of the cells. *Biochem J* 437:555–64.

172. Chen K et al. (2015) Broad H3K4me3 is associated with increased transcription elongation and enhancer activity at tumor-suppressor genes. *Nat Genet* 47:1149–57.

173. Shahbazian MD, Grunstein M (2007) Functions of site-specific histone acetylation and deacetylation. *Annu Rev Biochem* 76:75–100.

174. Mullican SE et al. (2011) Histone deacetylase 3 is an epigenomic brake in macrophage alternative activation. *Genes Dev* 25:2480–8.

175. Hollenhorst PC et al. (2011) Oncogenic ETS proteins mimic activated RAS/MAPK signaling in prostate cells. *Genes Dev* 25:2147–57.

176. Rothhammer T et al. (2004) The Ets-1 transcription factor is involved in the development and invasion of malignant melanoma. *Cell Mol Life Sci* 61:118–28.

177. Spangler B et al. (2012) ETS-1/RhoC signaling regulates the transcription factor c-Jun in melanoma. *Int J Cancer* 130:2801–11.

178. Ben-batalla I et al. (2010) Deregulation of the Pit-1 transcription factor in human breast cancer cells promotes tumor growth and metastasis. *J Clin Invest* 120:4289–302.

179. Tudrej KB, Czepielewska E, Kozłowska-wojciechowska M, Sci AM (2016) SOX10-MITF pathway activity in melanoma cells. *Arch Med Sci* DOI: 10.5114/aoms.2016.60655.

180. Shakhova O et al. (2012) Sox10 promotes the formation and maintenance of giant congenital naevi and melanoma. *Nat Cell Biol* 14:882–90.

181. Garraway LA et al. (2005) Integrative genomic analyses identify MITF as a lineage survival oncogene amplified in malignant melanoma. *Nature* 436:117–22.

182. Potterf SB, Furumura M, Dunn KJ, Arnheiter H, Pavan WJ (2000) Transcription factor hierarchy in Waardenburg syndrome: Regulation of MITF expression by SOX10 and PAX3. *Hum Genet* 107:1–6.

183. Bissell MJ, Hines WC, Berenblum I (2011) Why don' t we get more cancer ? A proposed role of the microenvironment in restraining cancer progression. *Nat Publ Gr* 17:320–29.

184. Reya T, Morrison SJ, Clarke MF, Weissman IL (2001) Stem cells, cancer, and cancer stem cells. *Nature* 414:105–11.

185. Dalerba P, Cho RW, Clarke MF (2007) Cancer stem cells: models and concepts. *Annu Rev Med* 58:267–84.

186. Folkman J (1971) A controlled trial of ganciclovir to prevent cytomegalovirus disease after heart transplantation.*N Engl J Med* 18:1182–6.

187. Kerbel RS (2008) Tumor Angiogenesis. *N Engl J Med* 18:2039–49.

188. Ferrara N, Gerber H, Lecouter J (2003) The biology of VEGF and its receptors. *Nat Med* 9:669–76.

189. John A, Tuszynski G (2001) The role of matrix metalloproteinases in tumor angiogenesis and tumor metastasis. *Pathol Oncol Res* 7:14–23.

190. Pugh CW, Ratcliffe PJ (2003) Regulation of angiogenesis by hypoxia : role of the HIF system. *Nat Med* 9:677–84.

191. Liao D, Johnson RS (2007) Hypoxia : A key regulator of angiogenesis in cancer. *Cancer Metastasis Rev* 26:281–290.

192. Ke Q, Costa M (2006) Hypoxia-Inducible Factor-1 (HIF-1). *Mol Pharmacol* 70:1469–1480.

193. Xu Q et al. (2005) Targeting Stat3 blocks both HIF-1 and VEGF expression induced by multiple oncogenic growth signaling pathways. *Oncogene* 24:5552–60.

194. Ordon R (2013) Inhibition of VEGF expression through blockade of Hif1 a and STAT3 signalling mediates the anti-angiogenic effect of melatonin in HepG2 liver cancer cells. *Br J Cancer* 109:83–91.

195. Cao Y et al. (2005) Observation of incipient tumor angiogenesis that is independent of hypoxia and hypoxia inducible factor-1 activation. *Cancer Res* 65:5498–5505.

196. Meierjohann S (2015) Hypoxia-independent drivers of melanoma angiogenesis. *Front Oncol* 5:102.

197. Zhang et al. (2009) FoxM1B transcriptionally regulates vascular endothelial growth factor expression and promotes the angiogenesis and growth of glioma cells. *Cancer Res* 68:8733–42.

198. Breier G et al. (2002) Transforming growth factor-beta and Ras regulate the VEGF/VEGF-receptor system during tumor angiogenesis. *Int J Cancer* 148:142–8.

199. Schaafhausen MK et al. (2001) Tumor angiogenesis is caused by single melanoma cells in a manner dependent on reactive oxygen species and NF- k B. *J Cell Sci* 126:3862–72.

200. Barnhill RL, Levy MA (1993) Regressing Thin Cutaneous Malignant Melanomas (< 1 . 0 mm) Are Associated with Angiogenesis. *Am J oh Pathol* 143:99–104.

201. Brooks PC, Clark RA, Cheresh DA (1994) Requirement of vascular integrin alpha v beta 3 for angiogenesis. *Science* 264:569–71.

202. Brooks PC et al. (2016) Integrin alpha v beta 3 antagonists promote tumor regression by inducing apoptosis of angiogenic blood vessels. *Cell* 79:1157–64.

203. Hellwig-bu BT, Rutkowski K, Metzen E, Fandrey J, Jelkmann W (1999) Interleukin-1beta and tumor necrosis factor-alpha stimulate DNA binding of hypoxia-inducible factor-1. *Blood* 94:1561–7.

204. Feldser D et al. (1999) Reciprocal positive regulation of hypoxia-inducible factor 1alpha and insulin-like growth factor 2. *Cancer Res* 59:3915–8.

205. Salnikow K, Blagosklonny MV, Ryan H, Johnson R, Costa M (2000) Carcinogenic nickel induces genes involved with hypoxic stress. *Cancer Res* 60:38–41.

206. Haddad JJ, Land SC (2001) A non-hypoxic, ROS-sensitive pathway mediates TNF-alpha-dependent regulation of HIF-1alpha. *FEBS Lett* 505:269–74.

207. Kumar SM et al. (2007) Mutant V600E BRAF increases hypoxia inducible factor-1alpha expression in melanoma. *Cancer Res* 67:3177–84.

208. Li YM et al. (2005) A hypoxia-independent hypoxia-inducible factor-1 activation pathway induced by phosphatidylinositol-3 kinase/Akt in HER2 overexpressing cells. *Cancer Res* 65:3257–3263.

209. Sang N et al. (2003) MAPK signaling up-regulates the activity of hypoxia-inducible factors by its effects on p300. *J Biol Chem* 278:14013–9.

210. Niu G et al. (2008) Constitutive Stat3 activity up-regulates VEGF expression and tumor angiogenesis. *Oncogene* 21:2000–8.

211. Bao S et al. (2006) Stem cell-like glioma cells promote tumor angiogenesis through vascular endothelial growth factor. *Cancer Res* 66:7843–8.

212. Grange C et al. (2011) Microvesicles released from human renal cancer stem cells stimulate angiogenesis and formation of lung premetastatic niche. *Cancer Res* 71:5346–56.

213. Corominas-Faja B et al. (2013) Nuclear reprogramming of luminal-like breast cancer cells generates Sox2-overexpressing cancer stem-like cellular states harboring transcriptional activation of the mTOR pathway. *Cell Cycle* 12:3109–24.

214. Vazquez-Martin A et al. (2013) Reprogramming of non-genomic estrogen signaling by the stemness factor SOX2 enhances the tumor-initiating capacity of breast cancer cells. *Cell Cycle* 12:3471–7.

215. Vêncio EF et al. (2012) Reprogramming of prostate cancer-associated stromal cells to embryonic stem-like. *Prostate* 72:1453–63.

216. Chiou SH et al. (2010) Coexpression of Oct4 and Nanog enhances malignancy in lung adenocarcinoma by inducing cancer stem cell-like properties and epithelial-mesenchymal transdifferentiation. *Cancer Res* 70:10433–44.

217. Mahalingam D et al. (2012) Reversal of aberrant cancer methylome and transcriptome upon direct reprogramming of lung cancer cells. *Sci Rep* 2:592.

218. Carette JE et al. (2010) Brief report Generation of iPSCs from cultured human malignant cells. *Blood* 115:4039–42.

219. Kumano K et al. (2016) Generation of induced pluripotent stem cells from primary chronic myelogenous leukemia patient samples. *Blood* 119:6234–43.

220. Utikal J, Maherali N, Kulalert W, Hochedlinger K (2009) Sox2 is dispensable for the reprogramming of melanocytes and melanoma cells into induced pluripotent stem cells. *J Cell Sci* 122:3502–10.

221. Lin S-L et al. (2008) Mir-302 reprograms human skin cancer cells into a pluripotent ES-cell-like state. *RNA* 14:2115–24.

222. Malanchi I et al. (2008) Cutaneous cancer stem cell maintenance is dependent on beta-catenin signalling. *Nature* 452:650–3.

223. Zeng YA, Nusse R (2010) Wnt proteins are self-renewal factors for mammary stem cells and promote their long-term expansion in culture. *Cell Stem Cell* 6:568–77.

224. Guo G et al. (2010) Oncogenic E17K mutation in the pleckstrin homology domain of AKT1 promotes v-Abl-mediated pre-B-cell transformation and survival of Pim-deficient cells. *Oncogene* 29:3845–53.

225. Pan Y, Zhou C, Yuan D, Zhang J, Shao C (2016) Radiation Exposure Promotes Hepatocarcinoma Cell Invasion through Epithelial Mesenchymal Transition Mediated by H_2S/CSE Pathway. *Radiat Res* 185:96–105.

226. Dontu G et al. (2004) Role of Notch signaling in cell-fate determination of human mammary stem/progenitor cells. *Breast Cancer Res* 6:R605–15.

227. Takahashi K et al. (2007) Induction of pluripotent stem cells from adult human fibroblasts by defined factors. *Cell* 131:861–72.

228. Kasinski AL, Slack FJ (2011) Epigenetics and genetics. MicroRNAs en route to the clinic: progress in validating and targeting microRNAs for cancer therapy. *Nat Rev Cancer* 11:849–64.

229. Louie E et al. (2010) Identification of a stem-like cell population by exposing metastatic breast cancer cell lines to repetitive cycles of hypoxia and reoxygenation. *Breast Cancer Res* 12:R94.

230. Chen L et al. (2012) A model of cancer stem cells derived from mouse induced pluripotent stem cells. *PLoS One* 7:e33544.

231. Abaan OD et al. (2013) The exomes of the NCI-60 panel: A genomic resource for cancer biology and systems pharmacology. *Cancer Res* 73:4372–82.

232. Gillet J et al. (2011) Redefining the relevance of established cancer cell lines to the study of mechanisms of clinical anti-cancer drug resistance. *Proc Natl Acad Sci U S A* 108:18708–13.

233. Hausser HJ, Brenner RE (2005) Phenotypic instability of Saos-2 cells in long-term culture. *Biochem Biophys Res Commun* 333:216–22.

234. Ogino S, Galon J, Fuchs CS, Dranoff G (2011) Cancer immunology--analysis of host and tumor factors for personalized medicine. *Nat Rev Clin Oncol* 8:711–9.

235. Siolas D, Hannon GJ (2013) Patient-derived tumor xenografts: Transforming clinical samples into mouse models. *Cancer Res* 73:5315–9.

236. Hidalgo M et al. (2014) Patient-derived Xenograft models: An emerging platform for translational cancer research. *Cancer Discov* 4:998–1013.

APPENDIX A

GENERAL METHODS

Materials

Lab Chemicals were purchased from Sigma-Aldrich unless otherwise stated. Human MSCs were purchased from Lonza. The MSCs were harvested and cultured from normal bone marrow. Cells were tested for the ability of differentiation and the results showed that osteogenic, chondrogenic, or adipogenic lineage commitments are possible. Cells were positive for CD105, CD166, CD29, and CD44 and negative for CD14, CD34, and CD45 by flow cytometry (http:// www.lonza.com). The use of human MSCs in this work was reviewed and approved by the University of Illinois at Urbana-Champaign Biological Safety Institutional Review Board. Cell culture media and reagents were purchased from Gibco. BrdU reagent was purchased from Invitrogen. Tetramethylrhodamine-conjugated antirabbit IgG antibody, Alexa Fluor 647-conjugated antimouse IgG antibody, Alexa Fluor 555-conjugated antirabbit IgG antibody, Alexa488-phalloidin and 4,6-diamidino-2-phenylindole (DAPI) were purchased from Invitrogen. 12-well tissue culture plastic ware and glass coverslips (18 mm circular) for surface preparation were purchased from Fisher Scientific. Hydrazine hydrate was purchased from Fisher Scientific. Human extracellular matrix Proteins (fibronectin, collagen I and laminin α1) were purchased from Sigma. hMVECs were purchased from cell-systems. EGM-2 growth factor supplemented media was purchased from Lonza. The use of human cell lines in this work was reviewed and approved by the University of Illinois at Urbana-Champaign Biological Safety Institutional Review Board.

Polyacrylamide gel fabrication and Soft Lithography

Polyacrylamide gels were fabricated on a glass coverslip (18 mm) as reported previously.33 Hydrogels of varying stiffness were made by mixing varying amounts of acrylamide and bis-acrylamide to get the desired stiffness. To initiate the reaction, 0.1% ammonium persulfate (APS) and 0.1% of tetramethylethylenediamine (TEMED) were employed. The amino-silanized coverslips (3-aminopropyltriethoxysilane 3 min and glutaraldehyde 30 min) were added with the treated side down onto hydrophobically treated glass slides with 20 ul of the gel mixture. After an appropriate polymerization time for each stiffness condition, the gel-coated coverslips were gently detached. Hydrazine hydrate (55%) was added for 2 h to convert amide groups in polyacrylamide to reactive hydrazide groups.34 The gels were washed for an hour in 5% glacial acetic acid and for 1 h in distilled water. Polydimethylsiloxane (PDMS, Polysciences, Inc.) stamps were produced by conventional polymerization methods on silicon masters patterned with photoresist (SU-8, Micro- Chem), which were created using UV photolithography through a laser printed mask or unpatterned (flat) surfaces. After

Cell culture

MSCs from bone marrow were thawed from cryopreservation (10% DMSO) and cultured in Dulbecco's modified eagle's medium (DMEM) low glucose (1 g/mL) media supplemented with 10% fetal bovine serum (MSC approved FBS; Invitrogen), and 1% penicillin/streptomycin (p/s). Media was changed every 3 or 4 days.

Passage 4−7 MSCs were seeded on patterned and nonpatterned surfaces at a cell density of ~5000 cells/cm^2. MSCs were cultured for 10 days before analysis.

Immunofluorescence

Cells on surfaces were fixed with 4% paraformaldehyde (Alfa Aesar) for 20 min, permeablized in 0.1% Triton X-100 in PBS for 30 min and blocked with 1% bovine serum albumin (BSA) for 15 min. Primary antibody labeling was performed in 1% BSA in PBS for 2 h at room temperature (20 °C) (1:200 dilution). Secondary antibody labeling was performed using the same procedure with Tetramethylrhodamine-conjugated antirabbit IgG antibody, Alexa Fluor 488-phalloidin (1:200 dilution), Alexa647-conjugated antimouse IgG antibody, and 4,6-diamidino-2-phenylindole (DAPI, 1:5000 dilution) for 20 min in a humid chamber (37 °C). Immunofluorescence microscopy was conducted using a Zeiss Axiovert 200 M inverted research-grade microscope (Carl Zeiss, Inc.) or an LSM 700 (Carl Zeiss, Inc.) which is a four laser point scanning confocal with a single pinhole. Immunofluorescent images from the immunofluorescence microscopy or the LSM 700 were analyzed using ImageJ; the fluorescence intensity of single cells (over 20 cells) and multiple cells (over 20 patterns) for each condition were measured to compare marker expression. All results were confirmed at least three times. The relative intensity of the fluorescence was determined by comparing each intensity value to the average intensity of one condition.

Vascularization assays

Conditioned media was collected from the cultured B16F0s and the cells were fixed and stained at a desired time. 25 µL of matrigel was pipetted into each well of a 48 well plate. The plate was then placed in the incubator for 30 minutes to form the gel structure. hMVECs of low passage (p2-p6) were seeded at ~15,000 cells/well. 400 µL of conditioned media obtained from the gels at the desired time were added at each condition. The assay was incubated and Images of the wells were taken at different time-points using a Cannon Rebel DSLR camera on an inverted microscope at 40x zoom.